

UNIVERSITÀ DEGLI STUDI DI CATANIA
DIPARTIMENTO DI FISICA E ASTRONOMIA
XXXII CICLO DI DOTTORATO

FRANCESCO SCHILLACI

DESIGN AND REALIZATION OF A BEAM TRANSPORT LINE FOR HANDLING AND SELECTING LASER-DRIVEN ION BEAMS FOR MULTIDISCIPLINARY APPLICATIONS

PhD Thesis

PhD Coordinator:
Prof. V. Bellini

Tutor:
Prof. S. Romano

ACADEMIC YEAR 2018-2019

A Calliope,
La piccola musa che inspira ogno momento della mia vita

A Leo Icaro,
Che un giorno quel sole lo raggiungerà davvero, senza far scioglere le sue ali

A Mara,
Senza i cui silenzi questo lavoro sarebbe stato impossible da scrivere

A Maria Rosa e Ines,
Perchè se no si incazzano

Index

0 Introduction

Hadrontherapy is currently considered to be one of the most advanced and precise external radiotherapy techniques for tumour treatment [1]. Hadrons have advantages with respect to more conventional radiation sources (electrons and gamma-rays) in terms of both spatial precision of the released dose and biological effectiveness. The so called ***Bragg curves*** describe this characteristic behavior of ions which allows to spear the healthy tissues near the tumor, which is in contrast with X-ray or electron based therapy. Unfortunately, availability of hadrontherapy is still very limited worldwide despite considerable clinical evidence in its favour. The main reasons for this are huge costs for construction, installation and maintenance associated with complex accelerators (mostly cyclotrons and synchrotrons, and, in general, technical complexity of the facility management and the fact that other radiation therapies have a longer history of use. The use of more compact hadrontherapy approaches would obviously have a valuable impact on society.

Laser-plasma ion acceleration is a new field of Physics rapidly evolving thanks to the continuing development of high power laser systems, thus allowing to investigate the interaction of ultrahigh laser intensities ($>10^{19}$ W/cm^2) with matter. As a result of such interaction, extremely high electric and magnetic fields are generated. Such tremendous fields, which can be supported only in plasmas, allow to accelerate particles at relativistic energies by very compact approaches (in sub-mm distances). Typically, these high energy ion beams are produced in thin (μm-scale) solid targets and accelerated by a sheath field developed at the target-vacuum interface as a consequence of the generation of relativistic plasma electrons ("hot electrons") propagating into vacuum. Ion acceleration takes place until charge neutrality is restored and ultimately ions and electrons move together in a ballistic way. According to the state-of-the-art in laser-driven ion acceleration, maximum proton energies of several tens of MeV have been experimentally demonstrated with a relatively high yield (10^{10}–10^{12} protons/pulse) [2]. However, laser-accelerated ion beams are still not fully mature for some applications where additional features, such as low divergence, small energy bandwidth, spatial profile uniformity, shot-to-shot stability, are essential. New laser technologies which will be soon available for the scientific community, e.g., fully diode-pumped lasers at ELI-Beamlines [3, 4], will allow to investigate new regimes which are very promising in terms of future use of laser driven ion beams for various applications, also given the expected high stability of these laser systems.

Such non-conventional acceleration schemes have been intensively investigated in the last 15 years and the field is rapidly growing thanks to the continuing development of high power laser systems. The main goal of the laser-driven ion acceleration community is to deliver reliable and very compact approaches to be possibly used for societal applications, with the aim of reducing the overall cost of standard accelerator facilities [5]. In order to overcome the existing challenges new laser technologies have to be exploited, in particular enabling simultaneously high peak power (multi-Petawatt) and high repetition rate (up to 10 Hz) which are about to be available at ELI-Beamlines (Dolní Břežany, Czech Republic). As an example of possible advantages of a laser-based approach, transporting the laser pulse to the treatment rooms to generate the ion source closer to the patient would drastically reduce costs related to ion beamlines. Furthermore, laser-based hadron radiotherapy would uniquely offer the option of synchronous delivery of multiple beams of photons, electrons and different ion species (e.g., He and C ions), with enhanced capabilities for mixed field irradiations, an approach also of interest to cancer therapy [6].

0 Introduction

This work focuses on the design, development and installation of the beamline for selecting and handling the ion beams that will be accelerated at the ELI-Beamlines in the dedicated experimental hall ELIMAIA (ELI multidisciplinary applications of laser-ion acceleration). The beamline, partially characterized with conventionally accelerated beams, represents an extremely compact accelerator of 10m length (from the laser-target interaction point to the irradiation point) that would allow users to perform experiments using the unique ion beams accelerated with Peta-watt class laser available at ELI-Beamlines, with particular care for dosimetric and irradiation studies. Moreover, a cenceptual design for upgrading the core element of the beamline (the energy selector) is presented. This upgrade would allow to use the device also as a Thomson Parabola spectrometer which is a fundamental diagnostics for laser-driven ion beams. This spectrometer would allow to analyze ions with energies of few hundreds of MeV per nucleons with considerably high precision.

References

[1] Orecchia, R. et al., *Particle Beam Therapy (Hadrontherapy): Basis for Interest and Clinical Experience*. Eur. J. Cancer **2008**, 34, 459–468.
[2] Macchi, A. et al., *Ion acceleration by superintense laser-plasma interaction*. Rev.Mod. Phys. **2013**, 85, 751
[3] ELI-Beamlines. Available online: https://www.eli-beams.eu/en/ (accessed on 4 March 2018).
[4]ELIMAIA. Available online: https://www.eli-beams.eu/en/facility/experimental-halls/e4-ionacceleration/elimaia/ (accessed on 4 March 2018).
[5] Bulanov, S.V.; Khoroshkov, V.S. *Feasibility of Using Laser Ion Accelerators in Proton Therapy*. Plasma Phys. Rep. **2002**, 28, 453–456.
[6] DeLaney, T.F. et al. *Phase II study of high-dose photon/proton radiotherapy in the management of spine sarcomas*. Int. J. Radiat. Oncol. Biol. Phys. **2009**, 74, 732–739.

1 The physics of plasma based laser accelerators

Murphy's Law of Plasma Physics:
If a plasma can go unstable, then
it will do so in the most damaging
manner possible [5].

This chapter underlines the basics features of plasmas and laser plasma interactions. More detailed descriptions could be find in [1, 2, 4, 5, 6]. There will be also a brief description of different ion acceleration regimes for which more references will provided in the following.

1.1 Basics of plasma physics

A plasma is basically a fully ionized gas. For any temperature, an ordinary gas has a certain amount of ionized atoms even if the number of neutral particles exceeds the number of ions. On the other hand, for a plasma is the number of ionized particles that exceeds the number on neutral ones.

The most easy way to form a plasma is to warm up a gas to such a temperature that the mean energy of its particles is at least equal, or higher, to the ionization energy of its atoms. As a plasma can be obtained by heating a gas, sometimes it is referred as the *fourth state of matter.*

For a plasma with only one species of neutral particles, monovalent ions of the same kind and electrons, the ionization state at thermodynamic equilibrium is described by the so called *Saha equation:*

$$\frac{n_i n_e}{n_n} = \frac{2(2\pi m_e T)^{3/2}}{h^3} \exp\left(-\frac{E_i}{T}\right) \equiv f(T) \tag{1.1.1}$$

where n_e, n_i and n_n are the electron, ion and neutral atoms densities, E_i is the atoms ionization energy, m_e is the electron mass, h is the Plank's constant and T is the temperature in energetic units *(eV),* namely $T=k_B T_k$, being T_k the temperature in Kelvin.

The thermodynamic equilibrium is not a frequent condition for a plasma. A more realistic situation is the so called *local thermodynamic equilibrium (LTE)* which is characterized by the fact that the dynamic properties of plasma particles, such as electron and ion velocities, population among the excited atomic state and ionization state densities, follow *Boltzmann distribution:*

$$n_{jm} \propto \exp\left(-\frac{\varepsilon_{jm}}{T}\right) \tag{1.1.2}$$

but the temperature of the distributions is different for electron and ion.

The *Saha equation* is satisfied for plasma in *LTE* and a more general version of (1.1.1) for a plasma with different species of atoms and ions is derived in [2].

In contrast to complete thermodynamic equilibrium, in *LTE* the radiation may escape from the plasma, therefore it is not necessarily in equilibrium with the plasma particles. In this case all laws of thermodynamic equilibrium are valid except Planck's law.

LTE is mainly valid for high-density plasmas, where the frequent collisions between electrons and ions, or between electrons themselves, produce equilibrium. For this to happen it is necessary that the electron and ion densities must be high enough for collisional processes to be more important than the dissipative processes.

From a dynamical point of view a plasma is a statistically relevant number of charger particles interacting with and generating electromagnetic fields. In principle, the dynamics of a plasma is fully determined considering that the force acting on each relativistic particle is the Lorentz force and the electromagnetic fields evolution is governed by Maxwell equations. In cgs we have:

$$\begin{cases} \dot{\boldsymbol{x}}_i = \boldsymbol{v}_i \\ \dot{\boldsymbol{p}}_i = q_i \left(\boldsymbol{E}(\boldsymbol{x}_i) + \dfrac{\boldsymbol{v}_i \wedge \boldsymbol{B}(\boldsymbol{x}_i)}{c} \right) \end{cases} \tag{1.1.3}$$

$$\begin{cases} \nabla \cdot \boldsymbol{B} = 0 \\ \nabla \cdot \boldsymbol{E} = 4\pi\rho \\ \nabla \wedge \boldsymbol{B} - \dfrac{1}{c}\dfrac{\partial \boldsymbol{E}}{\partial t} = \dfrac{4\pi}{c}\boldsymbol{J} \\ \nabla \wedge \boldsymbol{E} = -\dfrac{1}{c}\dfrac{\partial \boldsymbol{B}}{\partial t} \end{cases} \tag{1.1.4}$$

where $\boldsymbol{x}_i$ and $\boldsymbol{p}_i = m_i \gamma_i \boldsymbol{v}_i$ are the vector position and momentum of the i-th particle and ρ and $\boldsymbol{J}$ are the source term calculated starting from particles' phase space distribution without doing any spatial average operation in order to include binary collision in the model.

From equations (1.1.3) and (1.1.4) it is easy to understand that if we consider a plasma with N charges, coupled one to another via their self-consistent electromagnetic fields, we would have to solve a system of $6N$ coupled equation.

This approach is very impractical both numerically and analytically, but the model can be simplified focusing our attention to collisionless plasmas. The validity of the collisioneless model is evaluated considering the *Debye length* and its relation with other parameters.

1.1.1 Debye length

In order to understand the meaning of the Debye length we consider a hydrogen-like fully ionized plasma with electron and ion densities n_e and n_i respectively. If the plasma is in LTE condition, then the electron and ion densities are $n_e = n_i = n_0$ everywhere; it means that the plasma is in an unperturbed state.

Now we suppose to perturb the system with a point-like charge $Q>0$ at rest in the origin of the coordinates frame surrounded by plasma particles. In vacuum the electrostatic field of Q would be $\phi(r) = Q/r$ but inside the plasma the electric charge density ρ_e to be used in Poisson equation have to take in account even the polarization charge density due to the difference between the electron and ion density near the charge Q which can be written as $e(n_i - n_e)$. Then Poisson equation for our problem reads:

$$\nabla^2\phi = -4\pi\,\rho_e = 4\pi\,e(n_i - n_e) - 4\pi\,Q\,\delta(r) \tag{1.1.5}$$

In LTE conditions electron and ion densities follow the Boltzmann distribution:

$$n_j = n_0 \exp\left(-\frac{q_j \phi}{T_j}\right) \tag{1.1.6}$$

where *j=e, i* for electron and ion respectively and n_0 is the average electron and ion density in the unperturbed region where the plasma is neutral, i.e. far from the charge *Q*. Inserting equations (1.1.6) in (1.1.5) we get the self-consistent equation for the potential:

$$\nabla^2\phi = 4\pi\,e\,n_0\left[\exp\left(-\frac{q_i\phi}{T_i}\right) - \exp\left(-\frac{q_e\phi}{T_e}\right)\right] - 4\pi\,Q\,\delta(r) \tag{1.1.7}$$

This equation can be solved for great distances from the charge *Q,* where the potential energy is much less than thermal energy: $e\phi \ll T_{i,e}$

For such distances we can expand the RHS of (1.1.7) with the condition $r \neq 0$ to get:

$$\nabla^2\phi = 4\pi e^2 n_0\left(\frac{1}{T_e} + \frac{1}{T_i}\right)\phi \tag{1.1.8}$$

Using the point symmetry of the problem, and defining

$$\lambda_{D_{e,i}} = \sqrt{\frac{T_{e,i}}{4\pi\,n_0 e^2}} \quad \text{and} \quad \frac{1}{\lambda_D^2} = \frac{1}{\lambda_{D_e}^2} + \frac{1}{\lambda_{D_i}^2} \tag{1.1.9}$$

the above equation becomes:

$$\frac{1}{r^2}\frac{d}{dr}\left(r^2\frac{d\phi}{dr}\right) = \frac{\phi}{\lambda_D^2} \tag{1.1.10}$$

which solution, with the conditions

$$\begin{cases} \phi \to 0 \quad \text{if} \quad r \to \infty \\ \phi \to \dfrac{Q}{r} \quad \text{if} \quad r \ll \lambda_D \end{cases} \tag{1.1.11}$$

is:

$$\phi = \frac{Q}{r}\exp\left(-\frac{r}{\lambda_D}\right) \tag{1.1.12}$$

The solutions (1.1.12) with the second condition (1.1.11) means that close to the charge *Q* its potential is the usual Coulomb potential because there is no screening effect. On the other hand, if $r>\lambda_D$ the potential is much weaker than the usual Coulomb potential because of the screening effect of the plasma, implying that the effective range of Coulomb interaction is shortened to a distance of the order of λ_D. In other words, on the sphere of radius λ_D there is a polarization charge that screens the electrostatic field. Such a sphere is

called *Debye sphere* and the characteristic screening distance is the *Debye length,* i.e. the space scale at which the plasma shields the electrostatic potential generated by a single point-like charge.

Note that the second equation (1.1.9) shows that for a plasma where the ion temperature T_i is not zero, also the ions contribute to the Debye shielding.

Now we assume that in a plasma with dimension $L > \lambda_D$, an external potential is introduced. In this case the created electric fields are shielded for a distance smaller than L. However, within dimensions of the order of λ_D the plasma is not neutral and the electric forces do not vanish there, although the plasma is neutral on the large scale. This situation describes the so called *quasineutrality* of the plasma.

Being $m_i \gg m_e$ it is reasonable to consider the ions as immobile in most of cases, specially for short time scales; it means $T_i=0$ and we can rewrite the Debye length as:

$$\lambda_D = \sqrt{\frac{T}{4\pi n_0 e^2}} \tag{1.1.13}$$

where T is now the electron temperature in energetic units *(eV)*.
With the above assumption it is easy to understand that the Debey shielding is effective only if the number of electron in the cloud surrounding charge Q is large enough. If there are only few electron in the Debey sphere the shielding is not relevant.

Therefore, defining the number of particles (e^-) in the Debye sphere as:

$$N_D = \frac{4}{3}\pi n_e \lambda_D^3 \tag{1.1.14}$$

the effective Debye shielding requires:

$$N_D \gg 1 \tag{1.1.15}$$

N_D is called *plasma parameter*, and condition (1.1.15) is strictly with the collisionless limit, as it will be shown later.

1.1.2 Fluid plasma description

The collisionless model can be further simplified to a fluid model if the phase space distribution can be considered as single valued for each point in space; i.e. for each point in space the velocity is defined univocally. The fluid model can be used to describe different collective behavior but it can not include wavebreaking phenomena in which different particles have different velocities in the same point.

A kinetic model that describes the state of the particles of a plasma can be developed by means of a distribution function $f_j(\boldsymbol{x}, \boldsymbol{p}, t)$ which represent the particles density of species j in the phase $(\boldsymbol{x}, \boldsymbol{p}=m\gamma\boldsymbol{v})$. In this way the number of particles in an elementary volume $d\boldsymbol{x}d\boldsymbol{p}$ is:

$$n = f_j(\boldsymbol{x}, \boldsymbol{p}, t) d\boldsymbol{x} d\boldsymbol{p} \tag{1.1.16}$$

Averaging the distribution function over momenta we can obtain macroscopical quantities for each species j of particles:

$$
\begin{aligned}
n_j(\boldsymbol{x}) &= \int f_j(\boldsymbol{x},\boldsymbol{p},t)\,d\boldsymbol{x}\,d\boldsymbol{p} \quad \textit{particle density} \\
n_j\boldsymbol{u}_j(\boldsymbol{x}) &= \int \boldsymbol{v} f_j(\boldsymbol{x},\boldsymbol{p},t)\,d\boldsymbol{x}\,d\boldsymbol{p} \quad \textit{mean velocity} \\
[P_{kl}(\boldsymbol{x})]_j &= m_j \int \boldsymbol{v}_k \boldsymbol{v}_l f_j(\boldsymbol{x},\boldsymbol{p},t)\,d\boldsymbol{x}\,d\boldsymbol{p} \quad \textit{mean pressure} \\
\rho_j(\boldsymbol{x}) &= q_j \int f_j(\boldsymbol{x},\boldsymbol{p},t)\,d\boldsymbol{x}\,d\boldsymbol{p} \quad \textit{charge density} \\
\boldsymbol{J}_j(\boldsymbol{x}) &= q_i \int \boldsymbol{v} f_j(\boldsymbol{x},\boldsymbol{p},t)\,d\boldsymbol{x}\,d\boldsymbol{p} \quad \textit{current density}
\end{aligned}
\tag{1.1.17}
$$

If we suppose that the number of particles and the volume in the phase space do not change, as stated by Liouville theorem, it is:

$$\frac{df_j}{dt}=0 \tag{1.1.18}$$

and considering that $\boldsymbol{x}$ and $\boldsymbol{p}$ are both function of time, equation (1.1.17) reads:

$$\frac{\partial f_j}{\partial t}+\boldsymbol{v}\nabla_x f_j+\dot{\boldsymbol{p}}\nabla_p f_j=0 \tag{1.1.19}$$

that is *Vlasov equation* which does not take in account collisions between particles. On a time scale of the same order of collision frequency, we should include a collisional term and use *Boltzmann equation.*

Coupling Vlasov equation with equations of motion (1.1.3) we have:

$$\frac{\partial f_j}{\partial t}+\boldsymbol{v}\nabla_x f_j+q_i\left(\boldsymbol{E}(\boldsymbol{x}_i)+\frac{\boldsymbol{v}_i\wedge\boldsymbol{B}(\boldsymbol{x}_i)}{c}\right)\nabla_p f_j=0 \tag{1.1.20}$$

where the electromagnetic fields are given by Maxwell equations (1.1.4) that close the system and make it self-consistent.

If we consider the momenta of Vlasov equation we can describe the plasma with n-fluid models in which each species j of particles is treated as a separate fluid interacting with the others by means of electromagnetic fields. This is the standard technique used to solve Vlasov equation, but the high cost to pay is that we get a hierarchy of equations coupled by terms that represent the next moment, as it is possible to see writing the first two momenta:

$$
\begin{aligned}
&\int d\boldsymbol{p}\left[\frac{\partial f_j}{\partial t}+\boldsymbol{v}\nabla_x f_j+q_i\left(\boldsymbol{E}(\boldsymbol{x}_i)+\frac{\boldsymbol{v}_i\wedge\boldsymbol{B}(\boldsymbol{x}_i)}{c}\right)\nabla_p f_j\right]=0 \\
&\int d\boldsymbol{p}\,\boldsymbol{p}\left[\frac{\partial f_j}{\partial t}+\boldsymbol{v}\nabla_x f_j+q_i\left(\boldsymbol{E}(\boldsymbol{x}_i)+\frac{\boldsymbol{v}_i\wedge\boldsymbol{B}(\boldsymbol{x}_i)}{c}\right)\nabla_p f_j\right]=0
\end{aligned}
\tag{1.1.21}
$$

Integrating the first equation (1.1.21) one gets the zero order moment equation, namely the continuity equation, as expected having assumed a constant number of particles:

$$\frac{\partial n_j}{\partial t}+\nabla_x \boldsymbol{J}_j=0 \tag{1.1.22}$$

Integrating the second equation (1.1.21) one gets the first order moment equation,

namely the Euler equation expressing momentum conservation:

$$\frac{\partial \boldsymbol{J}_j}{\partial t}+\frac{1}{m}\nabla_{\boldsymbol{x}}[P_{kl}]_j-\frac{q_j n_j}{m}\left(\boldsymbol{E}+\frac{\boldsymbol{u}_i\wedge\boldsymbol{B}}{c}\right)=0 \tag{1.1.23}$$

In this equation appears the tensor pressure P that represents the next moment, anyway it is reasonable to truncate the set of equation if we are able to link the pressure with other thermodynamic variables of the plasma. Usually if the system is in LTE conditions we can close the system as follow:

- for a cold plasma in which the electromagnetic forces prevail we can set the pressure $P_j=0$;
- if the heat flux is so fast that the fluid can be considered isothermal and we can set $P_j= n_j T_j$;
- if the heat flux in negligible and we can use the adiabatic equation for pressure: $P_j/n_j^{\gamma}=constant$ where the adiabatic exponent γ is defined as the ratio between the specific heats at constant pressure and volume and it is related with the number of freedom degree of the system.

With the above assumptions the energy equation, the third order moment, is no longer required and the hierarchy of equations is truncated.

1.1.3 Plasma oscillations and electron plasma waves

Using fluid equations we can study a common form of collective motions in a plasma: the charge and electrostatic field oscillation associated with the motion of the electrons.

We start considering a cold plasma, which temperature is zero and therefore the thermal velocities of electrons and ions vanish. In hydrodynamic theory this means that no pressure forces exist in the plasma. Also, we assume that ions are a stationary background of charge which neutralizes the unperturbed plasma at each point.

If a perturbation, such as an electromagnetic wave traveling in the plasma, is applied only to electrons an electromagnetic field is created and we want to understand how the electrons move in this case.

For this problem the following Maxwell equation is of interest:

$$\nabla\cdot\boldsymbol{E}=4\pi\rho_e \tag{1.1.24}$$

where ρ_e is the electric charge density related to the current density by the continuity equation:

$$\nabla\cdot\boldsymbol{J}_e+\frac{\partial\rho_e}{\partial t}=0 \tag{1.1.25}$$

Using Ohm law $\boldsymbol{J}_e=-n_e e\,\boldsymbol{v}_e=\sigma\,\boldsymbol{E}$ in (1.25) and after deriving with respect of the time and using (1.1.24), owe obtain an equation for ρ_e:

$$\frac{\partial^2\rho_e}{\partial t^2}+\left(\frac{4\pi e^2 n_e}{m_e}\right)\rho_e=0 \tag{1.1.26}$$

This equation describes an harmonic oscillation of the density and the quantity in brackets has the dimensions of the square of an angular frequency $[rad^2/sec^2]$ and it is

called *plasma frequency:*

$$\omega_{pe}=\left(\frac{4\pi e^2 n_e}{m_e}\right)^{1/2}\simeq 5.64\times 10^4\sqrt{n_e} \tag{1.1.27}$$

To understand the meaning of ω_{pe} we can consider a slab of plasma and a perturbation dispacing the electrons through a small distance x in a direction normal to the slab, while the ions are fixed and at rest.

As shown in *Figure 1.1*, the electrons' displacement induces an effective surface charge density $+n_e ex$ on the face of the original slab and $-n_e ex$ on the shifted face.

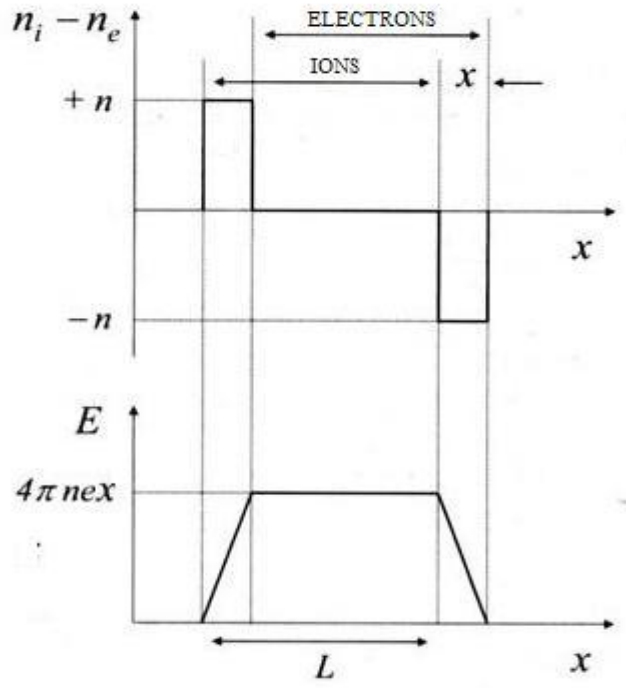

***Figure 1.1**: Violation of charge neutrality in a slab of plasma*

The charge separation creates an uniform electric field $E=4\pi n_e x$ that applies a restoring force on each electron. Newton's law of motion gives a simple harmonic motion of the electrons at the plasma frequency, then plasma oscillations are an expression of the plasma to preserve its electric neutrality. Plasma frequency is the resonance frequency of the collective electron density oscillations against the ion background.

Equation (1.1.26) actually does not describe a wave, that is, the oscillations do not propagate. In order to get a wave the plasma should have a non zero temperature. We can analyze the case in which the electrons have a temperature T_e and the ions are at rest, i.e. $T_i=0$. The fluid equations needed to solve the problem are the mass and momentum conservation:

$$\begin{cases}\dfrac{\partial n_e}{\partial t}+\nabla\cdot(n_e \boldsymbol{v_e})=0\\ m_e n_e\left[\dfrac{\partial \boldsymbol{v_e}}{\partial t}+(\boldsymbol{v_e}\cdot\nabla)\boldsymbol{v_e}\right]=-n_e e\,\boldsymbol{E}-\nabla P_e\end{cases} \tag{1.1.28}$$

where n_e, $\boldsymbol{v}_e$, $-e$ and m_e are the electron density, velocity, charge and mass, $\boldsymbol{E}$ is the electric field in the plasma and P_e is the electronic pressure linked with temperature via the state equation. For an ideal gas, with T_e in electronvolt, it reads:

$$P_e = n_e T_e \tag{1.1.29}$$

Moreover, using the adiabatic closure for the hierarchy of momenta, we can write:

$$P_e = C n_e^{\gamma} \tag{1.1.30}$$

being C a constant.

Using equations (1.1.29) and (1.1.30) ones get:

$$\nabla P_e = P_e \gamma \left(\frac{\nabla n_e}{n_e} \right) = \gamma T_e \nabla n_e \tag{1.1.31}$$

After using (1.1.31) in the momentum equation, the system (1.1.28) have to be solved together with Maxwell equation:

$$\nabla \cdot \boldsymbol{E} = 4\pi \left(n_i - n_e \right) \tag{1.1.32}$$

This equations are nonlinear but if the oscillation amplitudes are small and higher-order terms can be neglected we can use the following linearization procedure. We denote the equilibrium part by the subscript *0* and the oscillating amplitudes by the subscript *1*:

$$n_e = n_{e0} + n_{e1}; \qquad \boldsymbol{v}_e = \boldsymbol{v}_{e0} + \boldsymbol{v}_{e1}; \qquad \boldsymbol{E} = \boldsymbol{E}_0 + \boldsymbol{E}_1 \tag{1.1.33}$$

The equilibrium conditions for this model are:

$$n_{e0} = n_i = const.; \qquad \boldsymbol{v}_{e0} = 0; \qquad \boldsymbol{E}_0 = 0; \qquad \frac{\partial}{\partial t} \left\{ n_{e0}, \boldsymbol{v}_{e0}, \boldsymbol{E}_0 \right\} = 0 \tag{1.1.34}$$

Moreover, in order to neglect high-order terms, the linearization approach requires [2]:

$$\left(\frac{n_{e1}}{n_{e0}} \right)^2 \ll \frac{n_{e1}}{n_{e0}}; \qquad (\boldsymbol{v}_{e1} \cdot \nabla) \boldsymbol{v}_{e1} \ll \frac{\partial \boldsymbol{v}_{e1}}{\partial t}; \ldots \tag{1.1.35}$$

In this way the proper linearized system to be solved is:

$$\begin{cases} \dfrac{\partial n_{e1}}{\partial t} + n_{e1} \nabla \cdot (\boldsymbol{v}_{e1}) = 0 \\ m_e \dfrac{\partial \boldsymbol{v}_e}{\partial t} = -e \boldsymbol{E} - \gamma T_e \nabla n_{e1} \\ \nabla \cdot \boldsymbol{E}_1 = -4\pi e n_{e1} \end{cases} \tag{1.1.36}$$

For further simplicity we consider a one-dimension model so that all variables are function of time t and space x; for one freedom degree the adiabatic exponent is $\gamma=3$.

In this model we look for monochromatic wave solution with frequency ω and wave number $k=2\pi/\lambda$, so that:

$$\begin{cases} n_{e1} = n \exp[i(kx - \omega t)] \\ v_{e1} = v \exp[i(kx - \omega t)] \\ E_1 = E \exp[i(kx - \omega t)] \end{cases} \tag{1.1.37}$$

Using (1.1.36) in (1.1.37) a set of linear algebric equation is obtained whose solution is the following dispersion relation, also know as *plasmon,* describing electrostatic longitudinal waves:

$$\omega^2 = \omega_{pe}^2 + 3k^2 v_{th}^2 \tag{1.1.38}$$

where the thermal velocity in our 1D model is:

$$v_{th} = \sqrt{\frac{T_e}{m_e}} \tag{1.1.39}$$

The concept of plasma frequency can be used also to have a better understanding of the collisionless limit and how it is related with the plasma parameter.

In a fully-ionized plasma binary interactions between particles are mostly due to the Coulomb force whose range is the same order of the Debye length.

We consider a population of charged particle with density n mass m_0, charge e and mean velocity v_0 approaching a target particle at rest, with same charge and mass $M \gg m_0$.

It can be demonstrated that the high angle scattering rate is:

$$\nu_c = \frac{4\pi e^4 n}{m^2 v_0^3} \tag{1.1.40}$$

Using equation (1.1.13), (1.1.27) and (1.1.39) we can say that a thermal electron travels a Debye length in a plasma oscillation period:

$$\omega_{pe} = \frac{v_{th}}{\lambda_D} = \frac{2\pi}{\tau_{pe}} \tag{1.1.41}$$

It is easy to show, making use of the definition of N_D (1.1.14), that the ratio between ν_c and ω_{pe} is:

$$\frac{\omega_{pe}}{\nu_c} = \frac{\tau_c}{\tau_{pe}} \propto N_D \tag{1.1.42}$$

Now is clear that N_D, the number of particles in the Debye sphere, connect the collective motion with the collision time scale. Nevertheless, Debye shielding is effective if equation (1.1.15) $N_D \gg 1$ is true, that means that the collisionless limit, in which the collision time scale is slow with respect to collective phenomena, can be expressed by the condition:

$$\frac{\omega_{pe}}{\nu_c} = \frac{\tau_c}{\tau_{pe}} \propto N_D \gg 1 \tag{1.1.43}$$

1.1.4 Electromagnetic waves propagation in a cold plasma

The interaction between and electromagnetic wave and a plasma can be easily described starting from Maxwell equations in MKS units:

$$\begin{cases} \nabla \cdot \boldsymbol{B} = 0 \\ \nabla \cdot \boldsymbol{D} = \rho \\ \nabla \wedge \boldsymbol{H} = \boldsymbol{J} + \dfrac{\partial \boldsymbol{D}}{\partial t} \\ \nabla \wedge \boldsymbol{E} = \dfrac{-\partial \boldsymbol{B}}{\partial t} \end{cases} \tag{1.1.44}$$

The wave, traveling in the plasma, interacts with all species of particles, but the interaction with neutral atoms is much weaker with respect to the interaction with charged particles. Moreover, ions mass is much bigger than electrons mass, this means that also the interaction with ions can be neglected in first approximation.

The interaction between the wave and the electrons is described by the density current vector $\boldsymbol{J}$ whose expression can be derived solving the motion equation of the electron that reads:

$$m \frac{\partial \boldsymbol{v}}{\partial t} = e \boldsymbol{E} \tag{1.1.45}$$

where we have neglected collision and used the assumption that $\boldsymbol{v}$ depends only on the time. Moreover we have take in account that magnetic force is much weaker the electric one. A more detailed description that take in account collisional effect is in [4].

If we consider a monochromatic electric field $\boldsymbol{E} = \boldsymbol{E_0} e^{-i\omega t}$, we can look for a solution for the velocity with the same time dependance $\boldsymbol{v} = \boldsymbol{v_0} e^{-i\omega t}$. Hence the solution of (1.1.45) is:

$$\boldsymbol{v} = \frac{e \boldsymbol{E}}{-i \omega m_e} \tag{1.1.46}$$

The density current $\boldsymbol{J}$ is proportional to $\boldsymbol{v}$ then, after rationalization of (1.1.46), we have:

$$\boldsymbol{J} = ne \boldsymbol{v} = i \omega \frac{n e^2 \boldsymbol{E}}{\omega^2 m_e} \tag{1.1.47}$$

where n and m are the electron density and mass rispectively.

Using the vacuum permittivity ε_0 we can introduce in the above expression the plasma frequency, that in MKS units reads $\omega_{pe}^2 = \left(\dfrac{e^2 n}{m_e \varepsilon_0} \right)$ and writing:

$$\boldsymbol{J} = i \omega \frac{\varepsilon_0 \omega_{pe}^2 \boldsymbol{E}}{\omega^2} \tag{1.1.48}$$

We can insert this expression of $\boldsymbol{J}$ in the curl equation for $\boldsymbol{H}$ to have:

$$\nabla \wedge \boldsymbol{H} = i \omega \frac{\varepsilon_0 \omega_{pe}^2 \boldsymbol{E}}{\omega^2} - i \omega \varepsilon_0 \boldsymbol{E} = i \omega \varepsilon_0 \left(1 - \frac{\omega_{pe}^2}{\omega^2} \right) \boldsymbol{E} = i \omega \varepsilon \boldsymbol{E} = i \omega \boldsymbol{D} \tag{1.1.49}$$

We have found that a plasma is a *dispersive medium* because its permittivity depends on

the frequency of the radiation propagating through it: $\varepsilon = \varepsilon(\omega)$, being:

$$\varepsilon(\omega) = \varepsilon_0 \left(1 - \frac{\omega_{pe}^2}{\omega^2} \right) \tag{1.1.50}$$

In the previous section we have shown longitudinal waves in plasma. Now we can study the propagation of transversal waves starting form the usual realtions [3,4,7]:

$$k^2 = \omega^2 \mu \varepsilon + i\,\omega\,\mu\,\sigma \;\Rightarrow\; k = \beta + i\,\alpha \tag{1.1.51}$$

where:

$$\beta = \omega \sqrt{\frac{\mu\,\varepsilon}{2}\left[1 + \sqrt{1 + \frac{\sigma^2}{\omega^2 \varepsilon^2}} \right]}; \qquad \alpha = \omega \sqrt{\frac{\mu\,\varepsilon}{2}\left[\sqrt{1 + \frac{\sigma^2}{\omega^2 \varepsilon^2}} - 1 \right]} \tag{1.1.52}$$

In the collisionless limit $\sigma = 0$, as shown in [4], then we have, setting $\mu = \mu_0$:

$$\beta = \frac{\omega}{c} \sqrt{1 - \frac{\omega_{pe}^2}{\omega}}; \qquad \alpha = 0; \qquad n_{refr} = \sqrt{1 - \frac{\omega_{pe}^2}{\omega}} \tag{1.1.53}$$

It is easy to understand that if $\omega < \omega_{pe}$ the propagating coefficient β is an imaginary one. Then if we consider an electromagnetic plane wave propagating along z direction whose equation is

$$\boldsymbol{E} = \boldsymbol{E_0} \exp[i(kz - \omega t)] = \boldsymbol{E_0} \exp(i\beta z - \alpha z - i\omega t) \tag{1.1.54}$$

It is clear that the spatial term becomes a damping term. In this case there is no propagation, only a vanishing waves exponentially damped with a characteristic length:

$$l_{sd} = \frac{c}{\sqrt{\omega_{pe}^2 - \omega}} \tag{1.1.55}$$

called *skin depth*, and represents the length scale at which plasma damps electromagnetic waves with frequency below the plasma frequency, which is the cut-off.

For a fixed frequency of the electromagnetic wave, the density at which $\omega = \omega_{pe}$ is called *critical density* and can be defined, using equation (1.1.27), as:

$$n_c(\omega) = \left(\frac{m_e}{4\pi e^2} \right) \omega^2 \tag{1.1.56}$$

If the plasma density is bigger than critical density, namely $n_e > n_c$, the plasma is opaque and the wave is damped, otherwise the plasma is transparent and the wave can propagate without damping, in the collisioneless limit. In the first case the plasma is called *overdense,* or *overcritic*, in the second case is called *underdense.*

With the above conclusions, equations (1.1.53) show that the refraction index of a plasma is always less than the unit. The following plot of the refraction index versus the frequency, normalized with respect to the plasma frequency, shows that the value $n_{refr}^2 = 1$ is actually an asymptotic value [4].

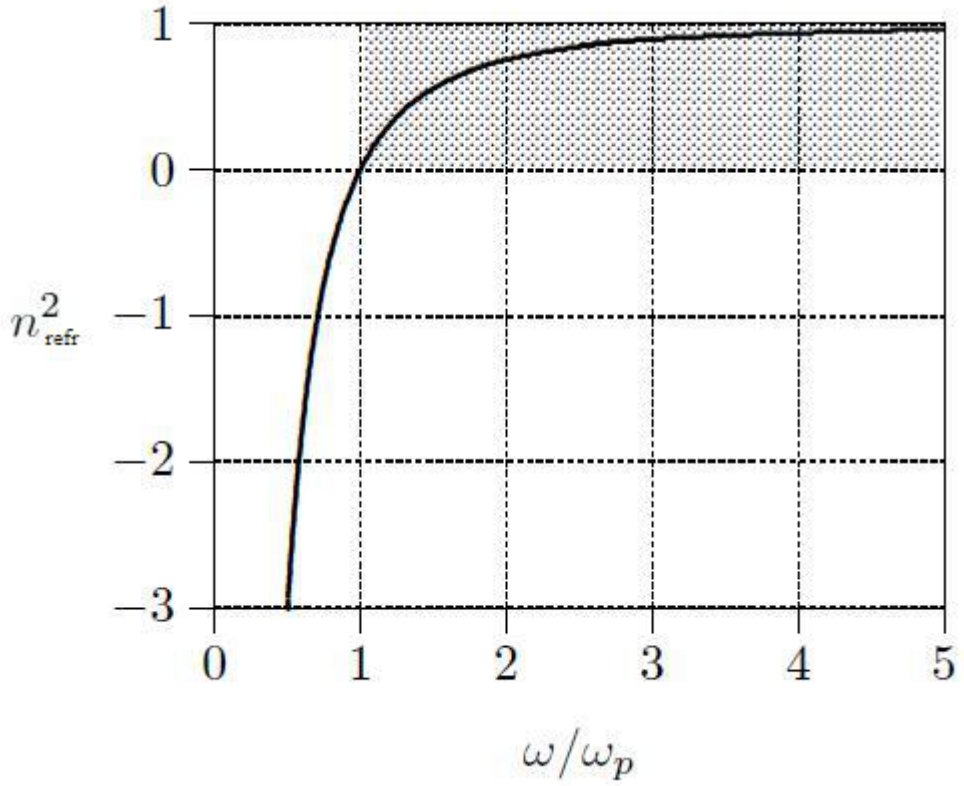

***Figure 1.2**: Plot of refraction index*

This means that the *phase velocity* of an electromagnetic wave in a plasma is always bigger than the light velocity:

$$v_\varphi = \frac{\omega}{k} = \frac{c}{n_{refr}} = \frac{c}{\sqrt{1-\frac{\omega_{pe}^2}{\omega}}} \tag{1.1.57}$$

Hence, we can look at the phase velocity as the the rate at which the phase of the wave propagates in space, but it is not propagation velocity of the wave in plasma. The actual propagation velocity is the *group velocity*, that corresponds with the velocity at which energy or information is conveyed along a wave and, for a plasma is:

$$v_g = \frac{\partial \omega}{\partial k} = c\sqrt{1-\frac{\omega_{pe}^2}{\omega}} \tag{1.1.58}$$

If we suppose that the plasma is in an external magnetic field $\boldsymbol{B_0} = B_0\,\hat{\mathbf{z}}$ along the z axis, the motion equation of the electron in this case reads:

$$m_e \frac{\partial \boldsymbol{v}}{\partial t} = e\,\boldsymbol{E} + e\,\boldsymbol{v} \wedge \boldsymbol{B_0} \tag{1.1.59}$$

that, using the *cyclotron frequency* $\omega_c = \frac{e\,B_0}{m_e}$, can be written as:

$$\frac{\partial \boldsymbol{v}}{\partial t} = \frac{e\,\boldsymbol{E}}{m_e} + \omega_c \boldsymbol{v} \wedge \hat{\boldsymbol{z}} \tag{1.1.60}$$

Solving this equation, one can find that plasma permittivity becomes a 3x3 hermitian tensor. It means that a magnetized plasma is an anisotropic medium. As a result of this anisotropy, studying the wave propagation one can see that the electromagnetic wave traveling in a magnetized plasma is decomposed in two waves with different propagating constant: one is called *ordinary wave (O-mode)* because, for a wave propagating perpendicularly to $\boldsymbol{B_0}$, it is identical to those obtained in the unmagnetized plasma; the other one is called *extraordinary wave (X-mode).*

Moreover, for a linearly polarized wave propagating along $\boldsymbol{B_0}$ direction, it can be shown that the polarization plane suffers a rotation of an angle:

$$\theta = VB_0 l \tag{1.1.61}$$

where l is the path length of the wave in the plasma and V is the *Verdet constant.* This effect is typical of optically active media and is called *Faraday effect.* Further details on magnetized plasmas can be found in [1, 2, 3].

1.2 Lasers

A laser (acronym of light amplification by stimulated emission of radiation) is a device that generates or amplifies electromagnetic radiation, ranging from the long infrared region up through the visible region and extending to the ultraviolet and recently even to the x-ray region.

Lasers are based on stimulated emission, discovered by Einstein in 1917 who postulated that an atom in an excited level could decay to lower energetic level either spontaneously or by stimulated emission.

Let E_1 and E_2 represent the two level of a system and we consider an electromagnetic radiation whose frequency satisfies:

$$h\nu = E_2 - E_1 \tag{1.2.1}$$

If the system is in its ground state it will absorb radiation and will get excited, but if the system is already excited it can decay with emission of a photon in a random direction (spontaneous decay) or with emission of a photon in the same direction of the electromagnetic incident photon, as shown in Fig.1.3:

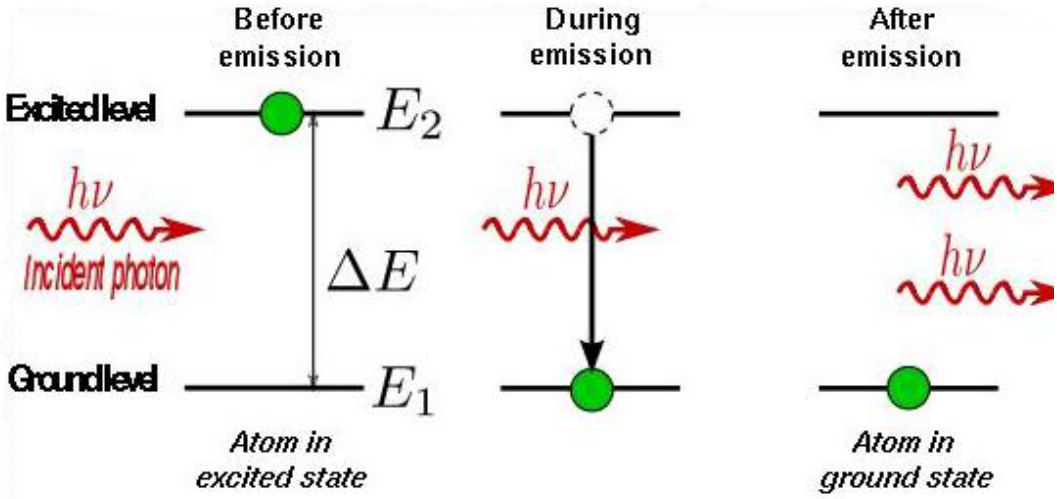

***Figure 1.3**: Representation of stimulated emission*

It can be demonstrated that the radiation emitted by stimulated emission is in phase, i.e. coherent, with the incident one.

Since the transition rate depends on the atoms number in the ground state, to be the system able to amplify the incident radiation, therefore it is able to emit radiation coherent with and exceeding the incident one, it is necessary that the number of atoms in the upper level, E_2, is greater than the number in the ground level, E_1. This condition, called *population inversion,* can not be achieved if the above two level system follows a Maxwell-Boltzmann distribution. On the other hand, population inversion is possible for system with three or more level [2, 9, 10].

Laser light is monochromatic since the amplification is done for frequency satisfying equation (1.2.1). Moreover, the optically active medium is used together with two mirrors, forming a resonant cavity and causing the natural line-width to be narrowed by many order of magnitude.

The *spatial coherence* that characterizes a laser is defined as the phase change of the electromagnetic field of two separated points. If the phase difference of two points that are separated by a distance L is constant in time, then this two points are coherent. The maximum value of L is called *coherent length.*

The *temporal coherence* is defined as the phase change of the electromagnetic field in time in a fixed point. If the phase in this point is equal at time t and $t+\tau$, for all times t, the the point is coherent during the time τ. The maximum value of τ is called *temporal coherence* of the laser.

The maximum power available from lasers reaches today intensities over $10^{21} W/cm^2$ in a femtosecond pulse. The field reaches $10^{12} V/m$ that is greater than the electric field binding the electrons to nucleus. When such a pulse interacts with matter, it instantly ionizes the target creating a plasma.

The key in reaching such high power is the *chirped pulse amplification (CPA)* technique, developed for radar devices more than 40 years ago. In the CPA scheme a pulse made by a low power laser (the oscillator in Fig 1.4) which is able to create a really short packet, *~50fs*, is first starched in time (chirped in frequency) by a factor $\sim 10^4$, then amplified and finally recompressed.

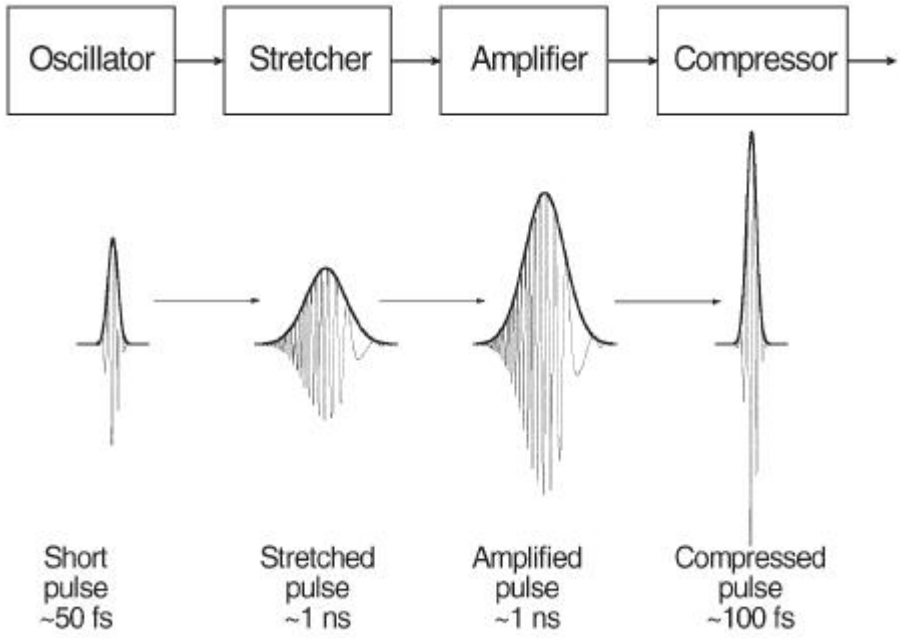

***Figure 1.4**: Scheme of CPA*

Stretching and compression are obtained using a pair of gratings, or prisms, that can be arranged to separate the output pulse spectrum from the oscillator in such a way that different wavelengths follow different path through the optical system. This enable pulse compression using the reverse procedure.

In CPA process not only an ultra-short high-intensity main pulse is produced, but also a weaker pedestal, or pre-pulse, due to the amplified part of the pulse that is not compressed again. As shown in the below intensity vs time plot.

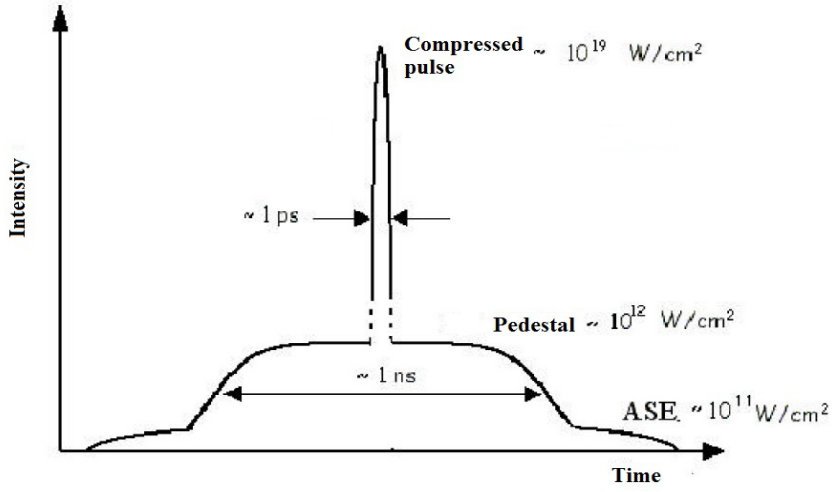

***Figure1.4a**: CPA pulse and prepulse or pedestal*

A third weaker component due to spontaneous emission can be easily suppressed (ASE).

Even if pre-pulse intensity is several order of magnitude smaller than main pulse, it is enough to create a plasma.

1.2.1 Laser interaction with matter

We have already said that high power laser pulses can ionize the target. The electrons escaping from nuclei will acquire a kinetic energy greater than they rest mass, then they become highly relativistic.

In this context a useful parameter is the so called *laser strength parameter*, defined as:

$$a_0 = \frac{eA_0}{m_e c^2} \tag{1.2.2}$$

namely it is the peak value of the laser potential vector normalized with respect to the electron rest mass. It is important because it value defines if a non-relativistic $(a_0 \ll 1)$ or a relativistic $(a_0 \geq 1)$ regime of laser-plasma interaction occurs [11]. This parameter can be related, [5], with the electric peak amplitude, E_L, of the laser by:

$$E_L = a_0 \frac{m_e \omega c}{e} \tag{1.2.3}$$

and, being $I_0 = cE_L^2/8\pi$, it can also be related with the peak intensity, I_0, and the wavelength, λ_L, of the laser by:

$$a_0 = \frac{e}{m_e c^2}\sqrt{I_0 \lambda_L \frac{2}{\pi c}} \tag{1.2.4}$$

The a_0 can be seen as the maximum momentum of an electron quivering in the laser field, normalized with respect to its rest mass, and the previous relation shows that relativistic regime is reached for laser intensity $I_0 > 10^{18} W/cm^2$.

The laser intensity needed to ionize an hydrogen atom can be estimate using Bohr model. At the Bohr radius the electric field strength is, in cgs units, $E_a = e/a_B$. The intensity at which the laser field matches the binding strength of the electron to the atom, the so called *atomic intensity*, is [5]:

$$I_a = \frac{cE_a^2}{8\pi} \simeq 3.51 \times 10^{16} W/cm^2 \tag{1.2.5}$$

A laser intensity $I_L > I_a$ will guarantee at least partial ionization for any target material, though this can occur well below this threshold. In fact an electron can be ejected from an atom it receives enough energy by absorbing a single photon with right frequency, as in the photoelectric effect, or absorbing several photons of lower frequency. Latter process is called *multiphoton ionization (MPI)* and depends strongly on the light intensity, or, that is the same, on the photon density. According perturbation theory, the *n*-photon ionization rate is given by:

$$\Gamma_n = \sigma_n I_L^n \tag{1.2.6}$$

where σ_n decreases with *n*, but the dependence on I^n_L ensures that ionization events occur provided that the intensity is high enough $(>10^{10} W/cm^2)$.

The above relation is true until the atomic binding potential remains undisturbed, as

consequence of perturbation theory. If the laser electric field becomes strong enough it can distort the electric field felt by the electron. In this case the Coulomb barrier will be change in a finite height barrier and the electron can escape from the atom via *tunneling ionization*. Moreover, if the electric field intensity is very high it can suppress the Coulomb barrier, in this case we can talk of *barrier suppression ionization (BSI)*, as a variant of tunneling ionization regime.

Keldysh parameter can be used to understand which regime (Tunneling or MPI) will prevail using a certain laser intensity:

$$\gamma = \sqrt{\frac{E_{ion}}{\Phi_{pond}}} \tag{1.2.7}$$

where E_{ion} is the ionization energy and Φ_{pond} is the *ponderomotive potential* of the laser field:

$$\Phi_{pond} = \frac{e^2 E_L^2}{4 m_e \omega_L^2} \tag{1.2.8}$$

expressing the effective quiver energy acquired by an oscillating electron in the laser field.

As a rule, tunneling regime prevails for strong fields an long wavelengths, hence when $\gamma<1$; multiphoton ionization prevails when $\gamma>1$, in this case laser electric field is not enough intense to perturb the potential barrier.

At the beginning of the interaction, when the pre-pulse impinges on the target, multiphoton ionization dominates, because of its low intensity. When the main pulse arrives tunneling effect dominates.

1.2.2 Ponderomotive force

We have shown that a plane electromagnetic wave propagates in a plasma with a phase velocity expressed by equation (1.1.57). For short laser pulses this result does not hold anymore because their focal spot has dimensions of the order of micron. Hence, short pulses create strong radial and longitudinal field gradients associated with the so-called *ponderomotive force* that can eject electrons from the regions where the field is higher and is responsible for longitudinal waves in plasma.

In the non-relativistic limit we can easily evaluate the effect of an electric field gradient assuming that the gradient is fairly weak and the displacement of a particle over a field oscillation period is small compared to the typical distance of the gradient.

The motion equation of a charged particle in an oscillating electric field along x axis is:

$$m\ddot{x} = qE_0 \cos(\omega t) \tag{1.2.9}$$

Integrating the motion equation twice with respect to the time and with the initial condition $\dot{x}_0 = 0$ we have:

$$x = x_0 - \frac{qE_0}{m\omega^2} \cos(\omega t) \tag{1.2.10}$$

that describes an oscillating motion over the equilibrium position x_0, as show in Fig. 1.5

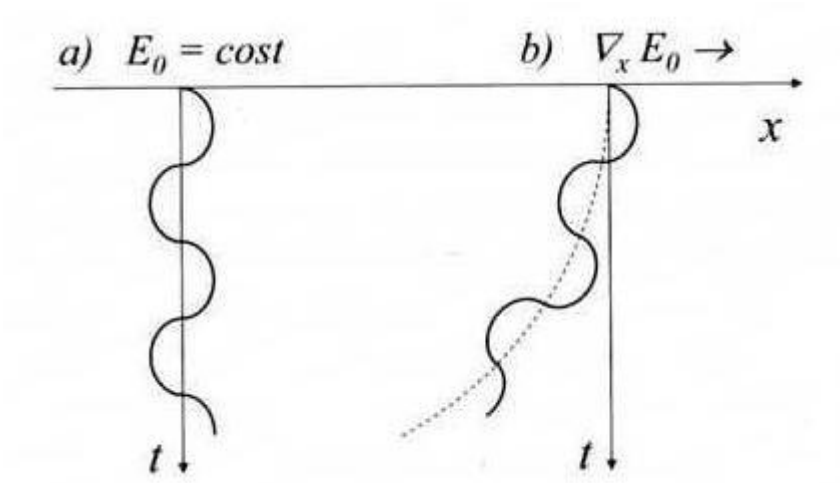

Figure 1.5: *Particle motion in an oscillating electric field in case of constant amplitude (a) and in case of a gradient field.*

If we suppose that E_0 amplitude is a weak growing function of x, then the electric field will restore the particle initial position more efficiently in the positive half_cycle of $cos(\omega t)$, where E is bigger. Hence, the particle will be accelerated in the opposite direction of the gradient field.

In order to integrate equation (1.2.9) we decompose the particle position in a slowly varying part $\bar{x}$, and in quickly varying part $\tilde{x}$. Then $x = \tilde{x} + \bar{x}$ where:

$$\bar{x}(t) = \langle x \rangle_T = \frac{1}{T}\int_{t-\frac{T}{2}}^{t-\frac{T}{2}} x(t')\,dt' = \frac{2\omega}{\pi}\int_{t-\frac{T}{2}}^{t-\frac{T}{2}} x(t')\,dt' \tag{1.2.11}$$

is the average value of $\bar{x}$ over a period of the electric field.

Taylor expansion of the electric field around $\bar{x}$ is:

$$E \simeq (E_0(\bar{x}) + \nabla_x E_0(\bar{x})\tilde{x})\cos(\omega t) \tag{1.2.12}$$

and equation (1.2.9) can be written as:

$$m\ddot{\bar{x}} + m\ddot{\tilde{x}} = q(E_0(\bar{x}) + \nabla_x E_0(\bar{x})\tilde{x})\cos(\omega t) \tag{1.2.13}$$

With the above assumptions we have $\ddot{\bar{x}} \ll \ddot{\tilde{x}}$ and because of weak spatial dependance of the field amplitude we can set $E_0(\bar{x}) \gg \nabla_x E_0(\bar{x})\tilde{x}$. Then for the quickly varying part of the motion we have an oscillation with frequency ω:

$$\tilde{x} \simeq -\frac{qE_0}{m\omega^2}\cos(\omega t) \tag{1.2.14}$$

For the slowly varying part, which represent the motion of oscillating center, we have, after averaging equation (1.2.13) over a field period:

$$\ddot{\bar{x}} = -\frac{q^2}{2m^2\omega^2}E_0(\bar{x})\nabla_x E_0(\bar{x}) \tag{1.2.15}$$

From the above equation we can see that the oscillating center is accelerated in the

opposite direction of the gradient field. Pondermotive force is responsible for this acceleration and can be expressed as:

$$\boldsymbol{F}_{\boldsymbol{P}} = -\frac{q^2}{4 m \omega^2} \nabla E_0^2 \tag{1.2.16}$$

that is the gradient of the ponderomotive potential (1.2.8).

It is important to note that ponderomotive force depends on the square of the charge, then its direction is the same for positive or negative particles; on the other hand its modulus in bigger for electron than for proton because of the dependence on *1/m.*

This force will tend to push electrons away from regions of locally higher intensity and therefore a single electron will drift away from the center of a focused laser beam picking up a quiver velocity:

$$v_{os} = \frac{eE}{m\omega} \tag{1.2.17}$$

The fully relativistic version of equation (1.2.16) reads:

$$\boldsymbol{F}_{\boldsymbol{P}} = -mc^2 \nabla \langle \gamma \rangle \tag{1.2.18}$$

where $\langle \gamma \rangle = \sqrt{1 + \frac{\langle p \rangle}{mc^2} + \frac{\langle a_0^2 \rangle}{2}}$, as shown in [5].

When ultra-short laser pulse begins to propagate in a underdense plasma, the pomedromotive force, pushing electrons while ions remains nearly unpertuberd because of their bigger mass, creates a longitudinal charge separation that results in a longitudinal electric field which pulls back the electrons again. This perturbation induces a plasma wave that travels in the wakefield at the group velocity of the pulse itself. This oscillation trails the laser pulse like the wake produced by a motorboat.

If the pulse wavelength is of the order of half plasma wavelength, i. e. the *quasi-resonant condition* holds:

$$L_L \simeq \lambda_p / 2 \tag{1.2.19}$$

the wake formation is very efficient. In fact, in these condition the ponderomotive force and the wake electric field change sing at the same frequency.

A schematic representation of wakefield generation is shown in Figure 1.6.

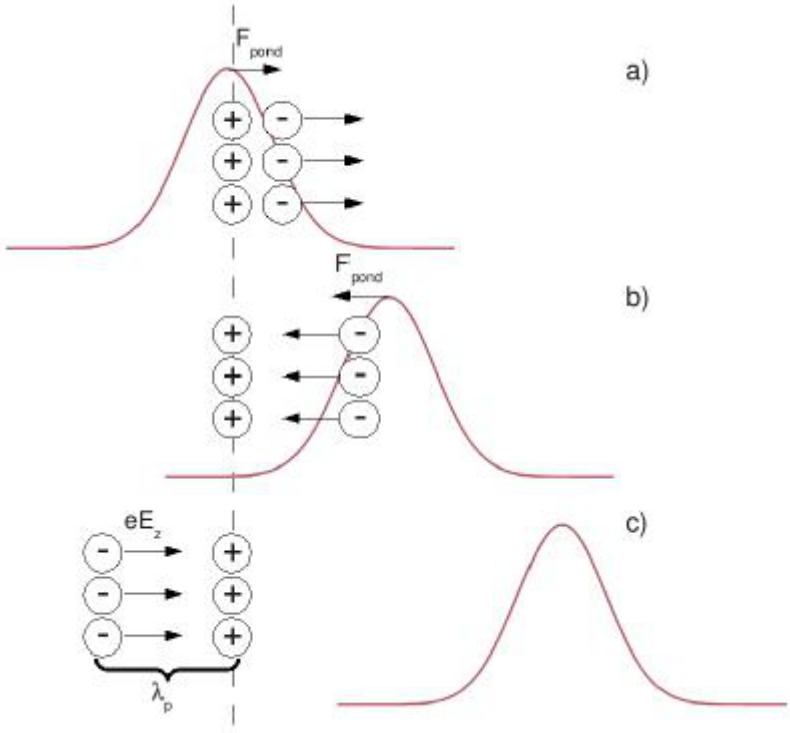

Figure 1.6: *Wakefield generation*

Wakefield generation can be used to accelerate electron bunch traveling in phase with the plasma wakefield generated by a laser pulse. This regime is called *Laser WakeField Acceleration (LWFA)*.

Obviously, for the laser pulse to propagate and create the wakefield, plasma must be underdense. Moreover if the parameter $a_0 \ll 1$ the wakefield is linear, if it is $a_0 \simeq 1$ it becomes non linear and the electron quiver motion becomes relativistic, if $a_0 \gg 1$ different regimes can be achieved.

1.2.3 Interaction with solids

When an electromagnetic wave with optical or near infrared frequency ω is focused on a gas, the plasma produced has an electron density n_e less than critical density $n_c = m_e \omega^2 / 4\pi e^2$. Hence the plasma is called *underdense* and the wave can propagates through it.

Interaction with a solid target is radically different, in fact the electromagnetic wave promptly ionizes the target forming an *overdense* plasma with $n_e > n_c$. The laser pulse can only penetrate in the skin layer $l_{sd} = c/\omega_p = (\lambda/2\pi)\sqrt{n_c/n_e}$ and the interaction is then a surface interaction.

In the interaction part of laser light is reflected but a significant fraction of laser energy may be absorbed by the target.

For short laser pulses with relativistic intensity, plasma temperature rises very fast and the collision in the plasma can be considered ineffective during the interaction. In this situation different collisionless absorption mechanism can arise, such as *resonance absorption,* $\boldsymbol{J} \wedge \boldsymbol{B}$ *heating, vacuum heating* [5, 2]. In any case the absorbed energy will result in the heating of part of the electron population at temperature much higher than the initial bulk temperature.

Laser energy absorption by electrons is a crucial phenomenon in ion acceleration and

will be dissed further.

Self-induced Transparency:

We have seen, in Sec. 1.2.1, how the electron motion in an electromagnetic wave becomes relativistic if field intensity is high enough. At extreme intensities, this motion can modify the refractive index of an overdense plasma to permit propagation [5]. This phenomenon is known as *self-induced transparency (SIT)*. If we consider a high intensity wave $(a_0 \geqslant 1)$ the electron quivering motion is highly relativistic and its relativistic factor take the form $\gamma_0 = \sqrt{1 + a_0^2/2} \simeq a_0/\sqrt{2}$.

The effective plasma frequency appearing in the dispersion relation should be corrected as:

$$\omega'_p = \frac{\omega_p}{\gamma_0} \propto \left(\frac{n_e}{a_0}\right)^{1/2} \tag{1.2.20}$$

being n_e the electron density. The plasma frequency gets smaller and the critical density moves to larger values. That means that the plasma at the former critical density becomes transparent and the laser pulse can propagate through it.

Hence, there will be a critical intensity above which the plasma loses its natural opacity, i. e. $\omega'_p \leqslant \omega$, and the condition for the laser strength parameter is:

$$a_0^{SIT} \geq \sqrt{2}\frac{n_e}{n_c} \tag{1.2.21}$$

In terms of electron density, we can state that the plasma is transparent for an intense laser if $n_c < n_e < \gamma\, n_c$.

The propagation of laser pulses through slightly ovecritical is gaining interest after some ion acceleration regimes have been proposed but is not straightforward to produce a target with $n_e \simeq n_c$, therefore such condition has not been accurately investigate.

1.3 Laser induced ion acceleration

When a laser pulse irradiates a solid target an overdense plasma slab is formed and several absorption mechanism can be involved. The absorbed laser energy accelerates and heats electrons in plasma. Moreover, if normal incidence is considered, the ponderomotive force pushes inward the electrons from the rear surface of the target creating a charge separation which produces an electrostatic field experienced by ions.

The first experiments, exploiting interaction of short *(τ < 1ps)* and intense *($I_l\lambda^2 > 10^{18} W/cm^2$)* laser pulses with thin solid foil, showed the production of protons beams in the range of several tens of *MeV* coming from the rear surface of the target.

The bunches produced exhibit a remarkable (*terrible)* collimation and a high energy cut-off; the maximum energy record of 94*MeV* has not been beaten yet [41]. On the other hand there have been significant improvement in the control of the beam quality and energy spectra that made possible to propose the laser-accelerated ions for therapy, even if many study are still required on the transport of the optically accelerated beams and post accelerations in order to delivery ions with right characteristics to the patients.

In most experiments the dominant regime is the so called *Target Normal Sheath*

Acceleration (TNSA) in which the accelerated protons come from the rear surface of the target and the accelerating field is due to the expansion of heated electrons around the target. Different regimes have been theoretically proposed and tested, in which the radiation pressure of the laser dominates on the heating process and the accelerated bunch is composed by ions coming from the irradiated surface of the target. These regimes are called *Radiation Pressure Acceleration (RPA)* and the accelerating mechanism depends on the target thickness.

The laser intensities available reaches $10^{21} W/cm^2$ and the corresponding radiation pressure is about *300Gbar*.

The physics of these regimes is not simple because of the non-linear phenomena involved in the extreme conditions of high power laser interactions with overcritical plasmas. Difficulties remain even considering simplified models, i.e. preformed plasma, no ionization, no collision and so on.

Before analyzing the accelerations regimes it worth to note that in the previous discussions we have regarded the ions as being fixed and providing a neutralizing background to the electron density fluctuations generated by the laser. At high intensities this situation alters quite dramatically due to the large electric field, of the order of *GV/m*, induced when many electrons are rapidly displaced from their initial positions. As a result, a substantial fraction of ions may be accelerated to energies in the multi-MeV range.

It is important to note that ions quiver motion in a laser field is negligible compared to that of electrons, because of ions bigger mass. For an ion of mass M_i and charge Ze its quiver velocity can be written as [5]:

$$\frac{v_i}{c} = \frac{Zm_e}{M_i} a_0 \tag{1.3.1}$$

Thus, to accelerate ions to relativistic velocities directly by the laser field, one would need intensities of $I\lambda^2 > 1024 W/cm^2$, or $a_0 \approx 2000$, which are well beyond the intensities available with current laser systems. In a plasma, however, the electrons mediate between the laser field and the ions via charge separation. In other words the laser displaces of heats electrons and the consequent electrostatic fields pulls on the ions. Because of their higher inertia, the ion response is delayed by a factor $[M_i / Zm_e]^{1/2}$ which can be related with the ratio between electron and ion plasma frequencies ω_p / ω_{pi}. Derivation of ion plasma frequency can be found in [1, 2, 4].

1.3.1 Target Normal Sheath Acceleration (TNSA)

In the interaction of an intense electromagnetic wave with a solid, the front surface of the target becomes ionized well ahead the pulse peak. The successive laser-plasma interaction heats the electrons via different absorption mechanism to high temperature *($T \approx$ MeV)* and their free path becomes bigger than the plasma skin depth and than the target thickness. These hot electrons have a diffusive motion both in the laser direction and in the opposite one. Thus they can propagate in the target reaching its rear surface where they expand into vacuum for several Debye lengths forming a cloud of relativistic electrons. The charge imbalance due to the cloud gives rise to an extremely intense longitudinal electric fields, which is responsible for the efficient ion acceleration. The most effective acceleration mechanism takes place at the rear surface of the target where the high intensity electrostatic field can ionize the atoms present on the unperturbed surface and then accelerates the ions produced. This mechanism is know as *Target Normal Sheath*

Acceleration (TNSA).

The accelerated multi-MeV protons from the rear surface of the irradiated solid foil is achieved no matter its composition, because they came from the hydrogen rich contaminants, such as hydrocarbons or water vapor, present on the target surface.

The energy spectrum of the protons is typically exponential with a high cut-off in the range of tens MeV.

Several theoretical models have been proposed in order to describe the TNSA regime, but the most efficient in predicting the energy cut-off and that gives also a good interpretation of the acceleration mechanism it the one proposed by Passoni [22], despite the strong assumptions. This model will be briefly described in the following.

The electron involved in TNSA regime can be two different population. The first is the *hot (or fast) electron* component, directly created by the laser pulse in the plasma plume at the front surface of the target. Its density is of the critical density order $(n_h \approx 10^{20}\text{-}10^{21} cm^{-3})$ and its temperature is of the ponderomotive potenzial order ($T_h \approx MeV$). The free motion of this hot electron beam through the target require the presence of a return current that locally compensates the flow of the hot electrons. In metallic target this current is provided by the second component of *conduction (or cold) electrons* that are put in motion by the electric field of fast electrons. The second electron component density is of the solid density order, that is, much bigger than fast component, so the required velocity for current neutralization is small and their temperature is much lower than hot electrons.

The ion population can be also divided in two species: one being the *heavy ions* of the target, possibly constituted of several ion species, with a low charge over mass ratio Z_H/M and density n_H the other one is *light ion* component usually present as contaminant on target surface, with charge Z_L and density n_L.

The acceleration is most effective on light ions while the heavy component provides a positive charge that offers more inertia and make the charge separation responsible for the huge accelerating field.

Now we assume one-dimensional geometry and we describe the electron population as a two-temperature distribution $n_e = n_h + n_c \approx n_c$, where the subscript c stays for the conduction and h stays for the hot electrons; moreover the target is a plane sharp-edged plasma slab. Then Poisson equation for the self-consistent electrostatic potential $\phi(r,t)$ is:

$$\frac{d^2\phi}{dt^2} = 4\%pie\left(N_e - Z_H n_H - Z_L n_L\right) \tag{1.3.2}$$

For short pulses, laser-target interaction occurs on a time scale shorter than typical ion motion scale, then heavy ions can be assumed immobile, while light ions are mobile but, because of the low density, their effect on the electrostatic potential evolution can be neglected. For simplicity, the cold electron population is assumed to have constant density n_{0c}, while the hot population is assumed to be in thermal equilibrium with the electrostratic potential, then described by a Boltzmann distribution.

The most energetic electrons can leave the system escaping from the self-consistent potential, because of this the self-consistent solution for the potential diverges at large distance from the target. Then one describes the hot electrons assuming a single temperature Maxwell-Jüttner relativistic distribution function and considers only electrons with negative energy, i. e. bound to the system.

With these assumptions the solution for the electrostatic potential at the target vacuum interface results to be a function of the temperature T and of the maximum energy of a bound electron, ε_{emax},:

$$\phi(0)=\phi(T,\varepsilon_{emax}) \tag{1.3.3}$$

In order to evaluate the the maximum ion energy and the energy spectrum the hot electron temperature, which determines the maximum binding energy, must be know. It is assumed to be described by:

$$T_h=mc^2\left(\sqrt{1+\frac{a_0^2}{2}}-1\right) \tag{1.3.4}$$

which relates the electron temperature with the laser irradiance $I\lambda^2$ via the parameter a_0.

The maximum proton energy, or the cut-off energy of the spectrum is then given by:

$$E_{cutoff}=Z_L\phi(0)=Z_L f(E_L,I_L) \tag{1.3.5}$$

Despite of the strong assumption the model successfully describes the scaling law of the proton acceleration in TNSA regime and is compatible with experimental results showing a linear dependence of $E_{cut\text{-}off}$ with $I^{1/2}$.

The main features of TNSA is that the energy spectrum has an exponential decay for increasing values with a clear cut-off as shown below.

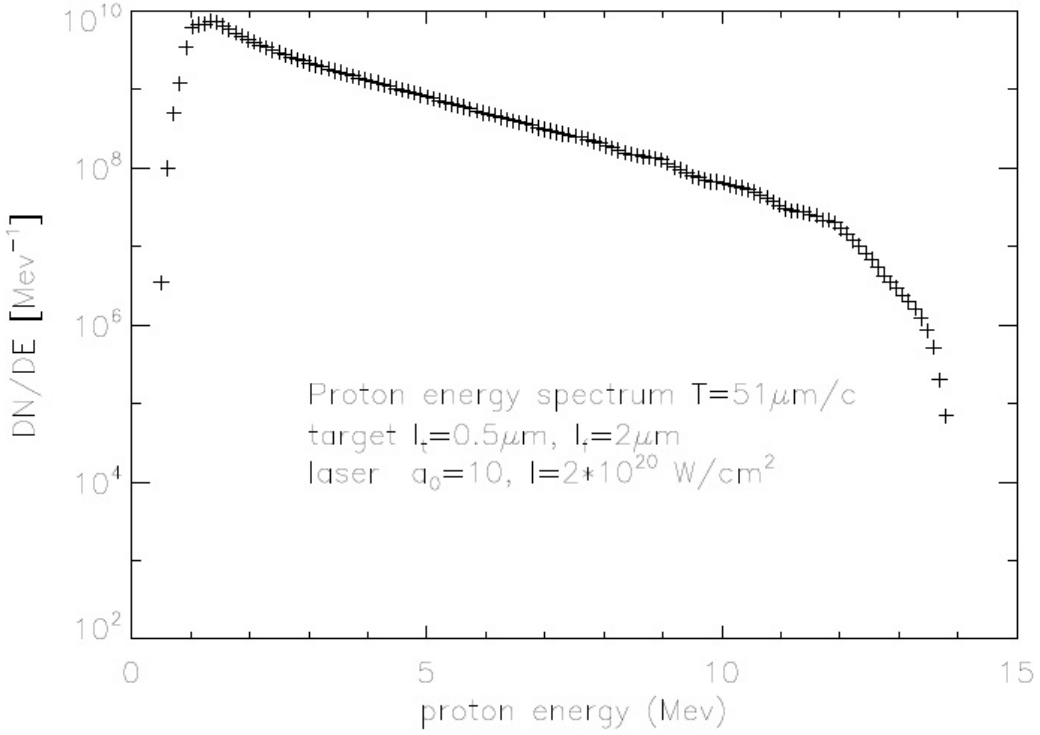

***Figure 1.8**: Energy spectrum of protons accelerated in TNSA regime*

The efficiency of TNSA acceleration can be enhanced increasing the efficiency of the energy transfer from laser to target. For this reason different design of targets can be considered where a foam layer is deposited on the target leading to a considerably energy absorption.

Moreover the angular spread is significant and the beam is not suitable for free propagation.

1.3.2 Radiation pressure Acceleration (RPA)

A possible route to accelerate ions up to relativistic energies has been investigated with numerical simulations and theoretical models and it is the acceleration regimes which start dominate over TNSA at higher intensity. Simulations show that if a thin target is irradiated with a laser intensity $I \geq 10^{23}\, W/cm^2$ its ions reach energies in the *GeV/nucleon* range and the scaling of the ion energy vs. laser pulse is linear.

Laser with such intensities are not currently available but RPA can dominate over TNSA at lower intensities if circularly polarized light is used instead of linearly polarized. In fact in this conditions electrons heating becomes negligible, ruling out TNSA which is driven from the space charge produced by energetic electrons escaping in vacuum, and the ponderomotive force acts directly accelerating electrons and ions.

Two different models exist for this regime, depending on the thickness of of the target: the *Hole Boring (HB)* for thicker target and the *Light Sail (LS)* for thinner ones.

Hole Boring:

In this regime the ion acceleration is due to the electrostatic field E_x arise from the electron displacement generated by the ponderomotive force, being x the propagation direction of the laser. A phenomenological model [20] considers a quasi-equilibrium between the ponderomotive force and the electrostatic force.

A target of thickness $h \approx \lambda_L$ is considered. At the initial stage the laser radiation pressure pushes the electrons creating a space-charge field E_x that balances the ponderomotive force, while the ions do not move significantly. So electron density is depleted on a layer of thickness x_d and ion density n_0 remains constant, as shown in figure 1.9.

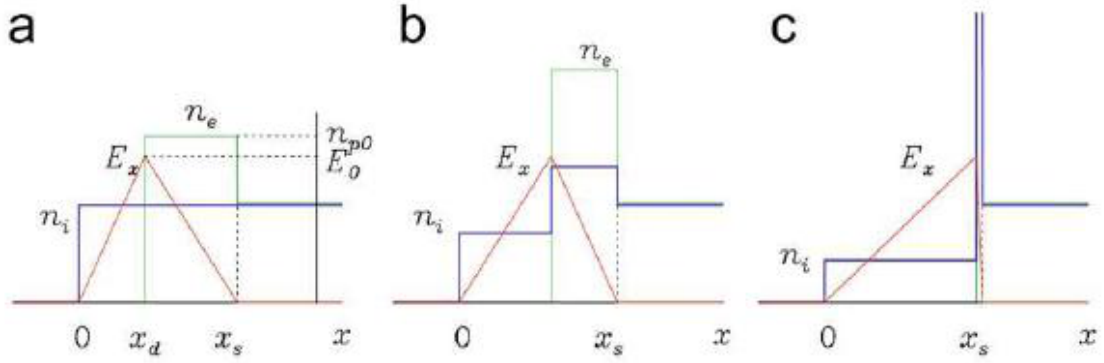

Figure 1.9*: Profile of ion density n_i (blue), electron density n_e (green) and electrostatic field E_x (red) at three different stage of ion acceleration [19]*

The resulting electric field has a maximum $E_0 = 4\pi e n_0 x_d$ which accelerates the ions in the depleted region. The ions move forward and pile up until their density becomes singular and the fast particles overcome the slowest ones leaving the accelerating region. It this last stage a *wavebreaking* occurres and the ions can not gain energy anymore.

What we can observe from simulation is that the fast ions form a narrow bunch of velocity v_m and penetrate into the overdense plasma; the others form another peak moving with velocity $v_b = v_m/2$, where v_b is the speed at with a hole is bored in the plasma.

The estimate of ion energy is:

$$E_I = 2Zm_e c^2 \frac{n_c}{n_e} a_0^2 \qquad (1.3.6)$$

which exhibits a linear dependency on the laser intensity, though the parameter a_0, whereas is inversely proportional to electron density.

The ion acceleration in this regime is rather low, but a target design with a low density might help, even if there are several difficulties in using target with intermediate densities.

Light Sail:

For a thin target of thickness $h < \lambda_L$, after the first acceleration the ions do not pile up to a singular density because they constitute the whole target. The laser is then able to further push the electrons repeating the acceleration stage. The laser interacts basically with electrons, but because the target is thin the ion motion is strictly bound with the electrons' and the target can be considered as a rigid object. Then the equation of motion of the target retrieves the model of a "flying mirror" pushed by the radiation pressure of the laser.

As shown in [25] the thinner is the target the higher is the efficiency of the accelerating process. However the main limit is imposed by the transparency limit, in fact the target remains opaque and is accelerated as a mirror provided that:

$$a \leq \frac{\pi n_e h}{n_c \lambda_L} \tag{1.3.7}$$

Considering the technical difficulties in preparing target near the transparency limit and the presence of instabilities shown in 2D and 3D simulations, this regime is not likely to be interesting for applications. Nevertheless the high laser intensity required for RPA regime is not currently available, the requirement of circularly polarization and high contrast, i. e. the ration between the peak of the main laser pulse and pre-pulse intensity, required to achieve this regime at lower laser intensity set others technical difficulties.

1.4 Ion-matter interaction

When a particle beams get through a medium a total or partial energy exchange occurs between the incident radiation and the target component. As a consequence the particles in the beams will loose their energy and will be deflected from the incident direction.

Ions are charged particles and undergo coulombian interactions. The nature of interactions are similar for any kind of ions and can be scaled from the corresponding proton interaction.

Protons travelling through matter can either interact with both nuclei and electrons that are close to their path. As the proton mass is much greater than atomic electrons, the deflection angle after an electronic interaction is extremely small and, to a good approximation, the protons travel on a straight path. The proton energy fraction transferred to the electron could either excites the atoms or ionizes it. Also the interactions with atomic electrons are so frequent that protons appear to lose energy continuously along their path.

Interactions with nuclei can be described as elastic collisions and are responsible for greater deflection angle. Anyway nuclear interactions are very rare and the dominant energy loss mechanism are the electronic collision.

The behavior of a proton in a medium can be described by the *stopping power* which represents the average rate of energy loss along its path in the matter. It can be expressed by the *Bethe-Block formula:*

$$-\frac{dE}{dx}=2\pi N_A m_e r_e^2 c^2 \rho \frac{Z}{A}\frac{z}{\beta^2}\left[ln\left(\frac{2\gamma^2 m_e v^2 W_{max}}{I^2}\right)-2\beta^2-\delta-2\frac{C(I,\beta\gamma)}{z}\right] \quad (1.4.1)$$

where r_e and m_e are the classical electron radius and the electron mass, A and Z are the atomic mass and number of the medium, I is the mean excitation potential of the target and ρ its density, β and γ are the particle velocity and its relativistic factor, W_{max} is the maximum energy transfer in a single electronic collision.

The last two terms in Bethe-Block formula are correction terms; the first one, δ, is the *density correction* describing the screening effect on the further electrons due to the polarization induced by the proton. Thus the interactions with these electrons are less important to the loss energy mechanism described by equation (1.4.1). The second one $C(I,\beta\gamma)$ is the *shell correction* which take in account the fact that proton velocity can be of the same order or even less of the atomic electrons. The original Bethe-Block formula was derived considering the atomic electrons at rest with respect to the incident particle.

It is important to note that the stopping power depends on the kinetic energy of the particle:

$$-\frac{dE}{dx}\propto\frac{1}{E} \quad (1.4.2)$$

Hence the stopping power increases with the decreasing of kinetic energy, it means that the proton will lose the more energy at the end of its path in the target as can been shown in figure 1.10.

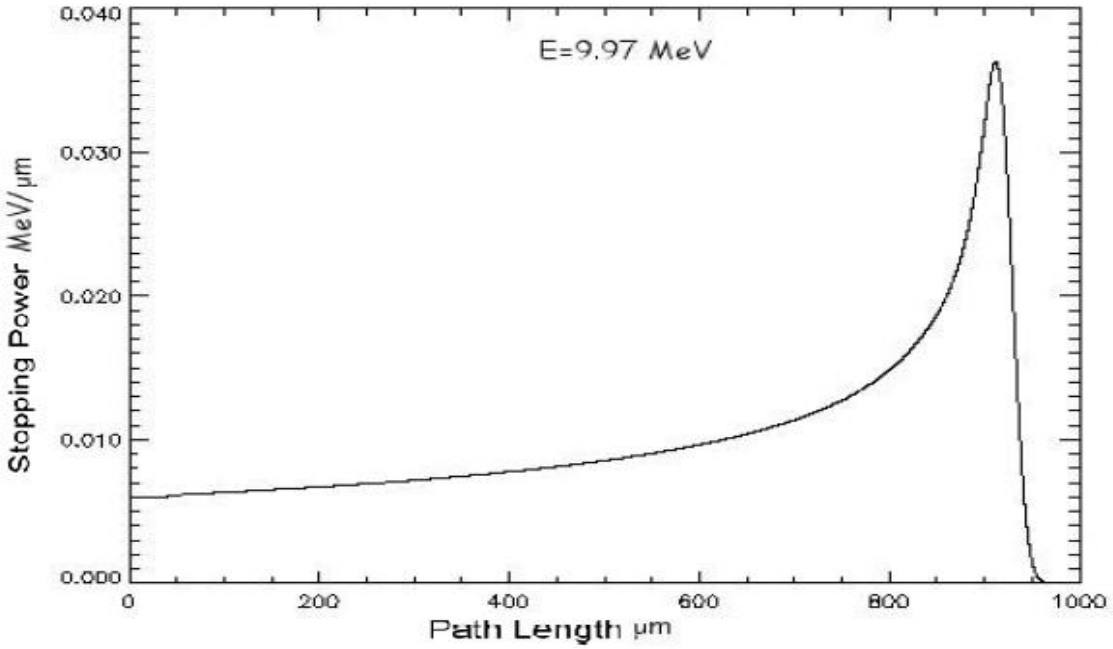

***Figure 1.10**: Bragg curve of a proton with initial energy of 9,97MeV in a mylar target.*

The plot of the stopping power of a proton during its travel through the matter is called *Bragg curve* and the pronounced peak, *Bragg peak,* occurs immediately before the particle comes to rest.

This characteristic behavior of ions allow to use them in cancer therapy sparing the healthy organs in the vicinity of the tumor, which is in contrast with X-ray or electron

therapy.

1.4.1 ELIMAIA-ELIMED: A Laser-Accelerator for User Experiments

Until now, most of the experiment on laser-driven proton accelerations have been performed in the TNSA regime. The ion bunches produced with laser-plasma interaction have peculiar characteristics which differ from beams of comparable energy produced with conventional techniques. They have a time duration in the pico-second range with extremely high dose rate [31], hence the interest for applications, especially medical ones is growing. On the other hand, literature reports that laser-driven ion beams have a very low emittance, because of the micrometric dimensions of the beam at the production point. In fact, the angular aperture of the ion beam is very large, and in some cases the emission cone can be of several tens of degrees. This peculiarity, together with the polychromaticity of the ion spectrum and the presence of different ions species in the same beam make the beams not directly suitable for applications.

Technologies for a practical use of laser-generated proton/ion beams are currently under study or realization, to enable precise control over the unique features of laser-driven particle beams [32,38] and, experiments have been already carried out demonstrating the possibility to control the beam and the dose deposition on sample with results comparable with conventional accelerators [39].

The ELIMAIA beamline [40] will be one of the key secondary sources of the ELI-Beamlines facility. ELIMAIA has been designed and developed at the Institute of Physics of the Academy of Science of the Czech Republic (IoP-ASCR) in Prague and at the National Laboratories of Southern Italy of the National Institute for Nuclear Physics (LNS-INFN) in Catania (Italy). The proposed technological and scientific solutions for the ELIMAIA implementation are the result of a complex investigation carried out with the main goal of fulfilling the specific requirements that have been coming from the international user community. The main identified user requirements are: wide energy and flux range, small energy spread (quasi-monoenergetic beams), homogeneous transverse beam distribution, shot-to-shot stability (energy and flux), variable beam spot size, full beam control (flux and dose) with <5% error, possibility of in-air user sample irradiation (e.g., for bio-samples), use of different ion species (H, He, Li, C). The general philosophy for the design, development and implementation of the ion beamline at ELI-Beamlines is based on three key features: user friendly approach, accurate monitoring and reliability of the accelerated ion beams and flexibility for its future upgrade.

A complete experimental platform (laser beamtransport and pulse treatment, ion source generation and in-situ characterization, ion beam transport, diagnostics and shaping, online dosimetry and in-air sample irradiation end-station) will be available for users to enable them to apply laser-driven ion beams in multidisciplinary fields. A 3D rendering of the ELIMAIA beamline (Ion Accelerator + ELIMED) is shown in Figure 1.11. The ELIMAIA beamline is located in the southern part of the experimental hall 4 (E4), in the basement of the ELI building (required from a radiation protection point of view). The available L3 and L4 (1–10 PW peak power level) lasers enter E4 from the eastern wall (only L3 is shown in Figure 1.11). The ELIMAIA beamline consists of two main subsystems:

(i) the Ion Accelerator and

(ii) the ELI MEDical applications (ELIMED) beam transport and dosimetry section. ELIMAIA subsystems and key equipment are also shown in Figure 1.12.

In the next sections the design of the beam transport line, namely the collection, selection and focusing sections of ELIMED is reported. Moreover, the design of the first upgrade will be discussed, which is, at the moment in the prototyping phase.

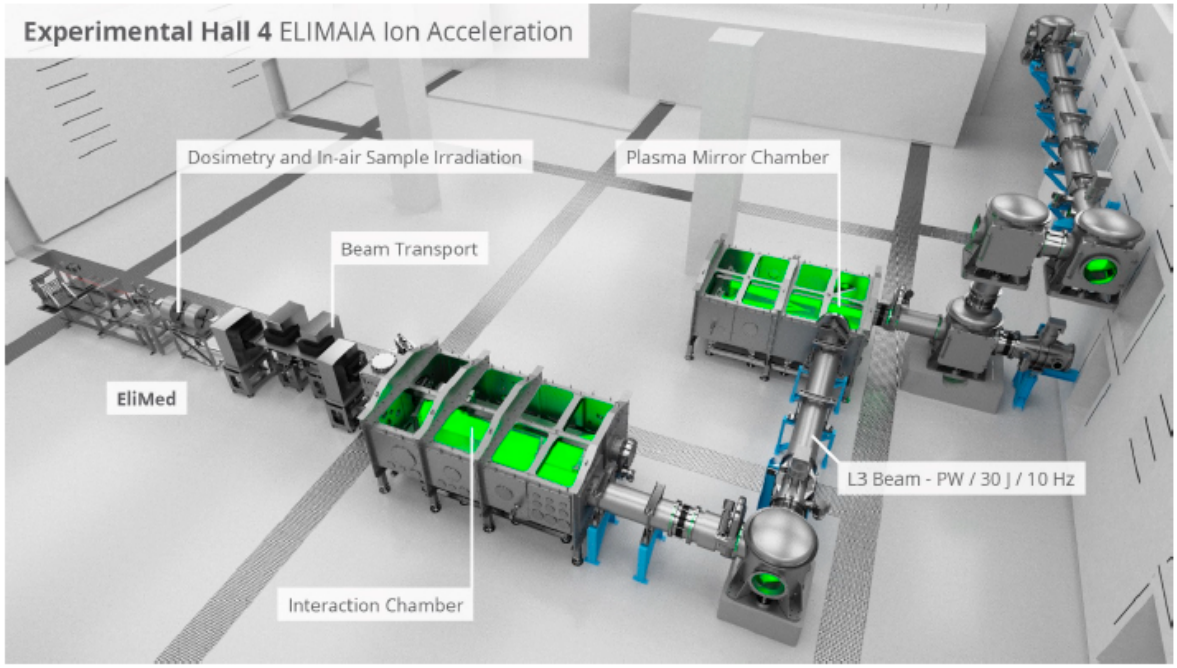

Figure 1.11: *Rendering of the ELI multidisciplinary applications of laser-ion acceleration (ELIMAIA) beamline in the experimental hall E4.*

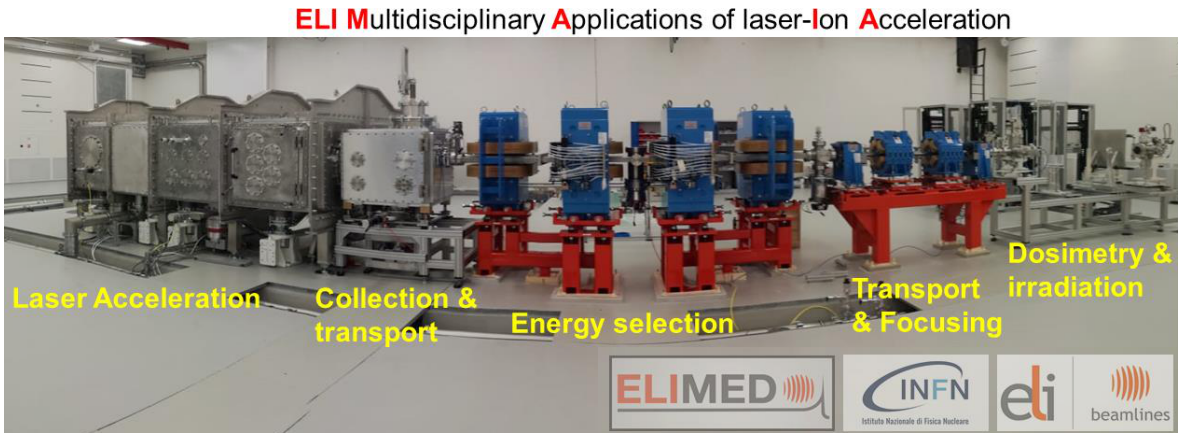

Figure 1.12: *The main sections of the ELIMAIA beamline (Ion Accelerator and ELI MEDical applications (ELIMED)) consist of different subsystems: (i) acceleration, collection and diagnostics; (ii) collection, selection and transport; (iii) dosimetry and sample irradiation.*

1.5 Bibliography

[1] G. Pucella, S. E. Segre, *Fisica dei Plasmi,* Zanichelli editore S.p.A, Bologna, 2010.
[2] S. Eliezer, *The Interaction of High-Power Laser with Plasmas,* IOP Publishing Ltd, 2002.
[3] J.D. Jackson, *Classical Electrodynamics,* John Wiley & Sons, Inc., 1975.
[4] S. Barbarino, *Appunti di Campi Elettromagnetici,* online book.
[5] P. Gibbon, *Short Pulse Laser Interaction with Matter,* Imperial College Press, 2005.
[6] W. L. Kruer, *The Physics of Laser Plasma Interactions*, Addison-Wesley, New York, 1988.
[7] G. Russo, *Classical Electrodynamics,* lectures notes.
[8] G. Russo, *The Physics of Nuclear Reactor,* lectures notes.
[9] S. Barbarino, *Appunti di Microonde,* online book.
[10] L. Pappalardo, *Interferometria e Olografia Applicate ai Beni Culturali,* online book.
[11] E. Esarey, C. B. Schroeder, W. P. Leemans, *Physics of laser-driven plasma -based accelerators,* Review of Modern Physics, 81(3):1229 (2009).
[12] A. Sgattoni, *Theoretical and numerical study of laser-plasma ion acceleration,* PhD thesis in Physics A.A. 2011.
[13] S. Sinigardi, *Dynamical aspects of optical acceleration and transport of proton,* Master Degree thesis in Physics A.A. 2009-2010.
[14] F. Rossi, *Development of algorithms for an electromagnetic particle in cell code and implementation on a hybrid architecture (CPU+GPU),* Master Degree thesis in Physics A.A. 2010-2011.
[15] F. Vittori, *Accelerazione Laser-plasma: primi risultati sperimentali dal progetto PlasmonX,* Master Degree thesis in Physics A.A. 2007-2008.
[16] V. S. Popov, *Tunnel and multiphoton ionization of atoms and ions in a strong laser field,* Physics-Uspekhi **47** (9) 855-885 (2004).
[17] D. Giulietti, L.A. Gizzi, *X-ray emission from laser-produced plasmas,* Rivista del Nuovo Cimento Vol. 21, N.10 (1998).
[18] L. Spitzer, R. Härm, *Transport phenomena in a completely ionized gas,* Physical Review Vol 89, N.5 (1953).
[19] A. Macchi, C. Benedetti, *Ion acceleration by radiation pressure in thin and thick targets.*
[20] A. Macchi, F. Cattani, T.V. Liseykina, F. Cornolti, *Laser acceleration of ion bunches at the front surface of overdense plasmas,* arXiv:physics/0411023v2 (2005).
[21] G. Hairapetian, R. L. Stenzel, *Expansion of a two-electron-population plasma into vacuum,* Physical Review Letters Vol. 61, N. 14.
[22] M. Passoni, L. Bertagna, A. Zani, *Target normal sheath acceleration: theory, comparison with experiments and future perspective,* New J. Phys. 12 045012 (2010).
[23] G. Turchetti, A. Sgattoni, C. Benedetti, P. Londrillo, L. Di Lucchio, *Comparison of scaling laws with PIC simulation for proton acceleration with long wavelength pulses,* Nuclear Instruments and Methods in Physics Research A 620 (2010) 51–55.
[24] P. Bolton, P. Londrillo, A. Sgattoni, M. Sumini, G. Turchetti., *Numerical investigation of optical acceleration of protons and perspective for hadrotherapy,* (2011 Preprint).
[25] P. Londrillo, A. Sgattoni, S. Sinigardi, M. Sumini, G. Turchetti, *Protons acceleration from CO_2 laser pulses for biomedical applications,* (2011 Preprint).
[26] G. Turchetti, *Mathematical models in beam dynamics*, personal note.

[27] P. Antici, M. Migliorati, A. Mostacci, L. Picardi, L. Palumbo, C. Ronsivalle, *A compact post-acceleration scheme for laser-generated protons,* Physics of Plasmas 18,000000 (2011).
[28] T. Toncian, M. Amin, M. Borghesi, C. A. Cecchetti, R. J. Clarke, J. Fuchs, R. Jung, T. Kudyakov, M. Notley, A. C. Pipahl, P. A. Wilson and O. Willi, *Propertiesof a plasma-based laser-triggered micro-lens,* AIP Advances 1, 022141 (2011).
[29] T. Toncian, M. Borghesi, J. Fuchs, E. d'Humières, P. Antici, P. Audebert, E. Brambrink, C. A. Cecchetti, A. Pipahl, L. Romagnani, O. Willi, *Ultrafast laser-driven microlens to focus and energy-select mega-electron volt protons,* Science Vol 312, pag 410, 21/04/2006.
[30] V. G. Vaccaro, M. R. Masullo, C. De Martinis, L. Gini, D. Giove, A. Rainò, V. Variale, L. Calabretta, A. Rovelli, S. Barone, S. Lanzone, *A side coupled proton LINAC module 30-35 MeV: first acceleration tests.*
[31] *Doria, D.; Kakolee, K.F.; Kar, S.; Litt, S.K.; Fiorini, F.; Ahmed, H.; Green, S.; Jeynes, J.C.G.; Kavanagh, J.; Kirby, D.; et al. Biological effectiveness on live cells of laser driven protons at dose rates exceeding 10^9 Gy/s, AIP Adv. 2012, 2, 011209.*
[32] M. Nishiuchi, H. Sakaki, T. Hori, P. R. Bolton, K. Ogura, A. Sagisaka, A. Yogo, M. Mori, S. Orimo, A. S. Pirozhkov, I. Daito, H. Kiriyama, H. Okada, S. Kanazawa, S. Kondo, T. Shimomura, M. Tanoue, Y. Nakai, H. Sasao, D. Wakai, H. Daido, K. Kondo, H. Souda, H. Tongu, A. Noda, Y. Iseki, T. Nagafuchi, K. Maeda, K. Hanawa, T. Yoshiyuki, T. Shirai, *Measured and simulated transport of 1.9 MeV laser-accelerated proton bunches through an integrated test beam line at 1 Hz*, PhysRevSTAB.13, 071304 (2010).
[33] U. Linz, J. Alonso, *What will it take for laser driven proton accelerators to be applied to tumor therapy?,* PhysRevSTAB.10.094801 (2007).
[34] M. Schollmeier, S. Becker, M. Geißel, K. A. Flippo, A. Blažević, S. A. Gaillard, D. C. Gautier, F. Grüner, K. Harres, M. Kimmel, F. Nürnberg, P. Rambo, U. Schramm, J. Schreiber, J. Schütrumpf, J. Schwarz, N. A. Tahir, B. Atherton, D. Habs, B. M. Hegelich, and M. Roth, *Controlled Transport and Focusing of Laser-Accelerated Protons with Miniature Magnetic Devices,* PRL 101, 055004 (2008).
[35] I. Hofmann, J. Meyer-ter-Vehn, X. Yan, A. Orzhekhovskaya, S. Yaramyshev, *Collection and focusing of laser accelerated ion beams for therapy applications,* Physical Review Special Topics - Accelerators and Beams 14, 031304 (2011).
[36] I. Hofmann, A. Orzhekhovskaya, S. Yaramyshev, I. Alber, K. Harres and M. Roth, *Laser accelerated ions and their potential for therapy accelerators,* GSI Internal Report.
[37] H. Sakaki, T. Hori, M. Nishiuchi, P. Bolton, H. Daido, S. Kawanishi, K. Sutherland, H. Souda, A. Noda, Y. Iseki, T. Yoshiyuki, *Designing integrated laser-driven ion accelerator system for hadron therapy at PMRC (Photo Medical Research Center),* Proceedings of PAC09, Vancouver, BC, Canada TU6PFP009.
[38] F. Schillaci et al., *Characterization of the ELIMED Permanent Magnets Quadrupole system prototype with laser-driven proton beams,* 2016 JINST 11 T07005
[39] L. Pommarel et al., *Spectral and spatial shaping of a laser-produced ion beam for radiation-biology experiments,* Phys. Rev. Accel. Beams, 20, 032801 (2017)
[40] D. Margarone et al., *ELIMAIA: A Laser-Driven Ion Accelerator for Multidisciplinary applications*, Quantum Beam Sci. **2** (2018) 8
[41] Wagner, F. et al., *Maximum Proton Energy above 85 MeV from the Relativistic Interaction of Laser Pulses with Micrometer Thick CH2 Targets*, Phys. Rev. Lett. 2016, 116, 205002

2 Feasibility Study of a Permanent Magnet Quadrupole system for the collection of laser driven-ion beams in the energy range of 3-60 MeV/u

The general idea of laser-people is:
"I need X Telsa, just put a random magnet there and it will work".
F. Schillaci

In this chapter the design of the ELIMED collection system is proposed showing the main idea and the issues linked with its realization. The approach starts with considering the layout and the performances of the core of the whole beamline (the energy selector system) and the development of the design aims at the production of a good quality beam suitable for application. At the end of the chapter, the realized system is described together with the diplacement mechanic system necessary for tuning the optics. The results of the characterization using standard proton beam performed at INFN-LNS are also shown.

2.1 Introduction

Laser-driven ion beams are promising alternative to conventionally accelerated beams even if they are not directly suitable for most applications because of the huge angular and energy spread. A beam-line made of two main elements for the correction of these issues is going to be designed in order to collect, select and transport laser-produced beams up to 60 MeV/u, offering, as output, a controllable beam in terms of energy spread (varying from the 5% up to the 20% for higher energy), angular divergence and hence, manageable beam spot size in the range 0.1-10 mm and acceptable transmission efficiency (namely 10^6-10^{11} ions/pulse assuming 10^9-10^{12} ions/pulse are produced at the interaction point within the energy range of interest).

In order to fulfil the requirements the two main elements of the beam-line are a collection system made of permanent magnet quadrupoles (PMQs) and an energy selection system (ESS) made of conventional resistive magnets. The aim of the collection system is to collect the particle within a certain energy range, correct the angular divergence of the beam and inject the particles in the selection system. The beams coming out from this first part of the beam-line (PMQs+ESS) will have characteristics similar to the conventional beams and, hence, easy to transport and shape with conventional magnetic lenses, such as resistive quadrupoles and steerers, which will be placed in the last part of the in-vacuum beam-line.

The above description of the beam-line proposed, makes it clear that the ESS is the core element around whom all the other magnetic devices have to be designed and realized. Hence, in the following a brief description of the selection system will be proposed.

2.1.1 The Energy Selection System; preliminary conceptual design

A sketch of the ESS is shown in Figure 2.1. Its layout is based on four resistive dipoles with alternating field, similar to a bunch compressor scheme, and its main trajectory parameters are also reported in the figure, according to the treatment proposed in [1].

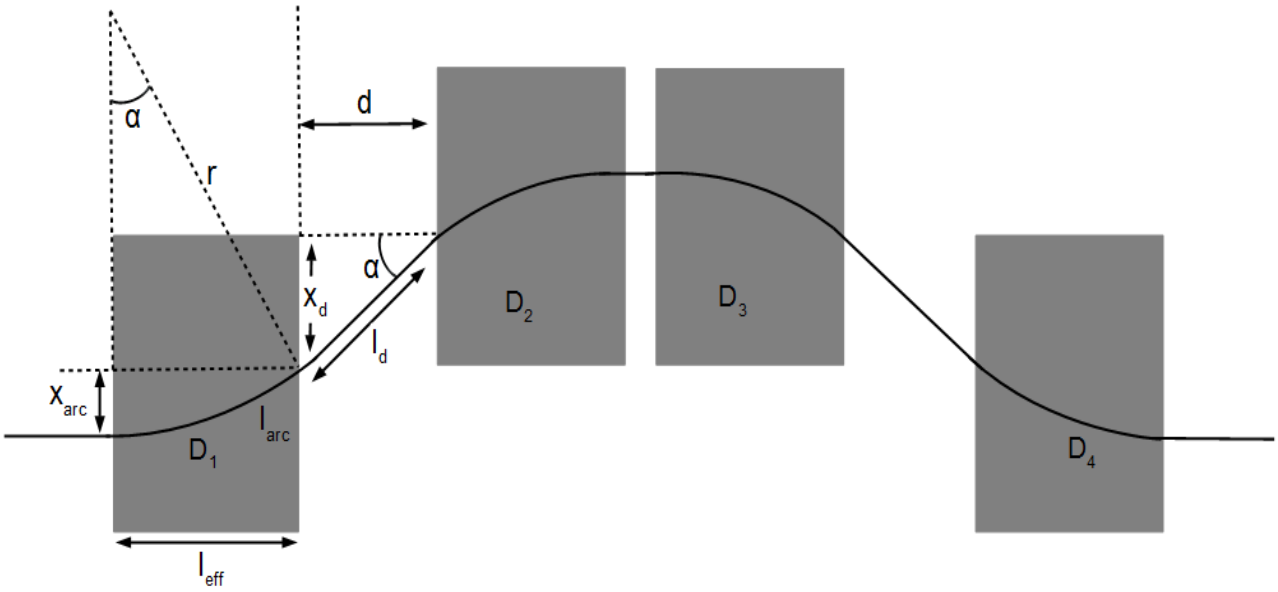

Figure 2.1: *Energy Selection System Layout and main trajectory parameters.*

Using the main trajectory parameters shown in Figure 2.1, it is possible to analytically define the characteristics of the ESS, in terms of radial and longitudinal dimensions of each dipole, field strength and selection slit size, necessary to have the wanted energy resolution. In fact, the bending radius *r* and the bending angle *α* of a dipole are both function of the particle momentum. Hence, the energy can be written using the following relativistic equation:

$$T = \sqrt{\left(\frac{qc(\Delta x - \tan\alpha)}{2\frac{(1-\cos\alpha)}{B}} \right)^2 + M0^2 c^4} - E0$$

which represents the calibration equation of the ESS, being *Δx* the radial displacement of the beam at the centre of the device and *q*, *M0* and *E0* the characteristics of the ion to be selected. The derivative of the previous equation times the slit aperture size *s*, namely $(dE/dx)*s$, gives the energy resolution of the device.

Different layout have been investigated and the better solution, in terms of compactness and performances, is the use of a single trajectory based device, as shown in Figure 2.2.

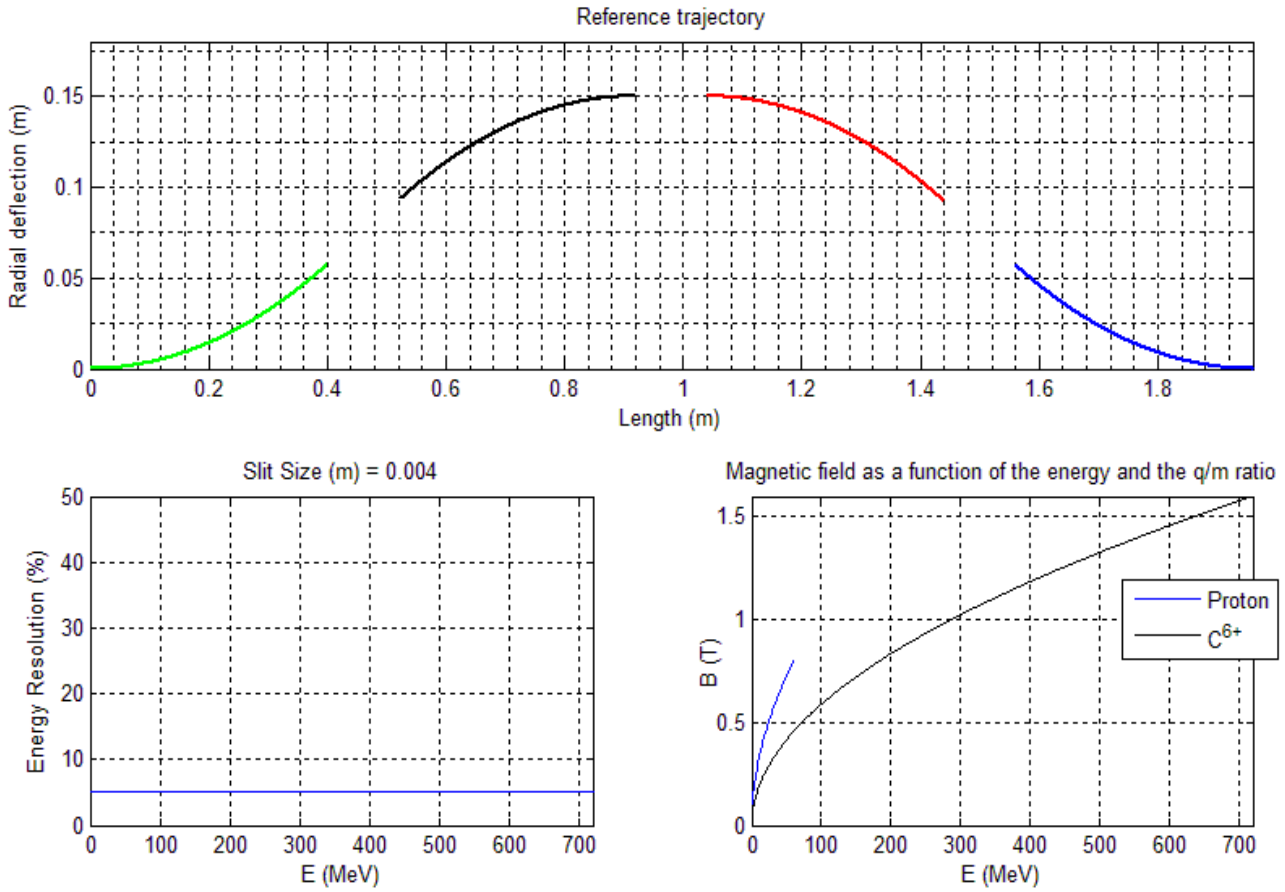

***Figure 2.2**: ESS preliminary characterization.*

For this system each magnet would be 400 mm long and the drift between each magnet would be 120 mm long, for a total length of 1.96 m. The working trajectory has maximum radial deflection of 150 mm at the device centre. The upper panel of Figure 2.2 shows the trajectory within the four dipoles (coloured lines). The selected path would guarantee a fixed energy resolution of about 5% if a 4 mm aperture slit is used. This resolution would be independent form the particle energy and ion species, as shown in Figure 2.2 left hand side of the bottom panel. What have to be changed, in order to put particle with different energy on the reference trajectory is the magnetic field, as shown in Figure 2.2 right hand side of the bottom panel, which have to vary between 0.17 up to 0.8 T for protons with energy ranging between 3 and 60 MeV, while it has to reach the value of 1.59 T for carbons with energy of 60 MeV/u.

The proposed layout would allow to vary the energy resolution changing the slit aperture size, which is an advantage as at higher energy, laser-produced particles are less abundant and a bigger slit is necessary to keep the transmission efficiency acceptable, as will be shown later. In order to have the requested resolution varying from the 5% up to the 20%, the slit aperture size have to vary in the range between 4 and 20 mm. With a single reference trajectory, the resolution depends on the slit aperture size and it fixed for all energies.

2.1.2 Permanent Magnet Quadrupole system features

The described layout allows to calculate the main beam parameters to be considered in order to properly and efficiently inject the beam into the ESS, which basically depend on the effective trajectory length, which is 2.132 m, on the collimators size placed upstream and downstream the

ESS, which reasonably have a diameter of 30 mm and the slit aperture size which is fixed to 30 mm on the transverse plane and variable on the radial, or dispersion, plane as described above. This parameters have been used to fix the main features of the collection system in terms of quadrupole number, bore diameter, geometrical length and field gradient. In fact, in this first analysis, the ESS has been simulated as a simple collimator system of the proper sizes and at the right relative distances and the PMQs features have been changed in order to produce the proper beam parameters for the injection in the "linearized" magnetic chicane. In this way the PMQs system results made of five quadrupoles as described in the next table.

n° of PMQ	Geometric length	Field gradient	Bore diameter
1	160 mm	101 T/m	30 mm
2	120 mm	99 T/m	30 mm
2	80 mm	94 T/m	30 mm

Once this first process has been completed, the PMQs magnetic design has been accomplished and the beam transport has been reviewed using the field maps, for monochromatic beams ranging from 5 up to 60 MeV/u. This procedure allows to tune the PMQs system for collecting a certain energy component to be injected in the ESS. Finally the tune PMQs system has been simulated using realistic TNSA spectra provided by the client.

In the next sections of this technical report, the magnetic design and the optics simulation, briefly mentioned above are extensively described.

2.2 Permanent Magnet Quadrupole system design

Magnetic lenses are used in conventional particle accelerators to deflect, focus and/or correct the beam along the transport lines. PMQs lenses have the advantage to be relatively compact with an extremely high field gradient, of the order 100T/m, within a reasonable big bore of few centimeters. A PMQs system allows to collect most part of the particles with wide divergence produced in the laser-target interaction process, providing a beam of good quality in terms of controlled size and divergence. For these reasons the interest in the application of PMQs in the beam handling of laser produced beams is growing in recent years [2, 3, 4]. Several PMQs designs have been proposed and developed based on pure Halbach scheme [5] or hybrid devices using saturated iron to guide the magnetic field [6, 7].

The design proposed for the collection system of the Laser Driven Ion Beamline for Multidisciplinary Applications has the main aim to collect a wide range of ion energies from 3MeV/u up to 60MeV/u and inject the beam in the ESS, hence, the system has to be versatile and has to ensure a reasonably good transmission efficiency. Thus, a big bore of at least 36 mm is necessary with a strong field gradient and high uniformity within, at least, the 80% of its active surface, which is not smaller than 30 mm in dimeter as a 3 mm screening pipe for magnet protection has to be set in the aperture. Considering these requirement the quadrupoles designed are based on a standard trapezoidal Halbach array surrounded by two external hybrid arrays made of rectangular block and iron. The inner array of 122 mm diameter is mainly responsible for the field quality of the quadrupole, the external arrays, of 223 mm and 322 mm respectively, are necessary to increase the volume of permanent magnet material to reach the required field gradient. A scheme of the PMQs

layout is shown in Figure 2.3.

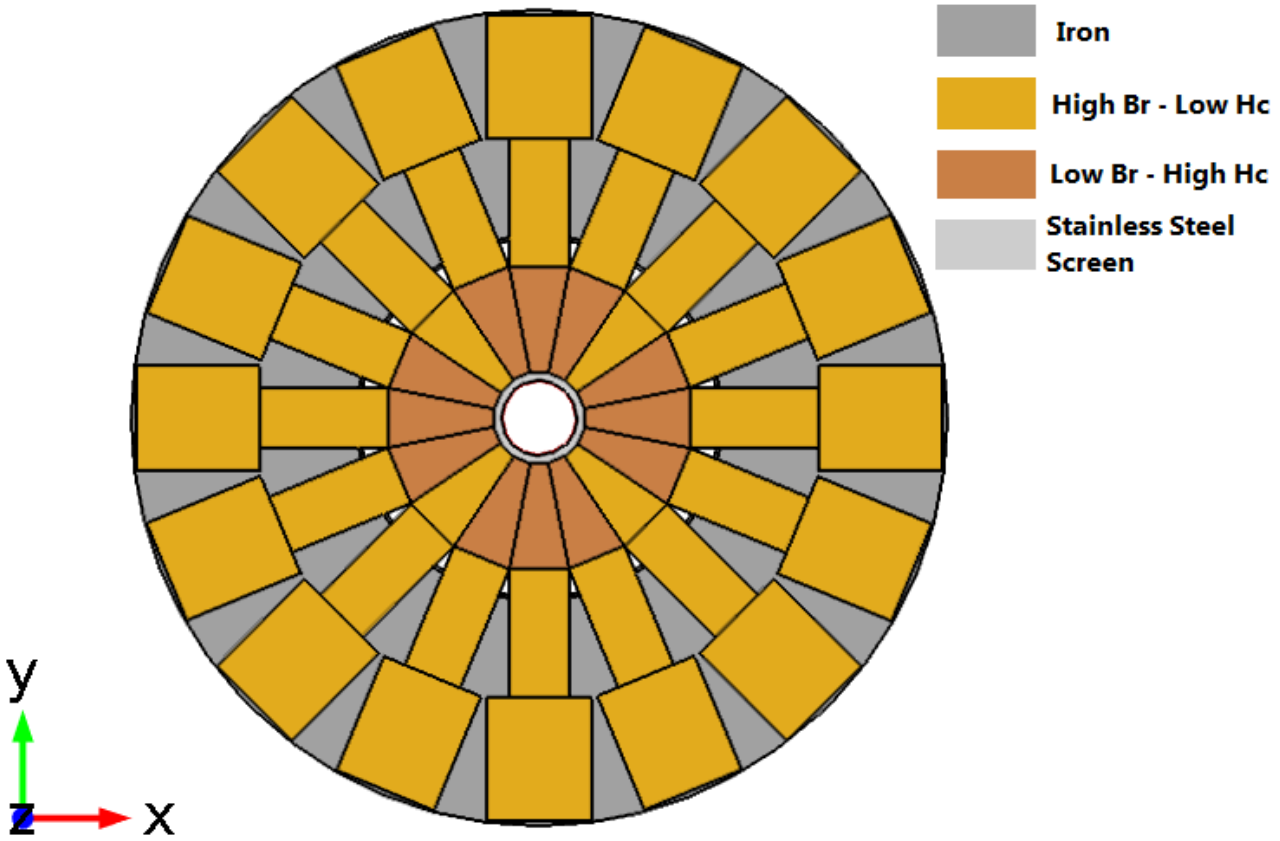

***Figure 2.3**: PMQ layout. The different colours are referred to the different material used.*

The choice if this layout, in which a pure Halbach array is mixed with hybrid Halbach arrays, is due to the fact that permanent magnet alloys are very brittle material and the realization of trapezoidal block is problematic from the mechanical point of view. This design, as shown later, results to be robust with a very good field quality and, at the same time more easy to realize respect to a pure Halbach array. As can be seen in Figure 2.3 the two external arrays are set within an iron matrix which has the function of supporting structure as well as magnetic flux guide. The inner array is made of two different permanent magnet alloys with different characteristics. This is due to the fact that the magnetic flux in the bore has a maximum value of about 1.8 T and for such high flux values local demagnetization phenomena can occur where the magnetic field components Hx and Hy have opposite direction respect to the permanent magnet magnetization direction and a value higher than the material coercitivity. This issue can be solved mixing materials with different coercitivity in some strategic places of the array. In particular in the proposed design the main magnetic material is NdFeB N48H with remanence Br = 1.39T and coercitivity Hc = 1273 kA/m and NdFeB N38UH (Br = 1.26 T and Hc = 1990 kA/m) as high coercitivity component set in the point at risk of demagnetization. Figure 2.4 shows the sectors where H field components are higher than the main magnetic material coercitivity, the red arrows are the H field directions and the blue arrows are the magnetization direction of each block.

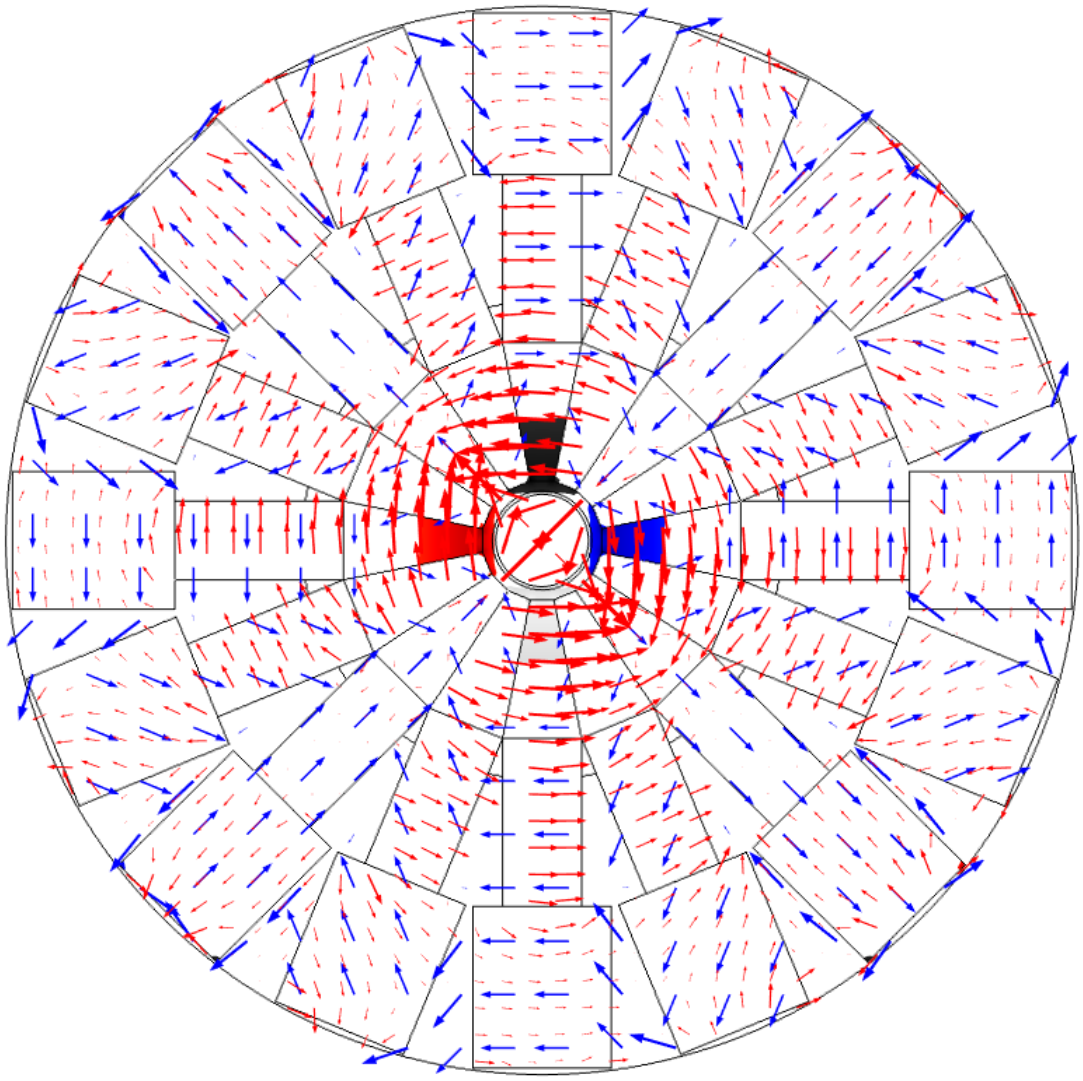

***Figure 2.4**: Demagnetization field components:coloured zones have a H field higher than NdFeB N48H coercitivity, red arrows are in the H field directions and blue arrows are in the magnetization directions of each block*

Comparing Figure 2.3 and Figure 2.4, it is evident that the parts of the magnetic array at risk of demagnetization are made of high coercitivity material. The volume occupied by the material is anyway bigger than necessary as a safety margin of 20% has been considered. The maximum value of the H field is 1.8 kA/m, this value determines the choice of the secondary magnetic alloy. The permanent magnet materials have been simulated by means of their BH curves in the temperature interval between 20°C and 60°C.

2.2.1 Thermal stability and neutron flux

Thermal stability and secondary neutron flux are usually an issue for NdFeB permanent magnet alloys. Both issue have been study with Monte Carlo simulations performed with the GEANT4 toolkit.

The geometrical set-up of the simulations is shown in Figure 2.5. Downstream the source is placed a stainless steel screen that will be used in front of the first quadrupole for the protection of the whole system, especially mechanicals components. After a small drift the quadrupole is placed

considering its protection screen, a 10 mm thick stainless steel foil, and the inner screening pipe, which have been considered 2.5 mm thick for these simulations. PMQs material have been simulated using the NdFeB density (d=7.4g/cm^3) and its specific heat (440 J/(kg*K)).

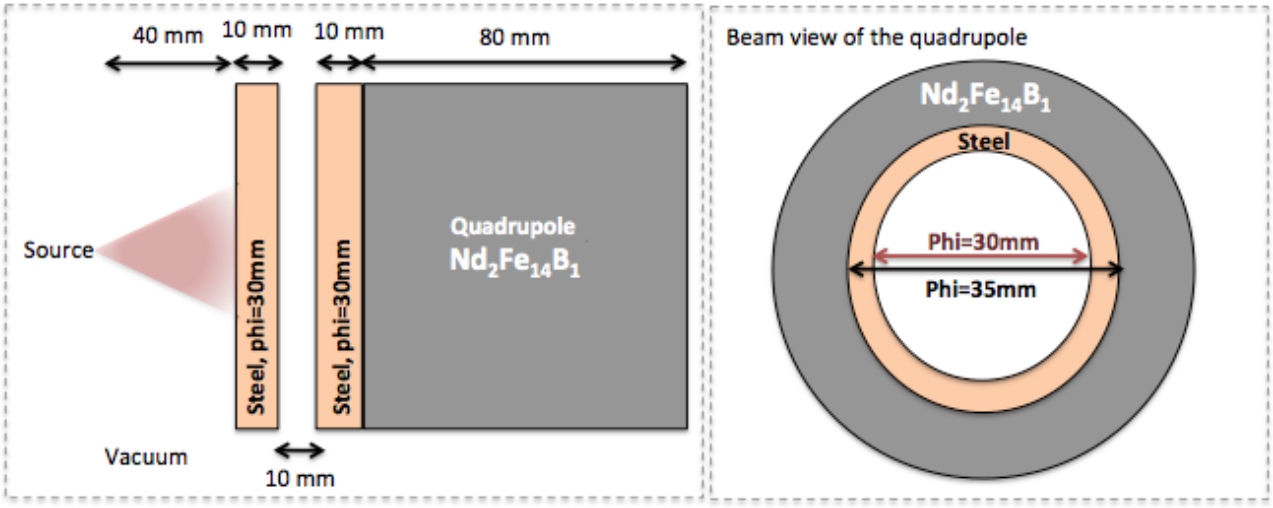

***Figure 2.5**: Geometrical set-up of the simulations.*

The used spectrum at the source is the one expected at ELIMAIA and shown in Figure 2.18 (red line), it has normalized to have 10^9@60 MeV ±5% and 10^{10}@60MeV ±5%. We have implemented an isotropic divergence of ±10° and ±2.5°, respectively, reproducing in this way two different scenarios which can be achieved with L3 and L4 lasers

The maximum temperature increasing, in both the worse and best case, has been 10^-3 K on the external layer of the PMQ screening pipe. Therefore, to be conservative, the inner quadrupole surface, in contact with the pipe, has been considered as to have the same temperature increasing.

In order to increase the total temperature from 20°, room temperature, to 60° (ΔT=40°), the total number of possible shot is of about 20000. This means that the PMQs can be used safely for 0.5 hour if the laser repetition rate is 10Hz and for 5 hours in the 1Hz repetition rate case. After that number of shots the vacuum chamber have to be opened to cool the PMQs down. This operational time is still conservative as the relaxation time between each particle bunch has not taken into account [11].

The neutron flux have been evaluated using the Bertini Cascade model implemented in GEANT4 (QGSP_BERT) [8] which is able to simulate the hadronic processes in our energy range with a very good agreement respect to the experimental data. The maximum neutron production is 10^2 neutrons/cm^2. In literature, radiation damage of permanent magnet is reported to occur for neutron flux much more higher [9, 10].

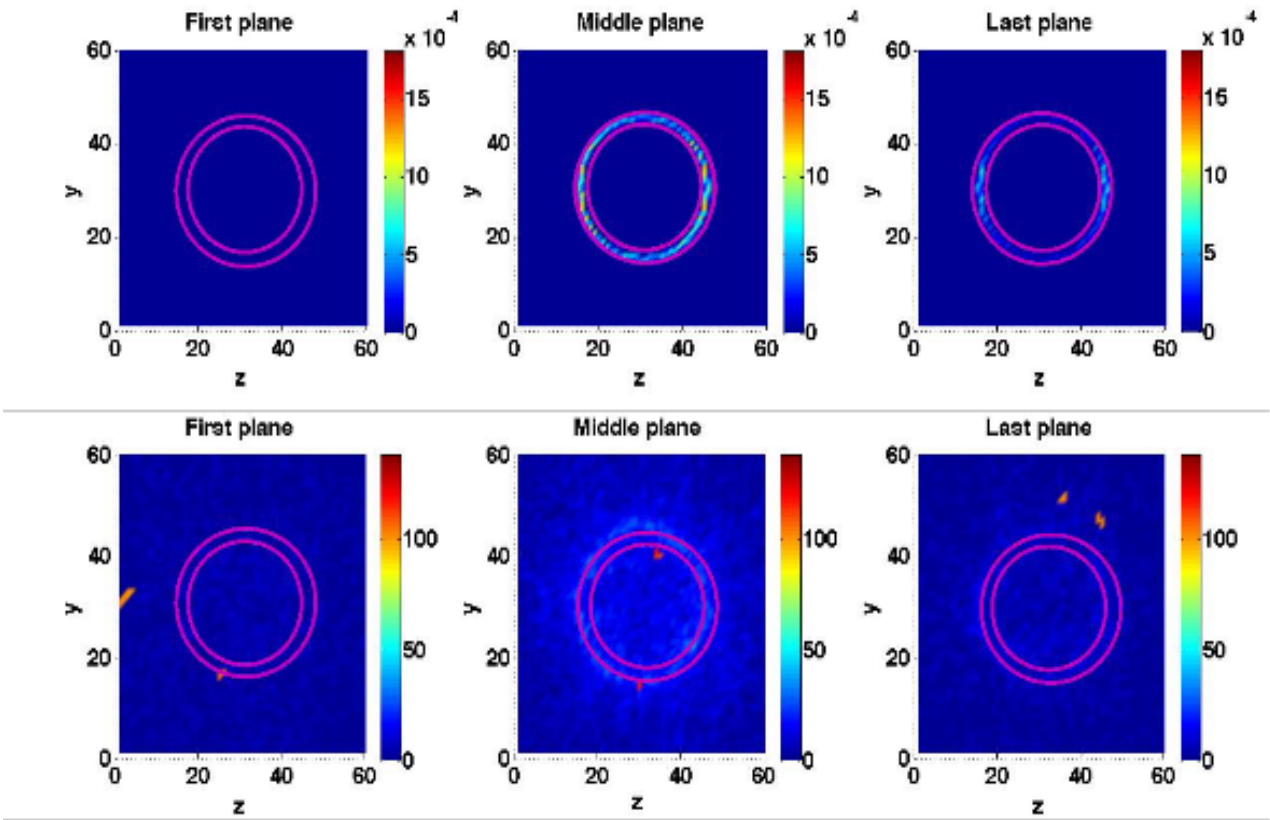

***Figure 2.6**:Temperature increasing in Kelvin (upper panel) and neutron production in neutron/cm^2 (bottom panel) for the first, middle and last plane of the quadrupole. Magenta circles delimit the inner shielding pipe..*

The results for the simulations in the worse case, which gives the most critical results, are shown in Figure 2.6. The upper panel resumes the results of the temperature increasing in the three different transverse planes of the quadrupole. In the bottom panel is shown the neutron flux. Anyway this preliminary results will be reviewed with more realistic laser-driven bunches, in terms of angular divergence.

2.2.3 Attraction/Repulsion Forces between PMQs

One more issue related with permanent magnets is the attraction/repulsion forces that can be extremely high when large volumes are involved. Hence, considering that the PMQs system won't be static as it as to be tuned for a certain energy, changing the relative distances between magnets and, also, the number and polarity of each quadrupole can be changed, it is important to evaluate these forces for the proper design of the mechanics and also for the elaboration of a safe procedure for the PMQs extraction and/or assembly.

The forces have been evaluated between a 160 mm length PMQ and a 120 mm PMQs, which represents the case in which the biggest volume of permanent magnets are interacting. The results have been benchmarked performing a comparison of the same calculations on a set of small PMQs [7] already realized and the measured forces.

The forces between the naked quadrupoles along the longitudinal axis are plotted in Figure 2.7. The calculations have been performed changing the relative distance between the quadrupoles from 22 mm (the minimum distance possible due to the 10 mm think stainless steel screens that will be set at the head and at the bottom of the quadrupoles) up to 192 mm. Form the plot it is possible to

see that the force are extremely high for small distances but they decrees quickly and are reasonably small at distances larger than 100 mm. This is important to identify the minimum working distances of the PMQs, in order to realize the proper mechanics, which has been set at 40 mm corresponding to a force of about 5 kN, and the minimum distance for the extraction of the magnets, which has been fixed at 180 mm corresponding to a force smaller than 80 N.

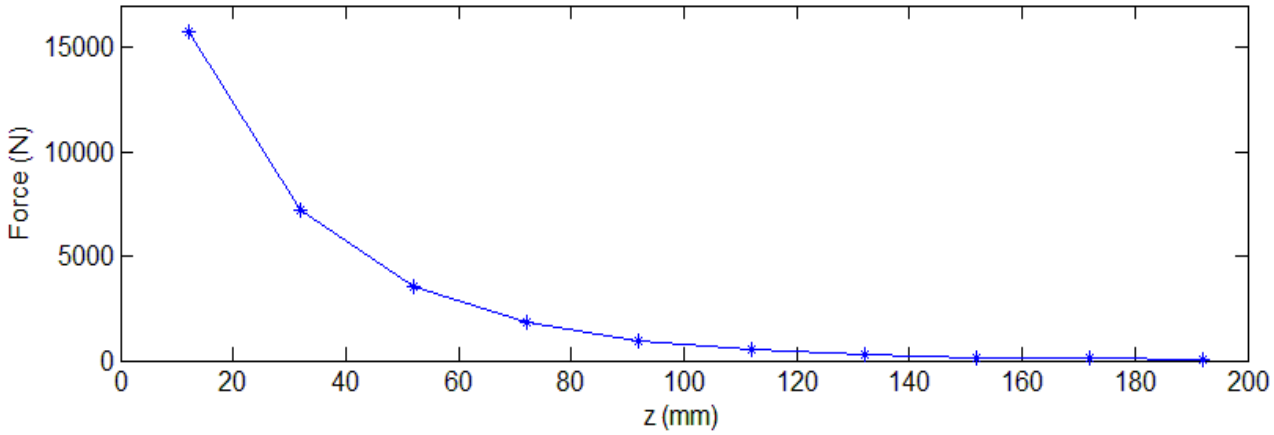

***Figure 2.7**: Force between two quadrupoles at different distances*

The transport efficiency of the system requires smaller distances between quadrupoles and different possible shields for the magnetic field responsible of these high forces have investigated. In general non-linear materials such as Mu-metal are used to screen magnetic field but they usually have low saturation and high permeability and are not efficient screens for this case. Different alloys such as G-IRON [12], which does not contain nickel, or MagnetShield [13] offering high saturation and relatively low permeability, see next table, and result more suitable for this application. Comparison of the screening efficiency among different alloys described and multilayer screens is shown in Figure 2.8. G-IRON and MagnetShield give very similar results in the simulations as they have almost the same magnetic features, and, for this reason, here only the results with G-IRON are reported.

	B_{sat} (T)	$\mu_{r\,max}$
Mu-metal	1.2	40000
Permimphy	0.75	80000
G-Iron	2	7000
MagnetShield	2.14	4000

In the case of G-Iron two different shielding thickness have been considered:

- 1 mm of shield on the backface of the longest quadrupole and 2 mm of shield on the frontface of the short quadrupole
- 2 mm of shield on both quadrupoles

in the case of Mu-metal and Permimphy on the 2 mm shield thickness on both quadrupole has been considered and the force reduction is less efficient than both the G-iron cases.

To increase the force reduction two multilayers screen have been designed and modelled at the front and back faces of the two quadrupoles:

- Multilayer Screen 1 is made of a 2 mm thick iron layer set between two stainless steel layers

of 3 mm of thickness and 2 mm of G-Iron

- Multilayer Screen 2 is made of a 1 mm thick iron layer alternatig with 1 mm of stainless steel in order to make a screen of 10 mm of thickness in total and than a 2 mm thick layer of G-Iron is used.

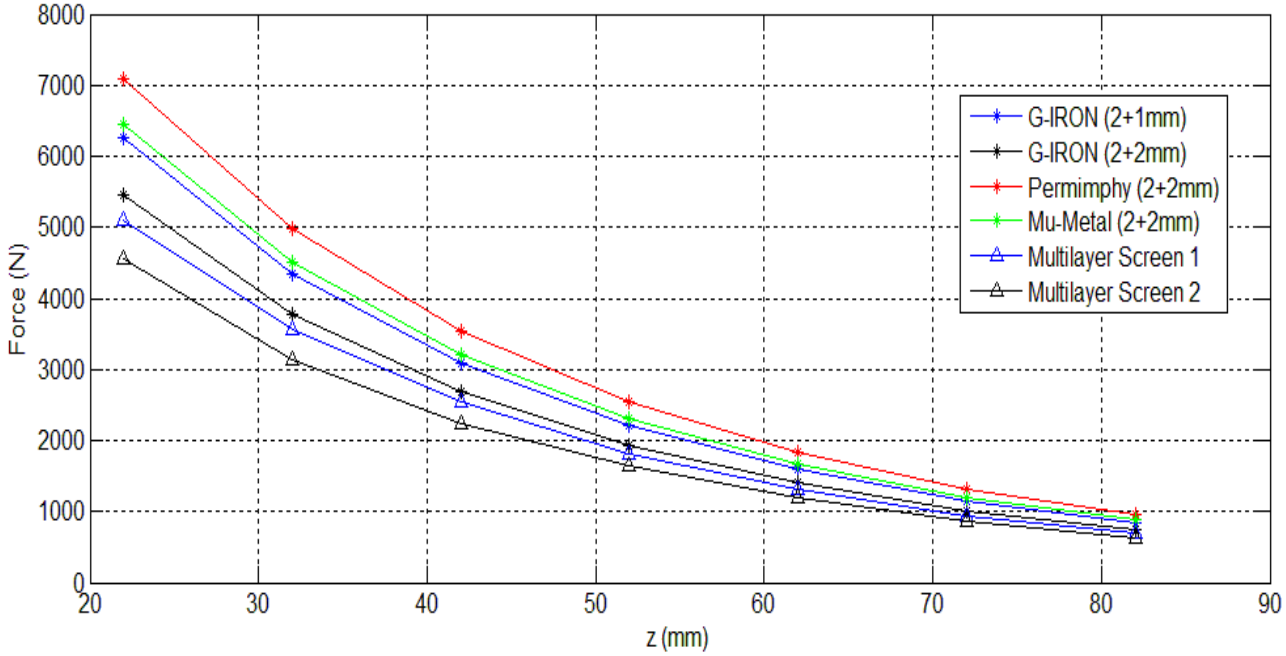

***Figure 2.8**: Force between two quadrupoles at different distances and with different screens*

In all the three cases in which 2 mm of G-Iron are used on both quadrupoles the forces results to be smaller than 3 kN if they relative distance is of 40 mm. This results is important as the relative working distance could be reduced to 25 - 30 mm. It should be noted, from Figure 2.8, that for distance higher than 75 mm all the different layers investigated have almost the same shielding efficiency. This is due to the fact that the total field intensity is smaller and the non-linear materials are not saturated and their efficiency is higher. This also justify the necessity to use material with high magnetic saturation.

The results obtained with G-Iron and MagnetShield alloys will be benchmarked on the prototype already developed before taking the final choice on the minimum distance allowed between two quadrupoles. In the following the optics and transport is simulated for the worse case of the naked quadrupoles.

Moreover, the presence of a magnetic shield so close to the PMQs could lead, again, to demagnetization problems as the field lines are forced to close themselves closer to the magnets. Hence, a similar demagnetization analysis above described has been performed for the different screen proposed showing, anyway, no risk of demagnetization.

2.2.3 PMQ field Analysis

The field analysis is here limited to the long (160 mm) quadrupole and within the active bore of 30 mm diameter. As described above, each PMQ can be seen as the combination of 16 sectors pure Halbach array and two 16 sectors hybrid arrays. Each sector has its own magnetization direction detailed in the next table, where the sectors are numbered from 0 to 15 in counterclockwise starting from the one laying on the positive x axes of Figure 2.9. Considering the symmetry of the array, the

magnetization directions can be reduced to the three main directions of sectors 0, 1 and 2.

n=0; θ = 90°	n=4; θ = 0°	n=8; θ = 270°	n=12; θ = 180°
n=1; θ = 112.5°	n=5; θ = 22,5°	n=9; θ = 292.5°	n=13; θ = 202.5°
n=2; θ = 225°	n=6; θ = 135°	n=10; θ = 45°	n=14; θ = -45°
n=3; θ = -22.5°	n=7; θ = 247.5°	n=11; θ = 157.5°	n=15; θ = 67.5°

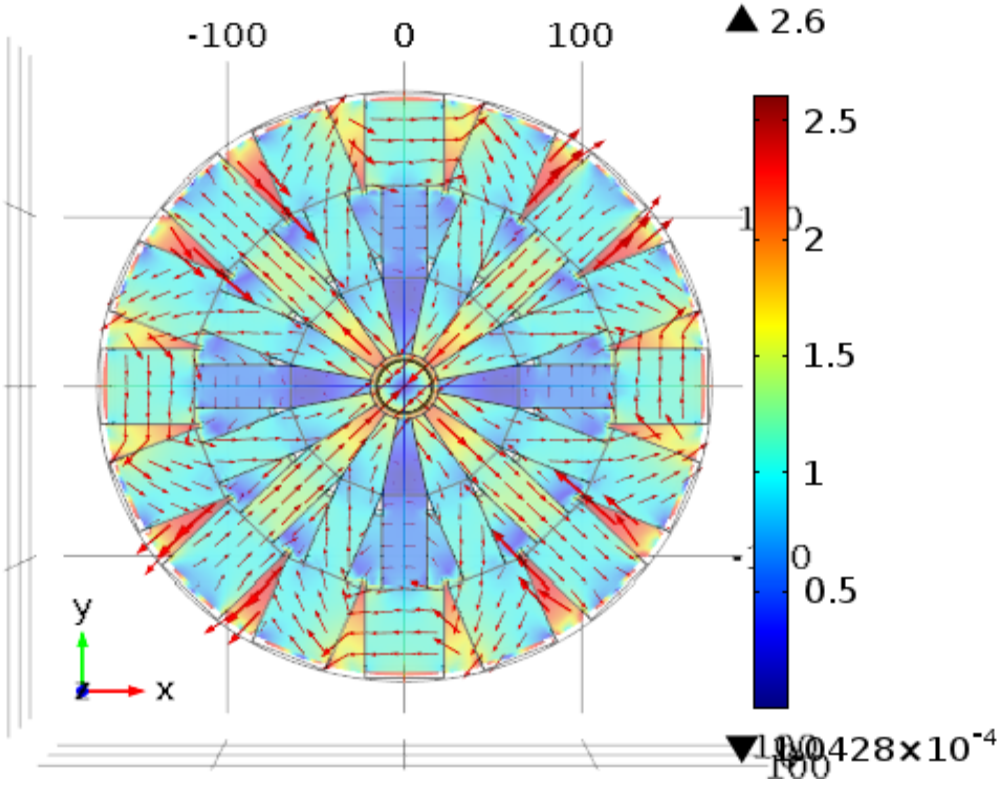

***Figure 2.9**: Magnetic flux density (colour surfaces) and directions (red arrows)*

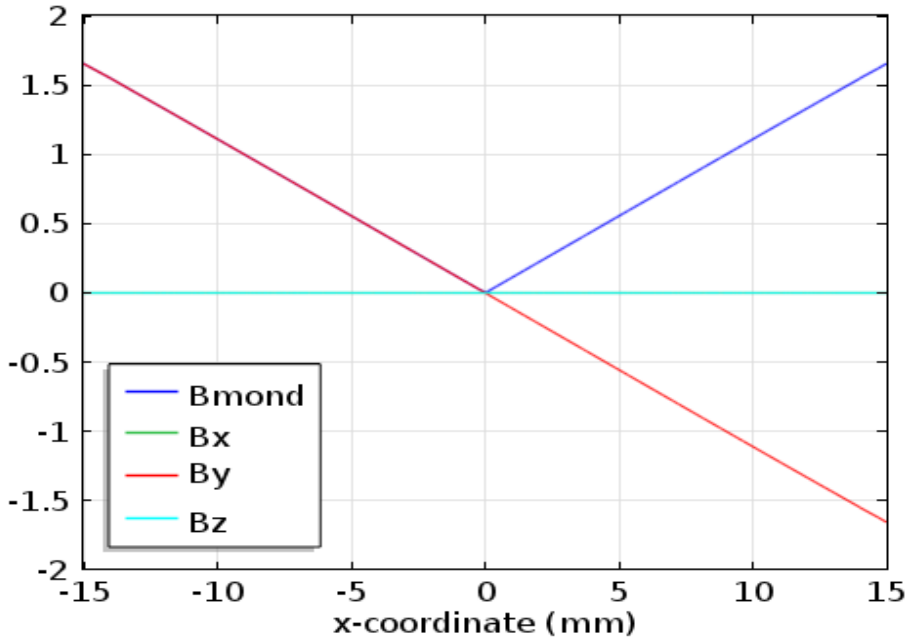

***Figure 2.10**: PMQ B field components along the x axes at the quadrupole center*

The magnetic field at the quadrupole center is shown in Figure 2.10. Its maximum is of about 1.55 T and the expected field gradient is of about 101T/m, as shown in Figure 2.11.

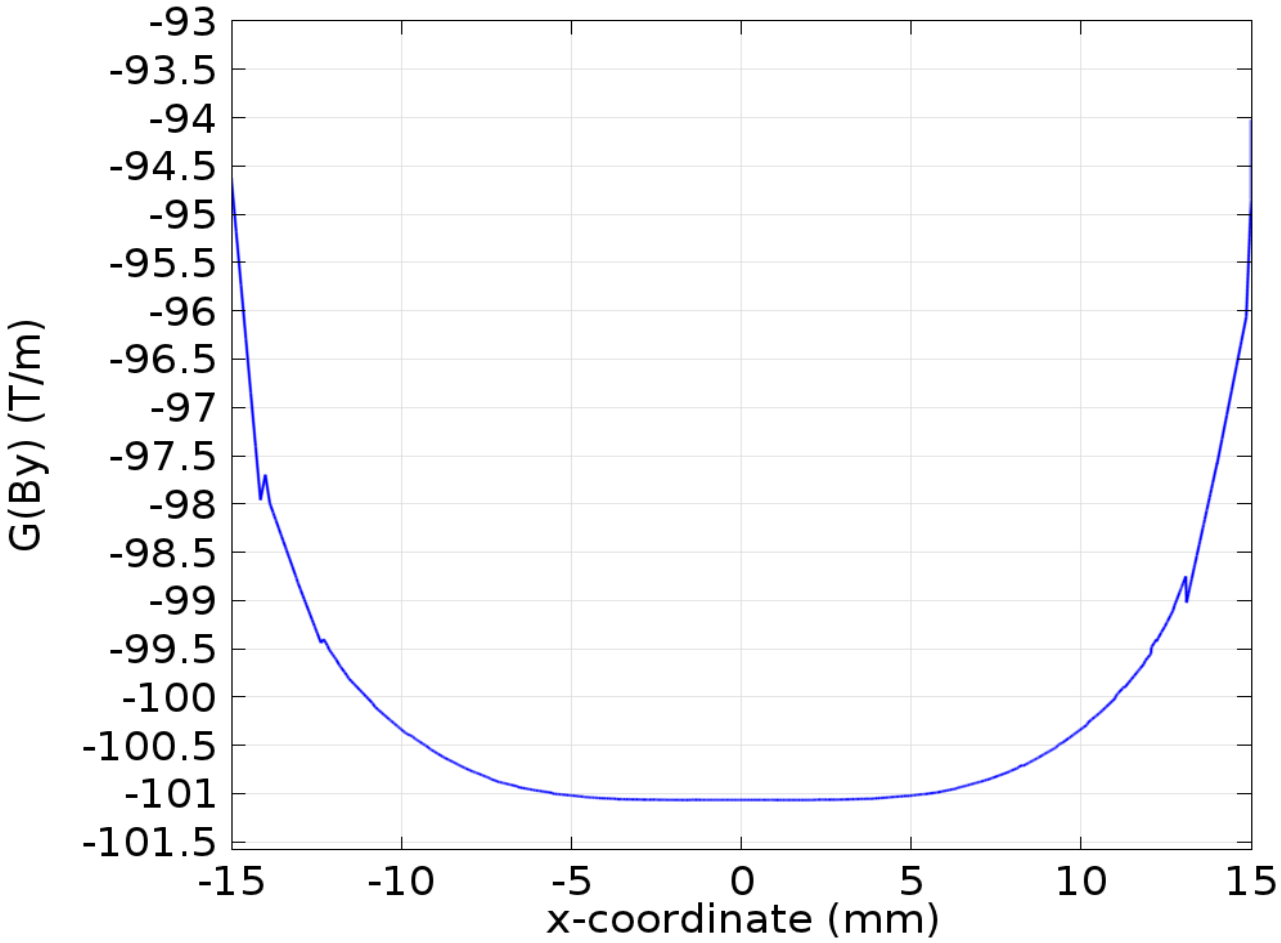

***Figure 2.11**:B field gradient at the quadrupole center*

A part from the maximum gradient it is important to evaluate the field quality of the quadrupoles given by the gradient uniformity (shown in Figure 2.12) and the integrated gradient uniformity (shown in Figure 2.13)

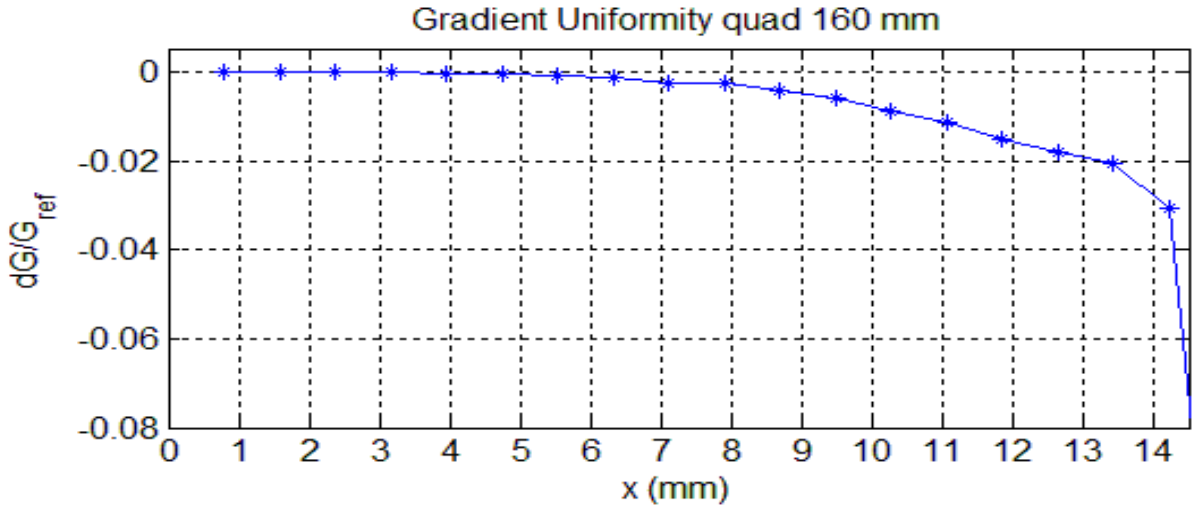

***Figure 2.12**: Gradient Uniformity for the 160 mm PMQ*

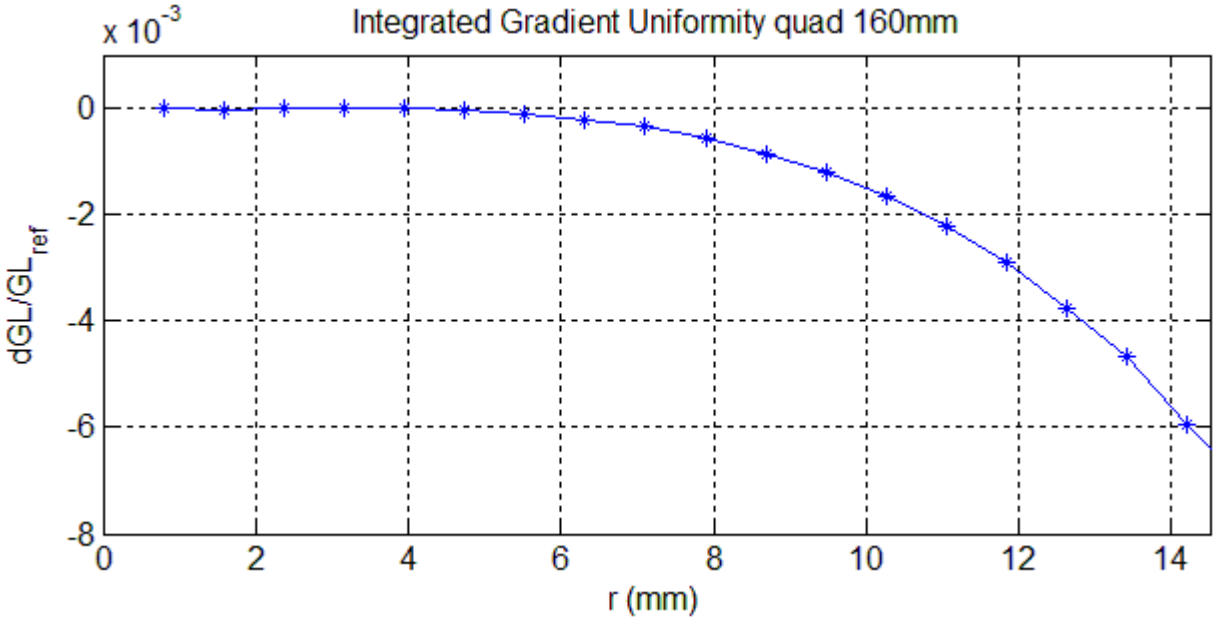

***Figure 2.13**: Integrated Gradient Uniformity for the 160 mm PMQ*

In the next table the uniformity analysis is summarized and compared with the analysis performed on PMQs with the same characteristics but designed as a pure Halbach array. As can be seen the field quality is not affected significantly in the proposed design.

	Gradient Uniformity		**Integrated Gradient Uniformity**	
	PMQs	*Pure Halbach*	*PMQs*	*Pure Halbach*
@ R = 7.5 mm (50% bore)	< 0.25%	< 0.1%	< 0.035%	< 0.03%
@ R = 12 mm (80% bore)	< 2%	< 1.5%	< 0.3%	< 0.3%
@ R = 14.5 mm (100% bore)	< 8%	< 3%	< 0.7%	<0.6%

The effective length of the quadrupole is 163 mm, for both the presented design and the pure ideal Halbach design, and the focal distance ranges from 15.2 mm, for 3 MeV protons, up to 69.1 mm, for 60 MeV protons.

The harmonic content is also important for the transport and have to be known and controlled. A part from the second field harmonic, which is the quadrupole component, the proposed hybrid design has a very small harmonic content and it is again similar to a pure Halbach design, as shown in Figure 2.14. In the plot are shown the normal harmonic components of a pure Halbach design, (blue circles) and of the presented design normalized with respect to the second harmonic, corresponding to the quadrupole harmonic, which is expressed in units of 10000, as usual standard [7 and its references]. Moreover the modulus of the complex harmonics (red circles), which takes in account the contribution of the skew harmonics is also plotted. The triangles are the harmonic values of the presented design. The quadrupole harmonic is not reported in figure, as its value is 10000 units for both cases. The normal harmonic content is basically the same for both pure and hybrid (0.31% of the main harmonic), the complex harmonic content is slightly different: 0.38% for a pure Halbach quadrupole and 0.39% for the hybrid design.

This results shown that the proposed design has basically the same features of a pure Halbach quadrupole resulting, on the other hand, a cost effective solution.

Details on the field uniformity and the harmonic components of the presented hybrid design are tabled in Appendix A.

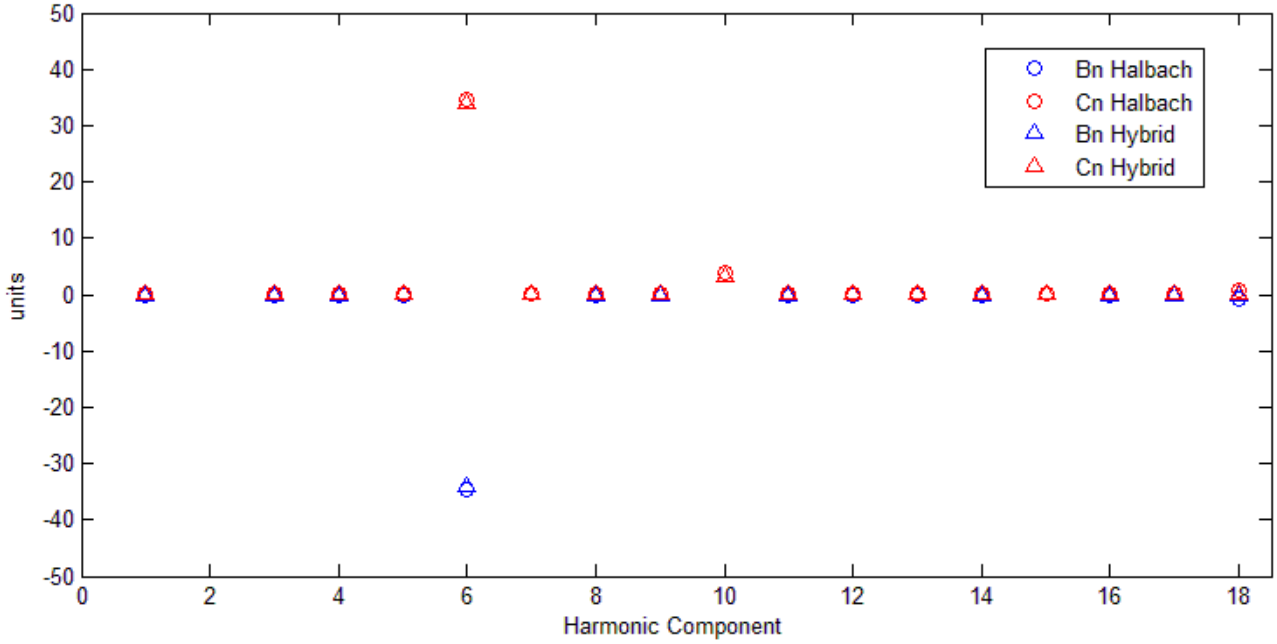

***Figure 2.14**: Harmonic content of the presented design and comparison with a pure Halbach quad.*

2.3 Beam-transport simulations

In the following the preliminary beam-transport simulation results are reported. The purpose of the simulations is to optimize the PMQs to inject a monochromatic beam component in the energy selector sketched, at the moment, as a collimator system geometrically placed along the beamline as described in Figure 2.2. There are three collimators in total: two of them are circular holes with a diameter of 30 mm that will be placed upstream and downstream the selector, the third one is the selection slit, which is a rectanglar aperture with height of 30 mm and variable width in the range between 5 and 20 mm in order to produce the required energy spread.

Figure 2.15 shows the scheme of the beamline. The laser-target interaction point is on the axis origin, follows the PMQs system and then the energy selection system. D1 and D4 are the collimators, D2 is the selection slit. The simulated beam has been considered monochromatic in a first phase, with 40 μm diameter circular shape at the production point and an uniform angular divergence of 11° (half angle). In the following are briefly described the results in the energy range between 5 and 60 MeV for protons and for C^{6+} at 60MeV/u, which is of interest for medical applications. In the following simulations the field maps of the quadrupoles described in the previous section are used. The goal of this preliminary simulations is the optimization of the PMQs in order to inject the beam in the energy selector avoiding the losses downstream of the collection system which has to stay confined in 1000 mm from the source. The optimal injection can be obtained having a beam parallel on the transverse plane (bottom panel of Figure 2.15) and a waist in correspondence of the selection point on the radial plane (upper panel of Figure 2.15). Actually a small divergence on the transverse plane can be allowed, as it would be possible to reduce this effect using the natural field index of the ESS dipoles, anyway more precise calculations are still needed. From the geometrical point of view other constraints have been considered: the minimum

allowed distance from the laser-target interaction point is 50 mm and the minimum allowed distance between each quadrupole is 40 mm, according to the worse case reported in the previous section.

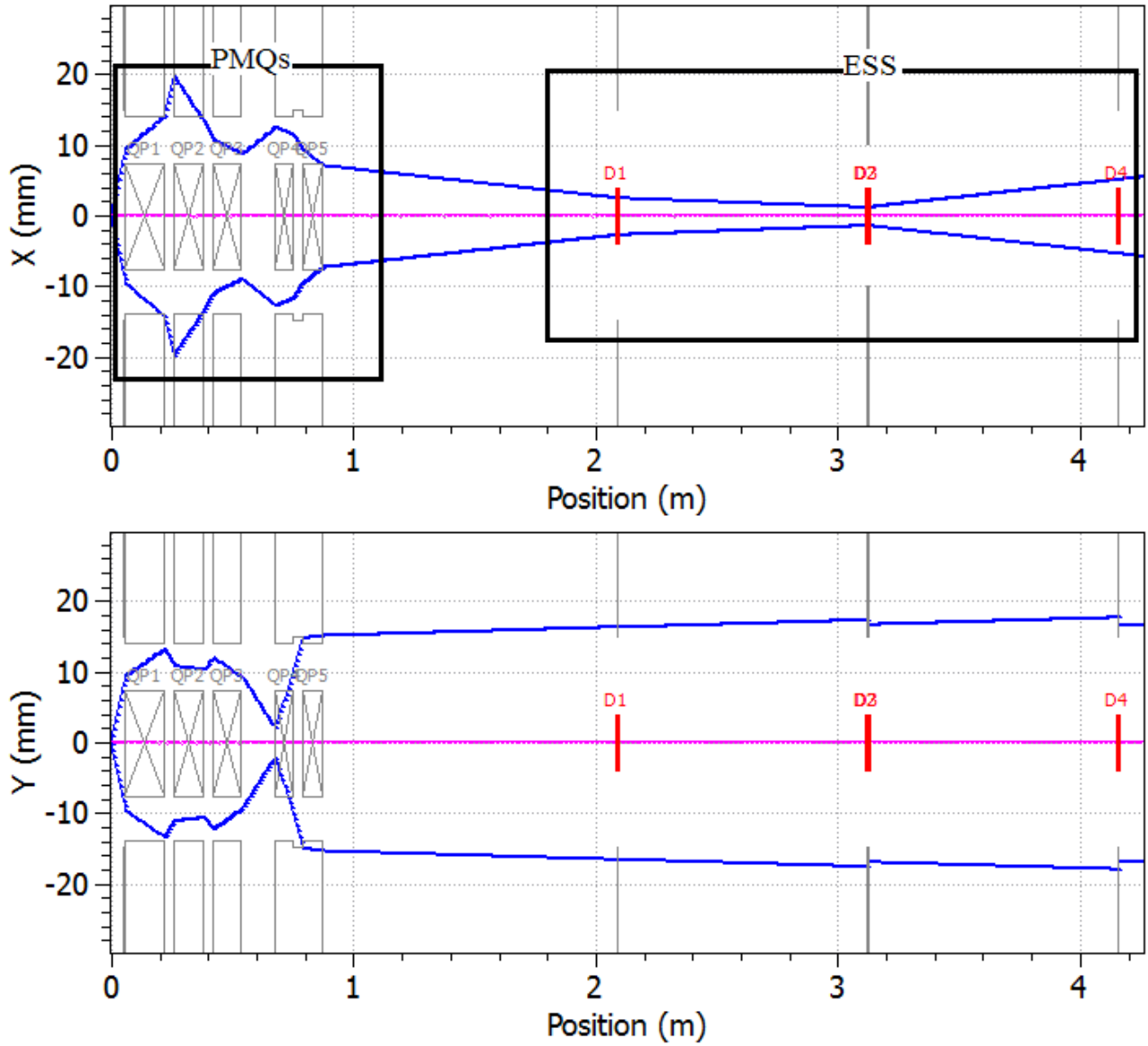

***Figure 2.15**: Scheme of the simulated beamline with envelop of 60 MeV protons*

2.3.1 60 MeV protons

The beam envelope is shown in Figure 2.15. The monochromatic simulations gives a transmission efficiency of 9%, with the losses basically limited in the PMQs system. The output beam is shown in the phase space plot in Figure 2.16.

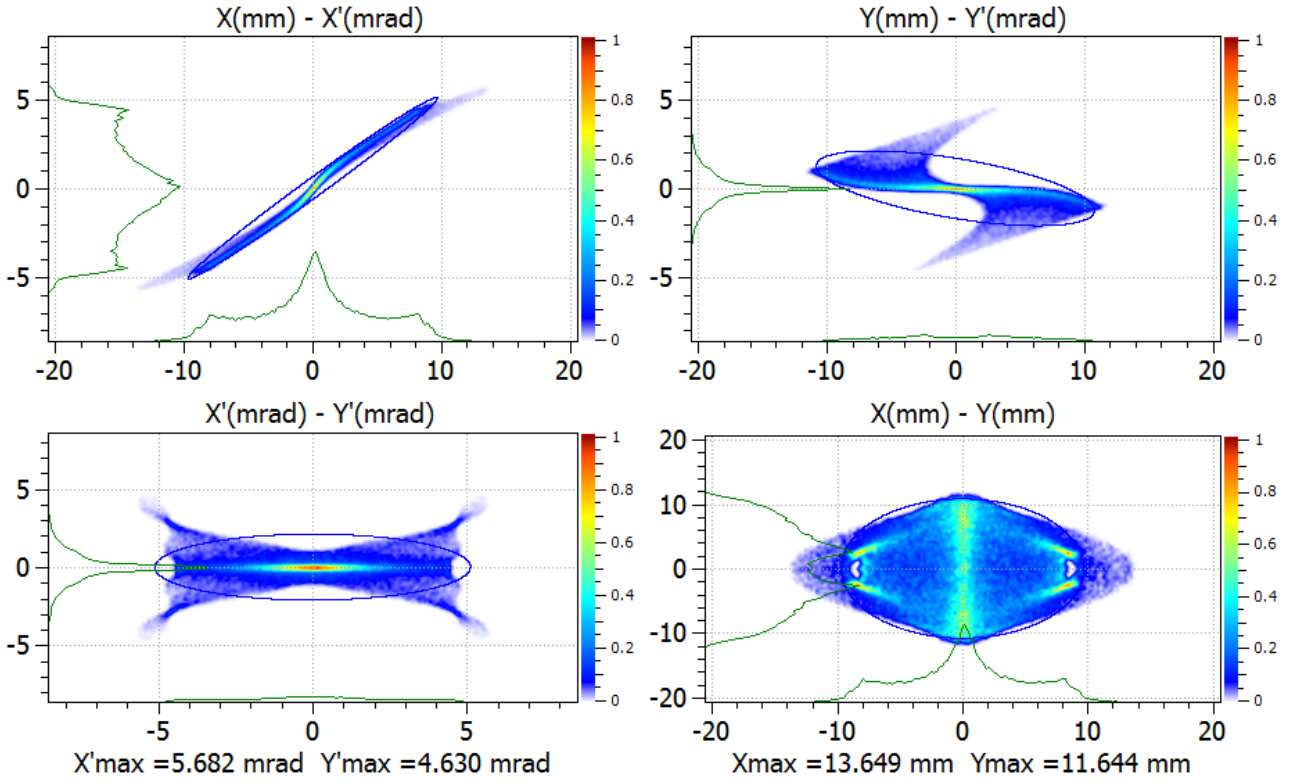

***Figure 2.16**: Phase space plot of the 60 MeV monochromatic proton beams downstream the ESS*

As can be seen the beam divergence is considerably reduced to 0.3°, which makes it possible to transport and shape the beam using the conventional quadrupoles. The filamentations of the beam are due to the natural field uniformity of the PMQ.

For this energy case, simulations with more realistic protons have been considered. The input spectrum is exponential, as provided by the client and the beam divergence is uniform distribution between 0° and the maximum angles associated to each energy, as retrieved from the client's data. Figure 2.17 shows the provided angular distribution (blue dots) and the function used to fit those data and reproduce the angles (red dots). The plot represents the half-angle distribution.

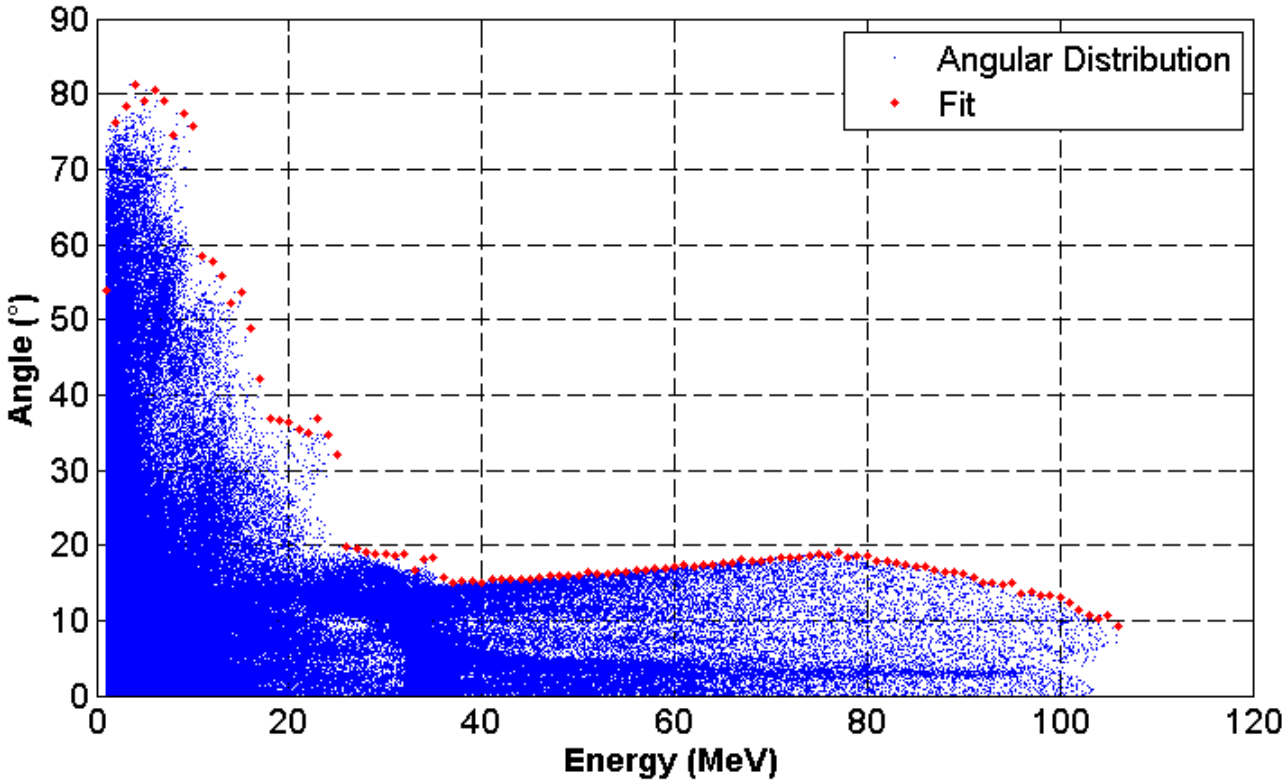

***Figure 2.17**: Provided angular distribution (blue dots) and function used as reference (red dots)*

Figure 2.18 shows the normalized spectrum at different positions along the beamline.

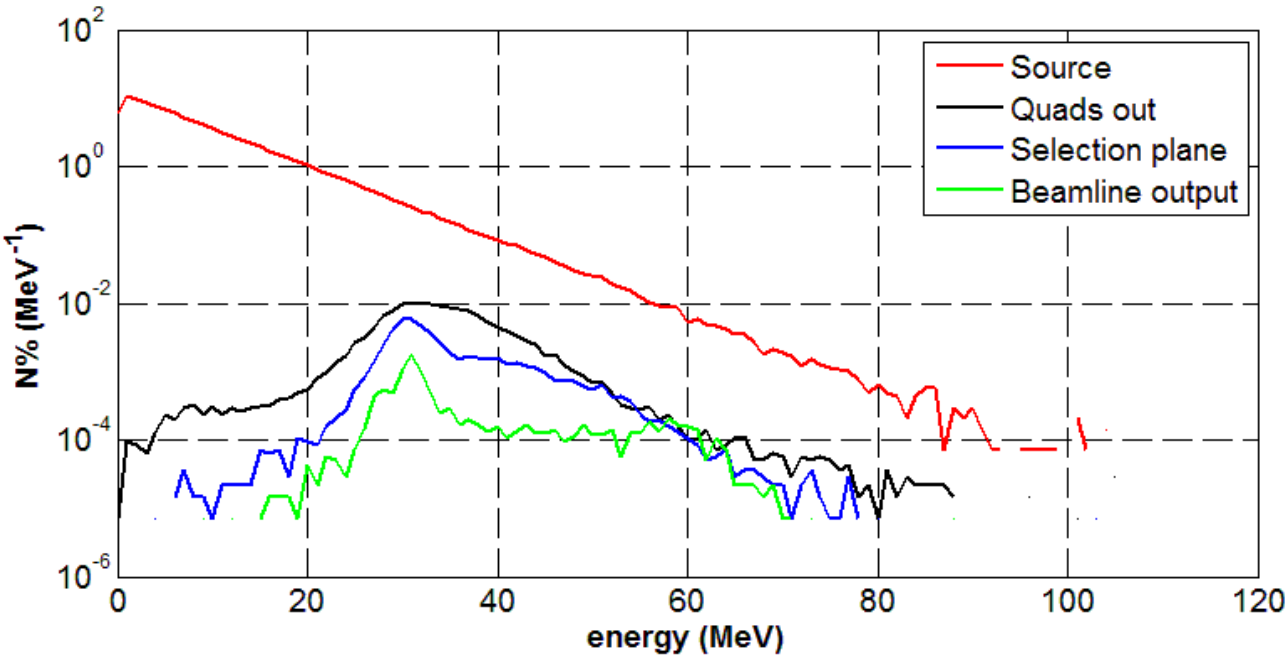

***Figure 2.18**: Particle spectrum at different positions along the beamline*

In Figure 2.18 the red line is the laser-accelerated spectrum, the black line is the spectrum transmitted by the PMQs system, the blue line is the spectrum at the selection plane and the green line is taken at the ESS exit. In this simulations the ESS is still simulated as a collimators system. What is important from this simulations is the fact that for the energy under consideration there is

no losses in the energy range of interest (60 MeV with a spread of 10%) apart from those in the PMQs system and the transmission efficiency in this range is of about 4%. This ensures a minimum number of particles of about 10^7 per pulse in the worse case.

Moreover the spectrum is not cleaned up by the ESS magnetic field, which justify the broad energy spread. Anyway such an output spectrum can be selected and the possibility to realize the ESS magnets with laminated iron, instead of using a solid core, would permit the possibility of fast changes in the magnetic field and to select beams with different central energies with a reasonably high amount of particles, even if the PMQs is not set up for those energies and the transmission efficiency is not at its maximum.

2.3.2 30 MeV protons

The beam envelope is shown in Figure 2.19. Four quadrupoles are necessary to transport and inject protons from 30 to 10 MeV. The monochromatic simulations gives a transmission efficiency of 8%, with the losses basically limited in the PMQs system. The output beam is shown in the phase space plot of Figure 2.20.

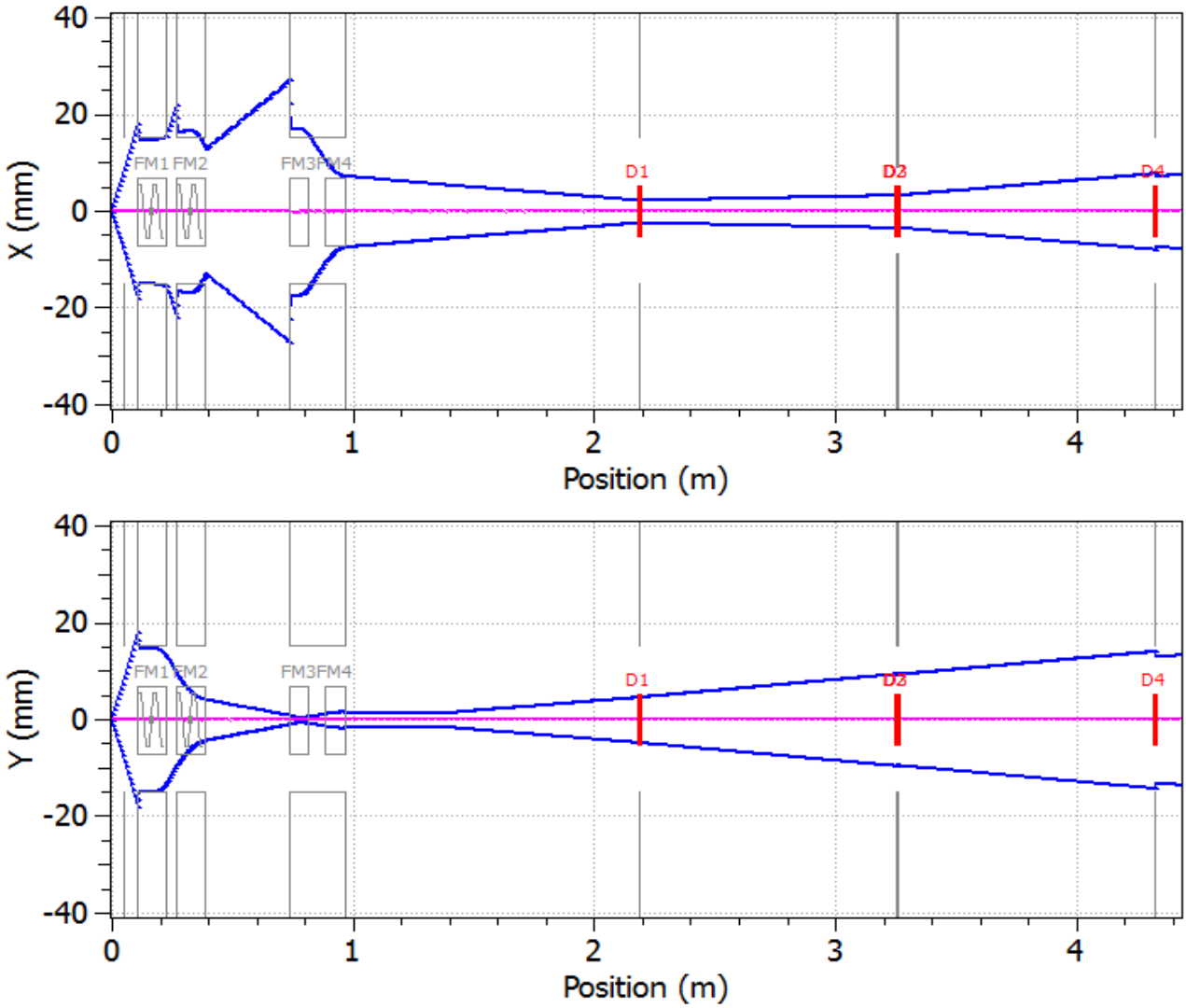

***Figure 2.19**: Scheme of the simulated beamline with envelope of 30 MeV protons*

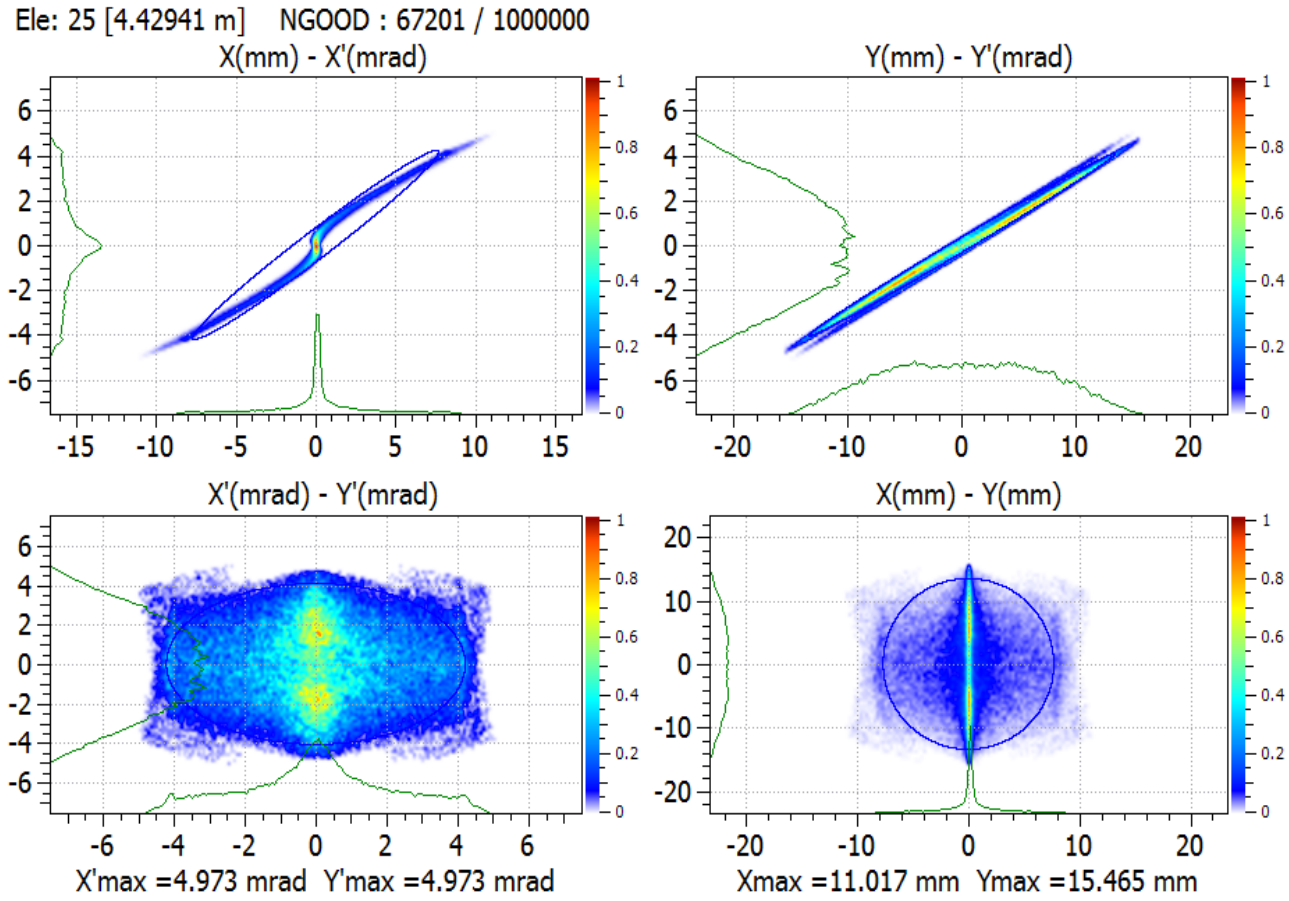

***Figure 2.20**:Phase space plot of the 30 MeV monochromatic proton beams downstream the ESS*

As can be seen the beam divergence is considerably reduced to 0.3°, which makes it possible to transport and shape the beam using the conventional quadrupoles. The filamentations of the beam are due to the natural field uniformity of the PMQ.

Again simulations with more realistic spectrum, as described in the previous section, have been performed and resumed in Figure 2.21.

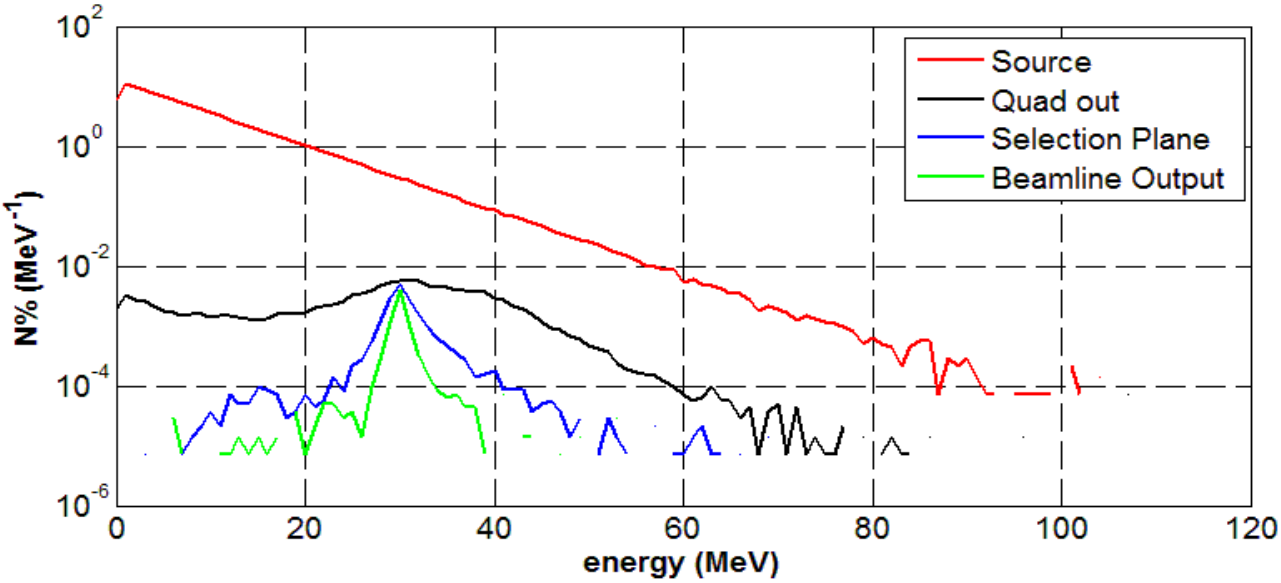

***Figure 2.21**: Particle spectrum at different positions along the beamline*

Again, for the energy under consideration there is no losses in the energy range of interest (30 MeV with a spread of 10%) apart from those in the PMQs system and the transmission efficiency in this range is of about 6%. This ensures a minimum number of particles of about 10^7 per pulse in the worse case.

2.3.3 5 MeV protons

The beam envelope is shown in Figure 2.22. Three quadrupoles are necessary to transport and inject protons with energies lower than 10 MeV. The monochromatic simulations gives a transmission efficiency of 1%, but in this case the half angle divergence is of about 15° (uniform distribution) and the injection is not properly optimized. The output beam is shown in the phase space plot of Figure 2.23.

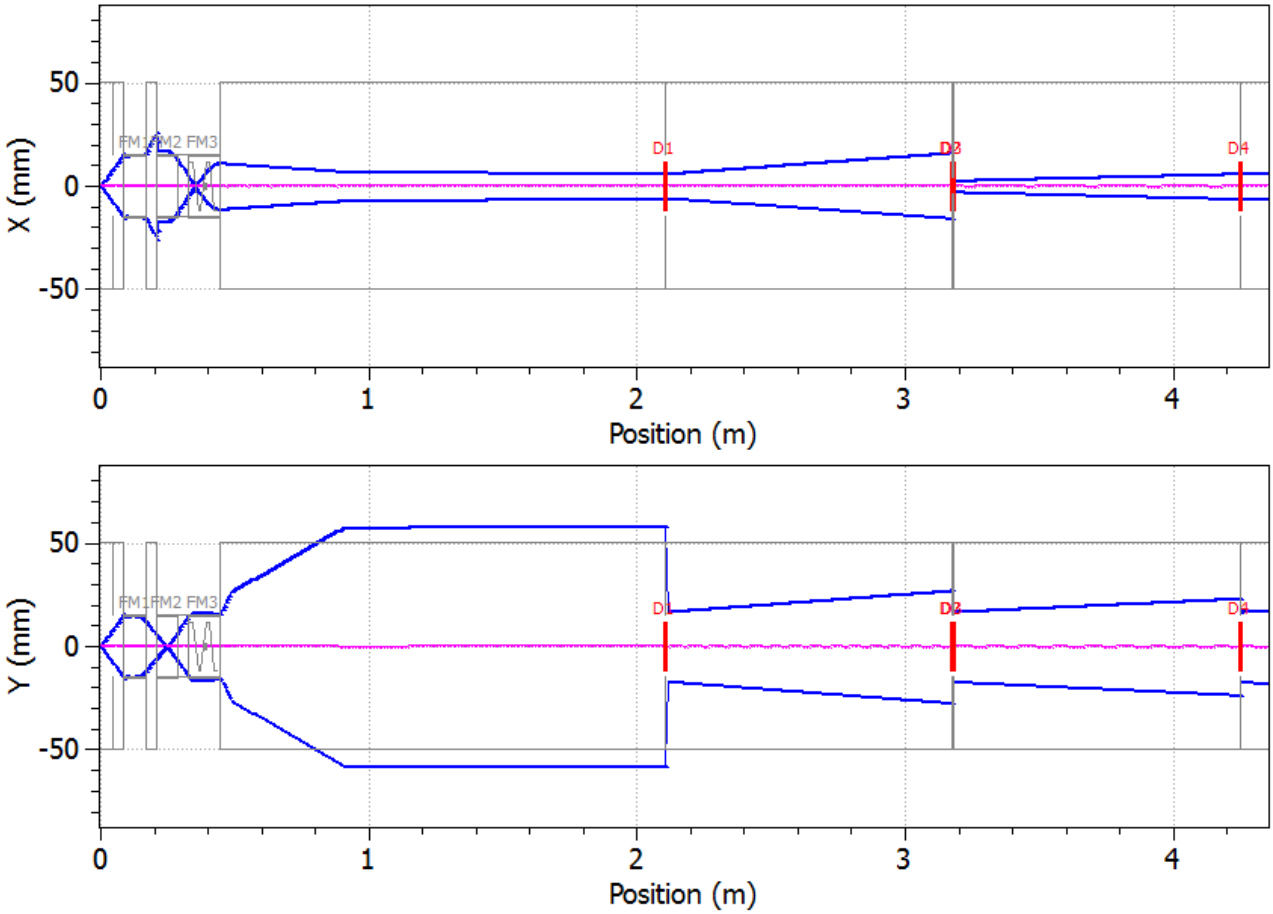

***Figure 2.22**: Scheme of the simulated beamline with envelope of 5 MeV protons*

As can be seen the beam divergence is considerably reduced to 0.23°, which makes it possible to transport and shape the beam using the conventional quadrupoles. The filamentations of the beam are due to the natural field uniformity of the PMQ.

Again simulations with more realistic spectrum, as described in the previous section, have been performed and resumed in Figure 2.24. In this case the transmission efficiency is well below to the 1%. It is due to the big angular diverge of low energy particles, which is considered uniformity distributed between 0° and 50° (and even bigger angles), see Figure 2.17. Anyway considering that at low energy there is a great abundance of particles, the minimum number of ion transmitted per pulse should be guaranteed. These results, especially this last one for the lowest energies can be

easily improved considering the more realistic gaussian angular distribution and optimizing the injection in the ESS as soon as its design will be completed.

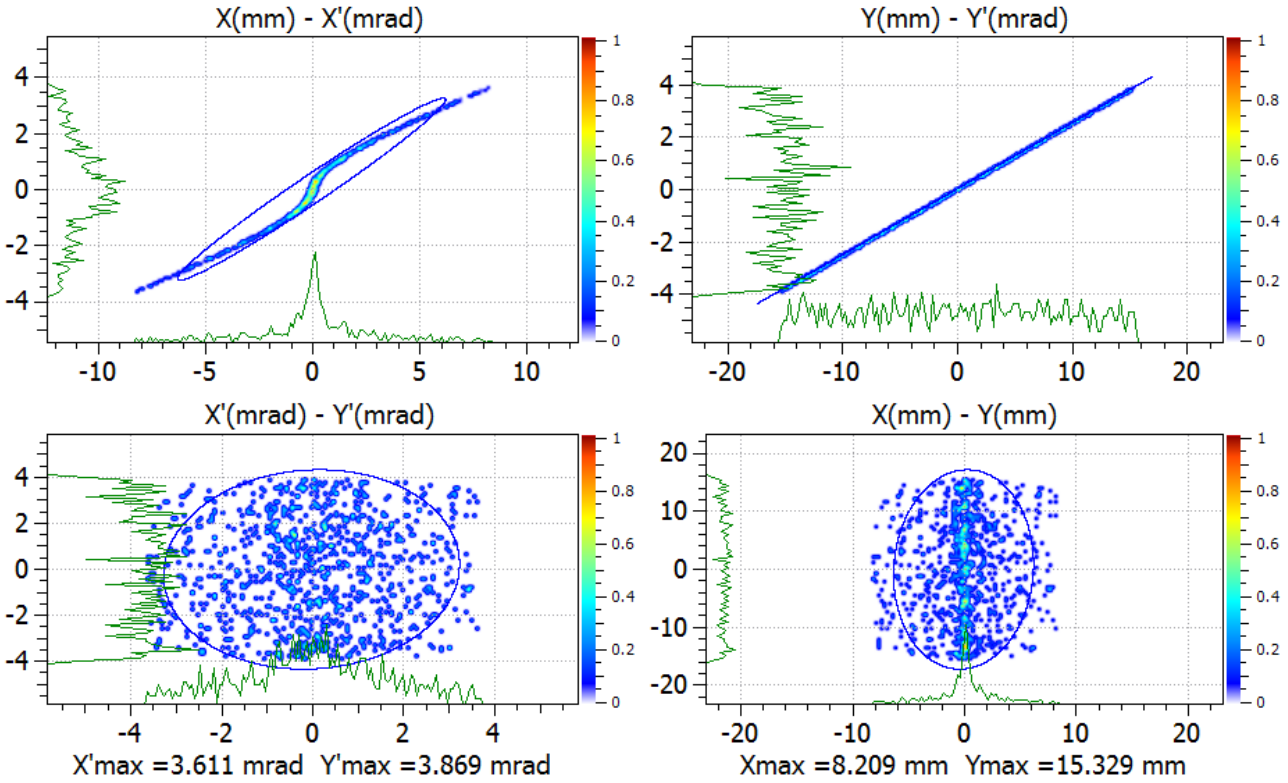

***Figure 2.23**:Phase space plot of the 5 MeV monochromatic proton beams downstream the ESS*

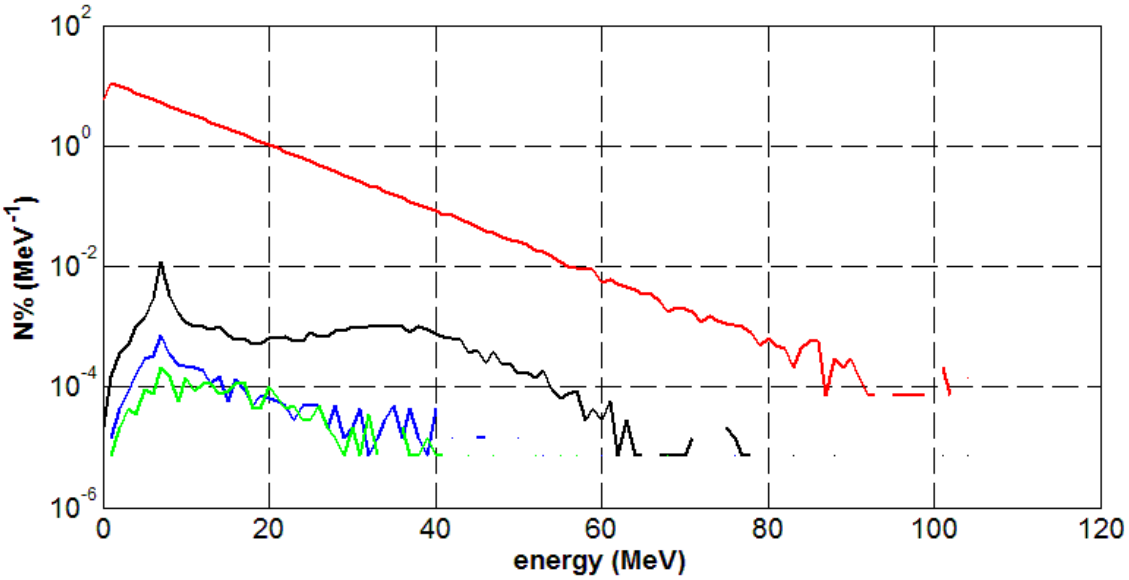

***Figure 2.24**: Particle spectrum at different positions along the beamline*

2.3.4 60 MeV/u carbon ions (C^{+6})

The system performances have been studied for other ion species and results for monochromatic C^{+6} at the maximum energy of 60MeV/u, of interest for medical applications, are here reported.

The beam envelope is shown in Figure 2.25. Four quadrupoles are required to inject the beam in the ESS. The transmission efficiency of the whole beamline is of about 4%, which is enough to guarantee the minimum number of particles transmitted. The angular spread is limited to 0.25°.

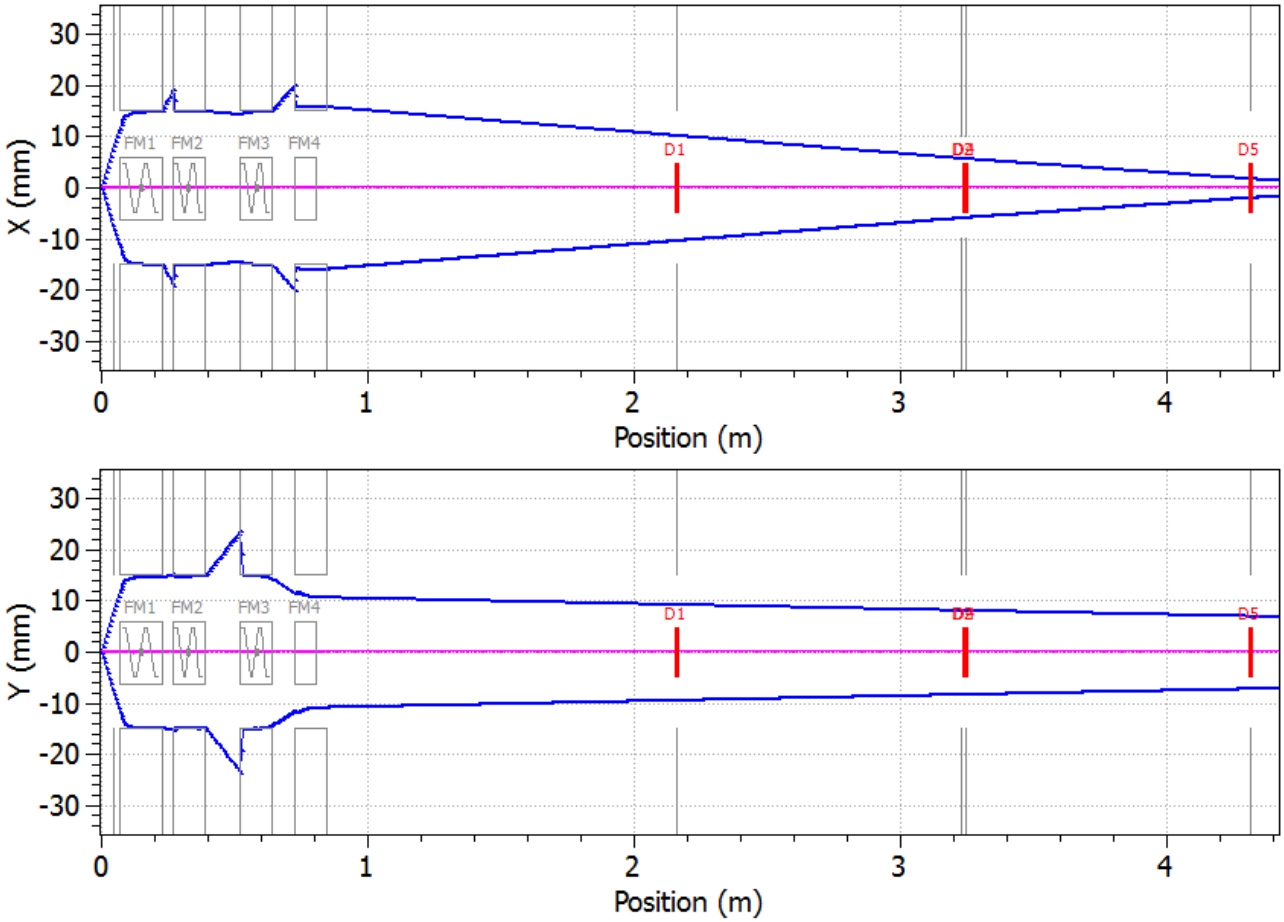

***Figure 2.25**: Scheme of the simulated beamline with envelope of 60 MeV/u C^{+6}*

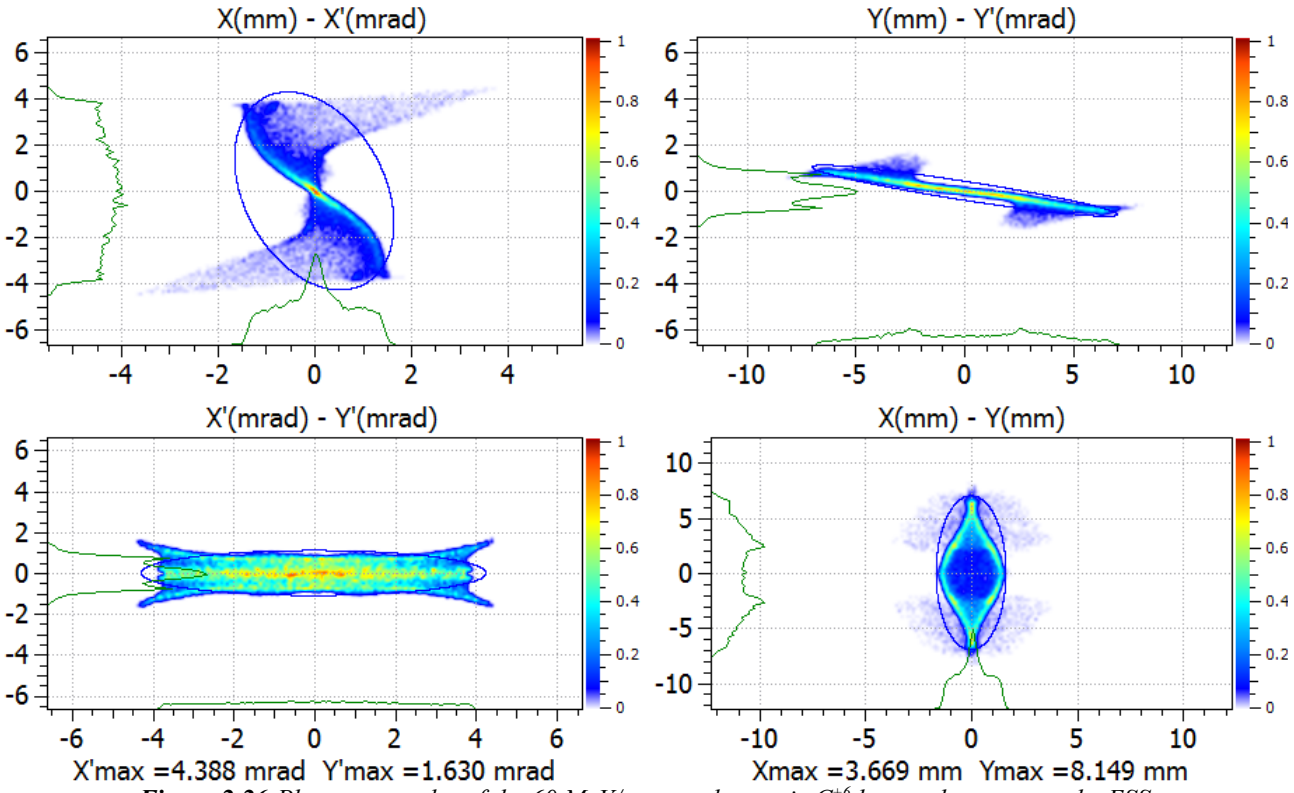

***Figure 2.26**:Phase space plot of the 60 MeV/u monochromatic C^{+6} beams downstream the ESS*

2.4 Final design, manufacturing and test of the collection system

The final design of the collection system, optimized in collaboration with the manufacturer (SigmaPhi), shows a more cost-effective and compact solution with only two arrays of permanent magnets. In fact, the final layout has an inner array of 148mm diameter made entirely of NdFeB N38UH and an outer array of 267mm in diameter made entirely of NdFeB N48H. Figure 2.27 shows the final layout.

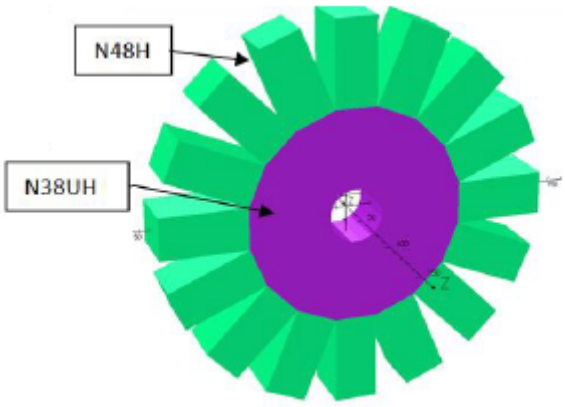

***Figure 2.27**:Final layout of the shortest PMQ*

The quadrupoles result a bit smaller in transvese dimension but field quality and gradient values

are respected as shown in Figures 2.28 and 2.29.

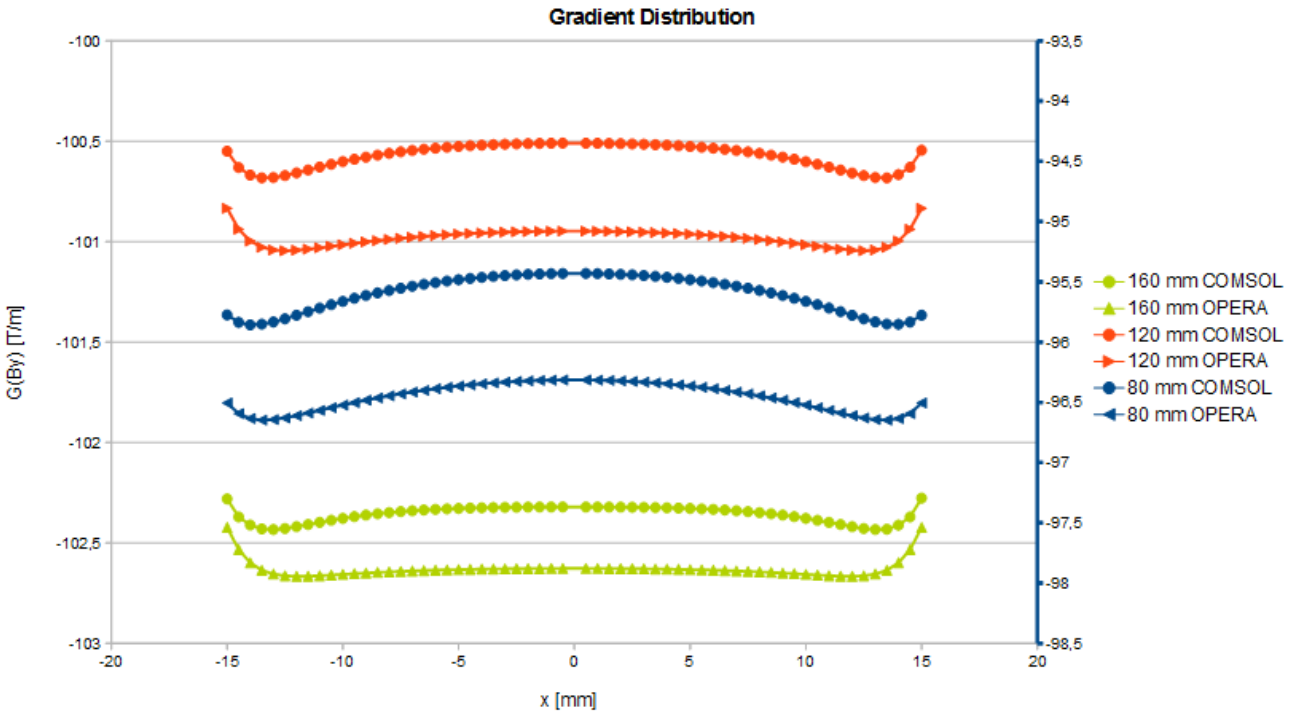

***Figure 2.28**: Gradient distribution calculated with OPERA 3D and COMSOL for the 3 types of quadrupoles.Scale on the right side is referred to the 80mm quads gradient.*

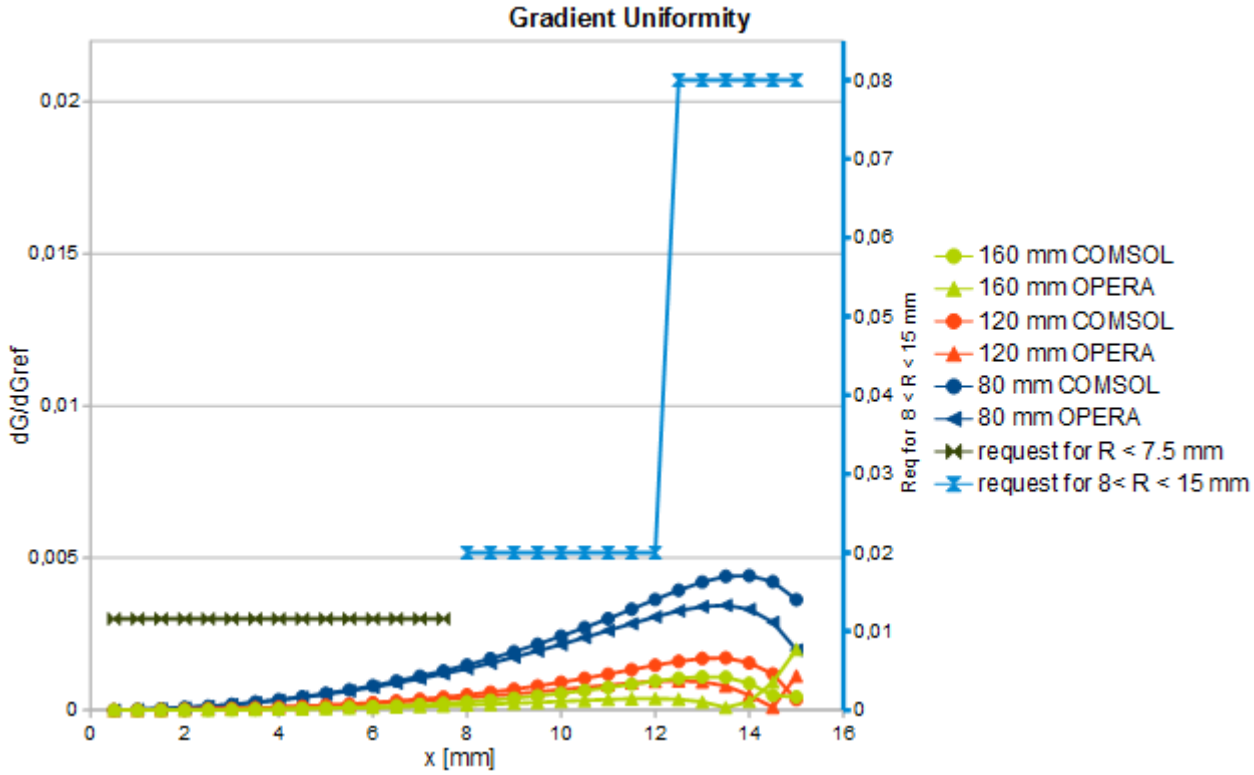

***Figure 2.29**: Gradient uniformity calculated with OPERA 3D and COMSOL for the 3 types of quadrupoles and comparison with requested values. Scale on the right side is referred to the request for R > 7:5mm.*

The final design has been validated against requests on field gradient and gradient uniformity, calculation being performed by two different teams using two different codes (Sigmaphi/OPERA 3D and INFN-LNS/COMSOL). The plots, especially the one in Figure 2.29, show that the field quality of the new simplified design complies with the request coming from the preliminary feasibility study. Difference between the two code results are due to mesh nodes number (higher in OPERA) and, to a scaling factor of about 0,5% for the maximum gradient value. The harmonic content evaluated with the two codes is also very similar with a total contribution of about 8 units with respect to the main b2 harmonic. Thes results have been confirmed by detailed magnetic measurement performed at SigmaPhi using the rotating coil method. In this way a precise characterization of the magnetic field has been done which was used also to simplify the alignment of the magnets, as it is explained in the following.

The quadrupoles are placed on a 6 axis motorized mechanic system, which allow to adjust the relative distance between the magnets with a precision of 0,1mm in the longitudinal direction. This system is necessary to tune the optics for different ion energies and it is design to withstand the extremely high attraction/repulsion force between the magnets. The full system is shown in Figure 2.30.

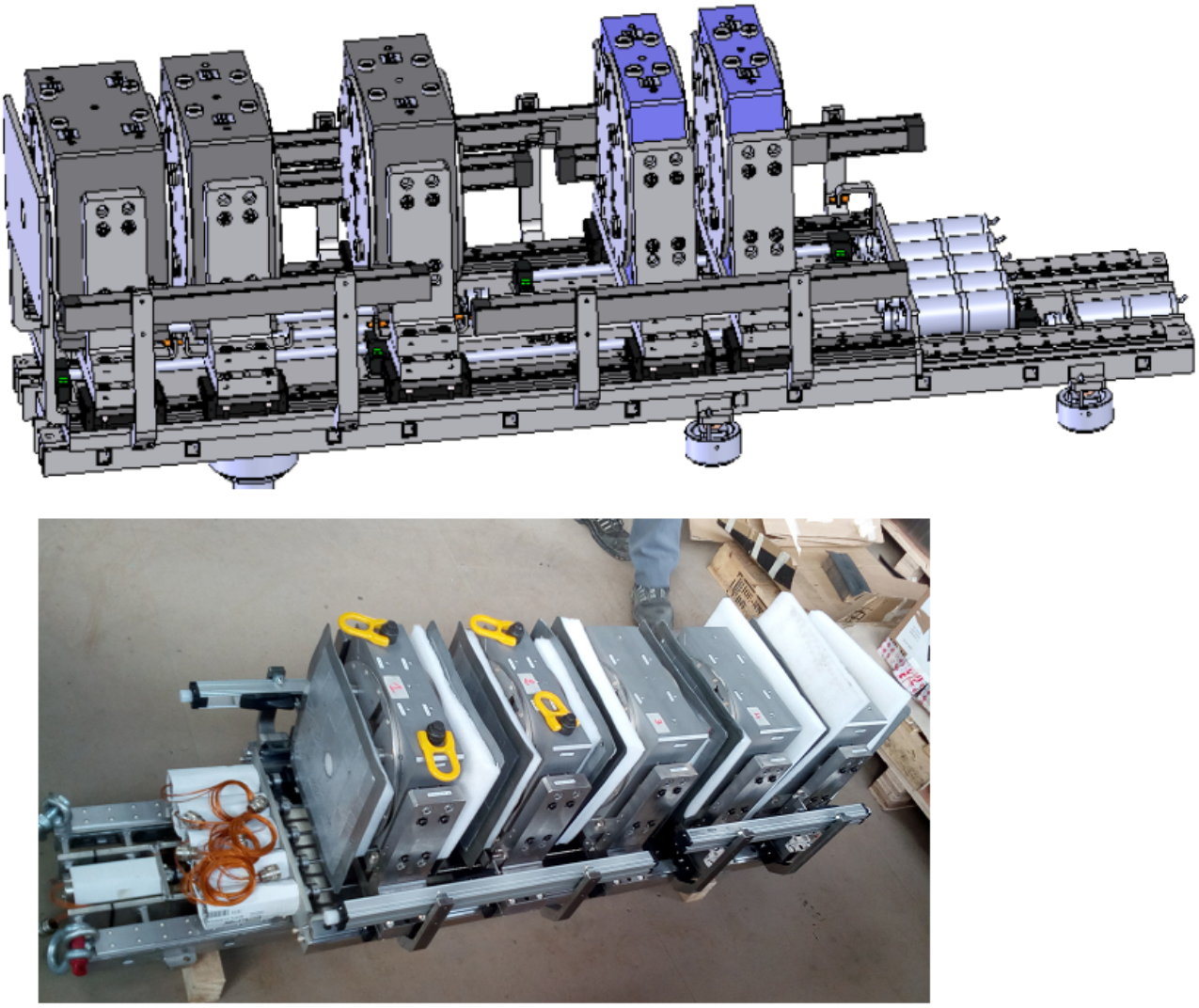

***Figure 2.30**: Full system complete with mechanics.*

Moreover, it allows to have all magnetic axis always alligned thanks to the use of calibrated

gauges which have been installed on the magnets yokes and on the yoke holders connected with the displacement system. The calibrated gauges have been realized according an accurate mapping with laser tracking of the yoke holders and according the rotating coil measurement of the magnetic field centre. In this way the quadrupoles are always aligned when set in place and only the main rail need to be aligned with respect to the beam axis.

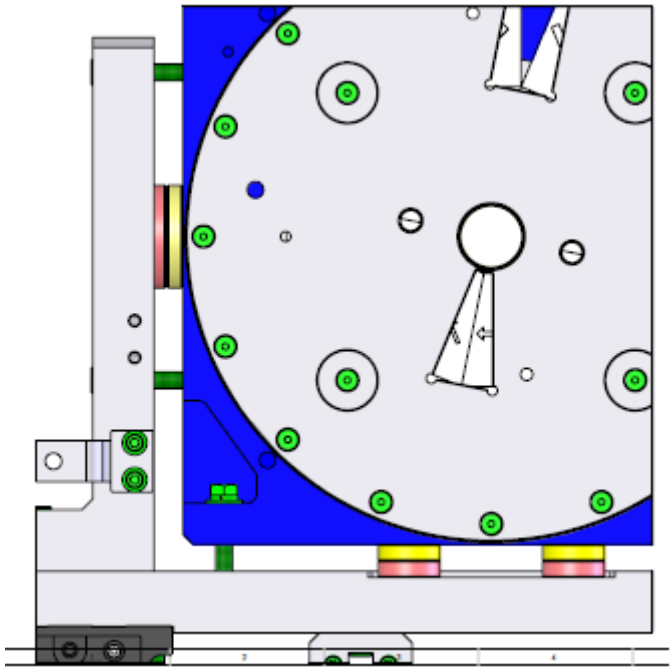

***Figure 2.31**: Detail of the magnet yoke (blue), yoke holed (grey), and calibrated gauges. The yellow gauges are installed on the yoke, the red ones are installed on the yoke holder.*

The PMQs system have been characterized at INFN-LNS using the 62 MeV proton beam accelerated by the superconductive cyclotron with the goal of demonstrate the performances of the system and its controllability. The beam optics along the quadrupoles has been analyzed using Gafchromic films EBT3 [14] and following the method proposed in [15]. Figure 2.32 shows the system installed at the 40° beamline at INFN-LNS.

***Figure 2.32**:PMQs with mechanics installed at INFN-LNS*

2.4.1 Test of the PMQs at LNS

The configuration is sketched in Figure 2.33. In order to control the emittance of the input beam a set of two 1mm diameter collimators has been installed before the PMQs. In this way the beam features (emittance and twiss parameters) are always reproducible and can be used as a reference value for the characterization of the system.

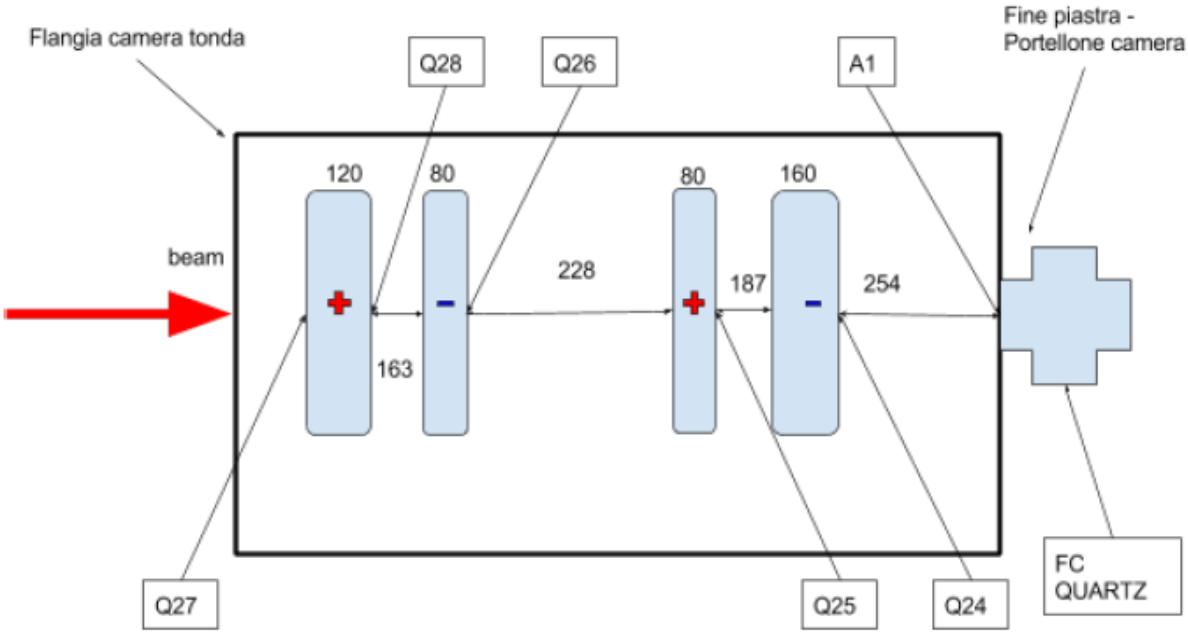

Figure 2.33: *Sketch of the setup used for the first measurement. Gafchromic names are indicated with the letter "Q".*

The beam emittance and twiss parameters at the system input have been evaluated in the point where the red arrow in Figure 2.33 points (namely at the chamber entrance) and they are reported in the next table.

Plane	ε [pi.mm.mrad]	β [mm/pi.mrad]	α
X	0,136	1,21	0
Y	0,036	1,02	0

The multiparticle envelope, using this beam features and realistic field maps for the quadrupoles is shown in the Figure 2.34. Comparison between the simulated and experimental beam spot shape shows a good agreement. The comparison is reported in Figure 2.35. It should be noted that in the GafChromic film the PMQs bore is marked (black lines)

The aim of the test is to demonstrate quanlitatively that the PMQs are reliable and their beam optics can be controlled. In fact, the technique used at LNS for alignement is based on the use of an optical theodolite which cannot guarantee a precision better than 1 mm, which is ten times higher than the tolerances of these permanent magnets. Considering this issue and also some usual fluctuation in the beam, the results show good agreement between simulations and experimental data. There is a small rotation on the beam spot after the second quadrupole and a consistent missalignement in the last measurment point. Both effects (skew quadrupole and steering) depend on the alignment precision of the PMQs system. Moreover the gafchormic films are placed manually, which is also another source of missalignment of the detector.

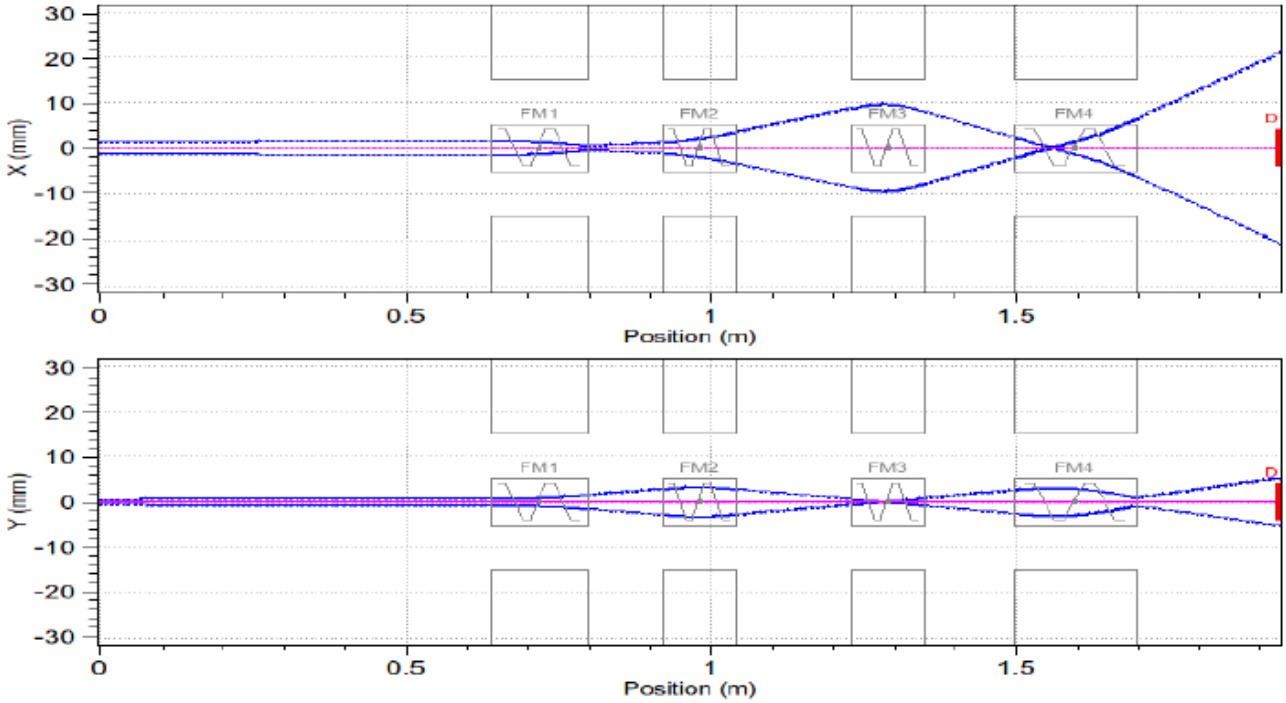

Figure 2.34: *The multiparticle envelope from optics simulation.*

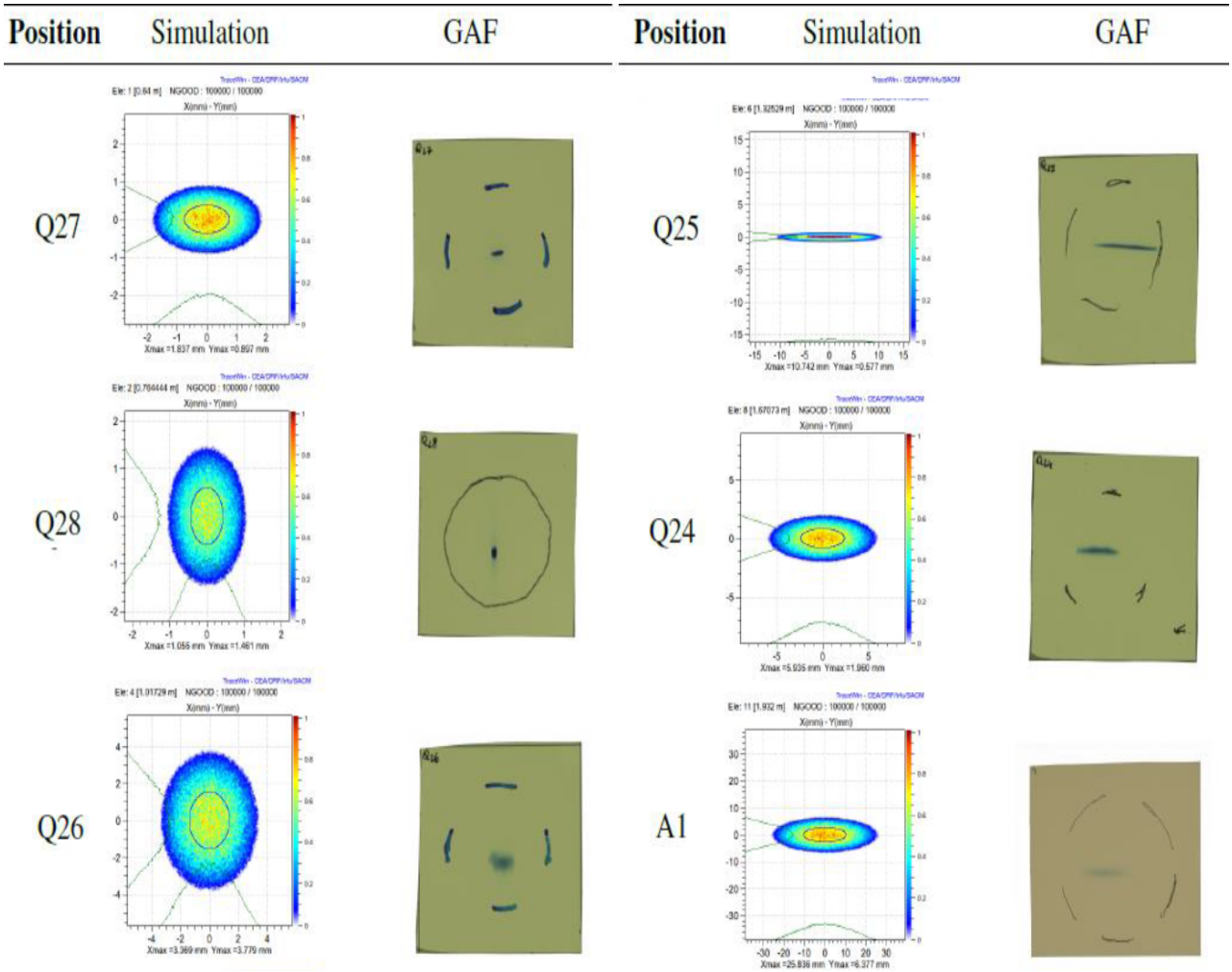

Figure 2.35: *Comparison between simulation and experimental beam spot size*

Appendix A

Field gradient uniformity

	Field Gradinet		Integrated Gradient		
R	**G(By)**	**dG/Gref**	**∫Bydz [T.mm]**	**GL(By)**	**dGL/GLref**
0,7895	-111,073049333149	0	-14.45102815139	-18,30463565843	0
1,5789	-111,072597558769	4,12594835625488e-6	-28.90092523792	-18,3039193173510	3,919975300138e-5
2,3684	-111,070685617708	2,15872530070259e-5	-43.3531092788082	-18,3046461399412	-5,73571009533e-7
3,1579	-111,068156579191	4,46843624874116e-5	-57.8050619592603	-18,3049362870991	-1,64510589613e-5
3,9474	-111,059587718038	0,00012294174089229	-72.2550483369704	-18,3046122453658	1,281214391791e-6
4,7368	-111,041563072770	0,00028755655492626	-86.7019213466627	-18,3037389509621	4,906979683199e-5
5,5263	-110,990961335214	0,00074969023323023	-101.145588860234	-18,3025351270901	0,000114945675695
6,3158	-110,945333355982	0,00116639975536430	-115.584092639051	-18,3008146678498	0,000209092973436
7,1053	-110,818322537142	0,00232635946682342	-130.014894383251	-18,2983925428280	0,000341636959511
7,8947	-110,824137535071	0,00227325246868870	-144.428520841198	-18,2942793065518	0,000566722257256
8,6842	-110,612922494234	0,00420222938627205	-158.827073105849	-18,2891781152190	0,000845870619499
9,4737	-110,444927735858	0,00573648570579515	-173.202815088617	-18,2825193704651	0,001210251716260
10,2632	-110,122807374957	0,00867833463094510	-187.552029100819	-18,2743002713619	0,001660018820471
11,0526	-109,844619209866	0,0112189612221087	-201.866066587971	-18,2640726912926	0,0022196944020688
11,8421	-109,415519462903	0,0151378275298886	-216.1368211234772	-18,2515537837603	0,00290475644085943
12,6313	-109,095674392172	0,0180588967690776	-230.34635370674098	-18,2357530017837	0,00376940983712733
13,4211	-108,838437359401	0,0204081816334340	-244.51883541640274	-18,2190504820065	0,00468340830080617
14,2105	-107,704343875191	0,0307655886852879	-258.5736144934712	-18,1959210199109	0,00594910312428590
15	-94,3782285520947	0,152469842120280	-272.6019926070946	-18,1734661738063	0,00717788148321454
Gref	**-109.4959**		**GLref**	**-18.2741**	

Harmonic Content

n	**|Cn| T/m**	**Cn (10^4 units)**	**Bn (10^4 units)**
1	8,425e-4	0,152	-0,146
2	55,554	10000	10000
3	2,776e-4	0,05	-0,033
4	3,221e-4	0,058	-0,054
5	1,417e-4	0,025	-0,025
6	0,193	34,769	-34,769
7	2,818e-4	0,039	0,022
8	6,94e-4	0,125	-0,072
9	3,417e-4	0,062	9,661e-4
10	0,022	3,954	3,954
11	4,218e-4	0,076	-0,062
12	2,026e-4	0,036	-0,023
13	2,997e-4	0,054	-0,044
14	3,381e-4	0,061	-0,057
15	1,545e-4	0,028	0,027
16	1,424e-4	0,026	-0,021
17	2,003-e4	0,036	0,036
18	0,005	0,837	-0,836
sum		39,525	30,9

2.5 Bibliography

[1] P. Castro, *Beam trajectory calculations in bunch compressors of TTF2*, *DESY TECHNICAL NOTE* 2003-01

[2] S. Becker, M. Bussmann, S. Raith, M. Fuchs, R. Weingartner, P. Kunz, W. Lauth, U. Schramm, M. El Ghazaly, F. Grüner, H. Backe, and D. Habs, *Characterization and tuning of ultrahigh gradient permanent magnet quadrupoles*,*Phys. Rev. ST Accel. Beams* 12 102801 (2009)

[3] H. Sakaki, M. Nishiuchi, T. Hori, P. R. Bolton, M. Tampo, A. Yogo, K. Kondo, S. Kawanishi, H. Iwase, K. Niita, *Simulation of Laser-Accelerated Proton Focusing and Diagnosis with a Permanent Magnet Quadrupole Triplet*,*Plasma Fusion Res.* 5 009 (2010)

[4] M. Schollmeier, S. Becker, M. Geißel, K. A. Flippo, A Blaževi´c, S. A. and Gaillard, D. C.Gautier, F. Grüner, K. Harres, M. Kimmel, F. Nürnberg, P. Rambo, U. Schramm, J.Schreiber, J. Schütrumpf, J. Schwarz, N. A. Tahir, B. Atherton, D. Habs, B. M. Hegelich, M. Roth, M., *Controlled Transport and Focusing of Laser-Accelerated Protons with Miniature Magnetic Devices*,*Phys. Rev. Lett.* 101 5, 055004, (2008)

[5] K. Halbach, *Physical and optical properties of rare earth cobalt magnets*,*Nucl. Instrum. Methods* 187 109 (1981)

[6] T. Mihara, Y. Iwashita, M. Kumada, C. M. Spencer, E. Sugiyama, *Superstrong Adjustable Permanent Magnet for a Linear Collider Final Focus*, *Proc. of the 12th Linear Accelerator Conference* SLAC Report No.SLAC-PUB-10878

[7] F. Schillaci, M. Maggiore, D. Rifuggiato, G. A. P. Cirrone, G. Cuttone, D. Giove, *Errors and optics study of a permanent magnet quadrupole system,* JINST accepted.

[8] A. Bungau, R. Cywinski, R. Barlow, C. Bungau, P. King, J. Lord, *GEANT4 modelling of heat deposition into the isis muon target*, Proceedings of 2011 Particle Accelerator Conference (TUP004), New York, NY, USA

[9] N. Simos, P.K. Job, N. Mokhov, *An experimental sudty of radiation-induced demagnetization of insertion device permament magnets*, Proceedings of EPAC08 (WEPC05) Genoa, Italy

[10] X.-M. Maréchal, T. Bizen, Y. Asano, H. Kitamura, *65 MeV neutron irradiation of NeFeB permanent magnets*, Proceedings of EPAC 2006 (THPCH13), Edinburgh, Scotland

[11] P. Knaus, *Transient thermal analysis of intense proton beam loss on a kicker magnet conductor plate*, CERN-LS-2000-034 BT

[12] http://g-iron.it/

[13] http://www.lessemf.com/mag-shld.html

[14] http://www.gafchromic.com/documents/EBT3Specifications:pdf

[15] F. Schillaci et al., Characterization of the ELIMED Permanent Magnets Quadrupole system prototype with laser-driven proton beams, March 2016, JINST doi:10.1088/1748-0221/11/07/T07005

3 Feasibility Study of an Energy Selection System for laser driven-ion beams in the energy range of 3-60 MeV/u

If your beam is bad, why do you need a good magnet?
W. Beeckman

Because a bad magnet won't help for sure!

In this chapter it is described the design of the ELIMED energy selection system, showing the main ideas behind the technical choices adopted for its realization. At the end of the chapter, the realized system is described and the results of its calibration using standard proton beam performed at INFN-LNS are also shown.

3.1 Introduction

In many laser laboratories it is common to find miniature magnets with huge gaps and very short mechanical length, used as spectrometers (both for ions and electrons). The analysed beam may have strange shape due to the crazy harmonic content of the magnetic field that such magnets have. Hence, interpretation of results and accuracy could be complex (leading at even more crazy results). An example is shown in Figure 3.0, where a C-shaped NdFeB *electron spectrometer* with 50mm of gap and 20mm of length is shown together with two typical spectrograms. The comet shape of the analysed beam is due to the extremely high quadrupole and hexapole components of the magnetic field (comparable with the dipole main harmonics). Moreover the magnet results to be extremely sensitive to the shot-to-shot beam fluctuations.

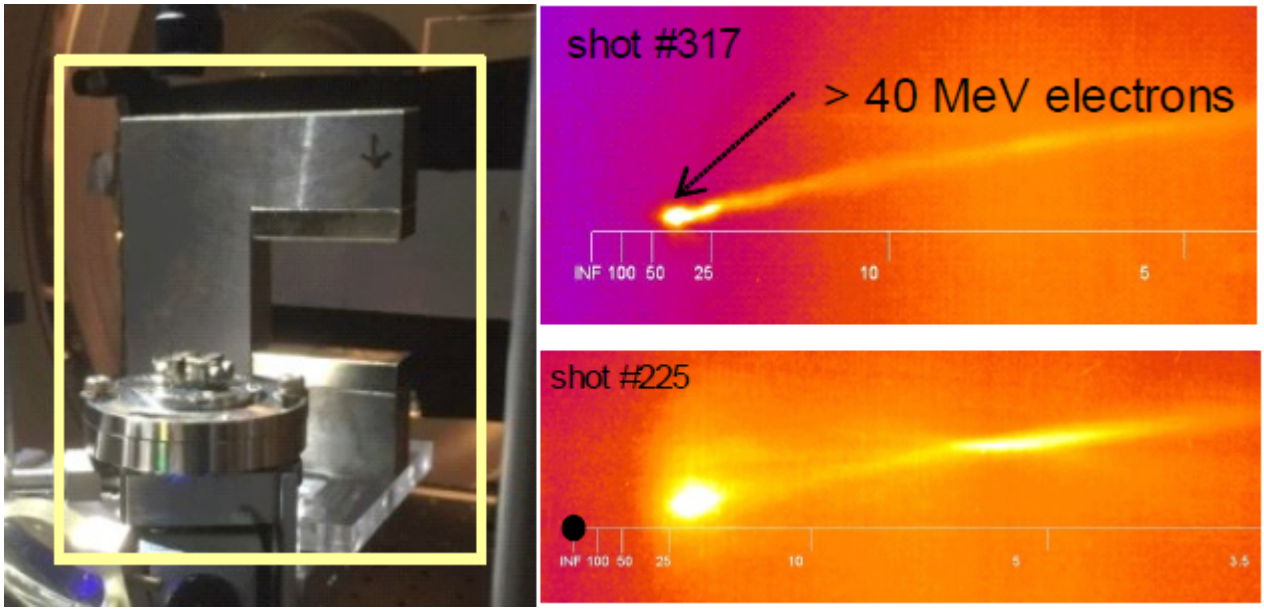

***Figure 3.0**: Example of a typical magnet used in laser laboratories (LHS) and its effect on the beam (RHS).*

The ELIMAIA-ELIMED beam lines aims to deliver a reproducible, controlled and well characterized ion beam for users interested in laser-accelerated beams applications with particular care in demonstrating the clinical effectiveness of these non conventionally accelerated beams. These are the reasons why the whole beamline and, in particular the energy selector, have been designed with an approach that follows the one used in the design of beamline for standard accelerators. Due to the low quality of laser-driven beam, some general constraint can be anyway relaxed, for example, the beam dynamics is analysed only for the first order, in fact second or higher order analysis would not give any additional improvement but may generate complexity and cost in the final manufacturing.

3.2 The Energy Selection System

A sketch of the ESS is shown in Figure 3.1. Its layout is based on four resistive dipoles with alternating field, similar to a bunch compressor scheme, and its main trajectory parameters are also reported in the figure, according to the treatment proposed in [1].

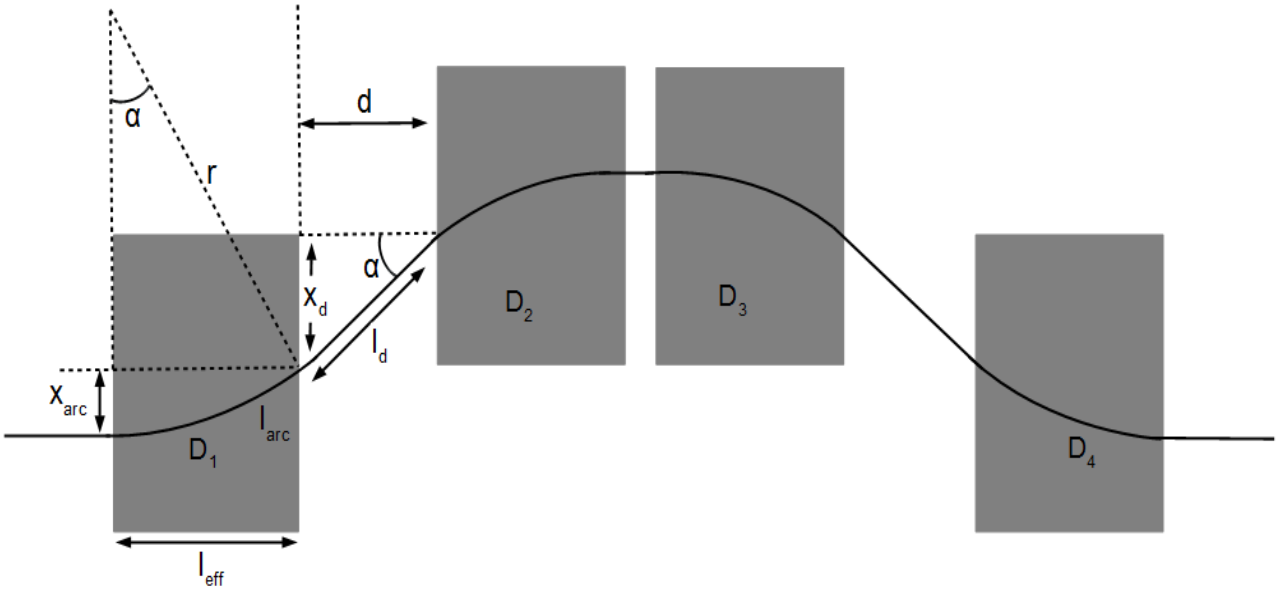

***Figure 3.1**: Energy Selection System layout and main trajectory parameters.*

Using the main trajectory parameters shown in Figure 3.1, it is possible to analytically define the characteristics of the ESS, in terms of radial and longitudinal dimensions of each dipole, field strength and selection slit size, necessary to have the wanted energy resolution. The main trajectory parameters necessary for the evaluation of the reference trajectory in the chicane are:

1. Bending radius r: $r = \frac{p}{Be}$ being p the particle momentum, B the magnetic field of a dipole and e the elementary charge. $Br = \frac{p}{e}$ is the magnetic rigidity.
2. Bending angle α: $\alpha = \arcsin\left(\frac{l_{eff}}{r}\right)$ being l_{eff} the magnet effective length, see scheme in Figure 3.1. The bending angle is in radians.

The path length in a dipole is given by:

$$l_{arc} = l_{eff}\frac{\alpha}{\sin(\alpha)} = r*\alpha \quad (3.1)$$

Between the dipoles D1 and D2, drift space, the particle path has an angle α with respect to the longitudinal axis. The length of the path in the drift is:

$$l_d = \frac{d}{\cos\alpha} \quad (3.2)$$

If all the dipoles are the same in terms of field strength and effective length and are separated by equal drift spaces, the path length in the selector is four times the path length in a dipole plus three times the path length in the drifts *d*:

$$L_{path} = 4*l_{arc} + 3*l_d \quad (3.3)$$

The transverse displacement of the orbit in the middle of the selector can be evaluated, as follows. The horizontal displacement of the trajectory inside a dipole is given by:

$$x_{arc} = r(1-\cos\alpha) = l_{eff}\frac{1-\cos\alpha}{\sin\alpha} \quad (3.4)$$

The horizontal displacement in the drift between two dipoles is:

$$x_d = d*\tan\alpha \quad (5)$$

Thus, the horizontal displacement with respect to the original beam axis introduced in the middle of the chicane, namely in the selection point:

$$\Delta x = 2*x_{arc} + x_d = 2*l_{eff}\frac{1-\cos\alpha}{\sin\alpha} + d*\tan\alpha \quad (3.6)$$

Equation (6) can be used to write the expression for the particle energy as a function of the horizontal displacement:

$$T = \sqrt{\left(\frac{qc(\Delta x - d\tan\alpha)}{2\frac{(1-\cos\alpha)}{B}}\right)^2 + M0^2c^4} - E0 \quad (3.7)$$

which represents the calibration equation of the ESS, being *Δx* the radial displacement of the beam at the centre of the device and *q*, *M0* and *E0* the characteristics of the ion to be selected. The derivative of the previous equation times the slit aperture size *s*, namely $(dT/dx)*s$, gives the energy resolution of the device:

$$E_{res} = \left(\frac{dT}{dx}\right)*s = \frac{\left(\frac{qc}{\frac{1-\cos\alpha_1}{B_1}+\frac{1-\cos\alpha_2}{B_2}}\right)*\sqrt{(E_0+T)^2 - M0^2c^4}}{E_0+T}*s \quad (3.8)$$

Different layout have been investigated and the better solution, in terms of compactness and performances, is summarized in Figure 3.2.

For this system each magnet would be 400 mm long (effective length 450 mm) and the drift between each magnet would be 500 mm long, for a total geometrical length of 3,100 m while the path length is 3,168 m. The reference trajectory has maximum radial deflection of 160 mm at the device centre. The upper panel of Figure 3.2 shows the trajectory within the four dipoles (coloured lines). The selected path would guarantee a fixed energy resolution of about 5% if a 4 mm aperture slit is used. This resolution would be independent form the particle energy and ion species, as shown in Figure 3.2 left hand side of the bottom panel. What have to be changed, in order to put particle with different energy on the reference trajectory is the magnetic field, as shown in Figure 3.2 right hand side of the bottom panel, which have to vary between 0.1 up to 0.45 T for protons with energy ranging between 3 and 60 MeV, while it has to reach the value of 1 T for carbons (C^{+6}) with energy of 60 MeV/u (and protons up to 270 MeV).

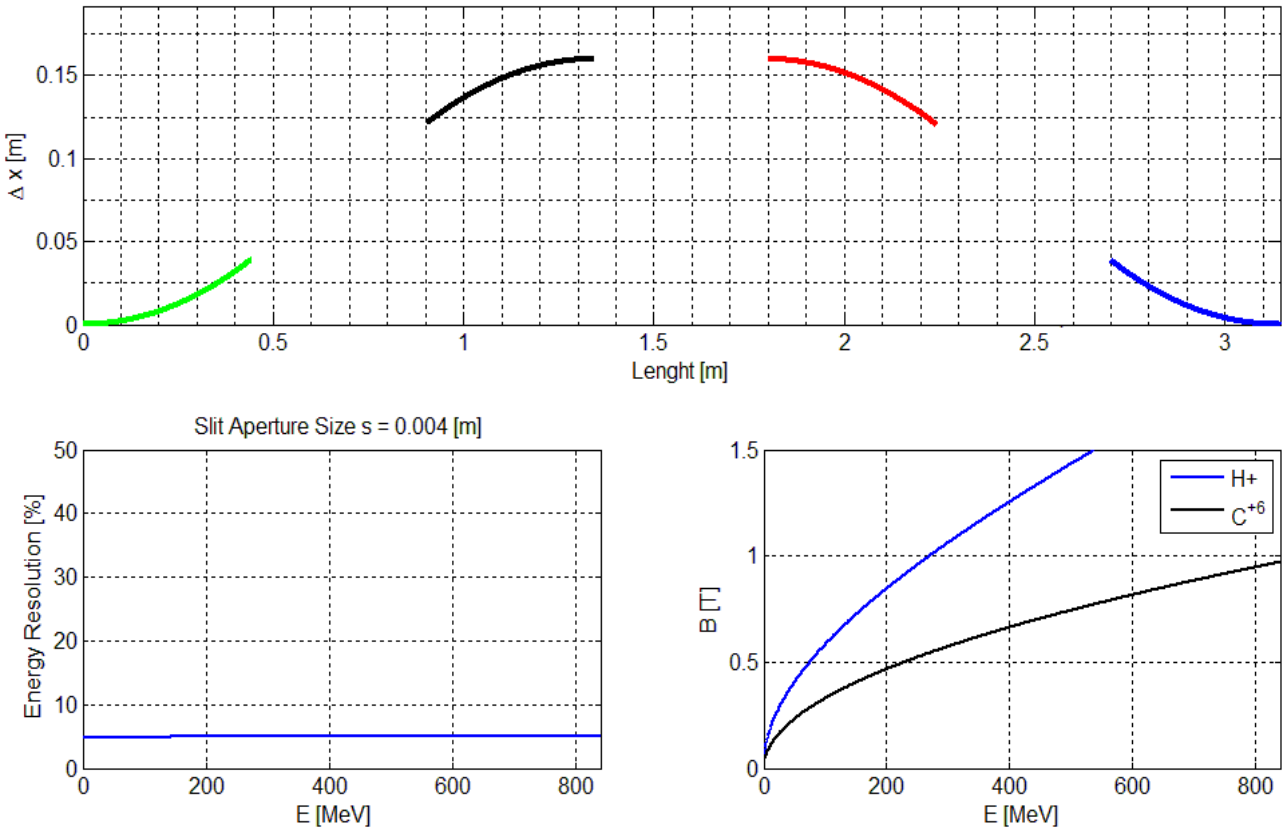

***Figure 3.2**: ESS preliminary characterization.*

The proposed layout would allow to vary the energy resolution changing the slit aperture size, which is an advantage as at higher energy, laser-produced particles are less abundant and a bigger slit is necessary to keep the transmission efficiency acceptable, as will be shown later. In order to have the requested resolution, see previous chapert, the slit aperture size have to vary in the range between 4 and 20 mm. This layout is different from the one described in the PMQs feasibility study as longer distances between dipoles have to be considered in order to avoid interactions between coils.

The described layout allows to define the dipole characteristics which are summarized in the next table. The allowed field variation range is considered slightly larger than necessary, for safety reasons. The radial extension of the Good Field Region (GFR) has been chosen two times larger than the particle path in the magnetic field, see Figure 3.2 upper panel.

n° of Dipoles	**B field**	**Geometric length**	**Effective length**	**Gap height**
4	0,085 – 1,2 T	400 mm	450 mm	59 mm
Good Field region (GFR)	**Field uniformity**	**Curvature radius**	**Bending angle**	**Drift between dipoles**
100 mm	< 0,5 %	2,5293 m	10,10° (176,3 mrad)	500 mm

Electromagnetic dipole are preferred to permanent magnet in this case as they can produce the required magnetic field within a considerably big gap, which means that the magnetic chicane will have a wide acceptance. The gap size reported in table has been chosen considering reduction due to the pole shim, the thickness of the vacuum chamber (5 mm) and at least 40 mm of free space.

Moreover, the use of collimators is necessary in order to avoid spatial mixing of particles in the first half of the chicane, which would reduce the ESS resolving power, and to refine the energy spread of the output beam. Thus a 30 mm diameter collimator will be set 200 mm upstream the first dipole, and another 30 mm diameter collimator will be set 200 mm downstream the fourth dipole. The effective length has been estimated as $L_{effective} = L_{geometric} + 2hk$, being h the gap height and k a constant specific to the yoke usually ranging between 0,3 and 0,6 [2] and fixed to 0,425 for this case.

Taking into account the collimators and the selection slit size, the angular acceptance of the ESS can be evaluated from simple geometric considerations. For example, considering that a 60 MeV beam has to be selected with an energy spread of 20% the slit aperture size required is 20 mm, which means that the beam has to be injected in the chicane with an angle of about 8 mrad in the radial direction; in the transverse direction the beam should have no divergence, but actually a small angular divergence is allowed as it can be compensated by the edge effect of the dipoles as will be shown in section 3.3. A back-trace in the magnetic chicane allows to evaluate the beam parameter required to match the ESS acceptance. The phase space plot of a matched beam at the ESS input is shown in Figure 3.3 and next table lists the beam parameters accepted by the chicane.

	XX'	**YY'**	**XY**
alpha	0,8401	0,3556	0,0002
Beta [mm/Pi.mrad]	2,7094	2,4484	0,9112
Emit[rms] Pi.mm.mrad [Norm]	2,9506	3,9324	24,15 mm^2
Xmax	**Ymax**	**X'max**	**Y'max**
14,97 mm	14,99 mm	8,632 mrad	7,162 rad

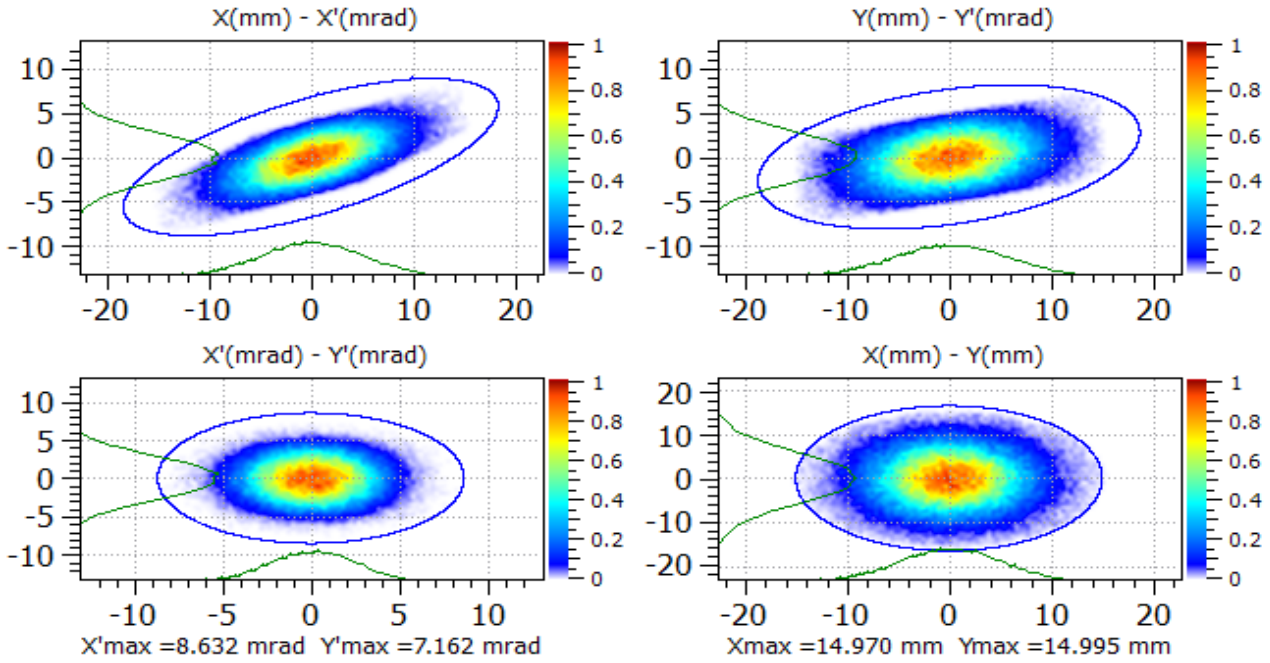

***Figure 3.3**: Beam phase-space plot representing the ESS acceptance. The ellipse represents the beam emittance at 6σ.*

A large acceptance for the energy selector is of fundamental importance to ensure a reasonable

high transmission efficiency as the beam has a wide divergence and the transport through the PMQs could cause growth of emittance due to the field uniformity which is reduced at the edge of the bore. Moreover, errors in the allignment between the target normal axis and the beamline have little effect on the selection and transmission efficiency, as will be shown in the following.

3.2.1 Electromagnetic dipole analytical design

The dipole has been designed in order to be as compact as possible, considering the maximum field required of 1,2 T, to ensure a high uniformity within the good field region and the required effective length. Moreover the possibility to vary the field intensity within one second has been taken into account, in order to develop a selection system that can also work as an active beam energy modulator system. Hence, the iron core of each dipole won't be a solid core but laminated, which also reduces the eddy currents in the yoke.

The dipole will be C-shaped. It gives the advantage to allow an easy access to the vacuum chamber and also the possibility to reduce the iron mass as C-shaped dipole can be displaced out of axis. As a first approach the magnet has been defined in terms of dimensions using an analytical approach [2]. The simple magnetic circuit in Figure 3.4 is used to define the dimensions of the iron core.

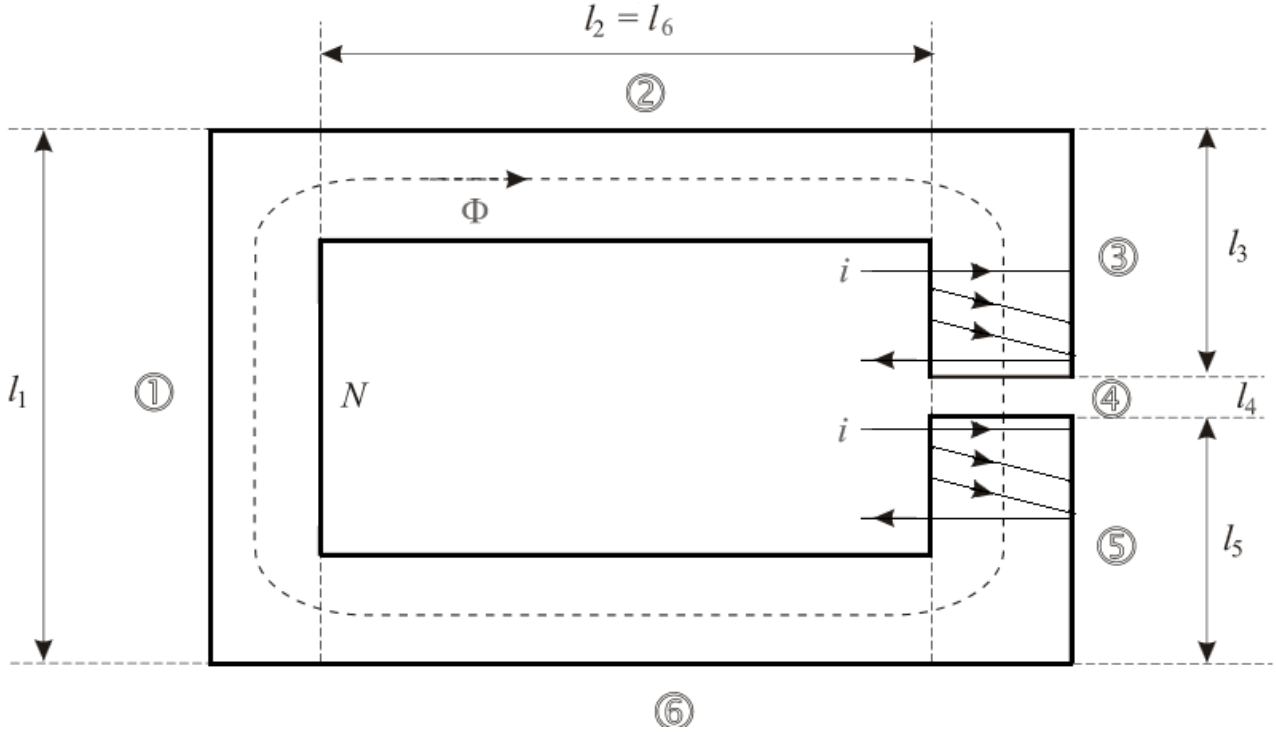

***Figure 3.4**: Example of a magnetic circuit for a C-shaped dipole*

The technique consists in the evaluation of the reluctances of each part of the magnetic circuit with length l_i as:

$$R_i = \frac{l_i}{\mu_0 \mu_r S_i} = \frac{N i}{\Phi} \quad (3.8)$$

being μ_0 the magnetic permeability of the vacuum, μ_r the relative permeability of medium, set equal to 2000 for the iron core and to 1 for the air gap, S_i the area of the radial section of each part of the circuit, Ni is the excitation current and Φ is the magnetic flux in Weber which depends on the maximum field value of 1,2 T and the area of the air gap radial section. The gap and the depth of the have been defined according the beam optics requirements, and the length of the different parts of

the circuit have been varied in order to maximize the efficiency of the magnet. For this magnet the efficiency is given by the total reluctance R_{tot} of the six parts of the magnetic circuit over the air gap reluctance R_4 and results to be:

$$\eta = \frac{R_{tot}}{R_4} = 98\% \quad (3.9)$$

This result predicts that there will be some saturated areas in the iron, but, on the other hand, allow to realize a magnet with a weight of less than 3 tons. In this case the required iron mass is 2,2 tons and the magnet dimensions resulting from equation (8) are:

l_1	$l_2=l_6$	$l_3=l_5$	l_4
1044 mm	140 mm	497 mm	59 mm

The excitation current is also evaluated from equation (8) once the geometry of the yoke is defined and, considering the maximum field required, it results to be Ni = 29 kAmp per coil. Considering a coil made of 176 turns (11x16 turns), a wire section of 10x10 mm^2 and a cooling channel of 6 mm of diameter, the required current desinty is 2,3Amp/mm^2. This gives a coil section of 115,5x168 mm (0,5 mm of insulator between each turn are considered) with a total copper mass of 435 kg. This design allows to define a preliminary design of the magnet but its finalization has to be accomplished with numerical methods in order to take into account the non-linear behaviour of the iron permeability, which can affect the excitation current value, and to define the pole shape which gives the required field quality.

3.2.2 Electromagnetic dipole design finalization

To obtain the required magnetic field intensity and uniformity in the GFR in the air gap, the pole tip need to be properly shaped and, as as the efficiency of the magnets is limited to 98%, saturation points where the iron behaviour becomes unpredictable, have to be far from the GFR [3,4]. The FEM codes COMSOL and OPERA have been used to define the pole shape in order to have the required field uniformity. A series of 2D simulations have been performed and, in the present design, the pole face edges have been contoured adding an overhang at the periphery to improve the field uniformity at the centre of the gap. The overhang has also been chamfered in order to avoid saturation. Figure 3.5 shows the dipole dimensions (upper panel) and the pole radial shape (lower panel). Saturation is limited to the periphery of the pole and in some small parts of the return yoke where the magnetic flux reaches values between 2 and 2,2 T, as shown in Figure 3.6. In this figure only the upper half of the dipole is reported, the blue rectangles represent the coil, the vacuum chamber in austenitic stainless steel AISI 316L has been also modelled and the field distribution inside the gap is also represented.

The field uniformity in the good field region is given by:

$$dB_y = \frac{B_y(x)}{B_y(0)} - 1$$

and is well within the requirement of 0,5% for all the different field values from 0,085 up to 1,2 T. In the plot of Figure 3.7 only these two cases are reported. The pole shape plays an important role in the field uniformity and, moreover, the fact that its variation is basically the same for the lowest and the highest fields means that the iron saturation has no effects on the field quality.

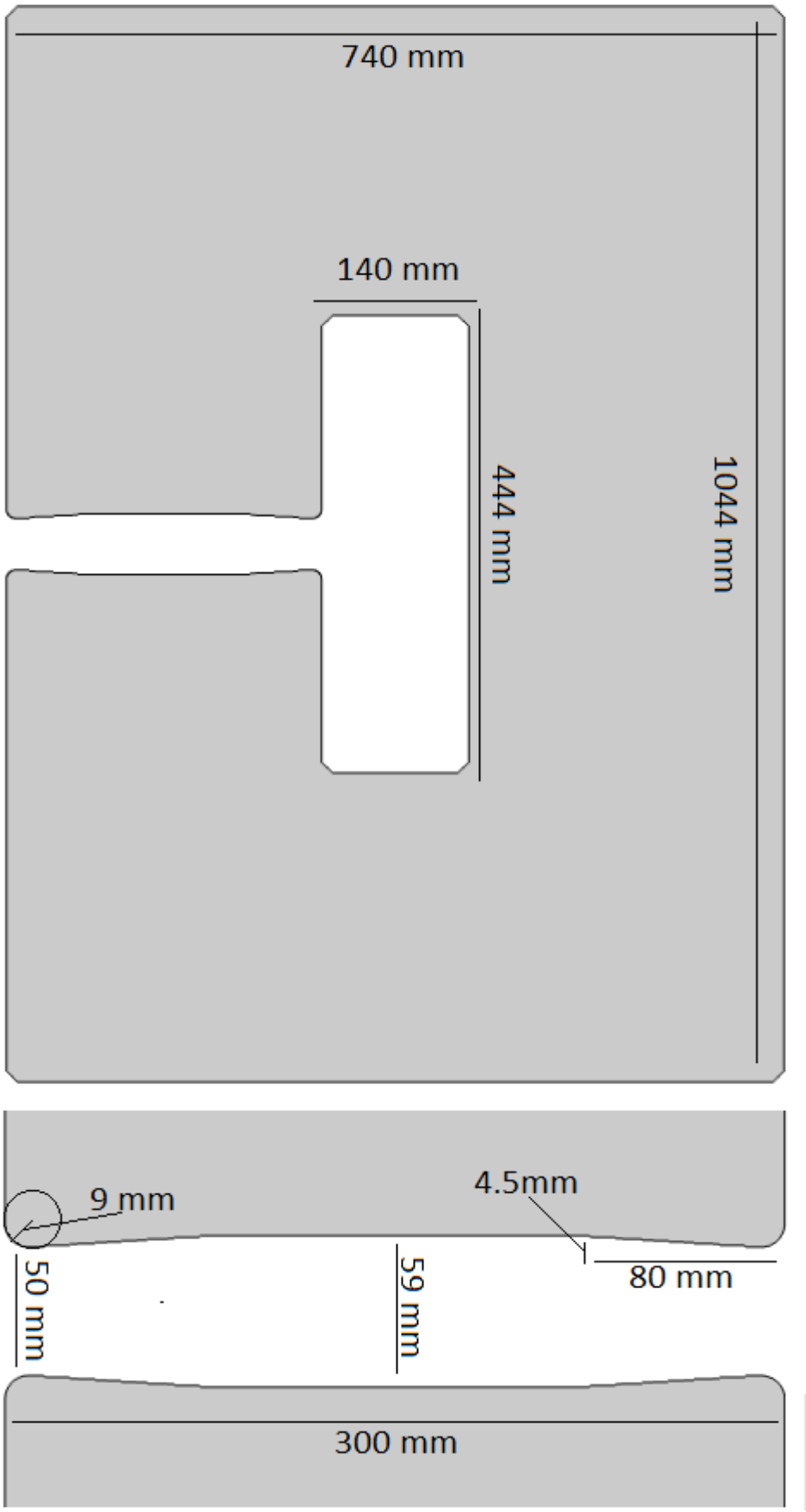

***Figure 3.5**: Dipole section (upper panel) and radial shimming.*

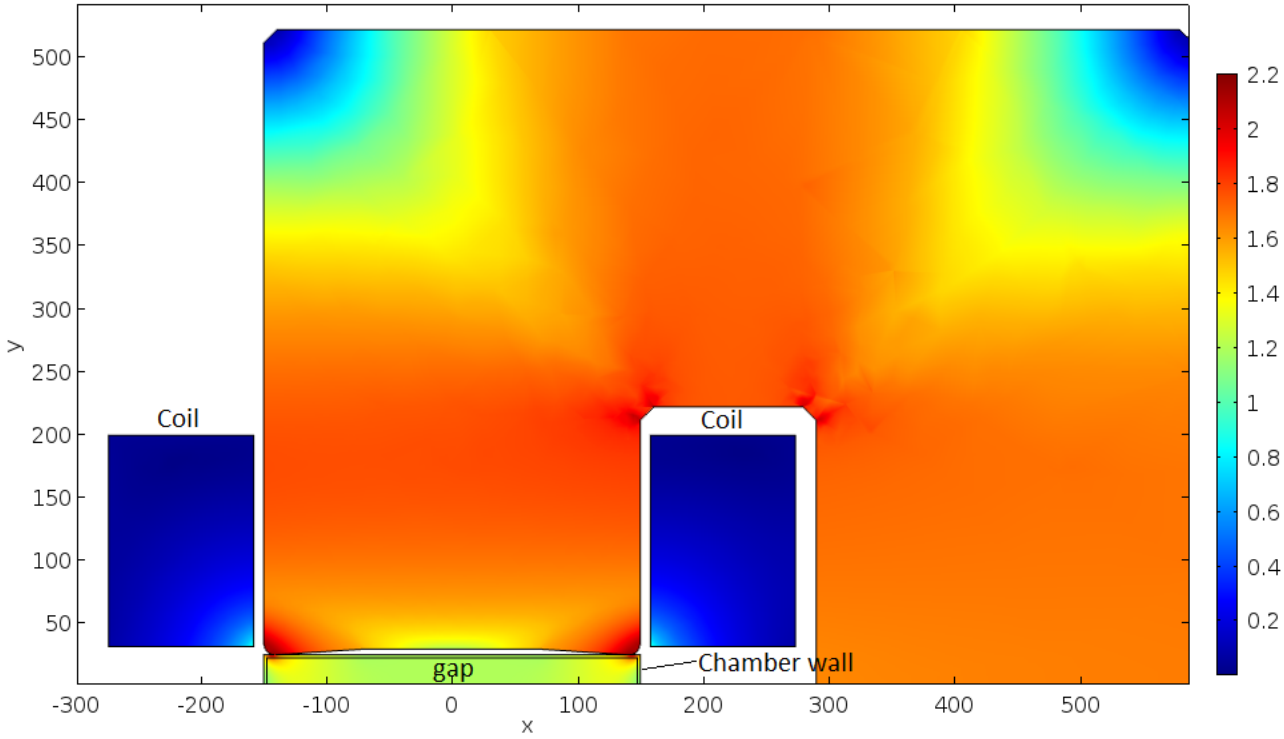

***Figure 3.6**: Dipole yoke field distribution.*

The relatively low efficiency of the magnet has effects only on the current density necessary to excite the coils. In fact, for lower fields, where the iron behaviour can be considered linear, the analytical model predicts the same current of the numerical simulation, but for fields higher than 0,85 T the analytical models fails as the iron becomes highly non-linear; for example according numerical simulation a current Ni = 32 kAmp is required to produce the maximum field of 1,2 T, which is about the 10% higher than the analytical value. The plot of the magnetic field as a function of the coil excitation current is show in Figure 3.8.

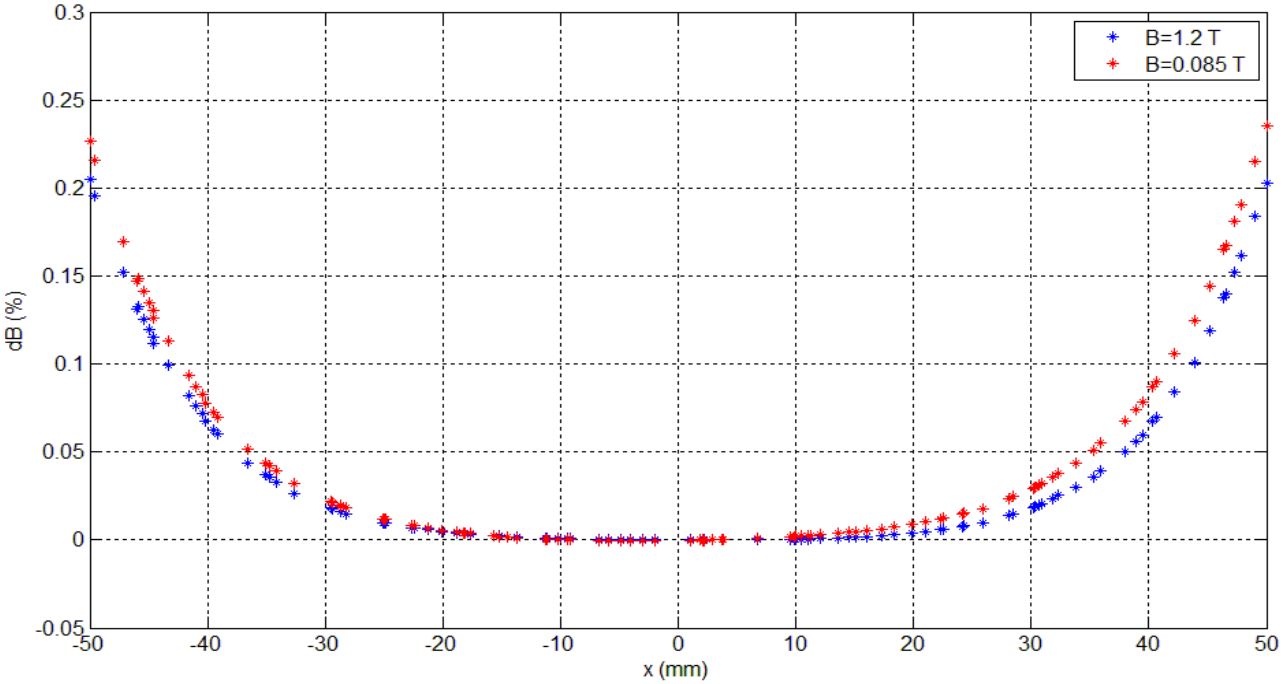

***Figure 3.7**: Field uniformity for the maximum field (blue stars) and minimum field (red stars).*

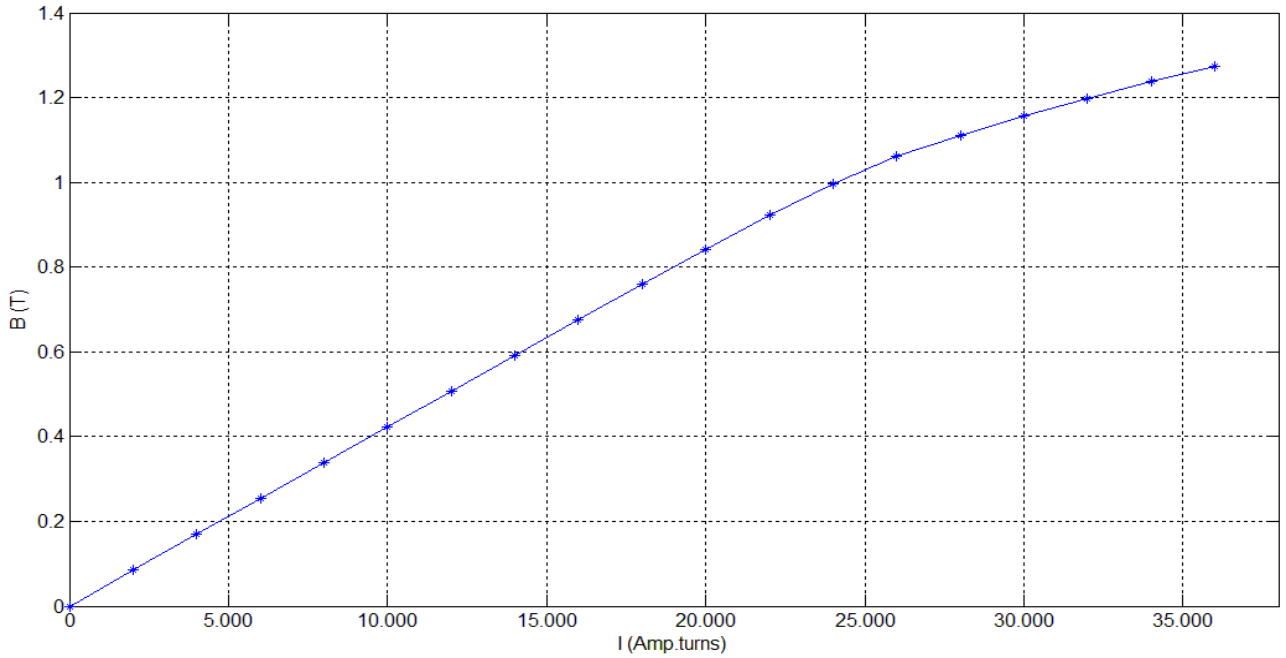

***Figure 3.8**: Magnetic field as a function of the coil excitation current.*

The cubic function $B = -0{,}02321\, I^3 - 0{,}05011\, I^2 + 0{,}4542\, I + 0{,}7637$ describes the curve in Figure 3.8 with good precision ($r^2 = 0{,}999$). A table of currents values and corresponding magnetic fields is in Appendix A.

The above results hold true also for the 3D case, which has been used to refine the longitudinal pole shape according the optics requirements. In fact, on the longitudinal pole shape depends the effective length of the magnet, which is given by [3,4,5]:

$$L_{eff} = \frac{\int_{-\infty}^{\infty} B_y(z)\, dz}{B_y(0)} \quad (3.10)$$

Magnetic saturation in the vicinity of the longitudinal edge results in a small decrease in the effective length with the increasing of the excitation current. Hence the effective length will be varying in a wide range as the dipoles of the chicane will be working at different fields. In fact if the longitudinal profile of the dipole has a simple rectangular shape the effective length ranges between 480 mm and 474 mm (from the minimum up to the maximum value of the excitation current) and the pole profile results highly saturated, as shown in Figure 3.9 where the iron parts with magnetic flux higher than 2 T are highlighted. This is usually not a problem for machines with identical dipoles, but the effective length is bigger than the required value coming from the design trajectory study and, as said before, it is better to avoid saturation close to the good field region. A suitable longitudinal Rogowski profile [5] can solve this saturation issues and also reduces the effective length variation for different fields. Rogowski profile is described by the analytical function reported in [5] but can be approximated by a number of straight lines resulting easier to realize. Different approximations of the Rogowski profile described by the red line in Figure 3.10 have been investigated and the best results, in terms of iron saturation and effective length variation range have been obtained using the green and blue straight lines in Figure 3.10. The pole saturation with the Rogowsky shape is shown in Figure 3.11. It is evident that the saturated parts of the iron are limited to the pole radial periphery, far from the good field region. The effective length variation is now between 451 mm and 448 mm which means three times smaller than the simple rectangular shape case and closer to the design trajectory requirements.

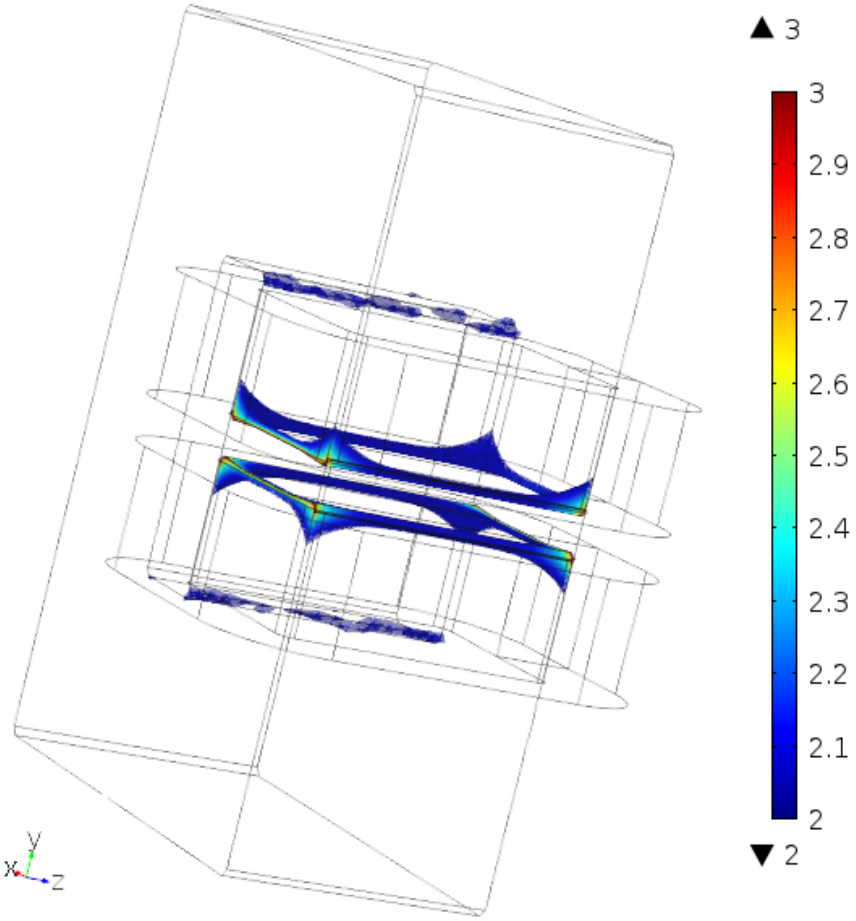

***Figure 3.9**: Saturated regions in a rectangular shaped dipole (z is the longitudinal direction).*

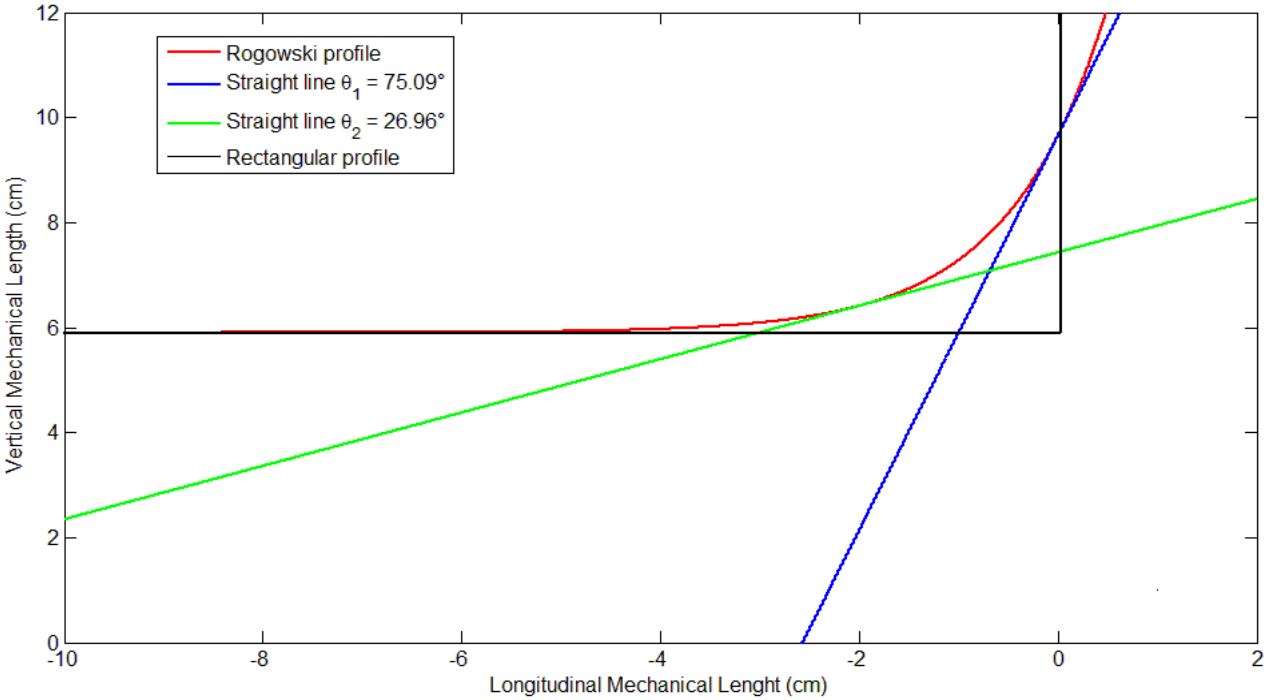

***Figure 3.10**: Rogowski profile (red curve) and the used strighlines (blue and green lines) to realize the dipole shape. In balck is the original rectangular dipole profile.*

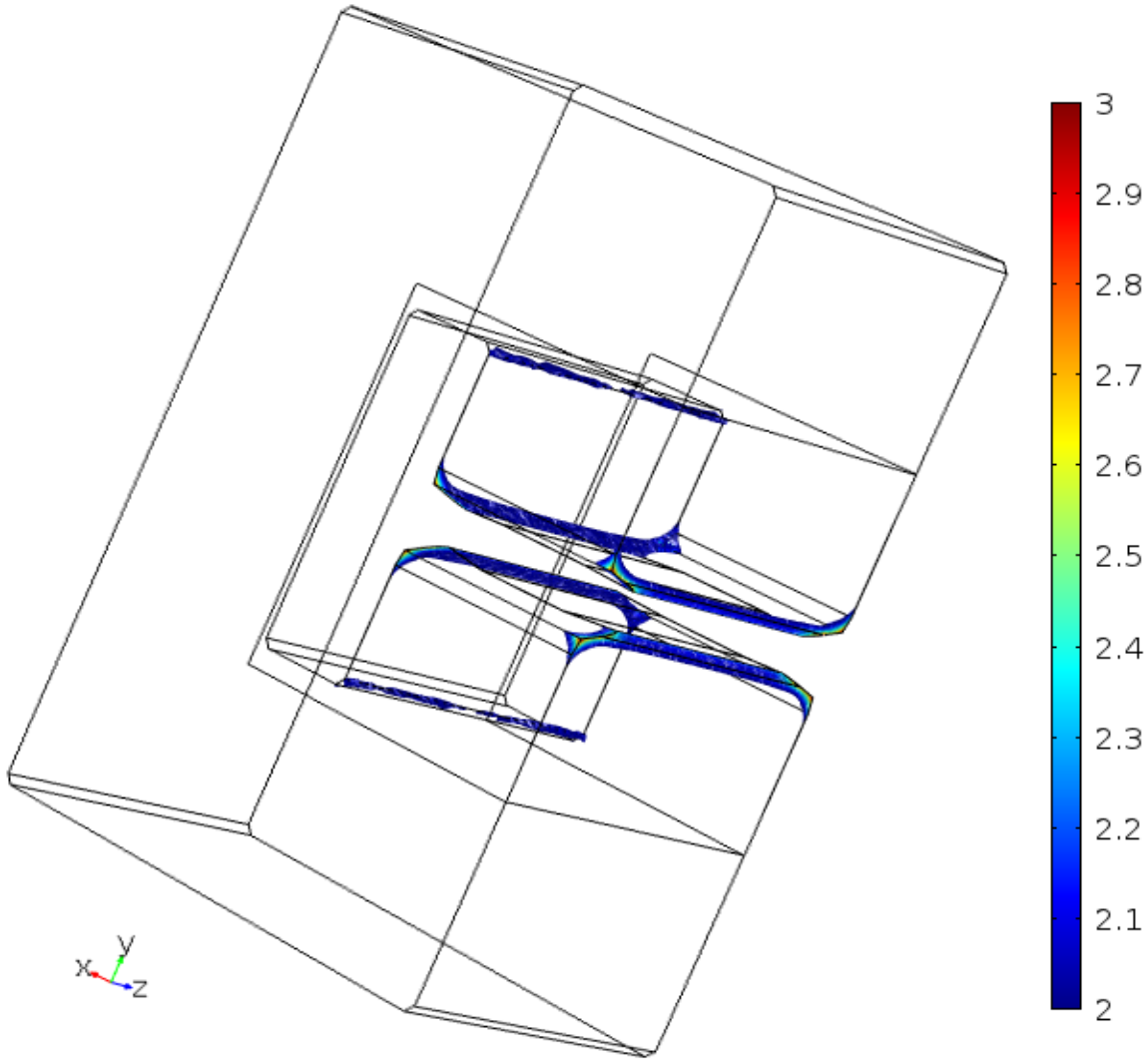

***Figure 3.11**: Saturated regions in a Rogowski shaped dipole (z is the longitudinal direction).*

Figure 3.12 shows the whole system, vacuum chamber included, and the reference trajectory. It should be noted that the magnets are not aligned and their axis is different from the input beam axis.

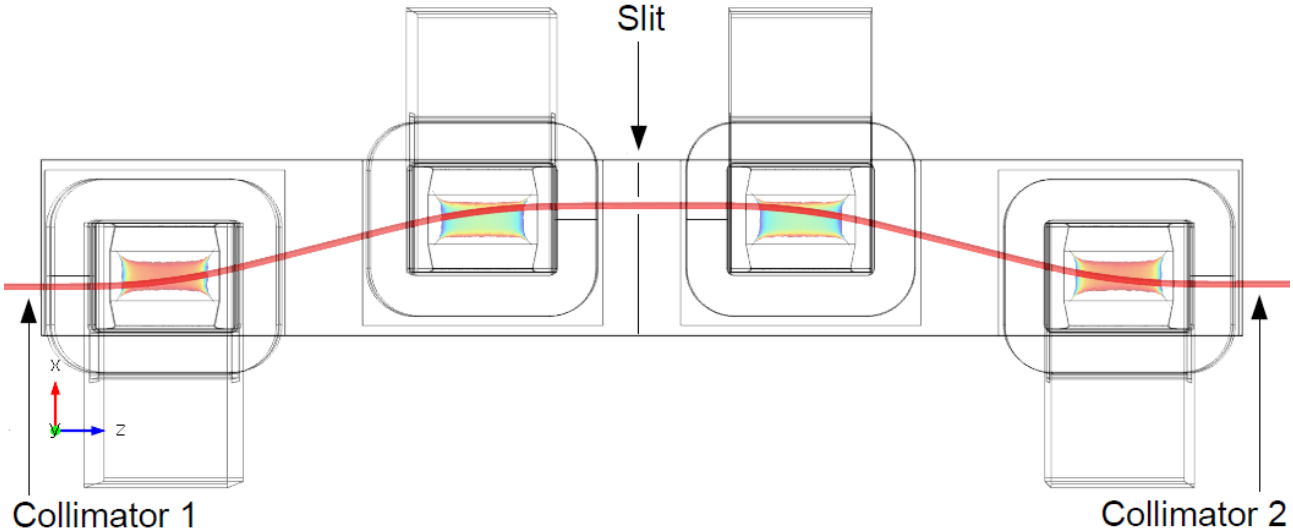

***Figure 3.12**: Energy Selector with vacuum chamber (sketched as a rectangle) and reference trajectory.*

In Figure 3.12 it is also shown that the reference trajectory passes within the good field region of each magnet and there is no steering effects due to the magnetic field of the chicane, in fact the input and output axes are the same.

Errors on the magnetic field coming from the design, rather than from fabrication, have been analysed. As the design of the dipole respects the symmetry, the first error source which arise is the sextupole field [6]. The formalism used for the field expansion is described in [7], taking into account that the main dipole harmonic is B_1. The radial field is analysed considering a circumference with radius of 20 mm at the centre of the dipole and the results for the lowest and highest fields are reported in the next table where the harmonic content is expressed in units of the main harmonic B_1 normalized to 10^4.

I [A] – B_{max} [T]	**B_1**	**B_3**	**Sum(B_n/B_1) (%)**	**Sum(C_n/C_1) (%)**
2000 – 0,085	10000	0,517	0,00949	0,00952
32000 – 1,2	10000	0,178	0,00372	0,00448

The results in the table show that the harmonic content is very small compared to the main harmonic and, as expected, the lowest field is more sensitive to the sextupole component. For the sake of precision, in this simulations the vacuum chamber in stainless steel AISI 316L has been included, but it results to be completely transparent to the magnetic field for the static case. The harmonic content in the previous table refers to a single dipole simulation.

The same analysis has been performed on the simulation of the whole system represented in Figure 3.12. As shown in the next table, the total harmonic content is always less than 1‰ and, even if the harmonic content for the central dipoles is slightly higher, interactions among magnets can be neglected.

I [A] – B_{max} [T]		**B_1**	**B_3**	**Sum(B_n/B_1) (%)**	**Sum(C_n/C_1) (%)**
2000 – 0,085	**Dipole 1**	10000	0,517	0,00564	0,02331
	Dipole 2	10000	0,515	-0,06738	0,07325
	Dipole 3	10000	0,482	-0,06038	0,06466
	Dipole 4	10000	0,520	0,00571	0,0242
32000 – 1,2	**Dipole 1**	10000	0,176	0,00212	0,0125
	Dipole 2	10000	0,165	-0,03927	0,0439
	Dipole 3	10000	0,146	-0,03335	0,0369
	Dipole 4	10000	0,179	0,00211	0,0116

3.2.3 Eddy current effects

As written before, an electromagnet based selection system can be used also as an active energy modulator for the laser produced beam, provided that the different energy components are properly injected. This means that the ESS should work varying the current with an frequency of 1 Hz. This frequency comply the laser frequency and is also not challenging to realize from the technical point of view. Anyway, the current ramping in the coils will produce eddy currents circulating in the vacuum chamber. This eddy currents can produce an effective sextupole field superimposed to the

dipole field [8, 9, 10, 11]. Hence the main dipole field distortions due to the current ramping have been investigated performing time dependent simulations with COMSOL. Two cases have been considered: in the first case one dipole has been simulated, in the second case a second dipole has been added. Time dependent simulations are extremely expensive in terms of computational resources and time, thus a conservative case has been considered: the current is ramped from zero up to 273 Amp per turn (48 kA on the coil) in 0,28 s, which means a maximum field of 1,5 T. This choice is related to the fact that higher magnetic flux variations cause higher induced currents in the chamber wall. The simulation is performed on a period of one second, namely between two laser shots.

In the first case, to reduce computation costs, the symmetry of the single dipole system has been used and the simulation has been solved for half of the magnet, as shown in Figure 3.13. This is a valid technique to solve problems presenting symmetries as long as the correct boundary condition is set on the symmetry plane. In this case the condition to be set is the tangential condition of the magnetic field $\vec{n}\cdot\vec{B}=0$, being $\vec{n}$ the normal vector to the symmetry plane.

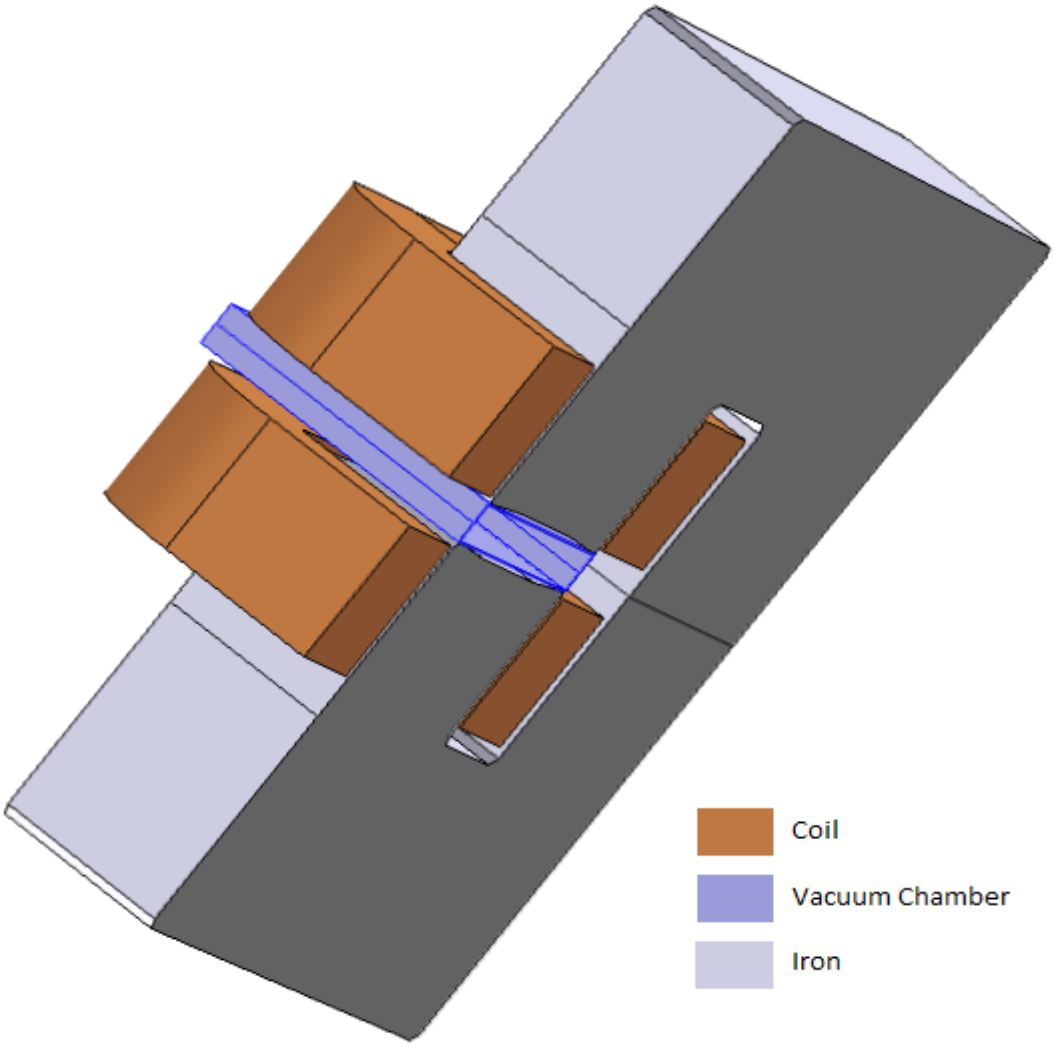

***Figure 3.13**: Simulation set up of case 1.*

Figure 3.14 shows the evolution of the induced current density in the chamber wall (blue line) while the coil current (red line) is ramping from zero to the maximum value and during the next steady state when the magnet is fully energized.

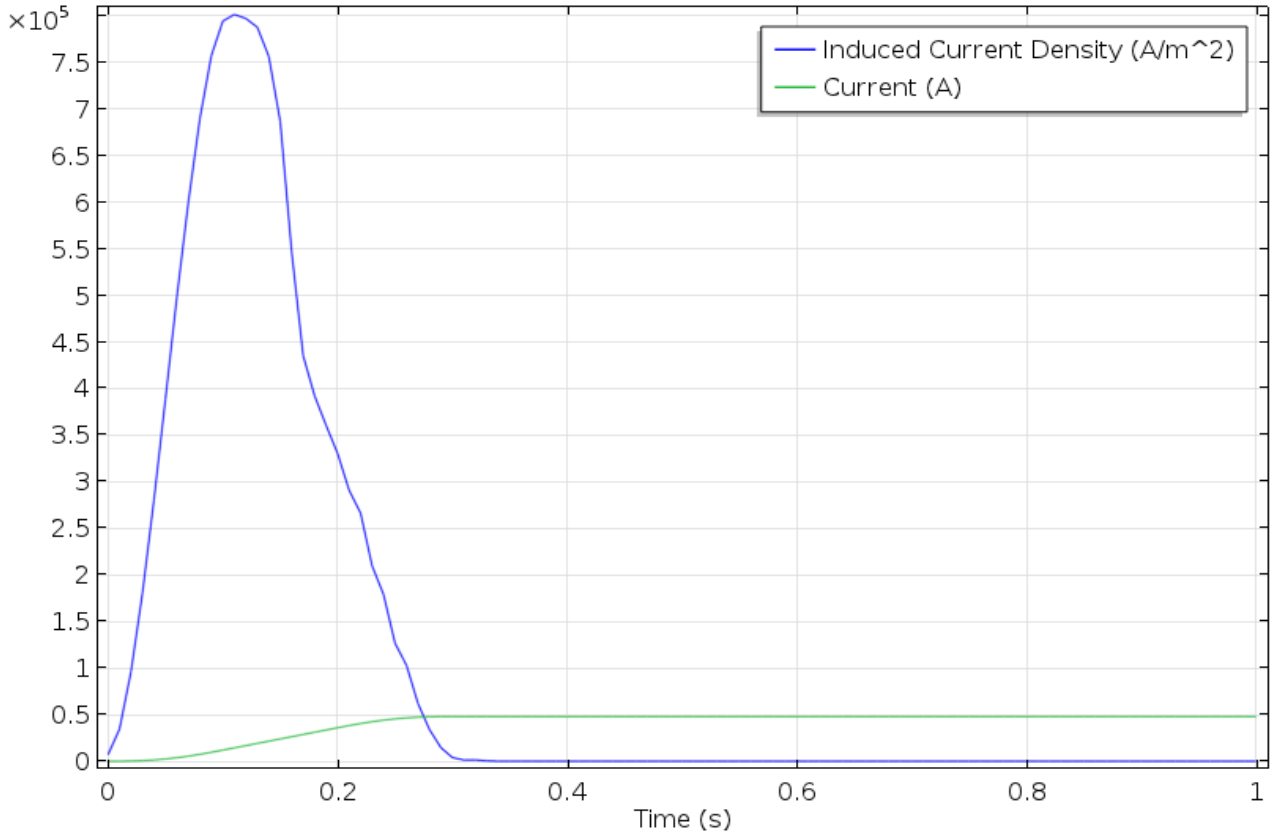

***Figure 3.14**: Evolution of the induced current density (in blue) and coil current (in red) in a time interval of one second.*

The induced current density has a maximum value of $8x10^5$ A/m^2, which is in agreement with the result obtained from the Faraday Law ($7{,}62x10^5$ A/m^2). The duration of the eddy current is slightly longer than the coil current ramp (~0,3 s) and in this time frame they are in the opposite direction with respect to the coil current. Figure 3.15 shows the coil current and the induced current density at

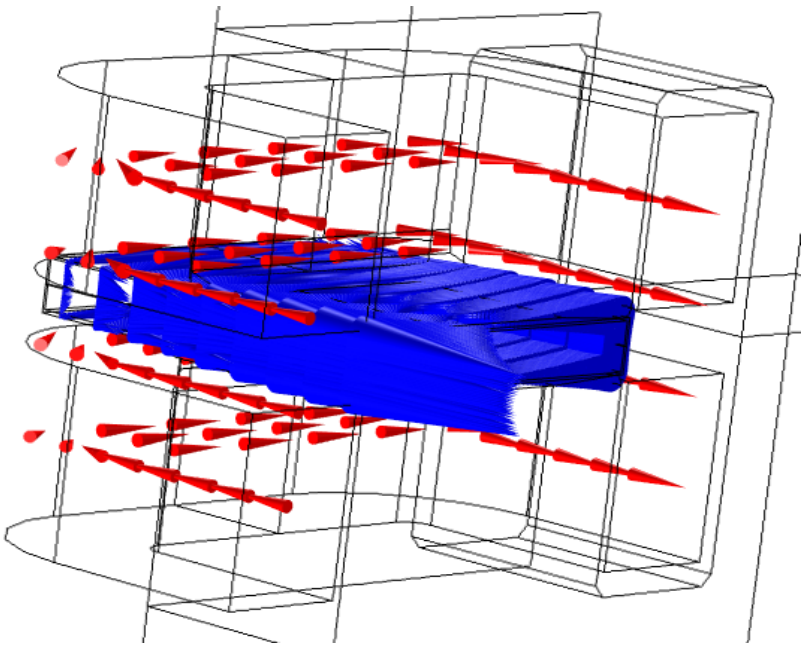

***Figure 3.15**: Coil current (red arrows) and induced current on the chamber wall (blue arrows) at t=0,14 sec.*

t=0,14 sec, namely, when the eddy currents reach their maximum value.

Again, the model respects the symmetry and the first errors that arise is the sextupole field which can have destructive effects on a beam with a very large energy spread. The plot of the third harmonic, in units of 10^4, as a function of the time is reported in Figure 3.16. It is evident that at the beginning of the ramp the sextupole strength is three order of magnitude higher than in the steady case, but after 0,3 sec it becomes smaller than 1 unit. Moreover, the complex harmonic C_3 has the same value of its real part B_3, which means that no skew components are introduced as expected, in fact the design symmetry is respected.

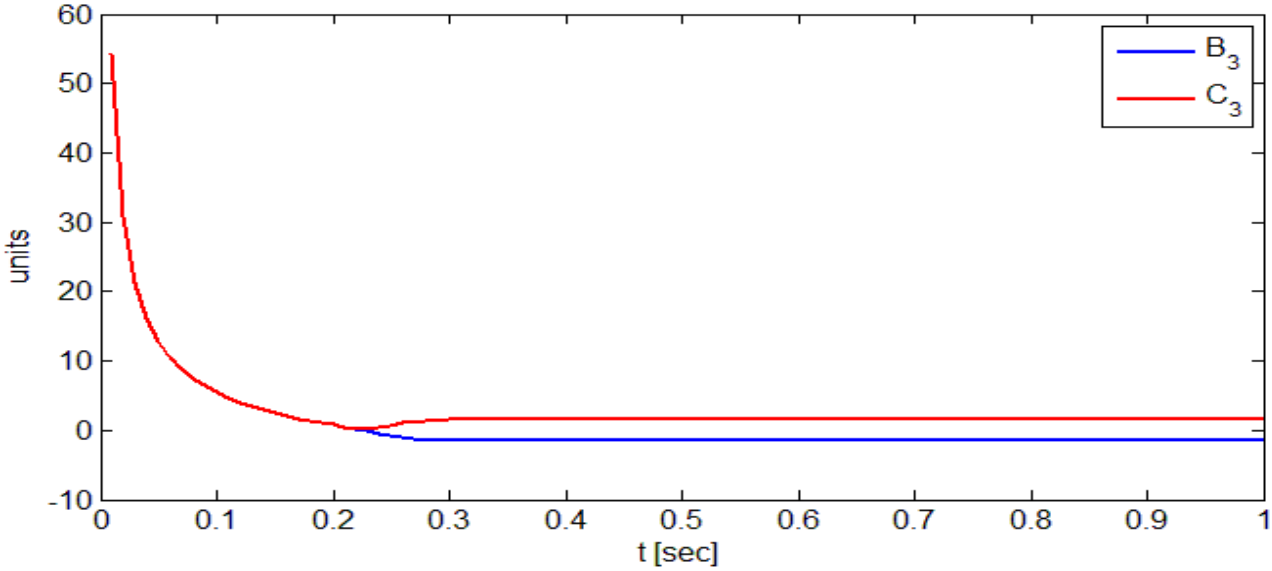

***Figure 3.16**: Evolution of the sexupole harmonic B_3 and the modulus of the related complex component C_3.*

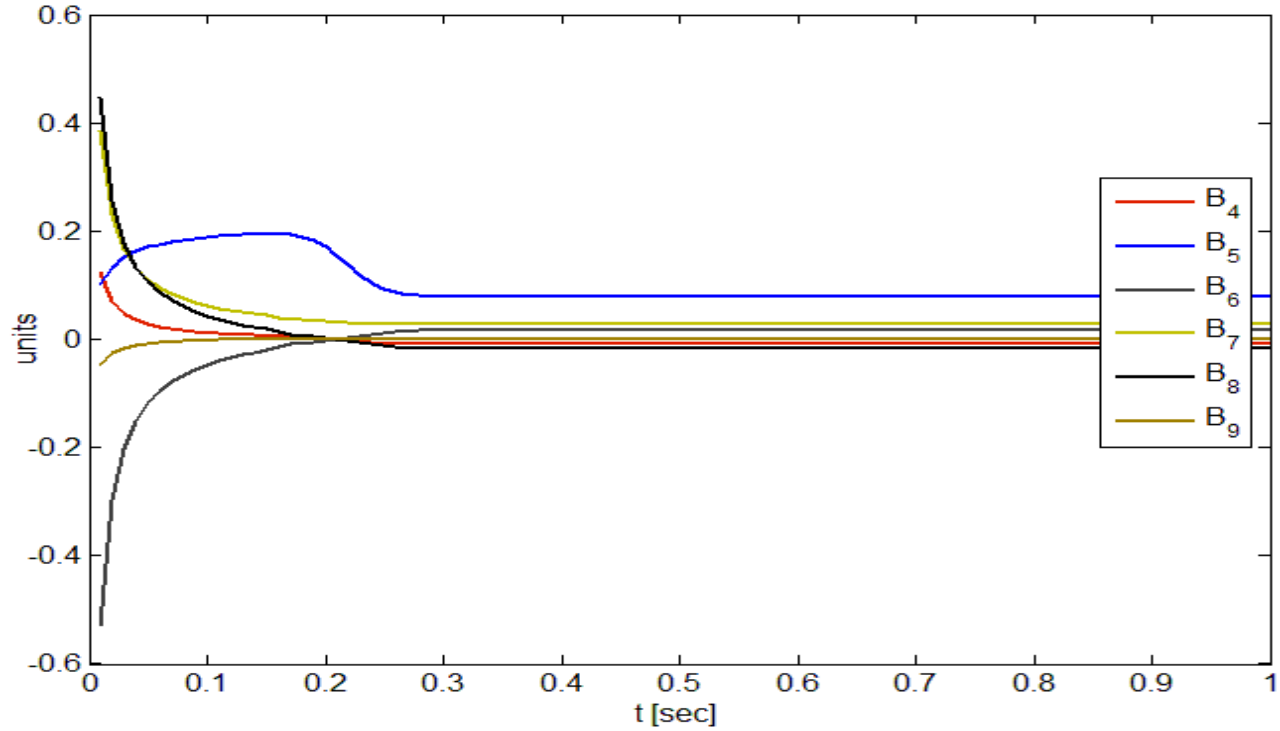

***Figure 3.17**: Evolution of the normal harmonics $B_4 - B_9$.*

The higher harmonics are also increased during the current ramp but as soon as the eddy currents

vanish they are restored to the steady case values. Figure 3.17 shows the normal harmonics $B_4 – B_9$ evolution in the considered time frame, higher order are not shown as they are considerably smaller. The contribution of the skew components is not considered because the design symmetry is not broken.

Finally, in Figure 3.18, the total harmonic component evolution is shown and compared with the steady case value. It is easy to notice that the sextupole harmonic dominates over the higher components during the current ramp and, for t>0,3 s, the steady case values (reference dotted values) are restored and the field has no distortions.

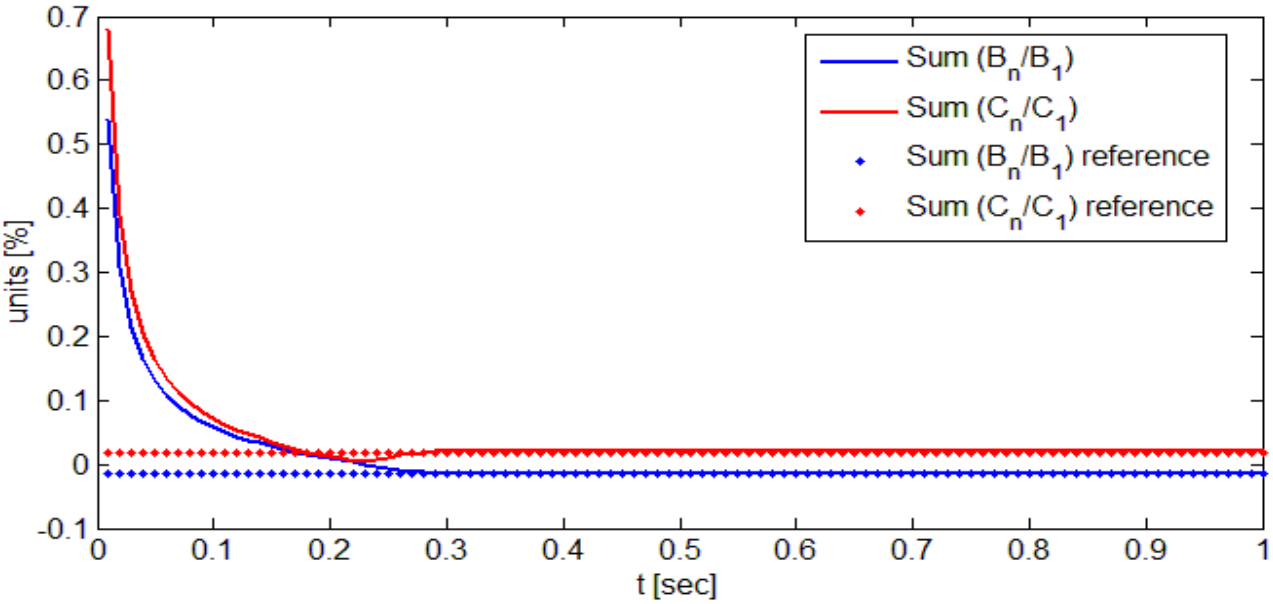

***Figure 3.18**: Evolution of the total harmonics content as a function of time. Blue line represents the normal harmonics, red line is the complex content, where skew harmonics are taken into account. Dotted line are the references value evaluated in the steady case.*

In the second case the first and the second dipole of the selection system have been simulated. Computation cost has been reduced exploiting the system symmetry as can be seen in Figure 3.19.

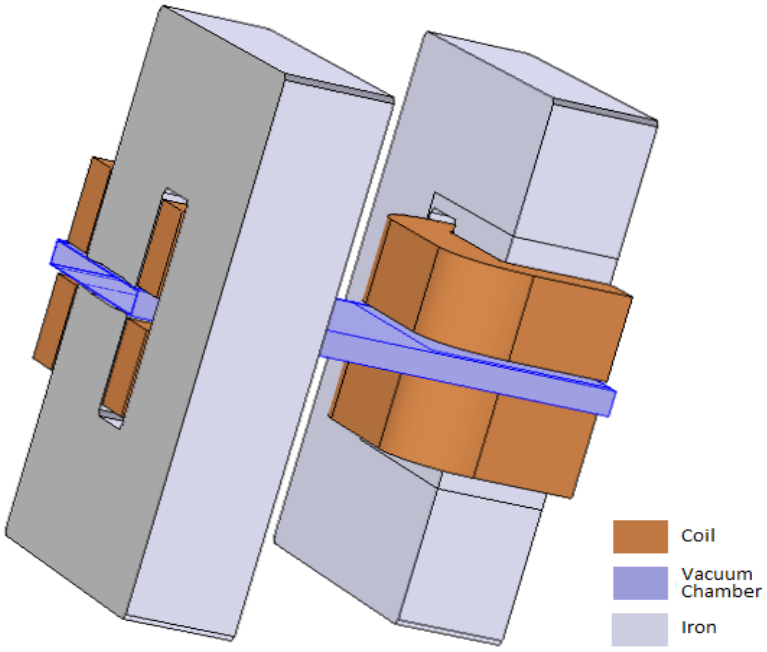

***Figure 3.19**: Simulation set up of case 2.*

The results for the 2 dipole case are similar to the 1 dipole case and only the evolution of the normal harmonic content is reported in Figure 3.20. In this case the sextupole field is much higher than the previous case, as the induced current density is also higher ($1{,}15*10^6 A/m^2$); its duration is again slightly longer than the current ramp time, as shown in Figure 3.21. In Figure 3.22 is shown the coil current and the induced current density at t=0.12 sec, namely, when the eddy currents reach their maximum value. It is evident here that there are two different interacting loops for the induced current on the chamber wall.

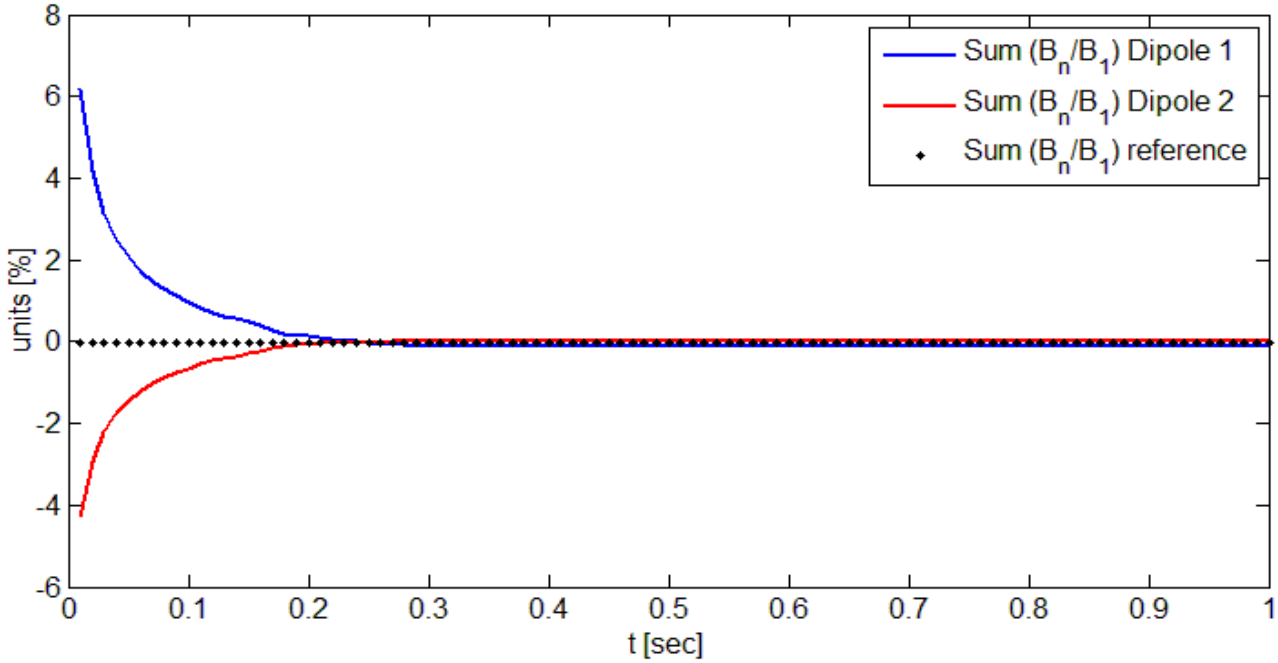

***Figure 3.20**: Normal harmonic content evolution for dipole 1 (blue line) and dipole 2 (red line). Black dots is the reference value in the steady case.*

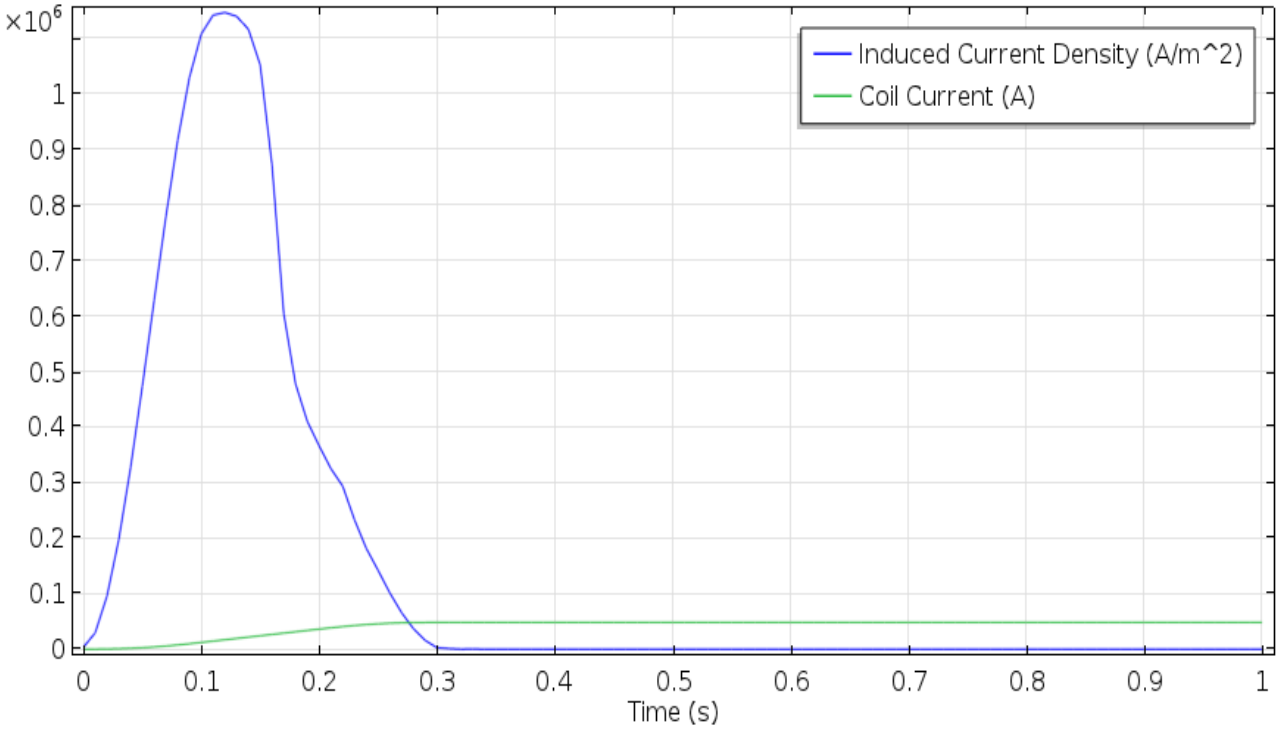

***Figure 3.21**: Evolution of the induced current density (in blue) and coil current (in red) in a time interval of one second.*

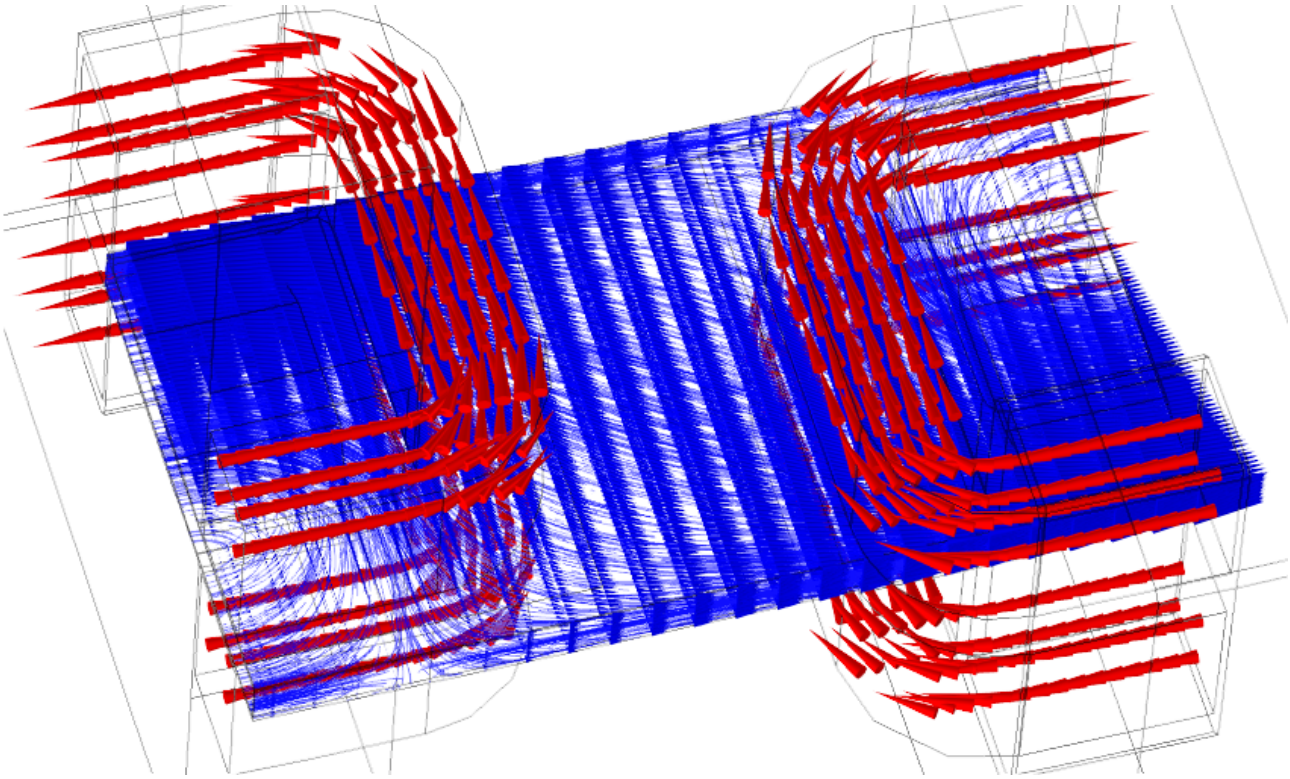

***Figure 3.22**: Coil current (red arrows) and induced current on the chamber wall (blue arrows) at t=0,12 sec.*

These results demonstrate the robustness of the magnetic design of the selection system. The system offers good field quality and the possibility to operate as an active energy modulator without field distortions, once the operating current value has been reached. It should be considered that, if used as an energy modulator, the field variations, and hence the current changes, would be rather small. In fact, a field variation of ±10% at maximum in two consecutive shots would be enough to select contiguous energy intervals. As an example, the field required to select 60 MeV protons is B_1=0,449 T; if the required energy spread of the selected beam is 20%, in the next shot the reference energy would be 54 MeV and the required field is B_2=0,425 T. The resulting induced current on the chamber wall would be, according the Faraday law and considering only one dipole, of about 10^4 A/m^2 which will have negligible effects on the magnetic field. Moreover, it should be also considered that the current ramping time could be longer in the real system, which is another source of eddy-current intensity reduction.

In the next section the beam-transport simulations of the whole beam-line (PMQs + ESS) are reported. Also the beam-line error study is presented. No simulations demonstrating the feasibility of the active energy modulation are presented at this stage as the mechanics of the PMQs is pretty slow, compared to the current ramping time, and more detailed study on the optics are necessary in order to find a set-up of the collection system able to ensure reasonable high transmission efficiency for a wide energy range.

3.2.4 Summary of dipole main features

n° of Dipoles	B field	Geometric length	Effective length	Gap height
4	0,085 – 1,2 T	400 mm	451 - 448 mm	59 mm
Good Field region (GFR)	**Field uniformity**	**Curvature radius**	**Bending angle**	**Drift between dipoles**
100 mm	< 0,5 %	2,5293 m	10,10° (176,3 mrad)	500 mm
Dipole weight	**Coil Section**	**Wire section**	**Water channel diameter**	**Insulator thickness**
2,2 tons (Yoke) 0,440 tons (Coils)	168x115,5 mm	10x10 mm	6 mm	0,5 mm
Number of turn per coil	**Max current**	**Max current per turn**	**Power consuption**	**Cooling Water ΔT~10 °K**
176 (16x11)	32000 A/turn	182 A	40 kWatt	16 l/min

3.3 Beam Transport simulations

In the following the preliminary beam-transport simulation results are reported. The optics calculations proposed in the PMQs feasibility study report have been reviewed and modified taking into account the new longitudinal dimensions of the energy selection system. In this case the ESS is no more simulated as a collimators system but the field maps are introduced. The first collimator is a 30 mm diameter circular aperture set 2,05 m from the target and 200 mm upstream the first dipole; the second collimator is identical and is set 200 mm from the last dipole, namely 5,55 m from the target. The third collimator is the selection slit, set at 3,8 m from the target; it is a rectanglar aperture with height of 40 mm, same as the inner vacuum chamber height, and variable width in the range between 4 and 20 mm in order to produce the required energy spread reported in the previous chapter. The thickness of the collimator, in stainless steel, have to be of at least 30 mm to stop proton with energy up to 150 MeV.

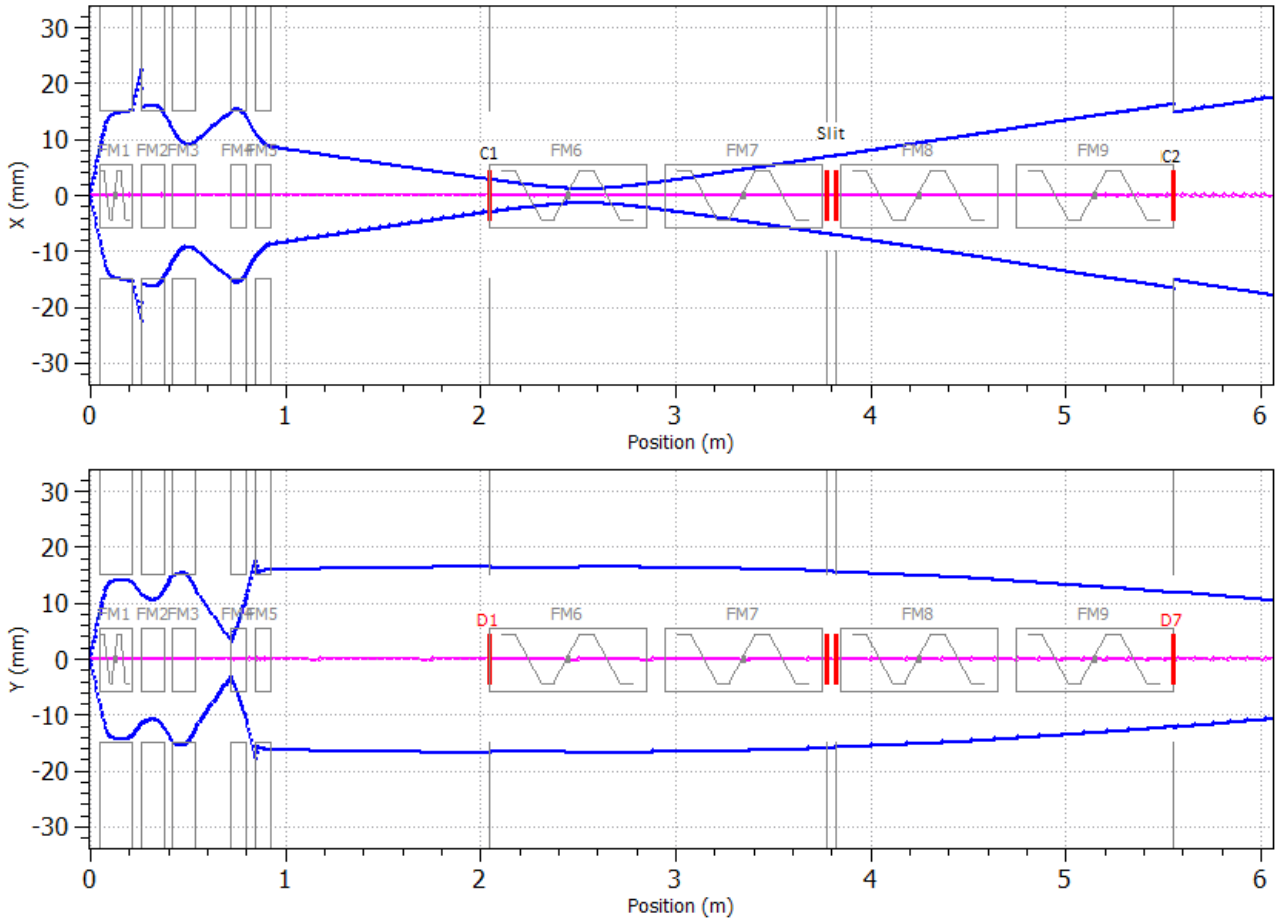

***Figure 3.23**: Scheme of the simulated beamline with envelop of 60 MeV protons.*

Figure 3.23 shows the scheme of the beamline. The laser-target interaction point is on the axis origin, follows the PMQs system field maps, named FM1-5, and then the energy selection system field maps, named FM6-9. The ESS field maps are 800 mm long, in order to take into account the fringe field effects. At the edge of the maps the magnetic field of the single dipole is of few tens of gauss. C1 and C2 are the collimators, the selection slit is between field maps FM7 and FM8 and is simulated taking into account its thicknes. The simulated beam has been considered monochromatic

in a first phase, with 40 μm diameter circular shape at the production point and an uniform angular divergence of 11° (half angle). In the following are briefly described the results in the energy range between 5 and 60 MeV for protons and for C^{6+} at 60 MeV/u, which is of interest for medical application. The goal of this preliminary simulations is the optimization of the PMQs in order to inject the beam in the energy selector maximizing the transmission efficiency of the whole beamline. The optimal injection can be obtained having a beam parallel on the transverse plane (bottom panel of Figure 3.23) and a waist before the selection point on the radial plane (upper panel of Figure 3.23). Actually a small divergence on the transverse plane can be compensated by the natural field index of the ESS, which focus the beam in the transverse plane. From the geometrical point of view other constraints have been considered: the minimum allowed distance from the laser-target interaction point to the first quadrupole is 50 mm, the minimum allowed distance between each quadrupole is 40 mm, and the distance between the target and the ESS entrance has been fixed at 2,05 m.

3.3.1 Reference trajectory definition in the ESS

The first thing done before starting simulations with realistic TNSA beams, is the check of the reference trajectory in the field maps of the ESS dipoles and the eventually high order effects of the magnetic field on the beam. This control has been performed using a probe beam with no divergence made of 100 particles set on a 30 mm diameter circumference; an additional particle at the centre of the circle has been added, which represents the reference particle. This control has been performed for different energies in the range between 5 and 60 MeV; according the energy to be transported in the magnetic chicane, the correct field maps have been calculated in COMSOL using the curve in Figure 3.2 bottom-right panel. As expected, the beam dynamics does not change with the energy if the magnets are properly tuned and, as an example, only the result for 60 MeV is reported in Figure 3.24.

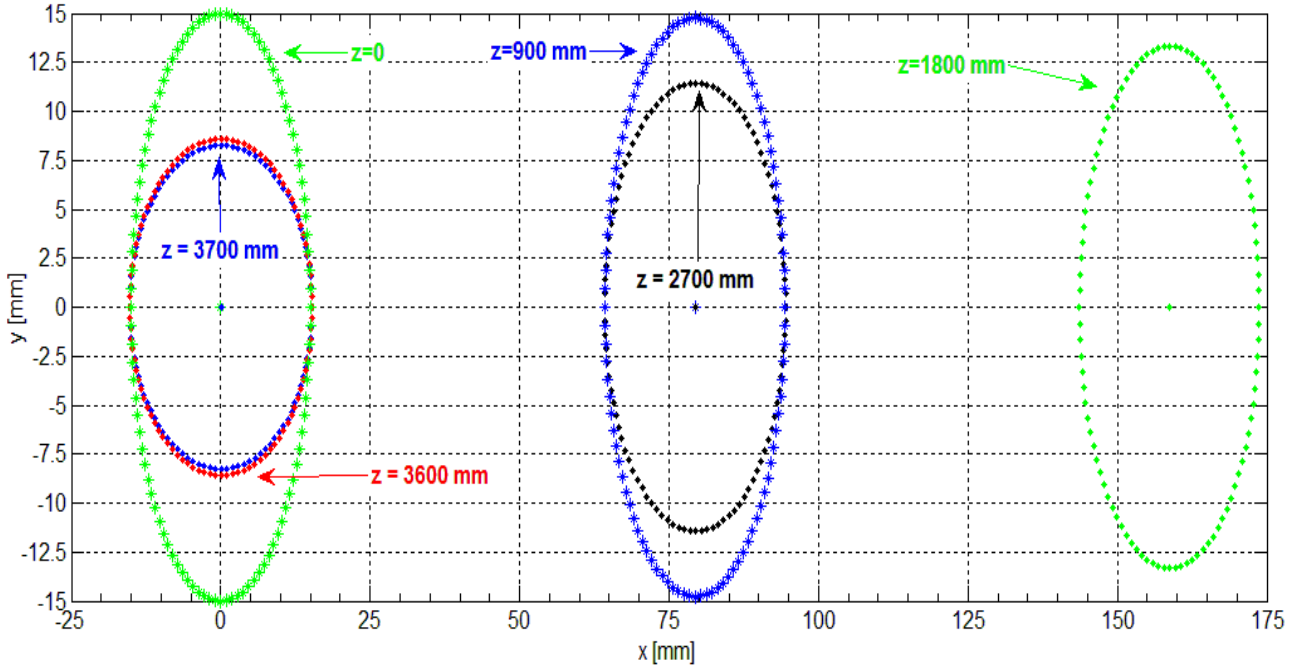

***Figure 3.24**: Probe beam profile at the beginning and at the end of each field map, x and y axes are in different scales.*

The probe beam is analysed in 6 different position: at the ESS entrance (z=0), at the output (z=3700 mm) and between each field maps, displaced in the simulation as in Figure 3.12. The

reference particle (at the centre of the circle) follows the design reference trajectory, the maximum deflection at the centre of the chicane is 160 mm but there is a small off set of 0,03 mm at the exit. The magnetic field does not change the radial beam diameter while the transverse diameter is considerably reduced form 30 mm to ~ 16 mm at the ESS exit. The focusing effect on the transverse plane is due to the fact that the dipole edges are perpendicular to the beam only at the entrance and exit of the chicane and in the central drift, in the first and last drift the beam makes an angle of 10,10° with the edge normal direction. This edge focusing effect is useful in this case, as discussed above. This demonstrate the good quality of the ESS optics.

3.3.2 60 MeV protons

The beam envelope is shown in Figure 3.23. The monochromatic simulations gives a transmission efficiency of 10%, with the losses basically limited in the PMQs system. The output beam (at 6,05 m from the target and 500 mm downstream the ESS output) is shown in the phase space plot in Figure 3.25.

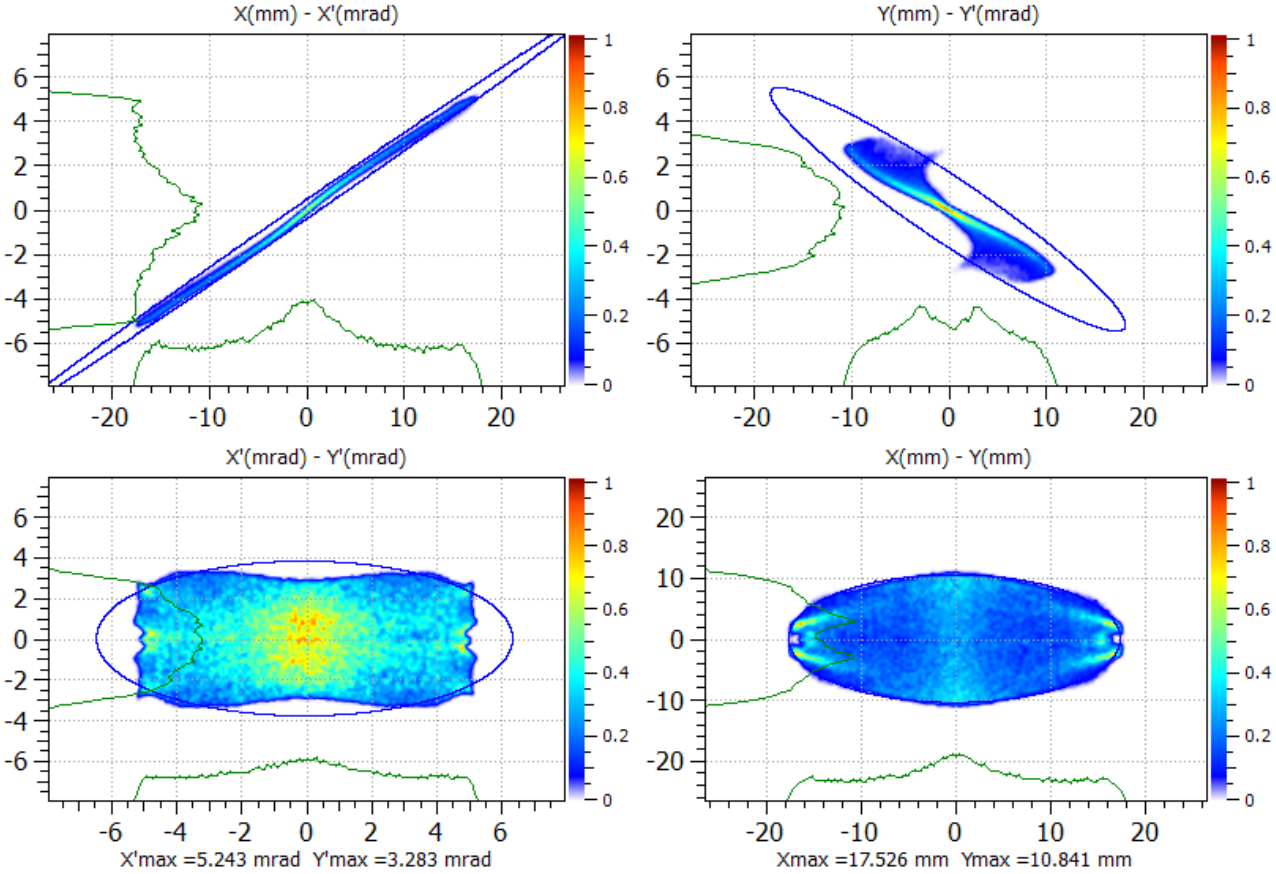

***Figure 3.25**: Phase space plot of the 60 MeV monochromatic proton beams downstream the ESS.*

The beam parameters are basically the same of those proposed in the PMQs feasibility study report. The beam divergence is considerably reduced to 0.3°, which makes it possible to transport and shape the beam using the conventional quadrupoles. The filamentations of the beam are due to the natural field uniformity of the PMQs.

For this energy case, simulations with more realistic protons have been considered with the same TNSA-like beam used in the PMQs feasibility study reported in the previous chapter. The input spectrum is exponential, as provided by the client and the beam divergence is uniform distribution between 0° and the maximum angles associated to each energy, as retrieved from the client's data.

Figure 3.26 shows the PIC (Particle in Cell)-simulated angular distribution (blue dots) and the function used to fit those data and reproduce the angles (red dots). The plot represents the half-angle distribution.

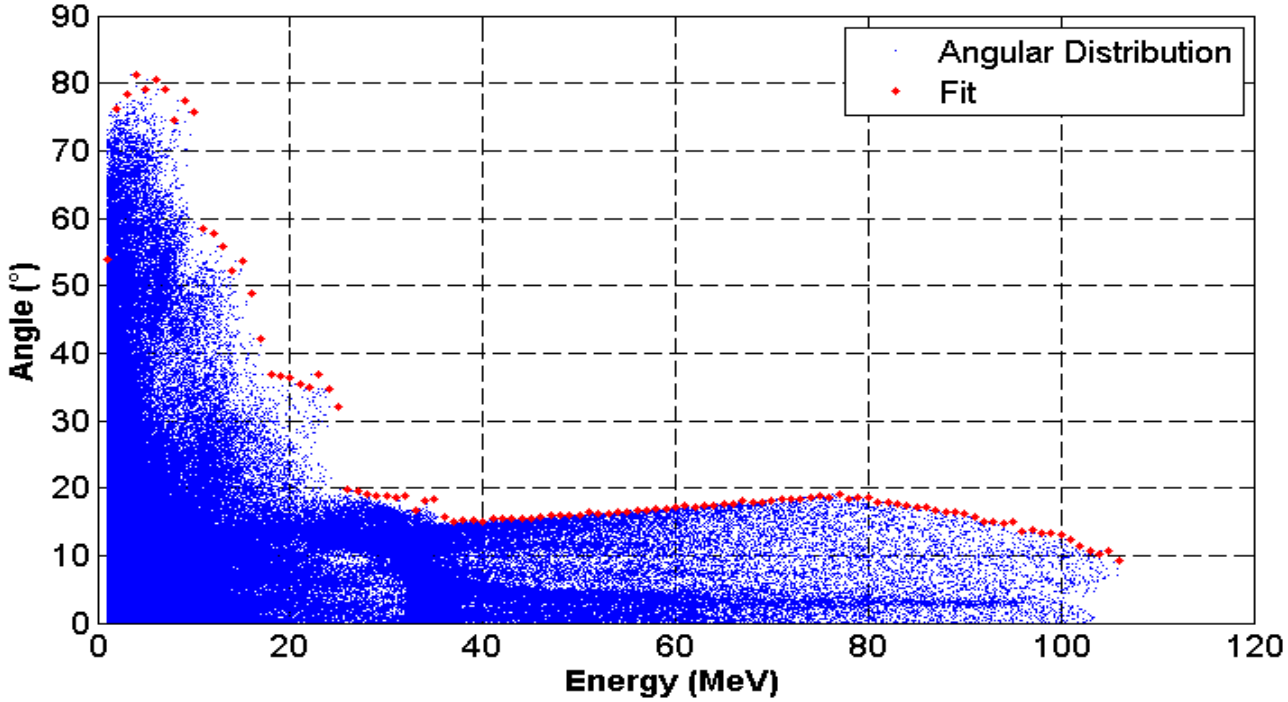

***Figure 3.26**: Provided angular distribution (blue dots) and function used as reference (red dots).*

The beam tracking with the TNSA-like beam along the beam-line is shown in Figure 3.27. In the upper part of the figure is shown the particle tracking along the beam-line while the lower part is a

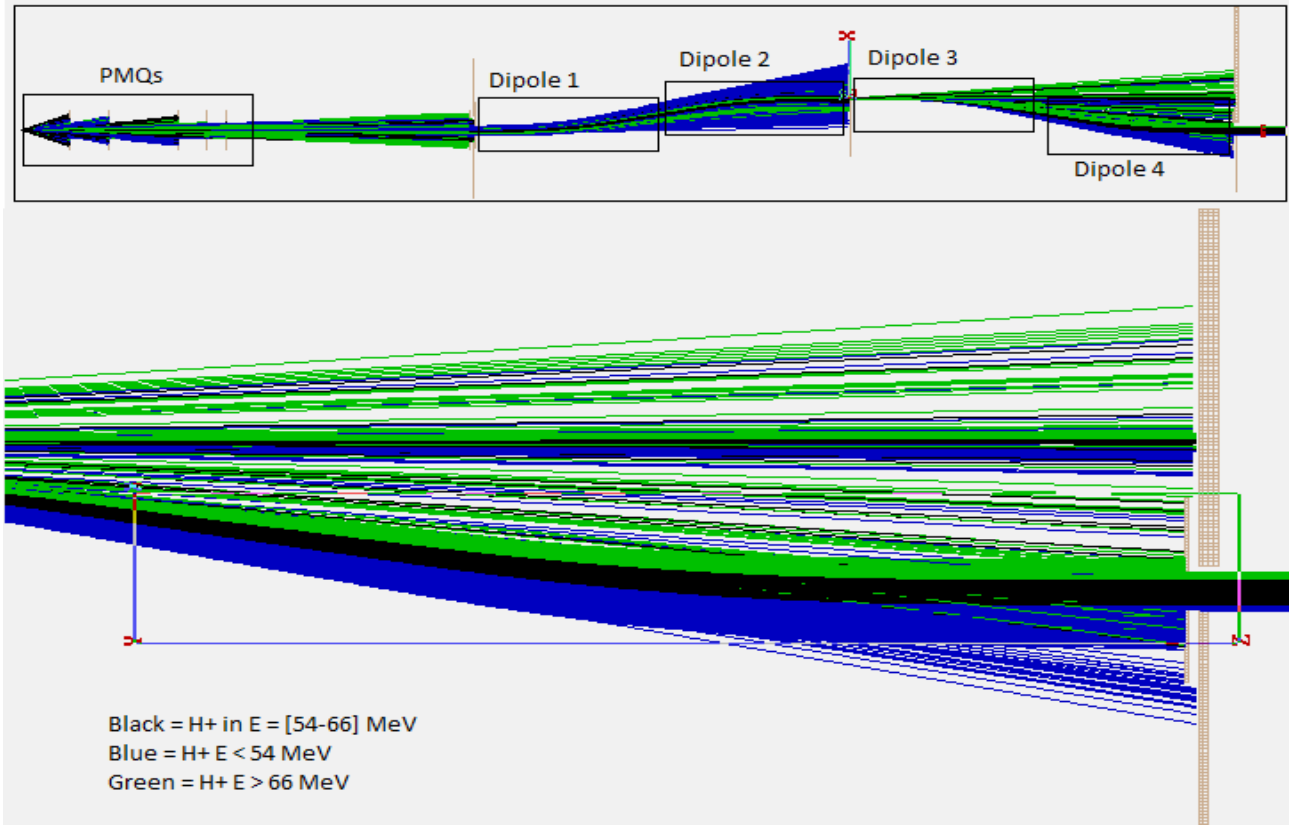

***Figure 3.27**: TNSA-like protons motion in the beamline.*

magnification of the last section of the beam-line. Particles are in different colours, those in the energy range of interest are in black. It is evident that the beam in the third dipole is quite small but the spectrum is still large. Hence, the particles have to be further dispersed and the last collimator is necessary to refine the selection. This demonstrates that four dipoles are necessary to properly select the beam.

Figure 3.28 shows the normalized spectrum at different positions along the beam-line and also a comparison with the output spectrum coming from the previous simulations in which the ESS was considered as a simple collimator system, green dots in the plot. The new output spectrum results to be selected with the required energy spread of the 20% and it is just a portion of the output spectrum proposed in PMQs feasibility study report, as expected. In the plot, the red line is the laser-accelerated spectrum and the red dots marks the energy range to be selected, the black line is the spectrum transmitted by the PMQs system, the blue line is the spectrum at the selection plane, just before the slit, and the green line is taken at the ESS exit. The transmission efficiency in this range is of about 4%.

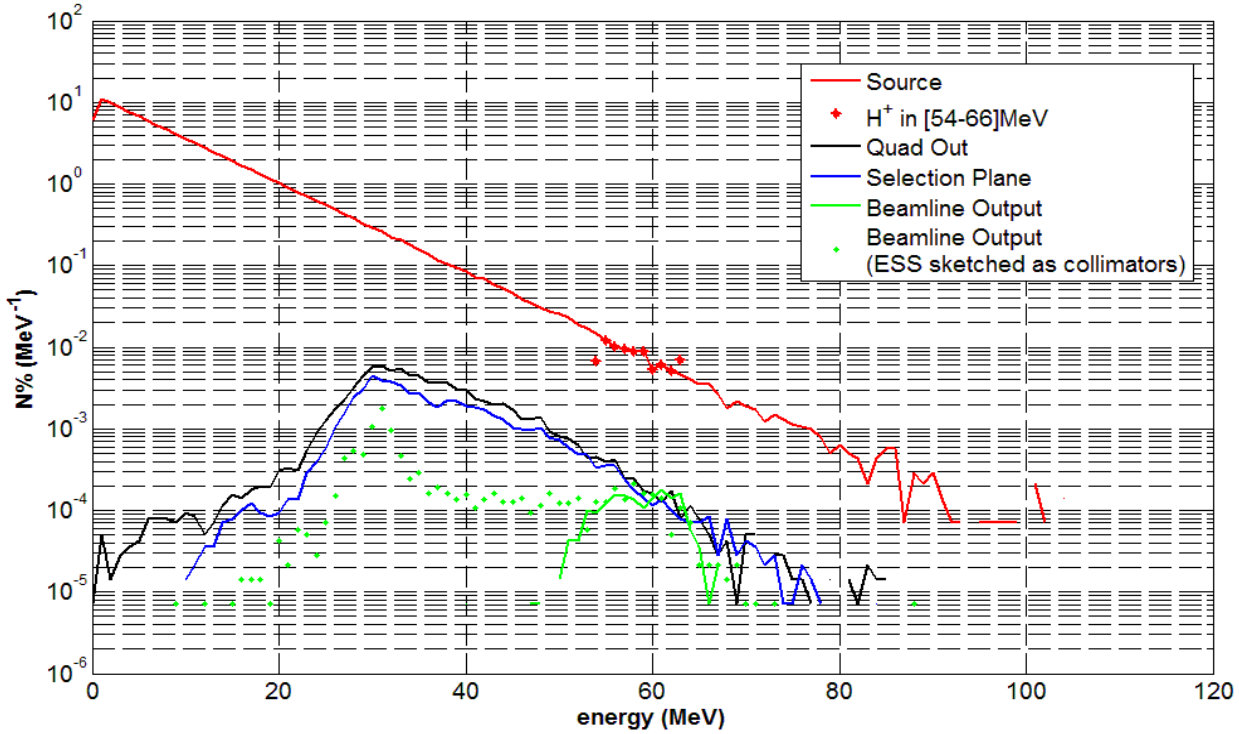

***Figure 3.28**: Particle spectrum at different positions along the beam line.*

The maximum divergence of the beam in the energy range of interest is bigger than ±15°, see Figure 3.26, and this limits the beam-line performances also because of the uniform angular distribution considered in the simulation. In the real case the angular divergence is gaussian with a certain full width half maximum smaller than 15°. As an example, a portion of the energy spectrum has been considered at the beam-line input and the angular distribution has been modelled with a gaussian function. In this case the energy range in input is slightly bigger than the output spectrum in Figure 3.28, namely between 50 and 68 MeV and the angular distribution has a FWHM of 5°. Using this approximation, the transmission efficiency of the beam line results to be of about 12% as shown in Figure 3.29.

The spectrum at the slit position, blue line in Figure 3.28, offers the possibility to select beams with different central energies with a change of the magnetic field in the ESS. Anyway the PMQs set up has to be properly studied in order to ensure a reasonable high transmission efficiency for

contiguous energy ranges without long displacements of the quadrupoles. In fact, some preliminary simulations, where the PMQs have a fixed setup, did not shown any significant result in this direction. The PMQs do not allow to use the ESS as an active energy modulator and a faster tunable collection system should be considered, such as a solenoid, as an upgrade of the beam-line.

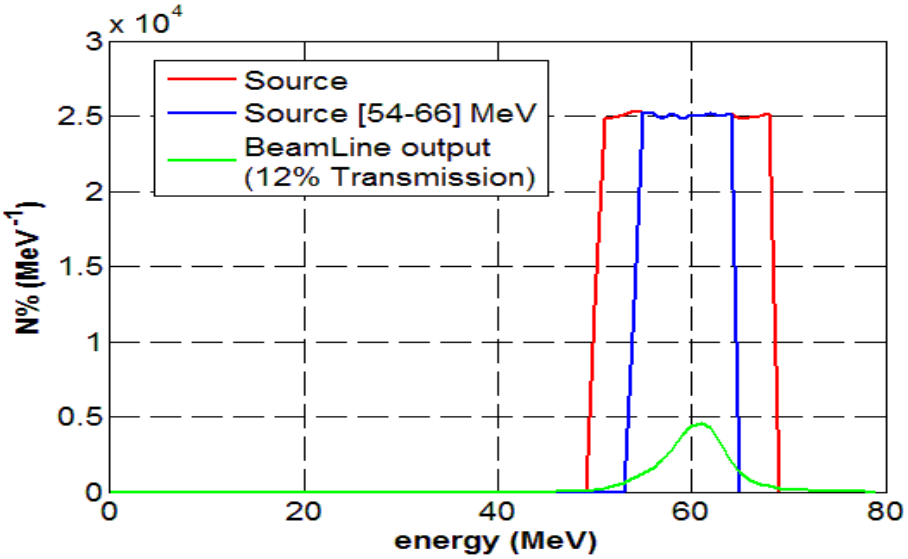

***Figure 3.29**: Particle spectrum simulated at the source (red and blue line) and selected spectrum (green line).*

3.3.3 30 MeV protons

The beam envelope is shown in Figure 3.30. Four quadrupoles are necessary to transport and inject protons from 30 to 10 MeV. The monochromatic simulations gives a transmission efficiency of 8%, with the losses basically limited in the PMQs system, a part from a small percentage in the

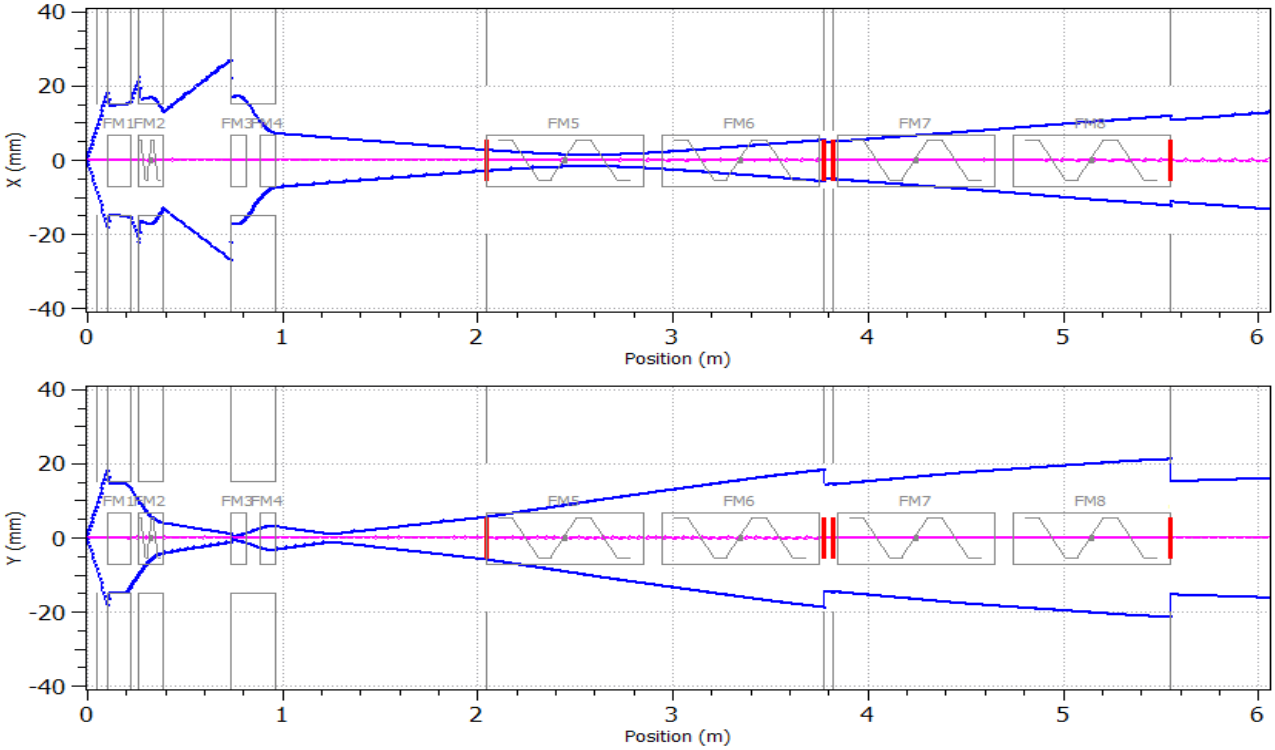

***Figure 3.30**: Scheme of the simulated beamline with envelope of 30 MeV protons.*

ESS due to a not perfect matching between the two systems. The output beam is shown in the phase space plot of Figure 3.31.

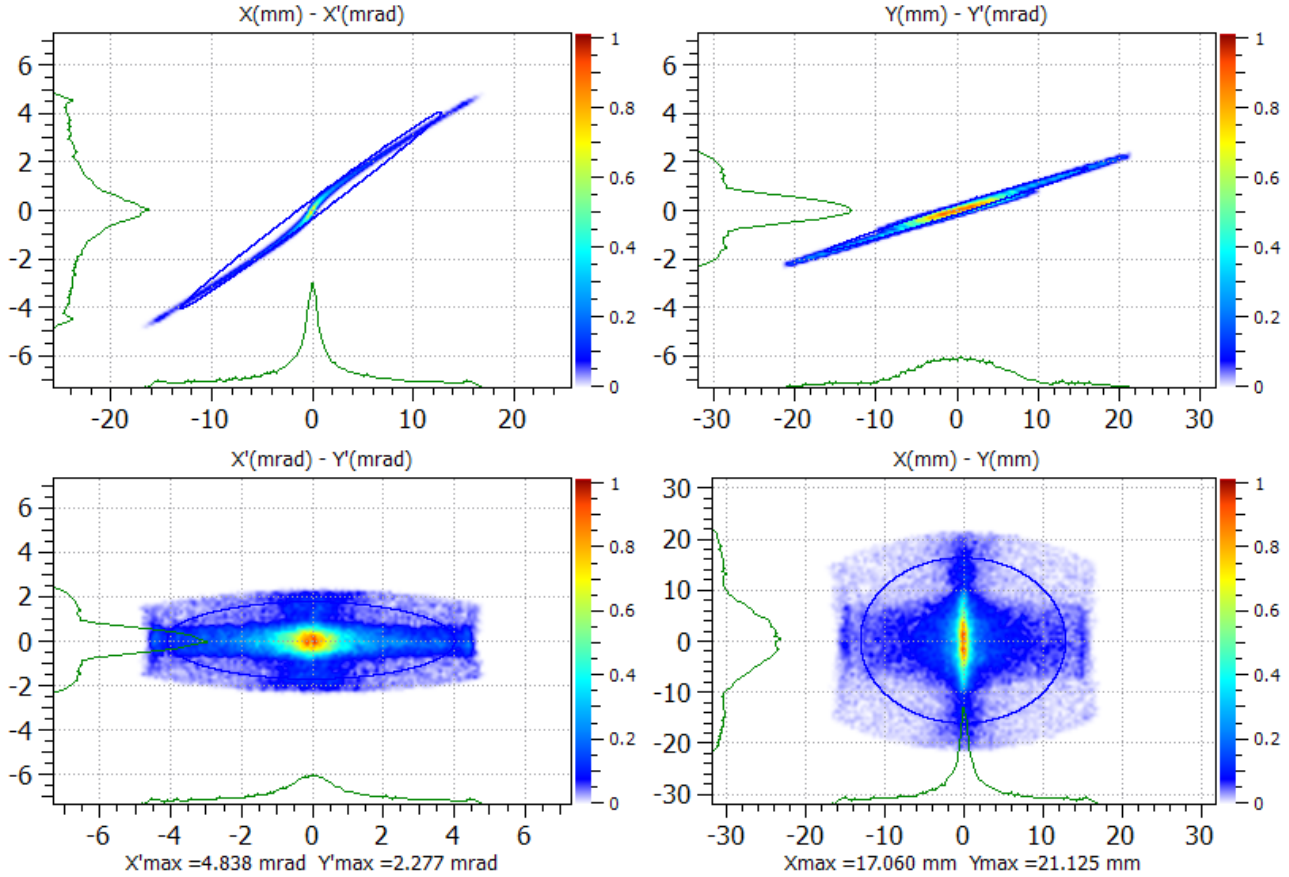

***Figure 3.31**: Phase space plot of the 30 MeV monochromatic proton beams downstream the ESS.*

The beam parameters are basically the same of those proposed in the PMQs feasibility study report. The beam divergence is considerably reduced to 0.3°, which makes it possible to transport and shape the beam using the conventional quadrupoles. The filamentations of the beam are due to the natural field uniformity of the PMQs.

For this energy case, simulations with more realistic protons have been considered with the same TNSA-like beam used in the PMQs feasibility study report. Results are resumed in Figure 3.32. The new output spectrum results to be selected with the required energy spread of the 10% and it is just a portion of the output spectrum proposed in PMQs feasibility study report, as expected. In the plot, the red line is the laser-accelerated spectrum and the red dots marks the energy range to be selected, the black line is the spectrum transmitted by the PMQs system, the blue line is the spectrum at the selection plane, just before the slit, and the green line is taken at the ESS exit. The transmission efficiency in this range is of about 6%.

Again, for the energy under consideration, a portion of the energy spectrum has been considered at the beam-line input and the angular distribution has been modelled with a gaussian function. In this case the energy range in input is slightly bigger than the output spectrum in Figure 3.32, namely between 24 and 35 MeV and the angular distribution has a FWHM of 5°. The transmission efficiency of the beam line results to be of about 14% as shown in Figure 3.33.

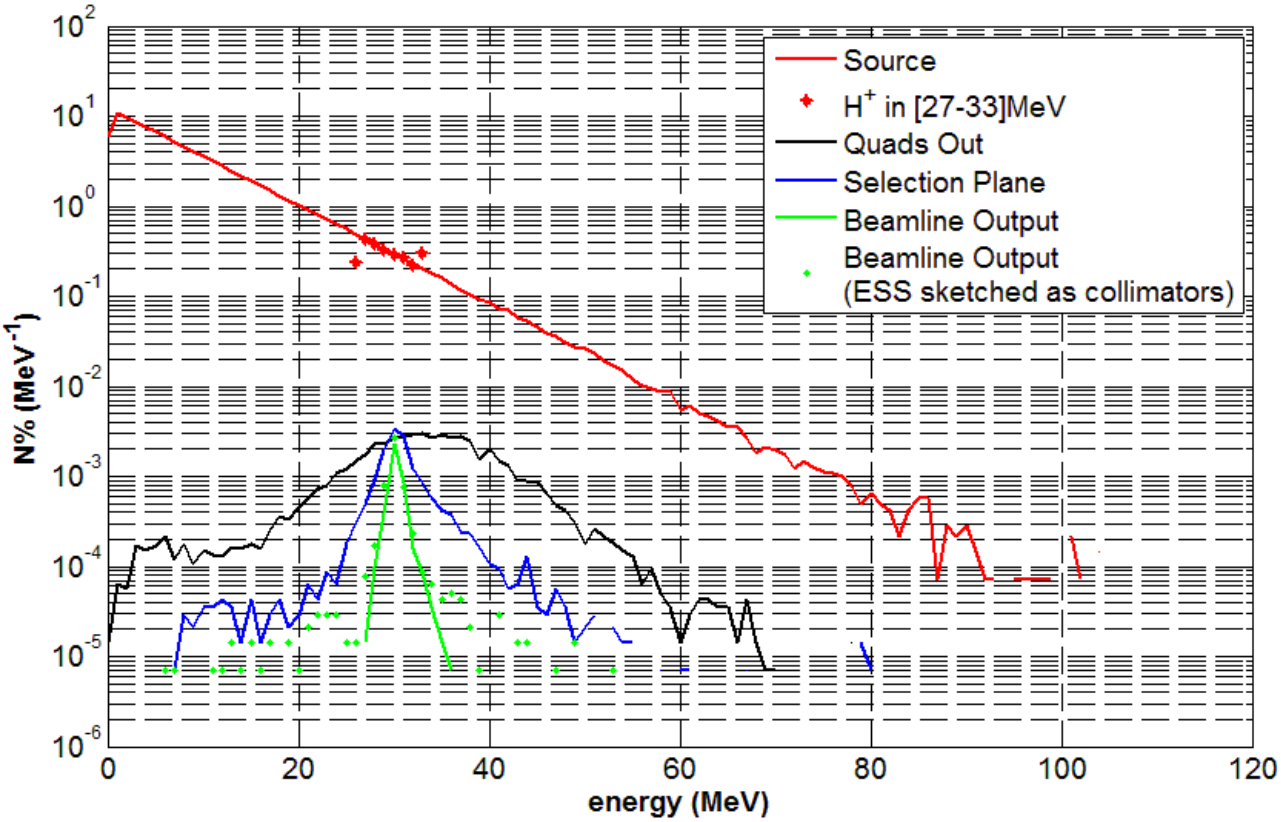

***Figure 3.32**: Particle spectrum at different positions along the beam line.*

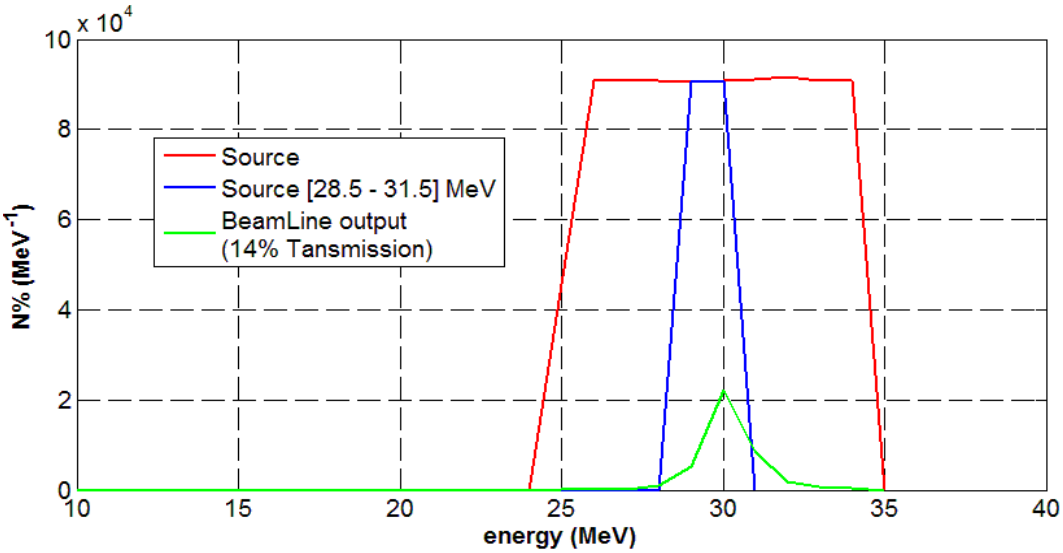

***Figure 3.33**: Particle spectrum simulated at the source (red and blue line) and selected spectrum (green line).*

3.3.4 5 MeV protons

The beam envelope is shown in Figure 3.34. Three quadrupoles are necessary to transport and inject protons with energies lower than 10 MeV. The monochromatic simulations gives a transmission efficiency of 1%, but in this case the half angle divergence is of about 15° (uniform distribution) and the injection is not properly optimized. The output beam is shown in the phase space plot of Figure 3.35.

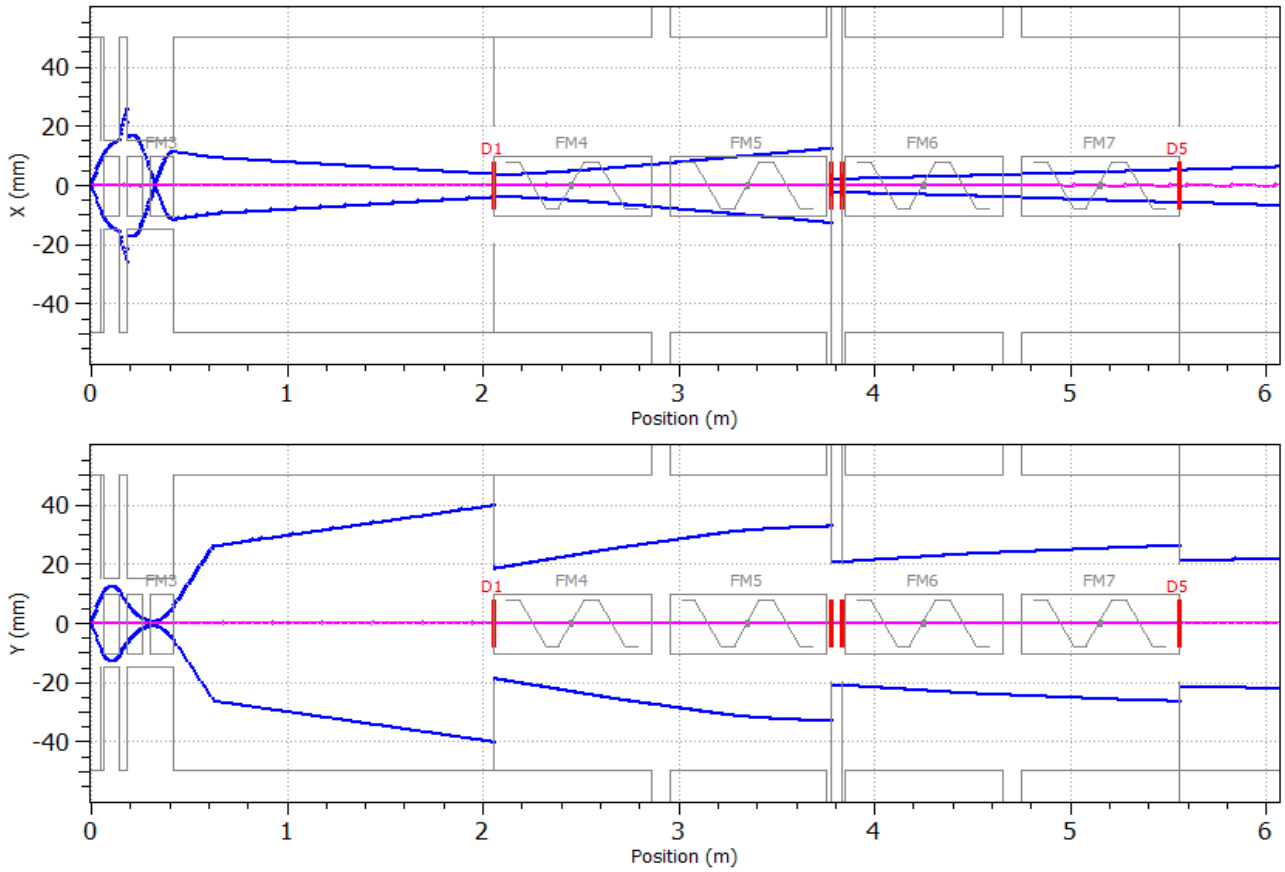

***Figure 3.34**: Scheme of the simulated beamline with envelope of 5 MeV protons.*

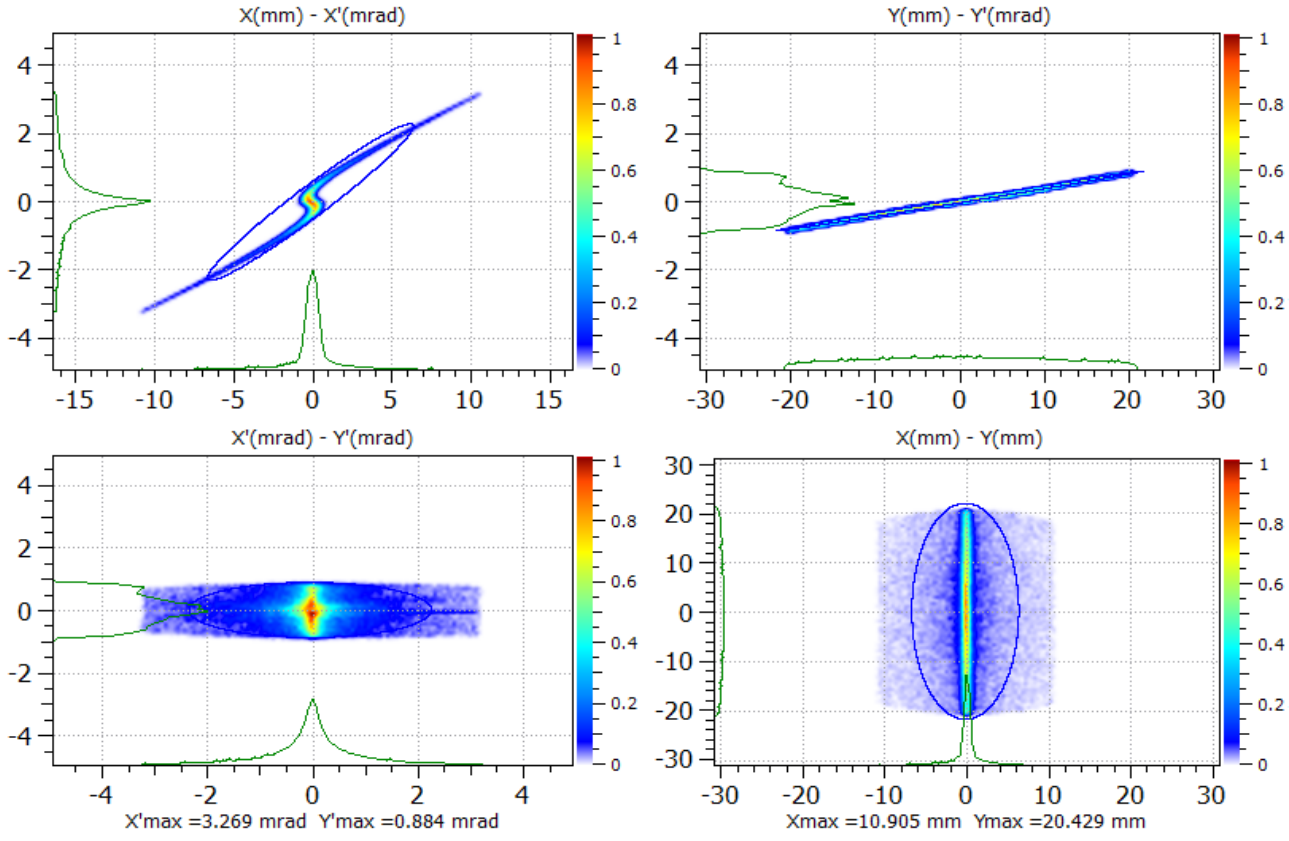

***Figure 3.35**: Phase space plot of the 5 MeV monochromatic proton beams downstream the ESS.*

As can be seen the beam divergence is considerably reduced to 0.23°, which makes it possible to transport and shape the beam using the conventional quadrupoles. The filamentations of the beam are due to the natural field uniformity of the PMQ.

Simulations with more realistic spectrum, as described in the previous section, have been performed and resumed in Figure 3.36, where only a small part of the spectrum is plotted. The new output spectrum results to be selected with the required energy spread of the 5% and it is just a portion of the output spectrum proposed in PMQs feasibility study report, as expected. In the plot, the red line is the laser-accelerated spectrum and the red dots marks the energy range to be selected, the black line is the spectrum transmitted by the PMQs system, the blue line is the spectrum at the selection plane, just before the slit, and the green line is taken at the ESS exit. The transmission efficiency in this range is well below to the 1%. It is due to the big angular diverge of low energy particles, which is considered uniformly distributed between 0° and 70°, see Figure 3.26.

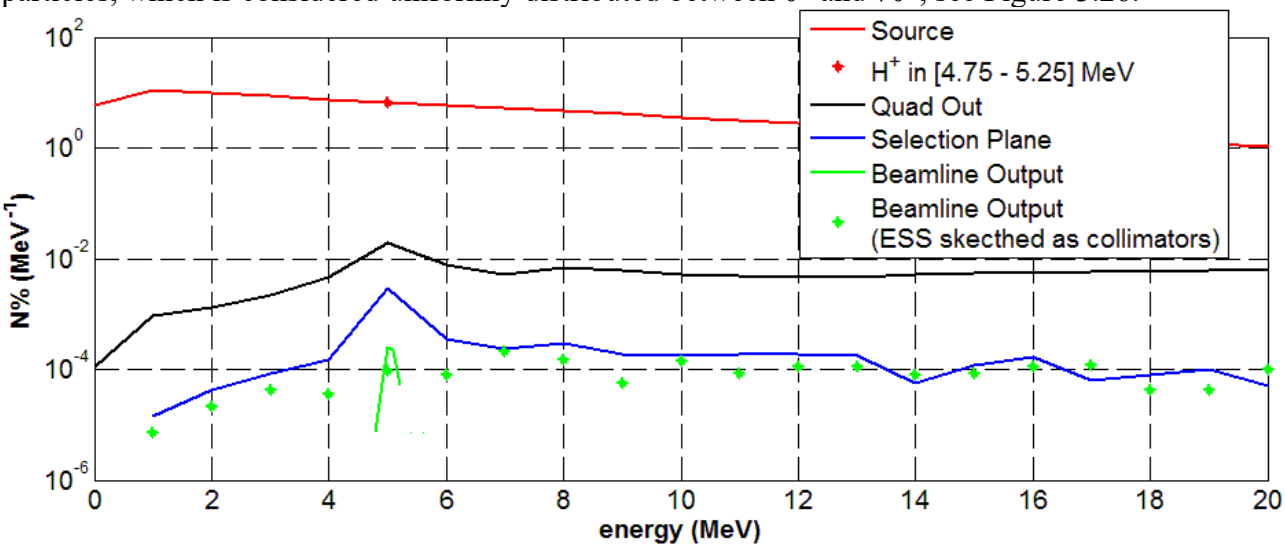

***Figure 3.36**: Particle spectrum at different positions along the beam line.*

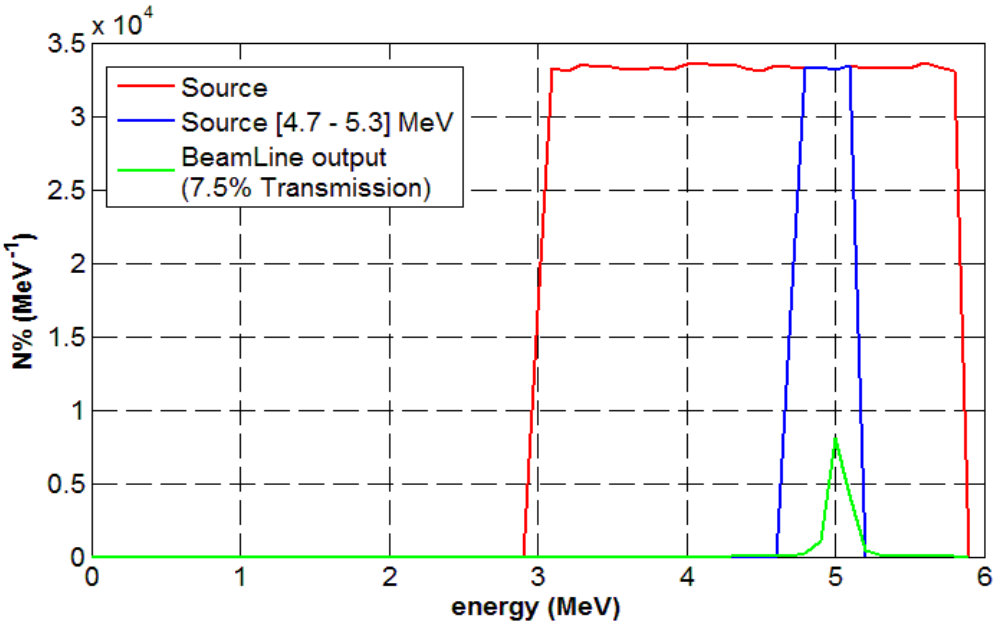

***Figure 3.37**: Particle spectrum simulated at the source (red and blue line) and selected spectrum (green line).*

Again, for the energy under consideration, a portion of the energy spectrum has been considered at the beam-line input and the angular distribution has been modelled with a gaussian function. In

this case the energy range in input is slightly bigger than the output spectrum in Figure 3.36, namely between 3 and 6 MeV and the angular distribution has a FWHM of 5°. In this case the transmission efficiency of the beam line results to be of about 7,5% as shown in Figure 3.37.

These results, especially the lowest energy case can be improved working on the optics simulations, that have to be considered preliminary as the injection in the ESS can be further optimized. The output beam has anyway good features in terms of divergence and energy distribution and can be shaped by a set of conventional resistive quadrupoles that have to be defined starting from the presented results.

3.3.5 60 MeV/u carbon ions (C^{+6})

The system performances have been studied for other ion species and results for monochromatic C^{+6} at the maximum energy of 60MeV/u are here reported.

The beam envelope is shown in Figure 3.38, the output beam is shown in Figure 3.39. Four quadrupoles are required to inject the beam in the ESS. The transmission efficiency of the whole beamline is of about 4%, which is enough to guarantee the minimum number of particles transmitted. The angular spread is limited to ~0.3°.

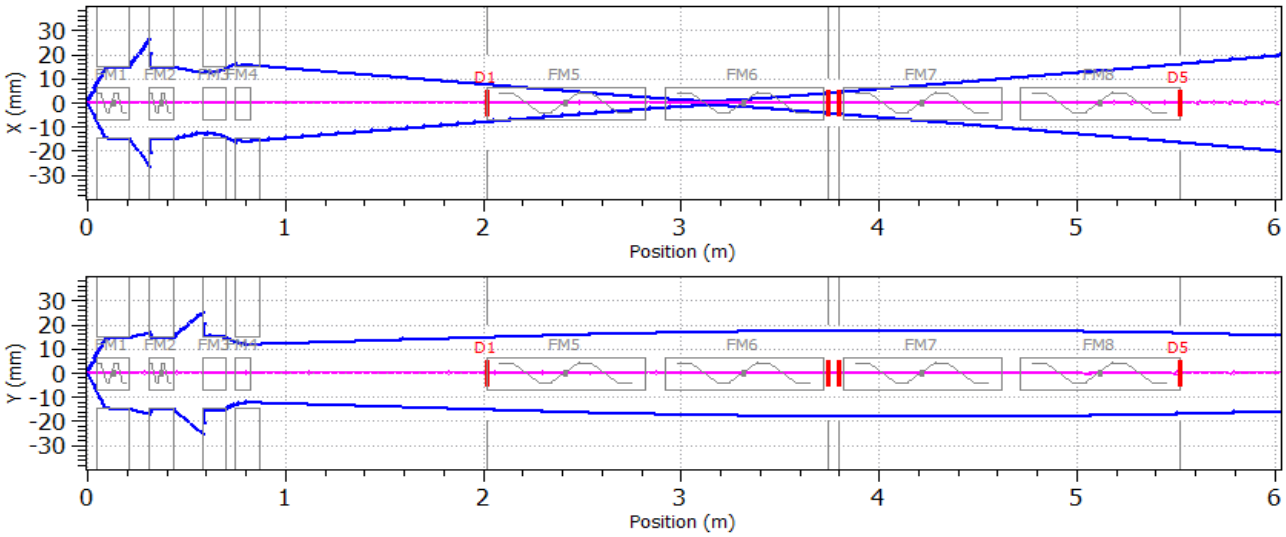

***Figure 3.38**: Scheme of the simulated beamline with envelope of 60 MeV/u C^{+6}.*

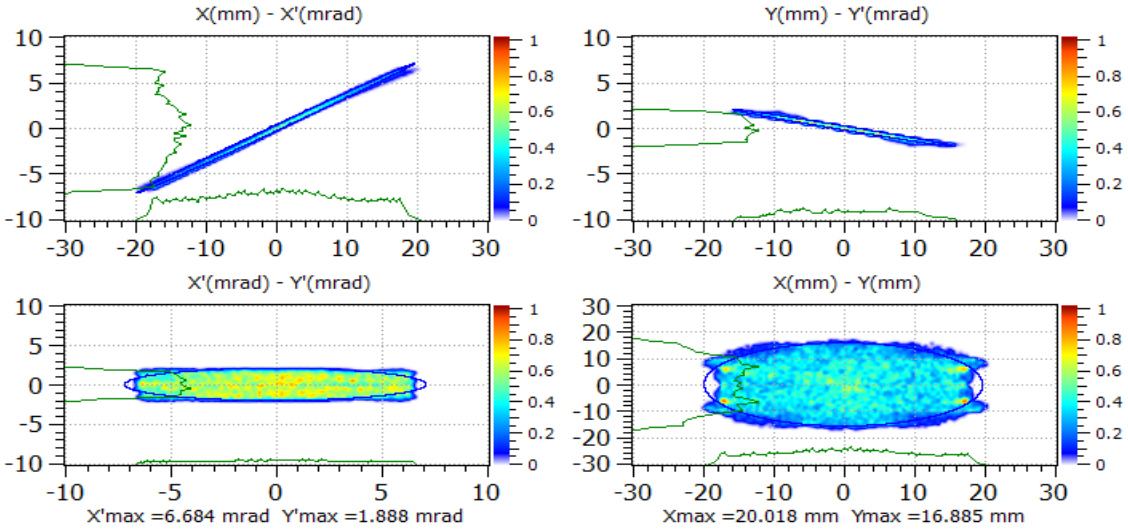

***Figure 3.39**: Phase space plot of the 60 MeV/u monochromatic C^{+6} beams downstream the ESS.*

3.3.6 Summary of output beam features

Reference Energy	Spread (slit size)	Losses	Beam - spot	Emittance (Pi.mm.mrad) [Norm]
60 MeV	20% (20 mm)	87,3% if angular spread has 5° FWHM	X radius: 15 mm Y radius: 12 mm	XX'=0,4142 YY'= 0,9158
30 MeV	10% (8 mm)	86% if angular spread has 5° FWHM	X radius: 14,6 mm Y radius: 15 mm	XX'=0,3272 YY'= 0,2114
5 MeV	5% (4 mm)	92,5% if angular spread has 5° FWHM	X radius: 9,2 mm Y radius: 15 mm	XX'=0,0939 YY'= 0,0313

3.4 Beam-line error study

The ELIMAIA beam transport line will have a total length of 9 m at maximum (the in-air part is not taken into account) and alignment is not critical for such a short line. The most critical part is the injection of the beam in the magnetic chicane, but, due to the ESS large acceptance, a precision of few hundreds of microns in the positioning of magnetic lenses will be enough to ensure the good functioning of the line. Moreover, positioning errors are systematic errors in the beam-line and the possible problems can be easily fixed improving the alignment during the commissioning phase or with small changes of the magnetic field of the electromagnets (ESS dipoles, steerers and resistive quadrupoles). On the other hand, random errors on the source centering and pointing cannot be handled easily and their effect on the beam optics has been evaluated.

According to preliminary study on L3 laser and L3 laser beam transport, the laser focal spot position on target is fluctuating within ±4 μm (centering error) and the pointing errors are fluctuating within ±400 μrad, which means that the beam can have an alignment error up to 50 μm on the first quadrupole and up to 400 μm on the last one. These errors are random with unpredictable shot-to-shot fluctuations and are comparable or bigger than tolerances established for the PMQs hence, the effects on the beam line have been evaluated in different steps:

step 1: each error source (centering and pointing) has been evaluated independently along the horizontal *x* axis and vertical *y* axis;

step 2: the errors on the centering, or on the pointing, have been evaluated on the target plane combining the errors on the two axis

step 3: errors on the target plane coming from the centering and the pointing have been combined

These results have been compared, for the 60 MeV proton beam, with the beam features in the case of no errors, namely the simulations proposed in the previous section for monochromatic protons. The beam here has a gaussian distribution of the particles in terms of divergence and spot size. The references details for the 60 MeV proton case are reported below. In particular we are interested on the particle losses which are 87,3%, on the beam centroid position and angle with respect to the beam-line axis (listed in table) and on the beam emittance growth evaluated as:

$$\frac{\Delta\epsilon}{\epsilon_i}=\frac{\epsilon_o-\epsilon_i}{\epsilon_i}=\begin{cases}38\%\,\epsilon_{XX'}\\204\%\,\epsilon_{YY'}\end{cases}$$

being ε_i the input beam emittance and ε_o the output beam emittance.

Beam centroid position and angle at the ESS output			
dx [mm]	**dx' [mrad]**	**dy [mm]**	**dy' [mrad]**
0.024	-0.032	0.017	0.0037

The huge emittance growth is related to the wide beam divergence and, as a consequence its big spot size within the PMQs which causes beam filamentations due to higher order harmonics close to the bore edge. This is anyway not an issue as the magnetic chicane has been designed with a very large acceptance and the beam emittance matches the ESS parameters listed in the table at page 70. The emittance evolution of the beam along the beam-line is shown in Figure 3.40, it is referred to the reference case with no errors, and it is evident that the highest variations in the emittance are within the first section of the beam-line, namely within the PMQs. In the chicane, the variations are basically due to the edge focusing effect in the transverse directions. The drop of the emittance at

the end of the chicane is due to the last collimator which cuts part of the beam halo.

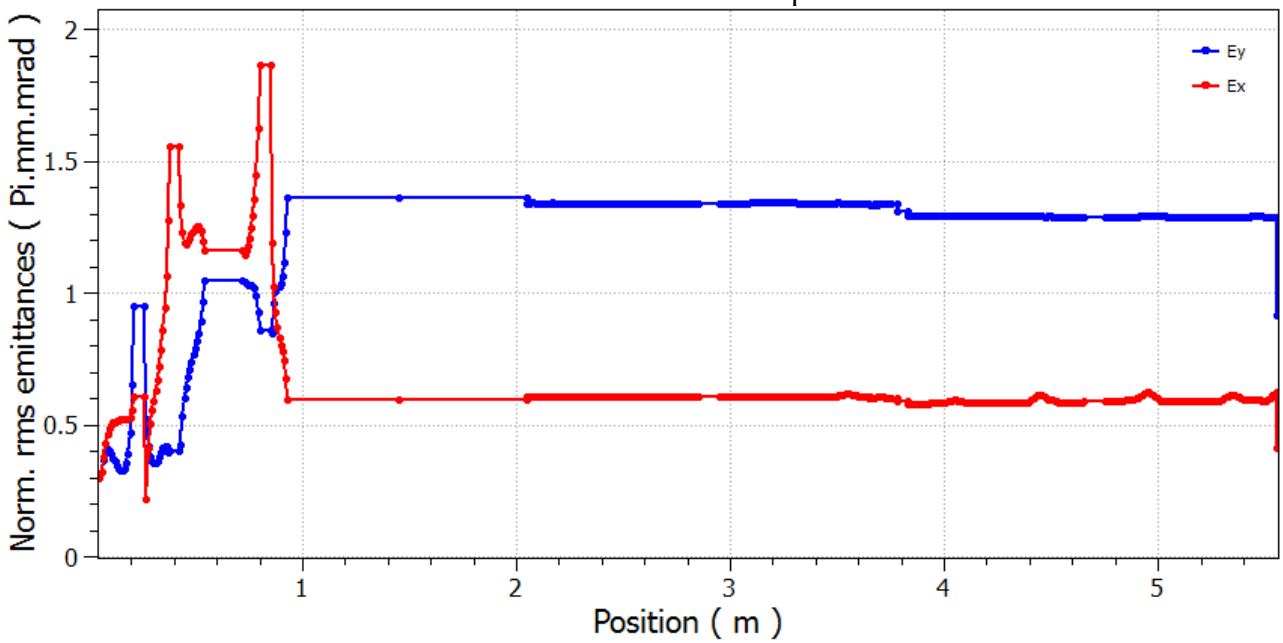

***Figure 3.40**: Beam emittances evolution in the beam-line. Red line represents $\varepsilon_{XX'}$ emittance, the blue line represents $\varepsilon_{YY'}$ emittance.*

The technique used to study the errors consists in fixing the maximum range of the error source (±4 μm for the centering and ±400 μrad for the pointing), then the range of variation is divided in intervals, or steps, centred on zero but with wider extension. A number of simulations is performed for each interval, extracting the error value in that interval. In this way it is possible to study how the errors affect the beam transport while they are growing up to their maximum value. In the presented study the errors variation range has been divided in 10 steps, which means that for each step the errors are increased by the 10% and for each step 100 beam-run simulations are lunched. The results are reported in the following.

3.4.1 Centering errors

Errors on the target centering are here analysed. The effects on the beam losses are summarized in the upper panel of Figure 3.41. The second and third panels report the errors effects on the growth of emittance in the radial and transverse plane. The blue line represents the case in which the errors are applied only to the x position of the target, the red line is the case for the y position of the target and the black line is the case in which the errors are in both directions at the same time.

The three plots in Figure 3.41 demonstrate that the target centering errors do not affect the beam-line transmission efficiency and also the emittance growth is not changed significantly.

The beam centroid position and angles are more sensitive to the target centering errors, as shown in Figure 3.42. The first and second panels describe the deviations of beam centroid position with respect to the reference axis, the third and fourth panels describe the beam centroid angle. Colour lines have the same meaning as before.

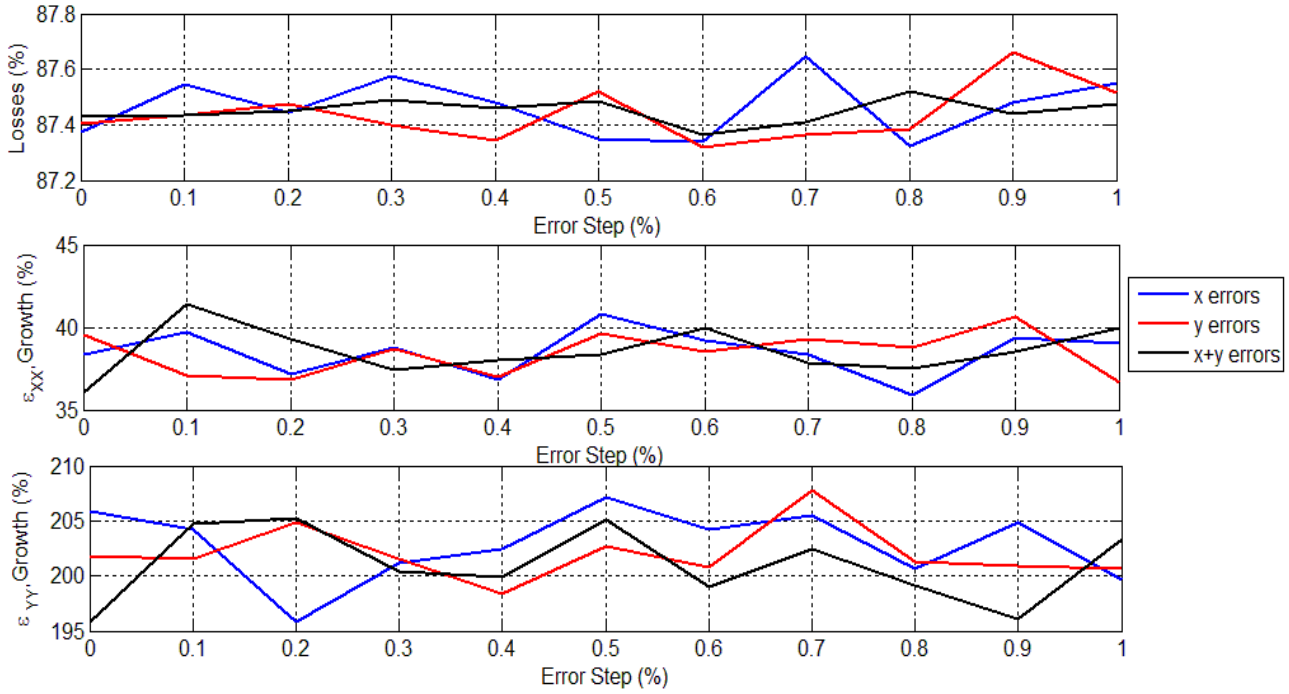

***Figure 3.41**: Target centering errors on the beam losses (upper panel) and emittace growth (middle and lower panel).*

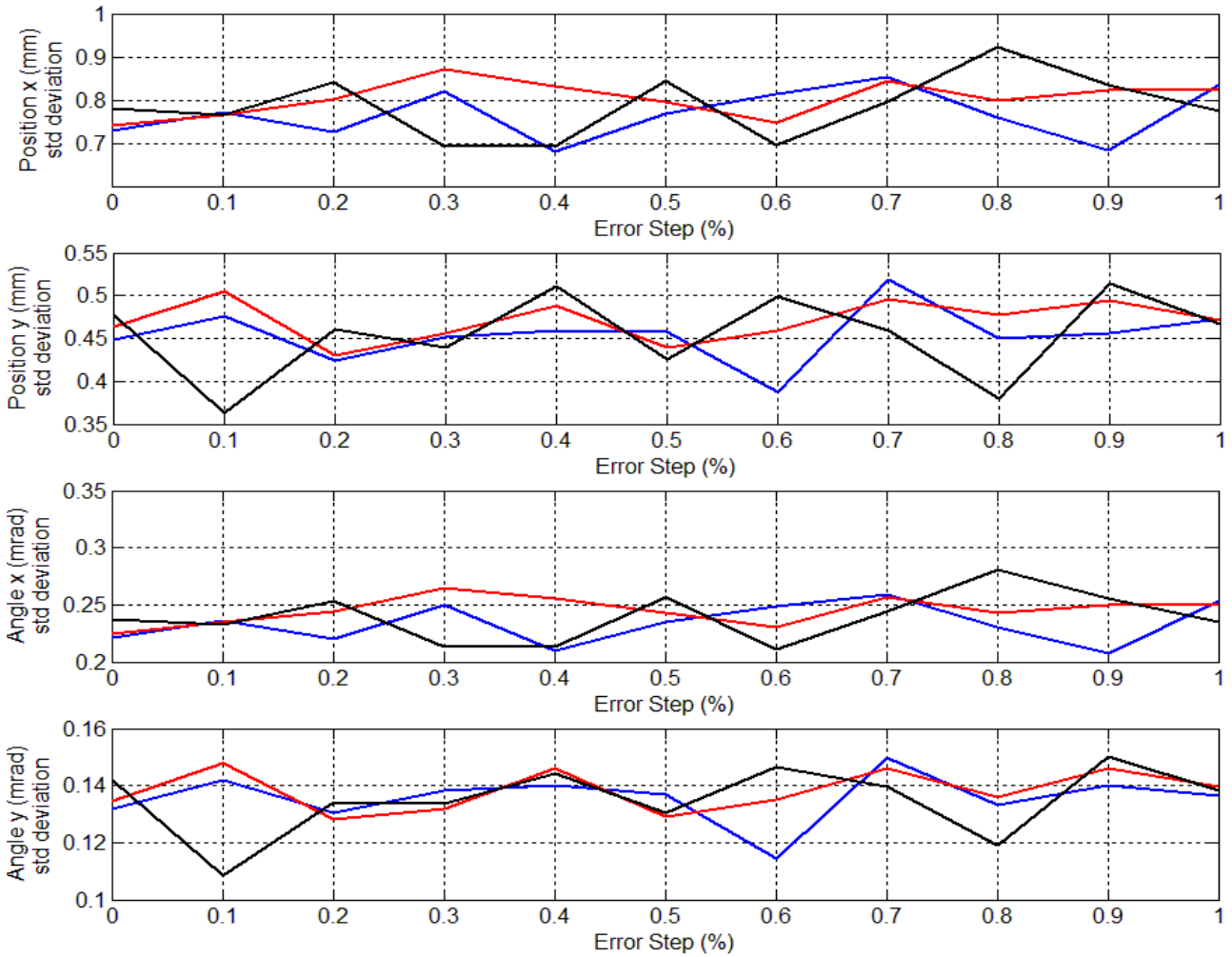

***Figure 3.42**: Target centering errors on the beam centroid position and angle.*

3.4.2 Pointing errors

Errors on the target pointing are here analysed. The effects on the beam losses are summarized in the upper panel of Figure 3.43.The second and third panels report the errors effects on the growth of emittance in the radial and transverse plane. Colour lines have the same meaning as before.

The three plots in Figure 3.43 demonstrate that the target pointing errors do not affect the beam line transmission efficiency and also the emittance growth is not changed significantly.

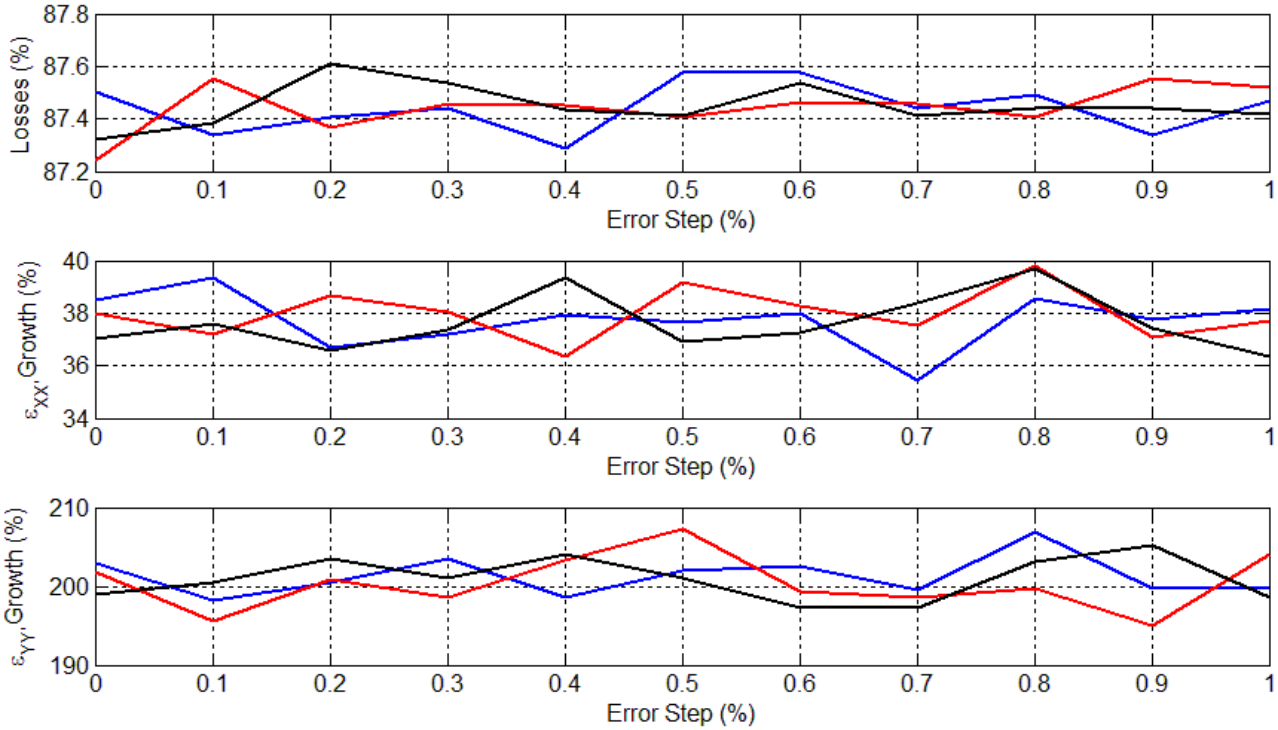

***Figure 3.43**: Target pointing errors on the beam losses (upper panel) and emittace growth (middle and lower panel).*

The beam centroid position and angles are more sensitive to the target pointing errors, as shown in Figure 3.44. The first and second panels describe the deviations of beam centroid position with respect to the reference axis, the third and fourth panels describe the beam centroid angle.

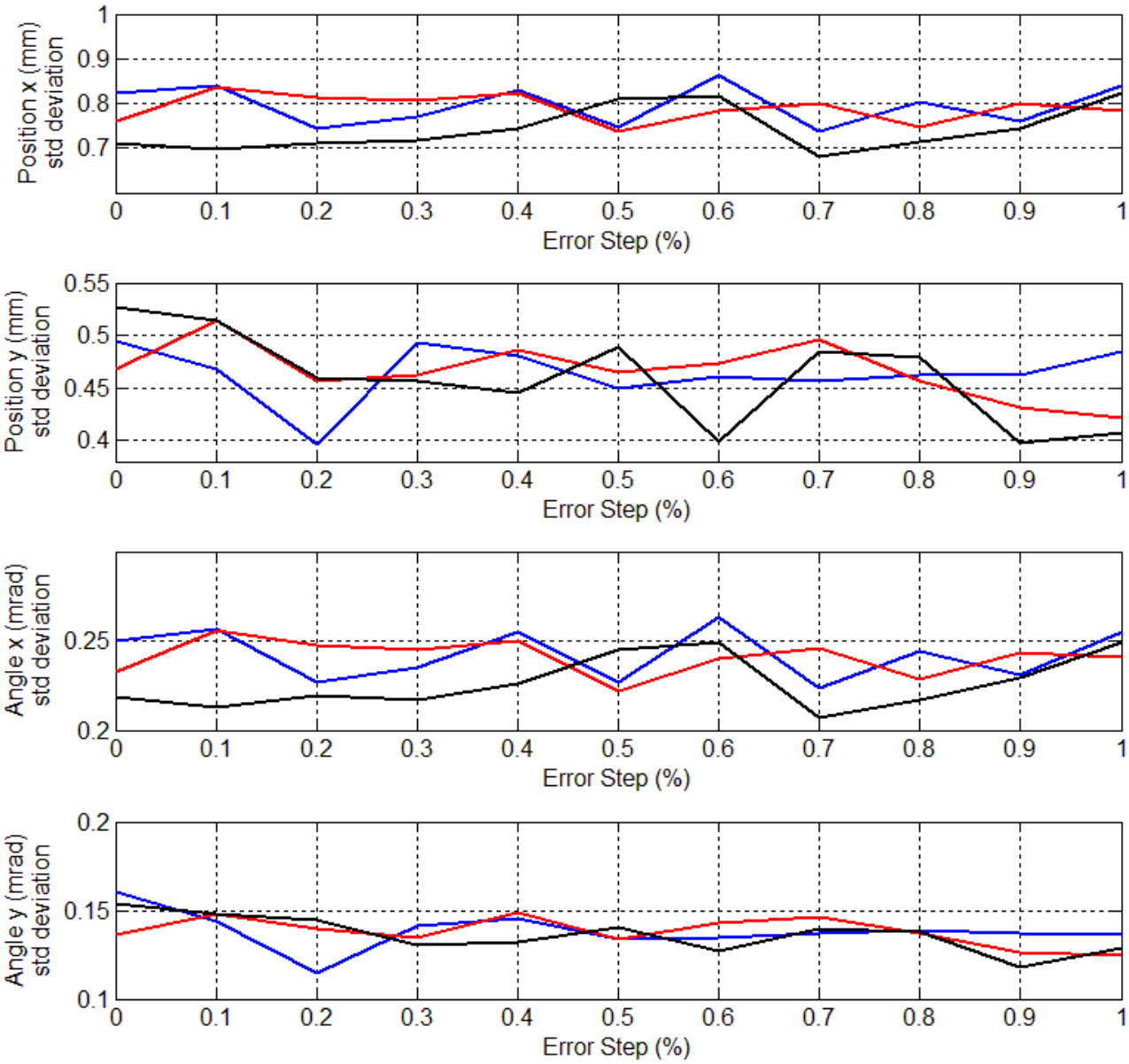

***Figure 3.44**: Target pointing errors on the beam centroid position and angle.*

3.4.3 Centering and Pointing errors

Errors on the target centering and pointing are here analysed. The effects on the beam losses are summarized in the upper panel of Figure 3.45.The second and third panels report the errors effects on the growth of emittance in the radial and transverse plane. Colour lines have the same meaning as before.

The three plots in Figure 3.45 demonstrate that the target pointing errors do not affect the beam line transmission efficiency and also the emittance growth is not changed significantly.

The beam centroid position and angles are more sensitive to the target errors, as shown in Figure 3.46. The first and second panels describe the deviations of beam centroid position with respect to the reference axis, the third and fourth panels describe the beam centroid angle. It should be underlined that the centroid position and angle errors are reduced in this case because combining the four errors sources there is a compensation effect that reduces the beam centroid off-set.

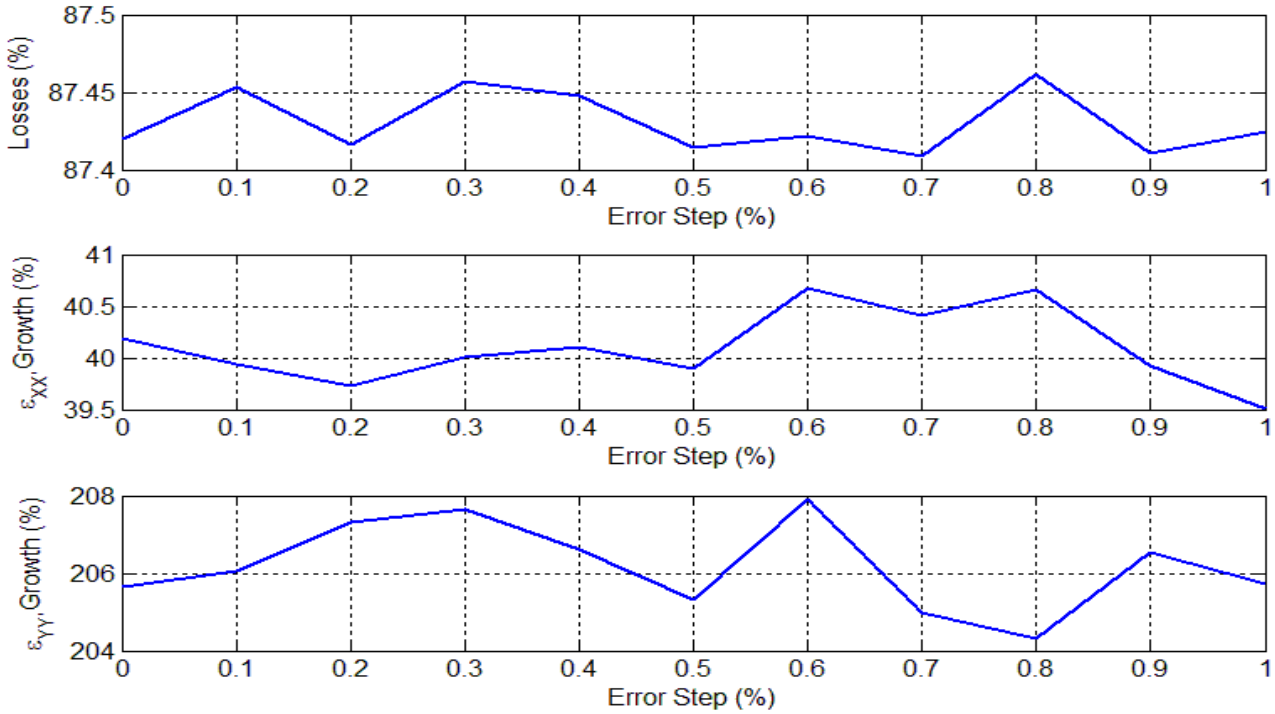

***Figure 3.45**: Target centering and pointing errors on the beam losses (upper panel) and emittace growth (middle and lower panel).*

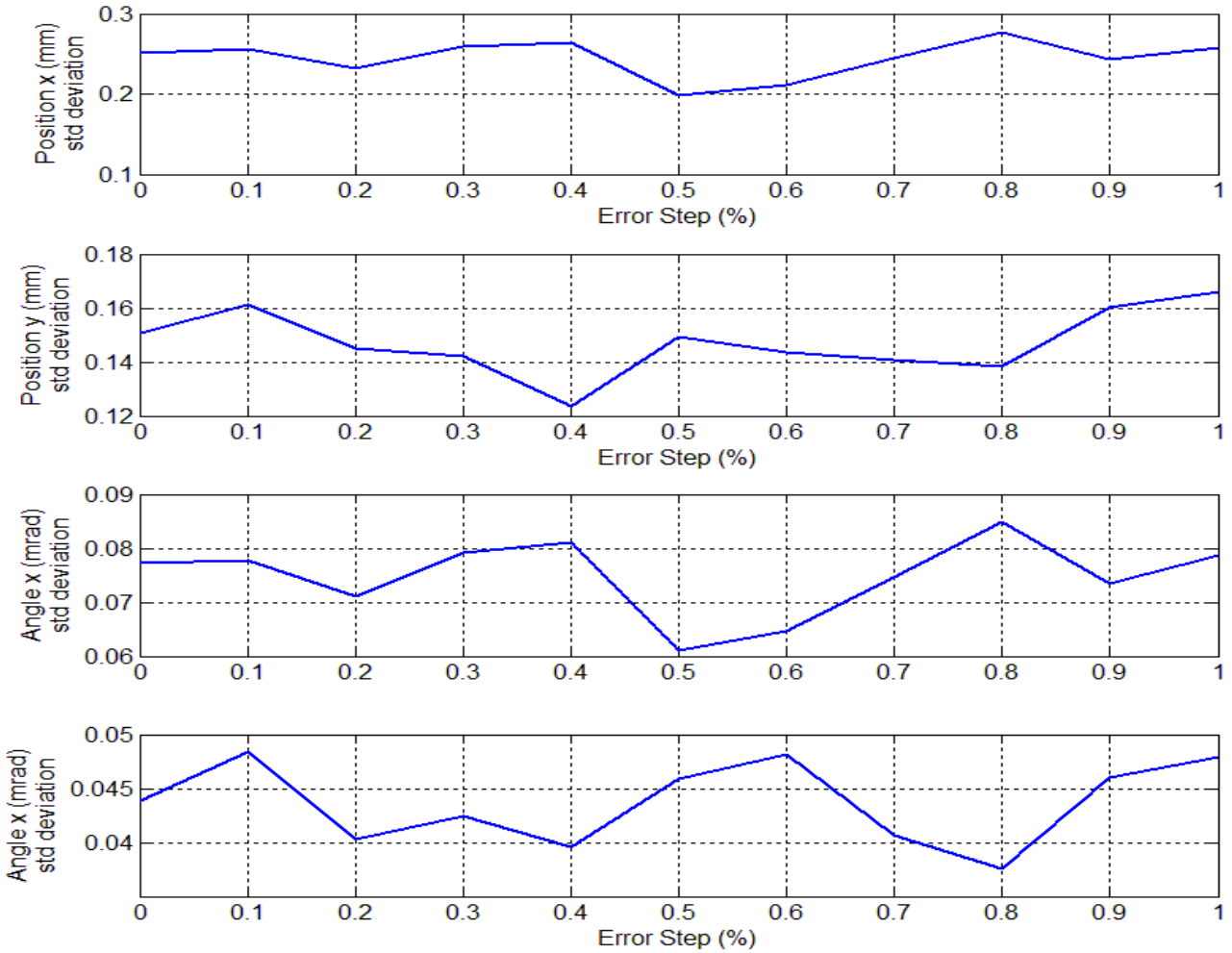

***Figure 3.46**: Target centering and pointing errors on the beam centroid position and angle.*

3.5 Final design, manufacturing and calibration of the energy selection system

The final design of the energy selector system was optimized in collaboration with the manufacturer (SigmaPhi) with the aim of respecting the field requirement but reducing power consumption. Moreover, the dipole design have been also slightly modified in order to reduce yoke saturation and guarantee mechanical stability of the vacuum chamber.

The dipole final design shows a different profile, optimized for focusing (and increasing) the magnetic field in the gap but also for reducing the saturation in lateral and longitudinal directions, see Figure 3.47

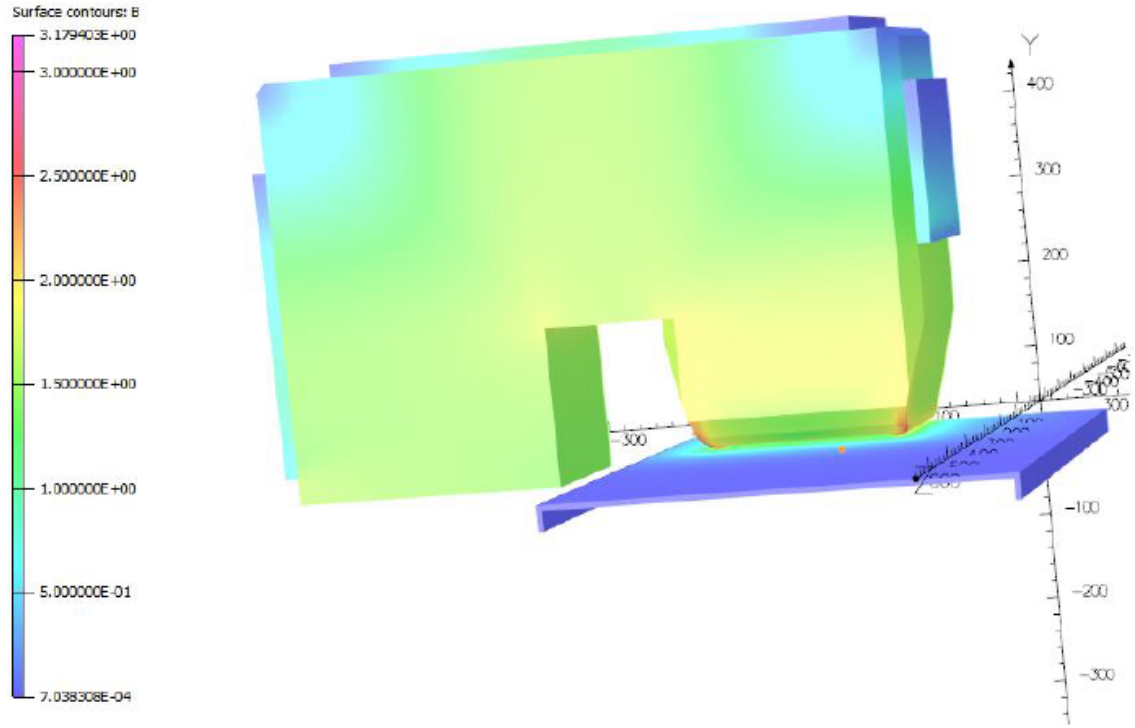

***Figure 3.47**: Field distribution in the finalized design of the yoke*

This new design of the yoke, together with a conductor with a smaller water channel, allows improve the operative range of the magnet with a considerable reduction of the power consumption. The main feature of the single dipole after the final design are in the next table, coil and power consumption are in the Appendix A of this chapter. With this improvement the single magnet results also a bit lighter (total weight is 2110 kg). The as built dipole model is in Figure 3.48 (LHS).

Laminated yoke Packing factor	**B field range**	**Mechanical length**	**Effective length range**	**Gap height**
99,00%	0,06 – 1,226 T	400 mm	450,23 – 448,34 mm	60 mm
Good Field region (GFR)	**Field uniformity**	**Integrated field uniformity**	**Bending angle**	**Harmonic components (b2 to b9)**
100 mm H 40 mm V	0,04%	0,03%	10,10° (176,3 mrad)	<0,6 unit after 0,8 sec

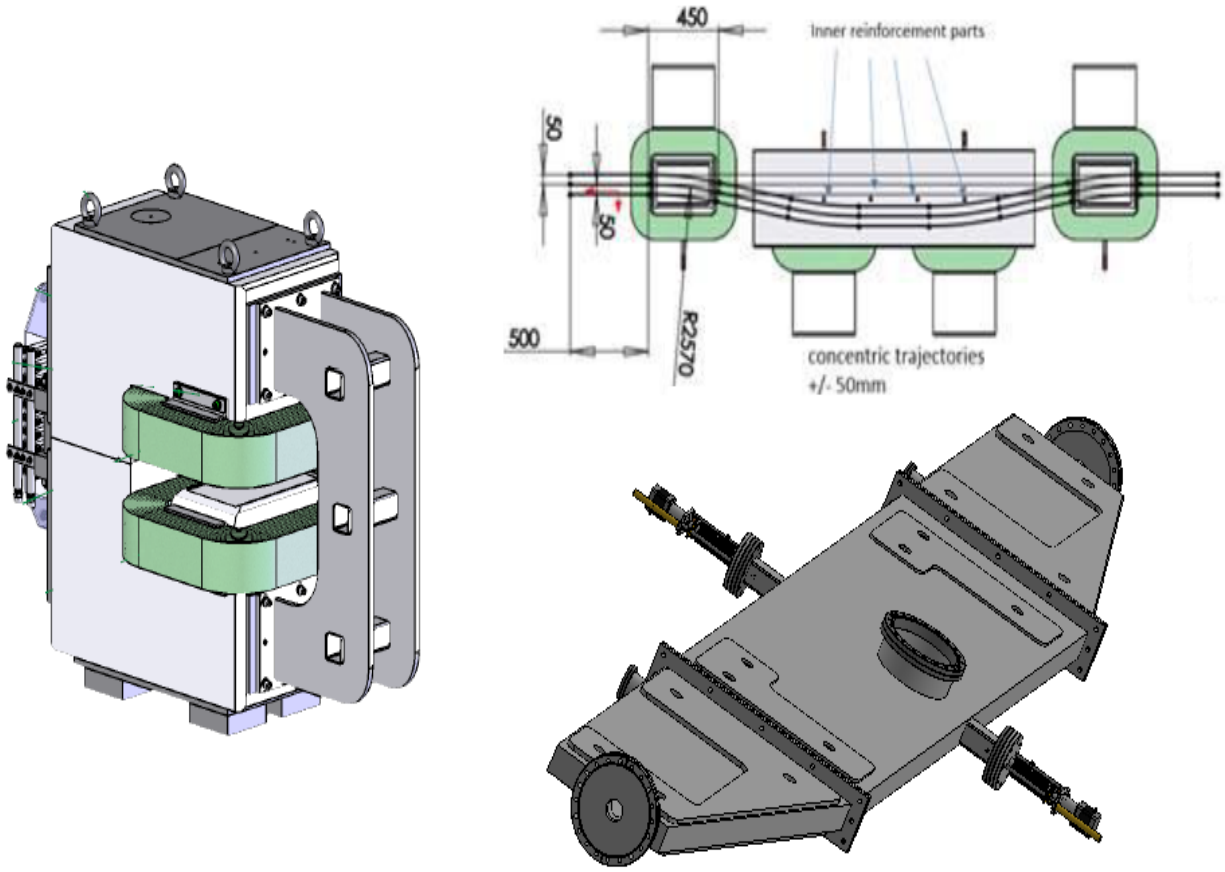

***Figure 3.48**: As built dipole model with reinforcement parts (LHS) and final vacuum chamber model with position of reinforcement pillar with respect to the main trajectory (RHS)*

The yoke lamination have been optimized with the view of realizing a device that can change field each second. The same analysis as proposed in 3.2.3 have been performed on the new dipole design showing negligible effects on the higher harmonics components when the field is stable or after 0,8 seconds after the current change.

The whole chicane has been designed and manufactured with the vacuum chamber and selection slit. In this case mechanical deformation due to vacuum and also due to yoke deformation with the magnetic field (typical in a C-shape dipole) have been evaluated and considered in the final design of magnets and chamber. The inner clearance of the vacuum chamber should be 40 mm, hence, the dipole yokes have been manufactured with reinforcement plates and bars (see previous Figure 3.48), obviously included in the field analysis. Also the vacuum chamber has some reinforcement plates on the outer surface but it was necessary to add 4 pillars inside the chamber whose position have been fixed in order to have no interference with the chicane reference trajectory and the main beam axis. The chamber final model is shown in Figure 3.48 (RHS).

The chicane has been calibrated at INFN-LNS using proton beams accelerated with the TANDEM (4,8 MeV, 10 MeV, 20 MeV and 24 MeV). The Superconductive Cyclotrone has been used to accelerate protons, C^{+6} and He^{+2} at 62 MeV/u. The system installed at the 40° beamline is shown in Figure 3.49 and the method used for the calibration is described in [12]. It basically consist in measuring the deflection of the particle in the symmetry plane using a Gafchromic film and comparing the result with the nominal expected deflection. Moreover, the beam position was checked at the chicane output in order to characterize and quantify the eventual steering effect due

to loss of symmetry in the final device (both because of manufacturing errors and misalignment) that makes the total field integral along the reference trajectory different from zero, which is the value in the ideal case. The selector installed at the 40° beamline is shown in Figure 3.49.

***Figure 3.49**: Energy selector installed at the 40° beamline*

Figure 3.50 shows the Gafchromic film irradiated with 62 MeV protons. As can be seen several beam spot positions have been acquired for each energy using different magnetic field. The reason is to have a more complete set of data to correct the magnetic field in case of considerable deviation from the nominal selection point at 160mm.

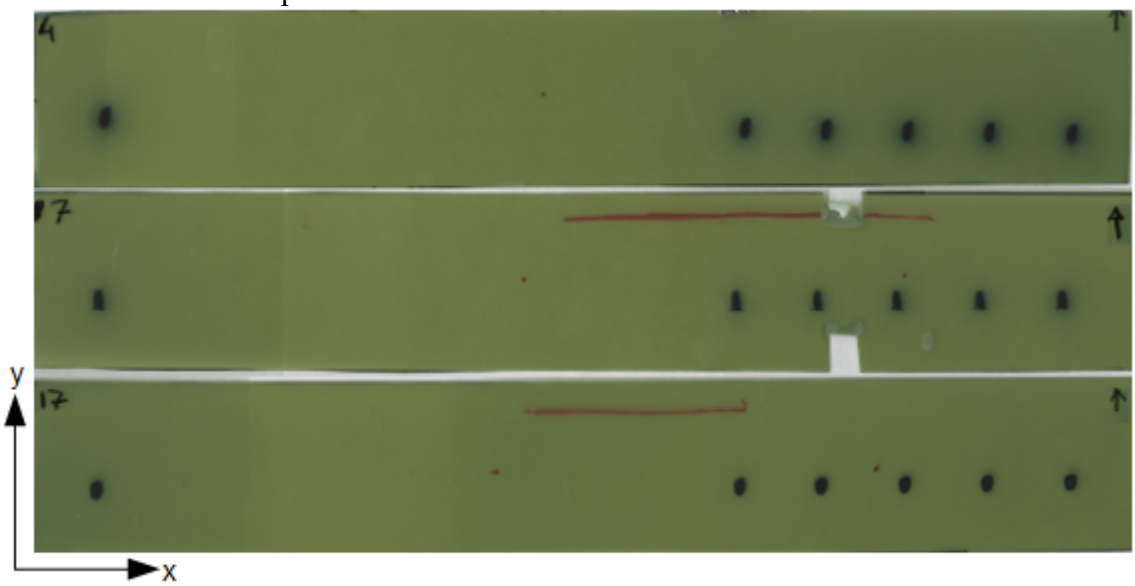

***Figure 3.50**: Gafchromic irradiated with 62, 24 and 10 MeV protons. The spot from the left side is obtained with B=0T*

The magnetic field values used for the test with 62 MeV protons, expected beam position and measured beam position are reported in the next table, showing that deviation from the nominal position is less than one mm, which is in the precision of the possible alignment with optical

theodolite.

B field [G]	Nominal position [mm]	Measured position [mm]	Deviation [%]
3630,3	127,5	128	0,4
4084,1	142,5	143	0,3
4537,1	160	160,5	0,3
4991,7	177,5	177	-0,3
5445,5	192,5	193,5	0,5

Data for the other energies of protons and also for carbon and helium ions have similar results, as expected and are not reported.

Figure 3.51 shows comparison among the experimental calibration curve and theoretical curves obtained analytically and with simulation using different codes and field maps. The agreement is optimal and within 1 mm, which is the error estimated due to the alignment precision. The good agreement among experimental data and theoretical curves confirms also the resolution, in fact it is calculated it is calculated as the derivative of the deflection on the selection point, see Eq. 3.8.

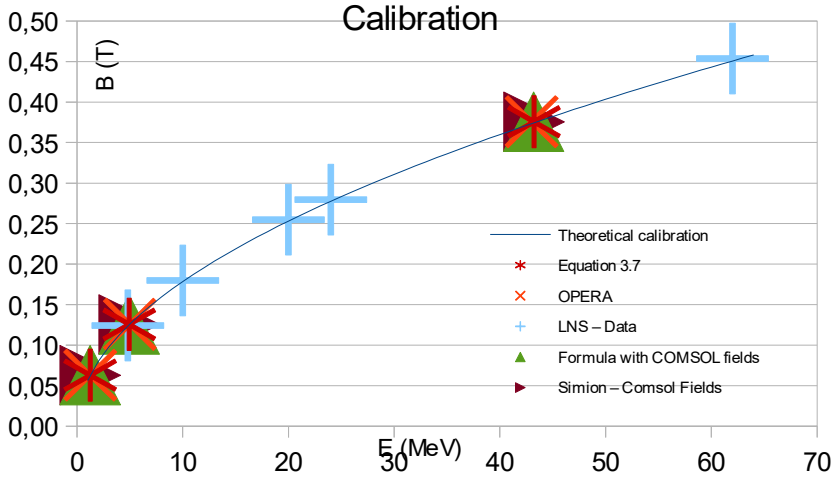

***Figure 3.51**: Comparison among experimental calibration curve and theoretical curves obtain with different methods*

The steering effect of the chicane have been evaluated using a quarz beam viewer at the output of the chicane and measuring the deviation of the beam position with respect to the beam reference axis (B=0).

In general the deviation for the different energies and ion species used was of few millimeters and the field adjustment in the fourth dipole was of some tens of gauss. The relatively small deviation in the beam position and the necessary field adjustment are compatible with the alignment precision obtained at LNS. Details are reported in the next table.

Proton energy [MeV]	D1-D2-D3 Field [Gauss]	D4 Field [Gauss]
4,8	1243,8	1220
10	1797,8	1775
20	2549,3	2485
24	2795	2780
62	4537,9	4462,9

Appendix A: as built coil features

Coil geometry:

Peak current (DC)	Wire section	Water channel diameter	Insulator thickness	Number of turn per coil
300 A – 22,2 V	10x10 mm	4 mm	0,5 mm	100 (10x10)

Power consuption: 6,66 kWatt per dipole, ~ 26,64 kWatt in total
Extimated water flow: 10,4 l/min (ΔT~10 °K)

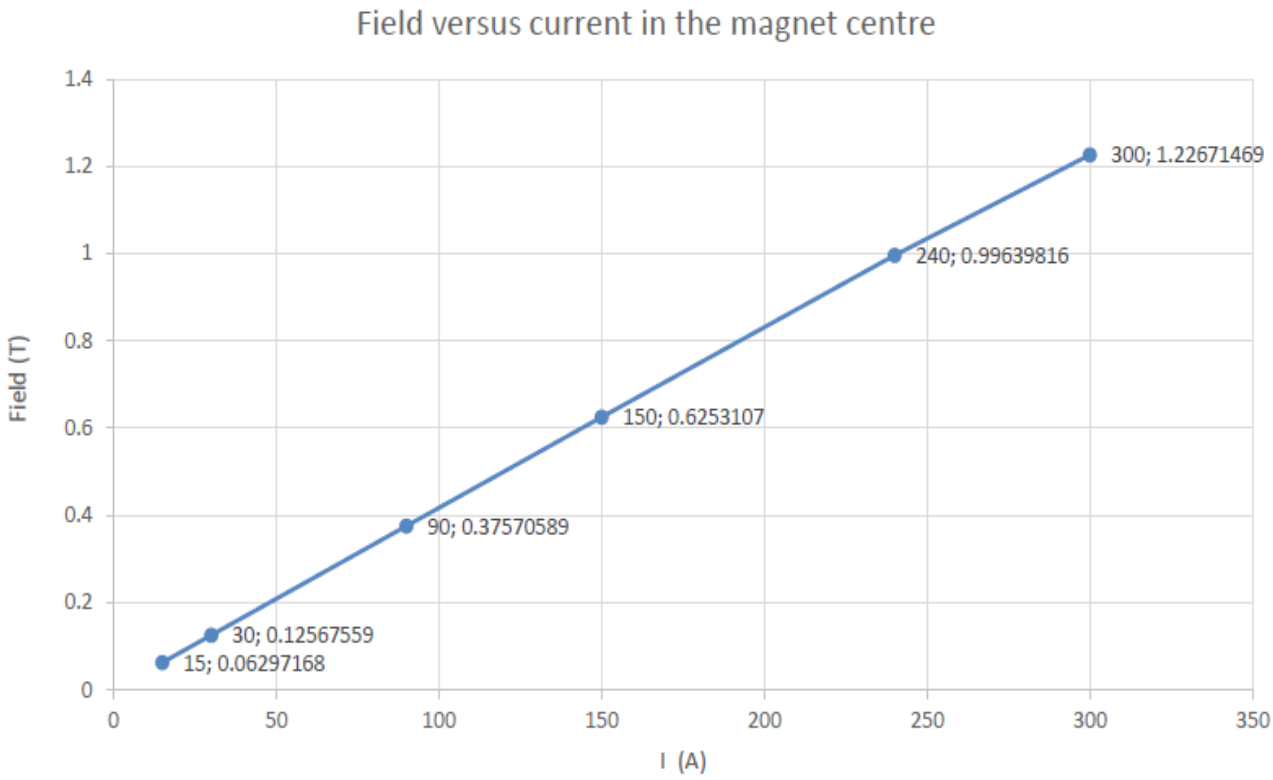

3.6 Bibliography

[1] P. Castro, *Beam trajectory calculations in bunch compressors of TTF2*, *DESY TECHNICAL NOTE* 2003-01

[2] T. Zickler, *Basic design and engineering of normal-conducting, iron-dominated electromagnets,* CERN-2010-004, pp. 65-102 arXiv:1103.1119 [physics.acc-ph]

[3] J. Tanabe, *Iron Dominated Electormagnets Design, Fabrication, Assembly and Measurements,* World Scientific Publishing Co. Pte. Ltd. (2005) ISBN: 981-256-381-4 (pbk)

[4] J. Itteera, K. Singh, V. Teotia, U. Priti, M. Sanjay, T. K. Taly, M. Joshi, R. Pushpa, *Design of a high field uniformity electromagnet for Penning trap*, Proceedings of the Indian particle accelerator conference, Variable Energy Cyclotron Centre, India (2013) .

[5] J. Ostiguy, *Longitudinal profile and effective length of a conventional dipole magnet*, Proceedings of the 1993 Particle Accelerator Conference, 1993., 2901 - 2903 vol.4, 10.1109/PAC.1993.309499

[6] B. C. Brown, *Field quality issues in iron-dominated dipoles at low fields*, FERMILAB-CONF-96-369 (1996)

[7] F. Schillaci, M. Maggiore, D. Rifuggiato, G.A.P. Cirrone,G. Cuttone, D. Giove, *Errors and optics study of a permanent magnet quadrupole system*, JINST 10 T05001 (2015)

[8] J. C. Bergstrom, L. O. Dallin, *Effects of Eddy Current Induced Sextupole Moments in the Booster During Ramping,* CLS Design note – 3.2.69.2 Rev. 0 (07/01/2000)

[9] S. A. Bogacz, S. Peggs, *Chromaticity Compensation – Main Injector Sextupole Strengths,* Main Injector note MI-0056, Fermilab, April 1991

[10] T. Toyama, D. Arakawa, S. Igarashi, J. Kishiro, E. Nakamura, K. Takayama, *The Eddy-current-induced Head-tail Instability at the KEKE-PS,* Proc. of the 1999 PAC, New York 1999.

[11] N .S. Sereno, *Eddy-current-induced Multipole Field Calculations,* Advanced Photon Source Note LS-302 (2003), http://www.aps.anl.gov/Science/Publications/lsnotes/content/files/aps_1418240.pdf

[12] F. Schillaci et al. *Design of the prototype of a beam transport line for handling and selection of low energy laser-driven beams*, NIMA 837 (2016) 80–87

4 Design of the in-vacuum transport elements for the ELIMAIA laser driven-ion beams

Laser-driven beams could be an alternative to conventional accelerator beams especially for cancer therapy. Actually, at the present state, if you want to use them for irradiation, well, I have this picture in my mind →
F. Schillaci

The ELIMED beamline is designed to make a beam of ions starting from the laser-accelerated particles and this is possible using the collection+selection systems. In this chapter the last magnetic elements of the ELIMED beamline are quickly described. There are two standard electromagnetic quadrupole to be used for refining the beam shape before irradiation of samples and two double axis steerer for correction of sistematic missalignment errors of the beamline. Preliminary beam-transport simulations are also presented.

4.1 Magnetic lenses of the final transport and focusing section

The last section of the ELIMAIA-ELIMED beamlines consists of 2 electromagnetic quadrupoles and two double axis steerers, or correctors.
These are pretty standard lenses and a quick overview of their as-built features is here reported.

The two electromagnetic quadrupoles will have the following magnetics and geometrics features.

	RQ_1	**RQ_2**
Yoke (packing factor)	Laminated (≥ 0.99)	Laminated (≥ 0.99)
Maximum gradient	10.2 T/m	10.2 T/m
Effective length	331.5 mm	331.5 mm
Mechanical length	296 mm	296 mm
Inner bore diameter	70 mm	70 mm
Useful beam diameter	50 mm	50 mm
Total harmonic content :	Cn = 2 units @ r=25mm	Cn = 2 units @ r=25mm
Distance between magnetic centre and geometric centre	< 0,1 mm	< 0,1 mm
Distance between quadrupoles (adjustable range)	100 – 400 mm	100 – 400 mm

The magnets (ESS dipoles and quadrupoles) will be working with the possibility to change the field each second, hence the yoke cannot be a solid iron core but will be realized using thin foils (usually 1 mm thick) separated by an insulator. This allows to minimize eddy currents and hysteresis of the yoke itself. The packing (or filling) factor represents the percentage of iron within the yoke volume and it is 99% for these electroquads.

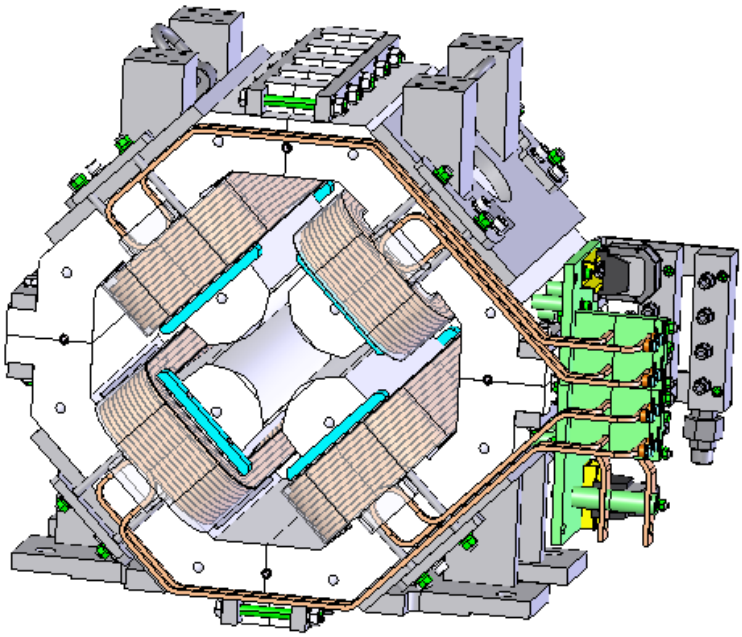

***Figure 4.1**: As-built electroquad model*

The electromagnetic quadrupoles will have a static field, but the possibility to change the magnetic field each laser shot (1 Hz repetition rate) will be ensured.

The two steering magnets have been designed according the beam-line error study proposed in the previous chapter, specification are in the next table.

	SM_1	**SM_2**
Maximum integrated field:	4,5 T.mm for both axes	4,5 T.mm for both axes
Maximum field	0.0345 T for both axes	0.0345 T for both axes
Yoke length	150 mm	150 mm
Total length	235 mm	235 mm
Inner clearance aperture	109 mm	109 mm

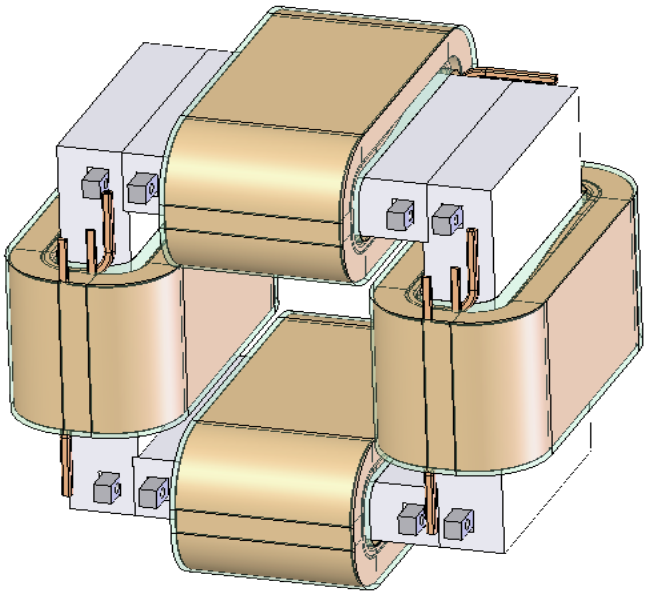

***Figure 4.2**: As-built steerer model*

The vacuum chamber for this last part of the beam-line is a single pipe. A cross-like chamber with six arms will be set between the ESS chamber and the pipe. The main pipe is in austenitic stainless steel 316L (same material for ESS vacuum chambers) with an inner diameter > 56 mm and an outer diameter < 69 mm. Flanges will be ISO DN 100 CF-R.

The beam line elements will be positioned as reported in Figure 4.2. Details on the relative longitudinal distances are reported in the next table, allowed tolerances are ±1 mm.

Collimator1-DM1 Collimator2-DM4	DM1-DM2 DM2-DM3 DM3-DM4	Collomator2–SM1	SM1 – RQ1	RQ1 - RQ2	RQ2 - SM2
220 mm	500 mm	300 mm	275 mm	400 mm	275mm

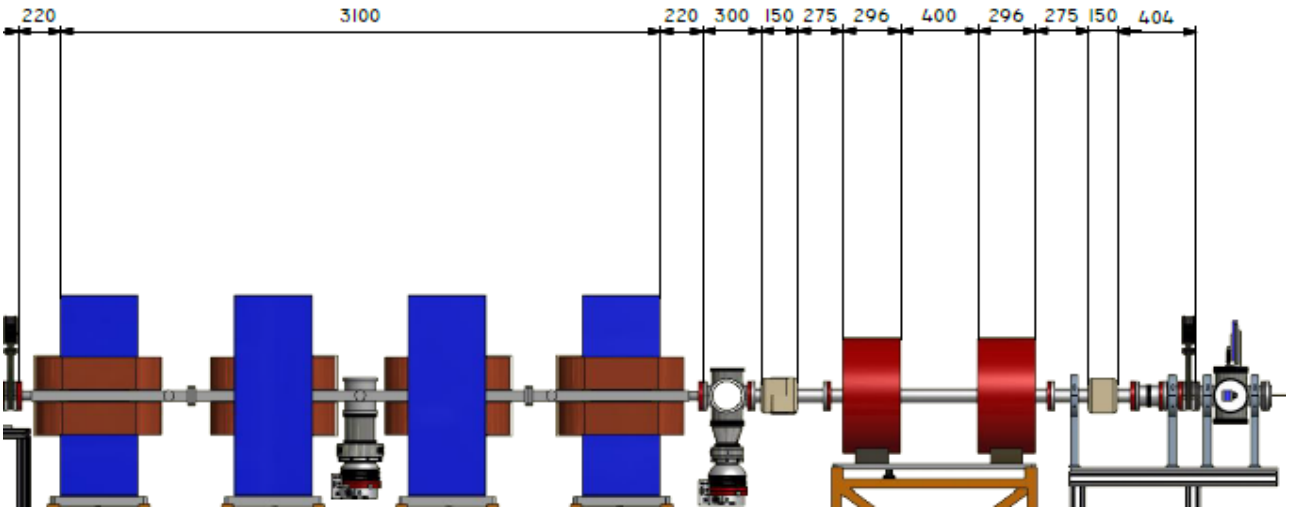

***Figure 4.3**: Beam-line element position.*

The last component of the in-vaccum system is a 6 arm cross-like chamber, in Fiugre 4.4, with the following flanges:

– 2 DN100CF on the beam-line axis, one flange is used for the connection to the in-vacuum transport line the other one has a kapton window fo the connection to the in-air transport line.
– 4 DN160ISO-K, two of them are used to set the TOF and SEM using proper mechanical actuator, one for the vacuum pump and one is free for additional user's device/sample.

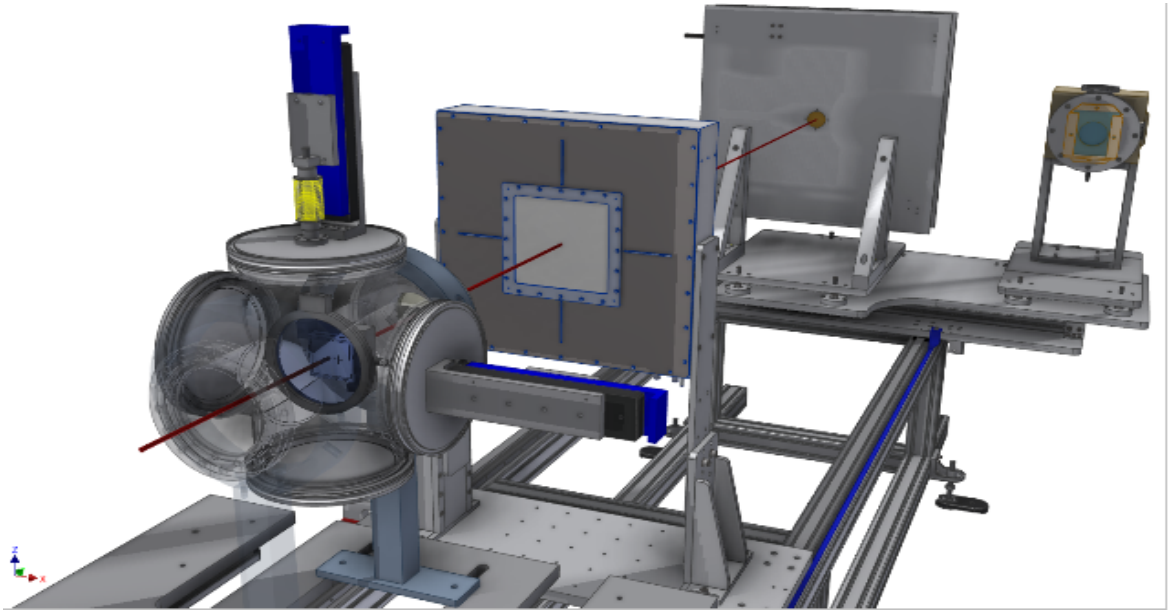

***Figure 4.4**: Detail of last component of the in-vacuum system*

4.2 Preliminary beam transport simulation

The following simulations are intended to be preliminary and have been performed only for monochromatic reference energy proton beam of 60, 30 and 5 MeV and are referred to the last part of the beam-transport line. Basically, the ESS out, as reported in the ESS feasibility study report are used as input for this simulations. Moreover the biggest error on angle and beam centroid position, as calculated in the beam-line error study presented in the ESS feasibility study report is introduced.

4.2.1 60 MeV protons

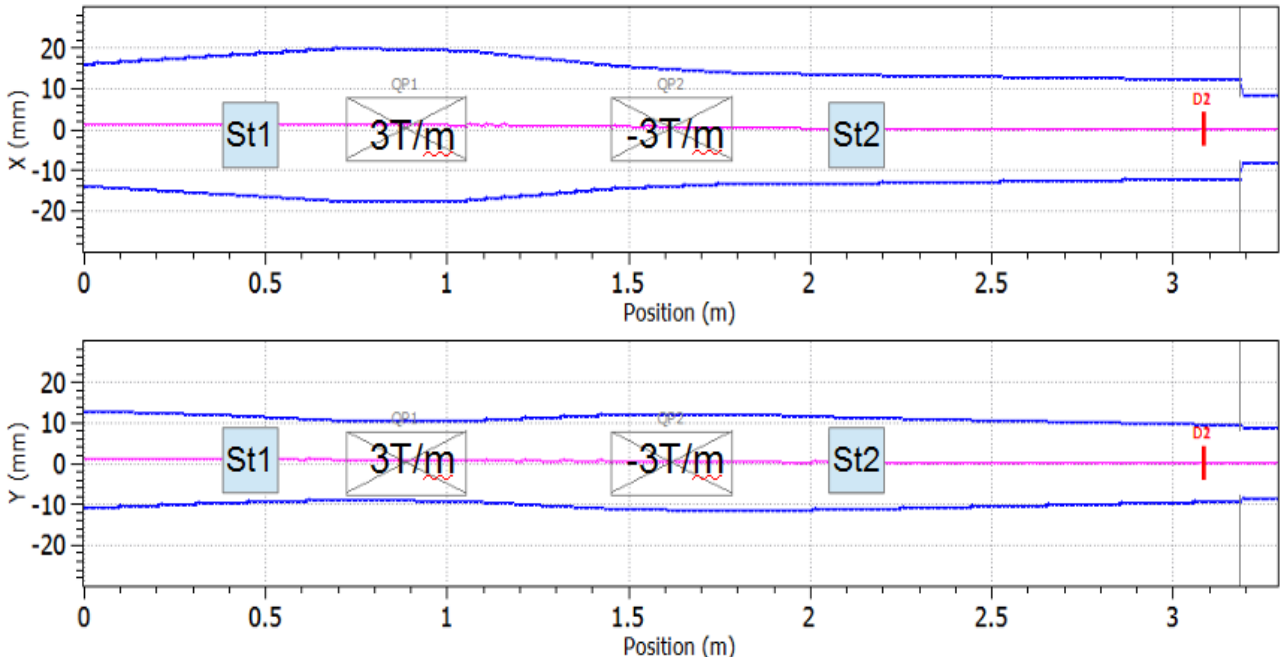

***Figure 4.5**: Beam envelope for 60 MeV protons. (St stays for Steering magnet mentioned as SM in the previous section)*

Figure 4.5 shows the 60 MeV proton envelop, with lenses positions (St1 and St2 are the corrector magnets, for quadrupoles is reported the used gradient). A collimator of 8 mm radius is used in order to cut tails and improve beam profile uniformity. The output beam is show in Figure 4.6.

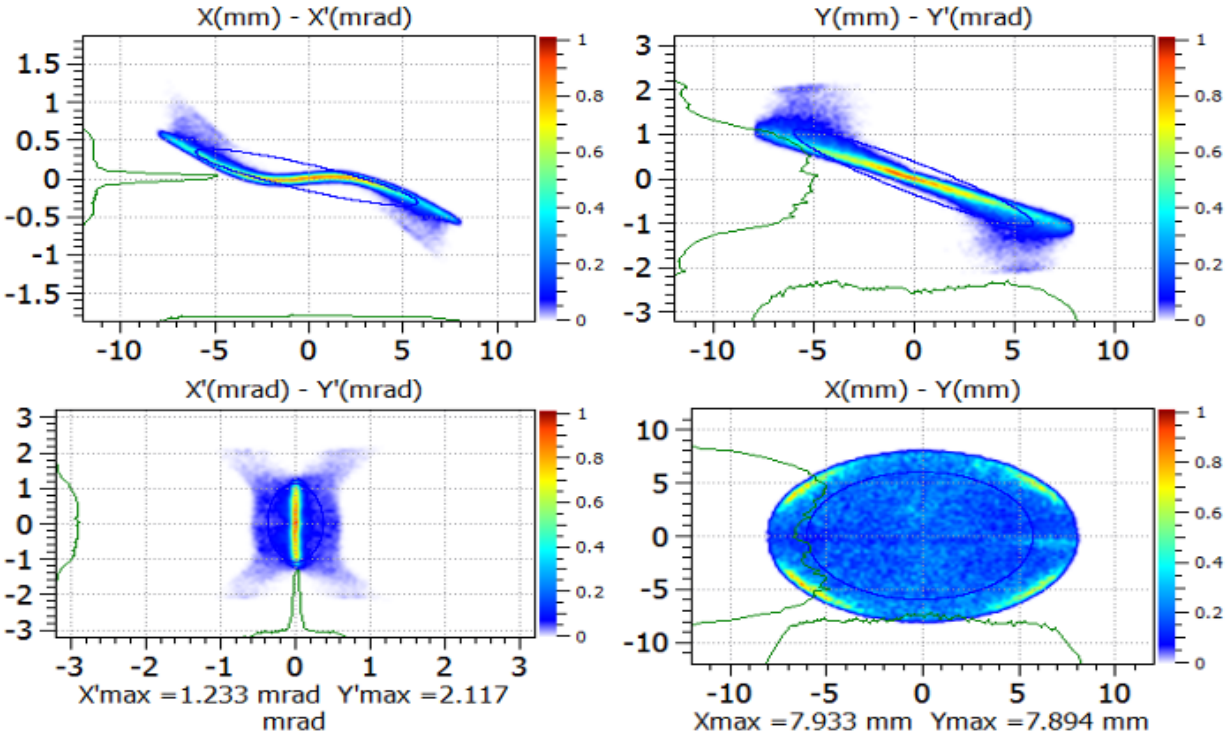

***Figure 4.6**: Phase space plot of the output proton beam*

4.2.2 30 MeV protons

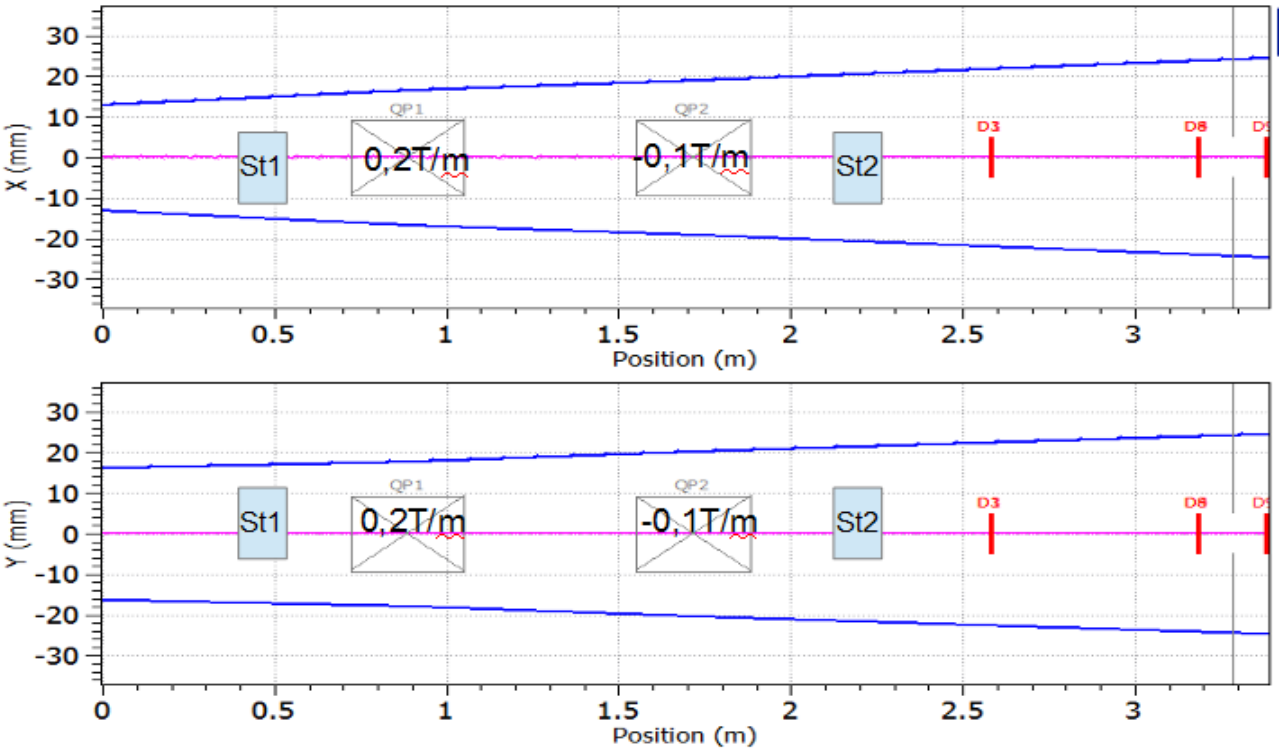

***Figure 4.7**: Beam envelope for 30 MeV protons. (St stays for steering magnet)*

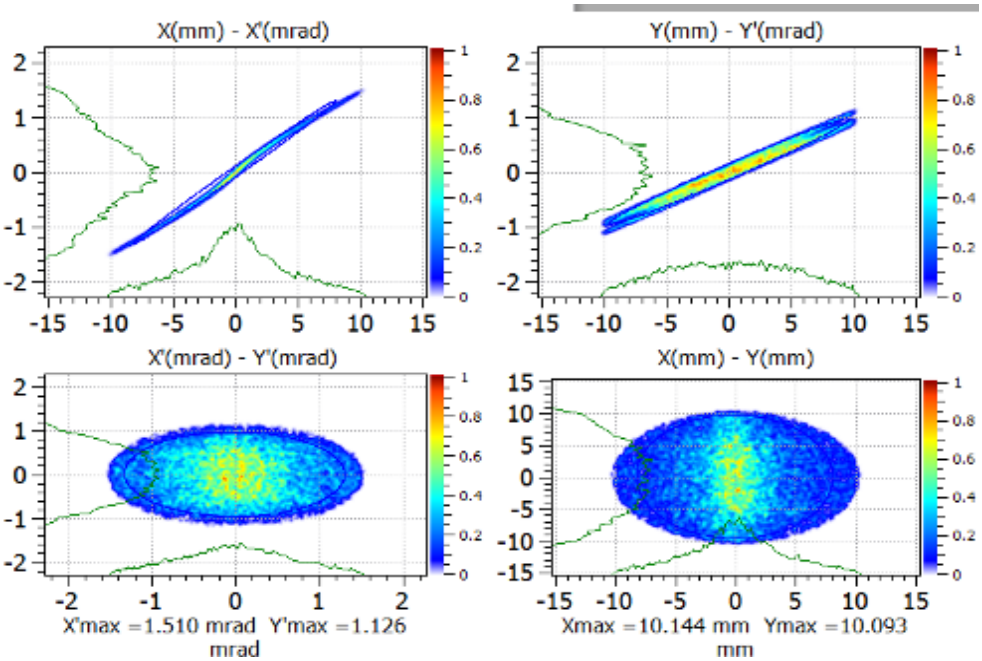

***Figure 4.8**: Phase space plot of the output proton beam*

Figure 4.7 shows the 30 MeV proton envelop, with lenses positions (St1 and St2 are the corrector magnets, for quadrupoles is reported the used gradient). A collimator of 10 mm radius is used in order to cut tails and improve beam profile uniformity. The output beam is show in Figure 4.8.

4.2.3 5 MeV protons

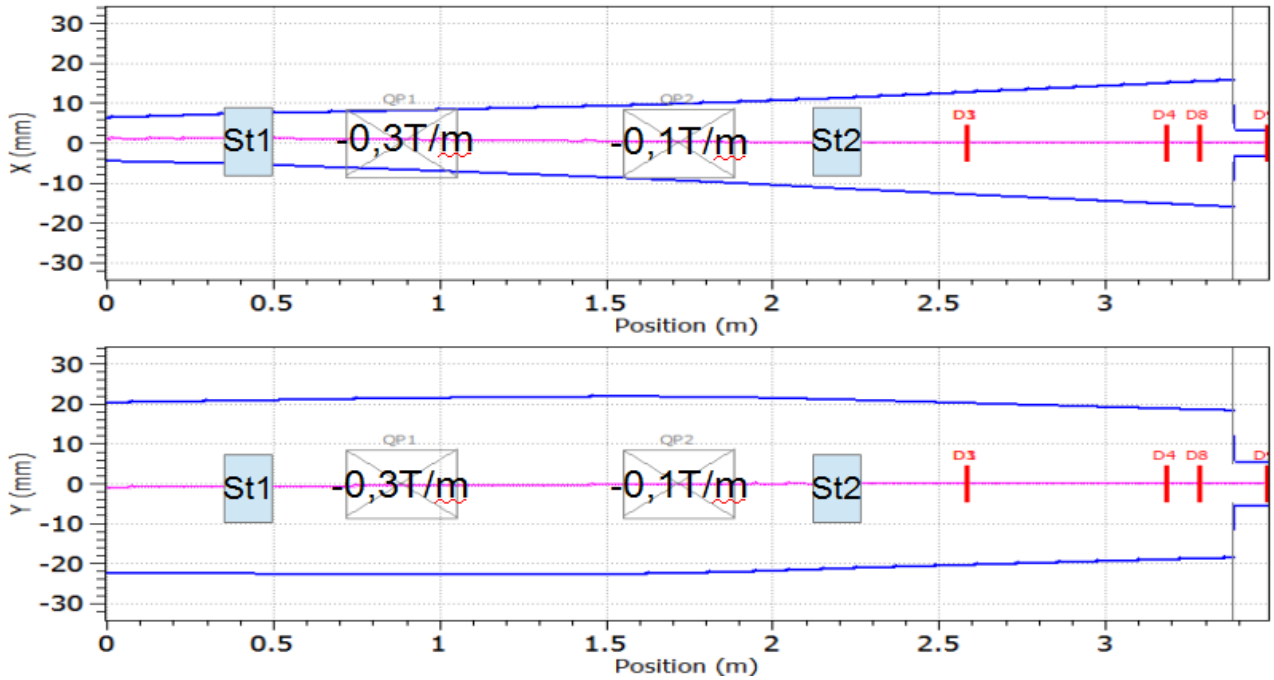

***Figure 4.9**: Beam envelope for 5 MeV protons. (St stays for steering magnet)*

Figure 4.9 shows the 5 MeV proton envelop, with lenses positions (SM_1 and SM_2 are the corrector magnets, for quadrupoles is reported the used gradient). A collimator of 5 mm radius is

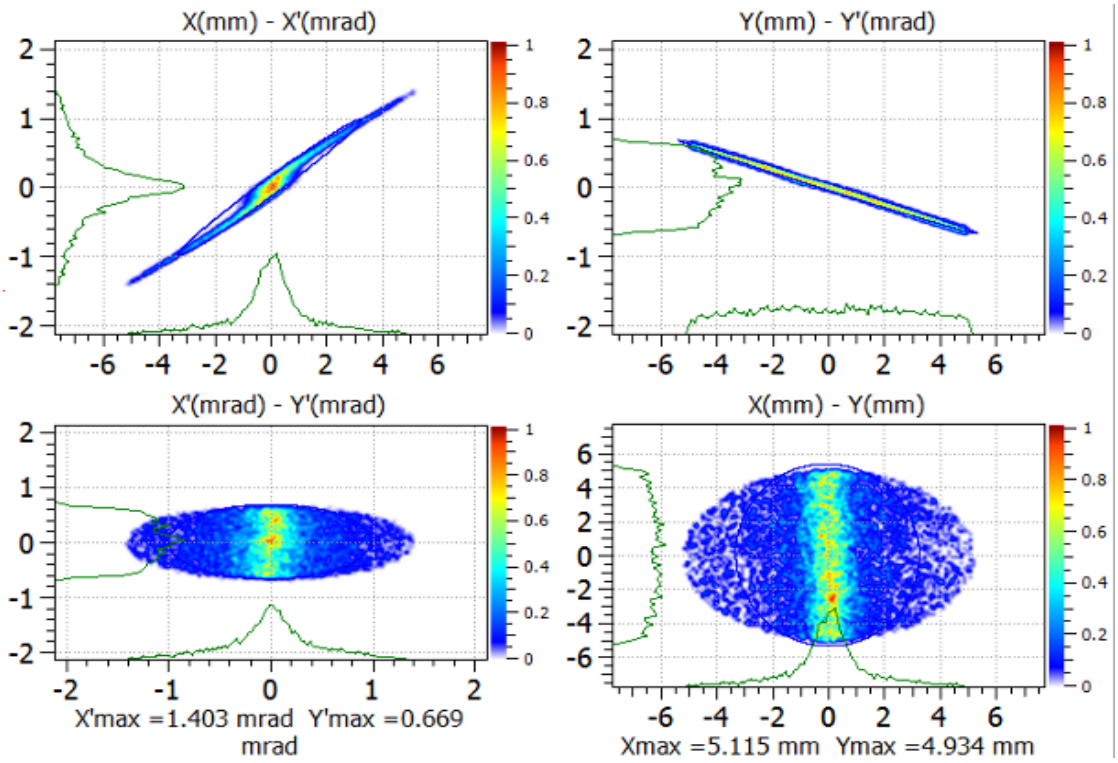

***Figure 4.10**: Phase space plot of the output beam*

used in order to cut tails and improve beam profile uniformity. The output beam is show in Figure 4.10.

The spatial profile of the beam does not appear to be really uniform because of the wide beam divergence. After few tens of mm from the source the beam is quite big and it passes in the region of the PMQ bore outside the good field region (see chapter 2). Hence, non-linear dynamics effects on the beam in the first section are the reason of the spatial profile uniformity. The issue could be corrected and the uniformity improved reducing the collimator size of the ESS (input and output collimators) with a small reduction of the transmission efficiency of the whole beamline. Updated source parameter are needed to improve the beam quality. For this reason it will be necessary to have an experimental characterization of the beam before the final commissioning.

Transmission efficiency in the last section (after the ESS) is of about 90% of the ESS output for each proton energy. This section has been designed with the goal to maximize the transmission reducing the losses, anyway part of the beam halo can be lost. The transmission efficiency can be lower if the beam is collimated in order to improve its profile.

Transmission efficiency at the ESS output is reported in the ESS feasibility study report. Please note that this results have to be considered preliminary. It is necessary to have updated information on the expected ELIMAIA proton beams in terms of angular aperture. Moreover the beam line transmission efficiency depends also on the minimum distance between the target and the first PMQ that should not exceed 50mm.

4.3 Final design and manufacturing

The as-built model of the whole beamline is in Figure 4.11. In Chapter 1 was presented a picture of the beamline after the installation.

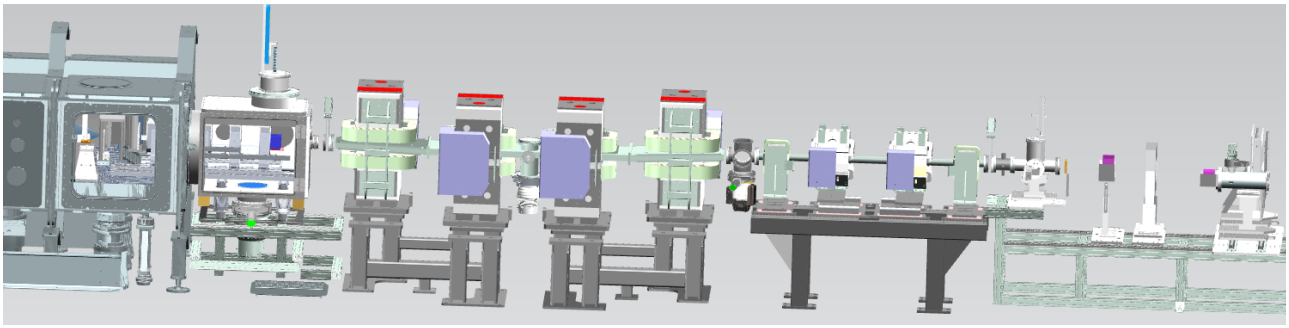

***Figure 4.11**: ELIMAIA-ELIMED as built model.*

Preliminary simulations of the whole beamline shows encouraging results in terms of beam quality and dose delivered at the irradiation point. In fact, the transmission efficiency can be close to 10% for the energy range of interest and, hence, the number of particle would be enough to deliver some centiGray per shot to the sample. The beam shape at the irradiation point for 30 $\pm$ 3 MeV protons is shown in Figure 4.12. Uniformity needs to be improved, but in any case it would be fundamental to study the beam line performances when the real produced beam will be characterized.

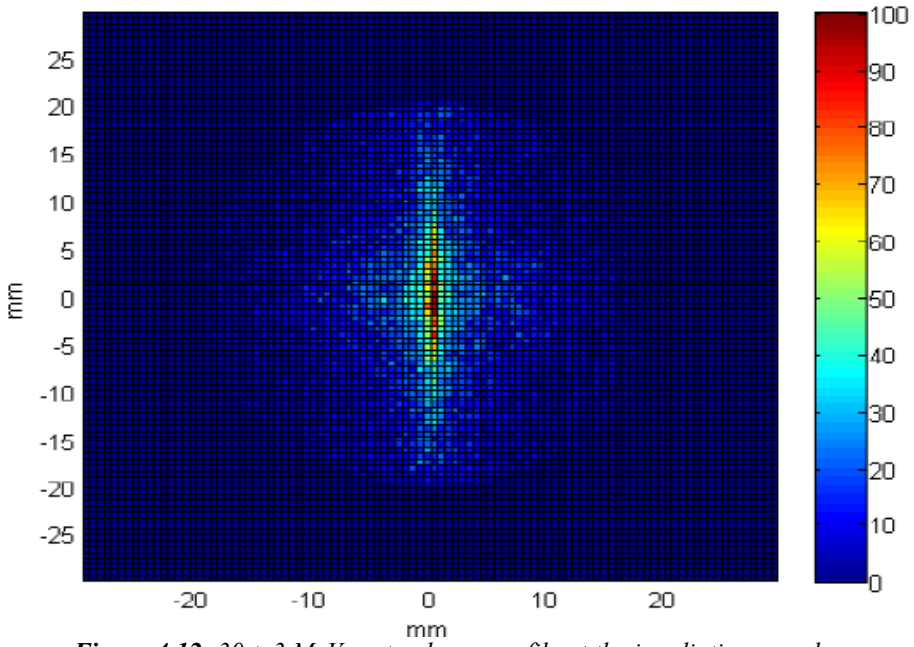

***Figure 4.12**: 30 ± 3 MeV proton beam profile at the irradiation sample.*

As a preliminary result and with the aim of showing the performances of the whole beamline from a practical point of view, a uniform energy distribution for protons between 50 and 70 MeV is here considered. The angular aperture is treated as a gaussian distribution with 5° HWHM. The transmission efficiency is shown in Figure 4.13. In this case, the transmission efficiency is of about 12%, which means about 9,2x10^{7} H^{+}/bunch (associated dose of about 0,05 Gy/bunch). The beam profile, shown in Figure 4.14, is anyway not ideal because of high inhomogeneity.

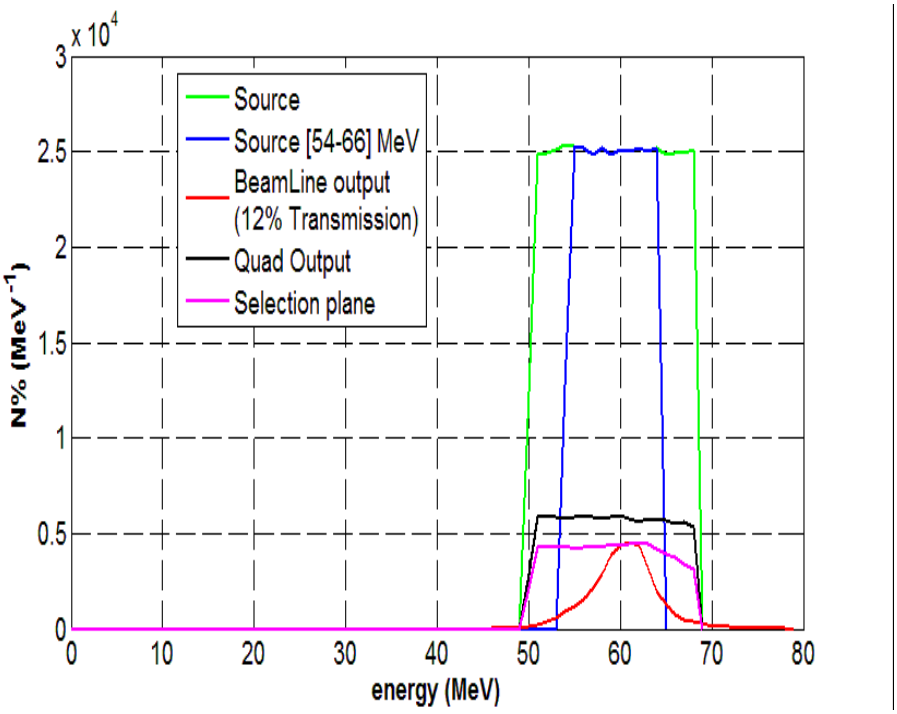

***Figure 4.13**: Transmission efficiency along the beamline for 54-66 MeV protons with gaussian angular aperture*

The same simulation for 30 MeV, in Figure 4.15, protons as reference energy shows similar result. It has to be noted that, in this case, the energy selection is more strict, in fact particles are selected with a resolution of ±5% with a smaller slit aperture size. The transmission efficiency is about 12% as in the previous case but, due to the exponential energy distribution, the transmitted particle number is higher (3,9x10^{9} H^{+}/bunch with an associated dose of about 0,3 Gy/bunch). Again the beam profile has very low uniformity.

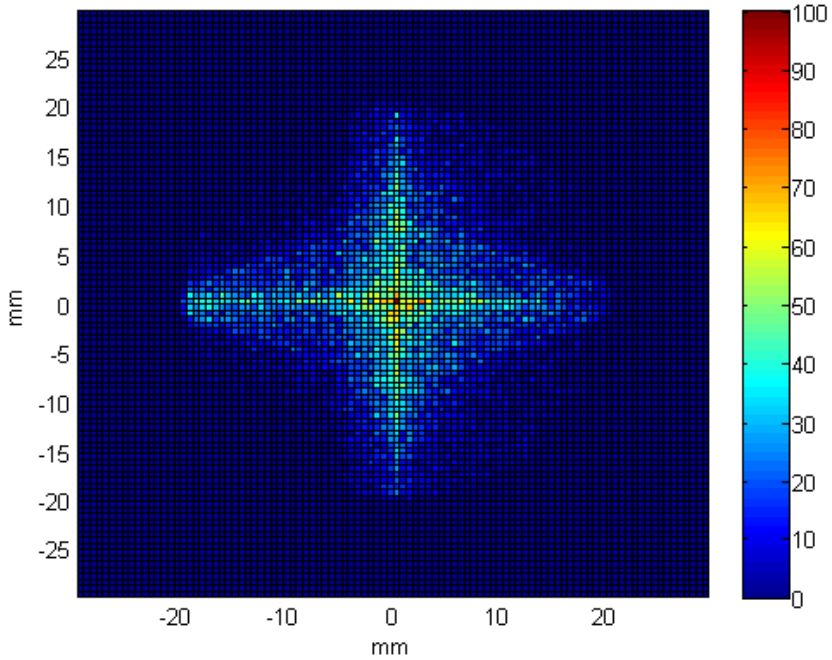

Figure 4.14: *Output beam profile, central energy 60 MeV*

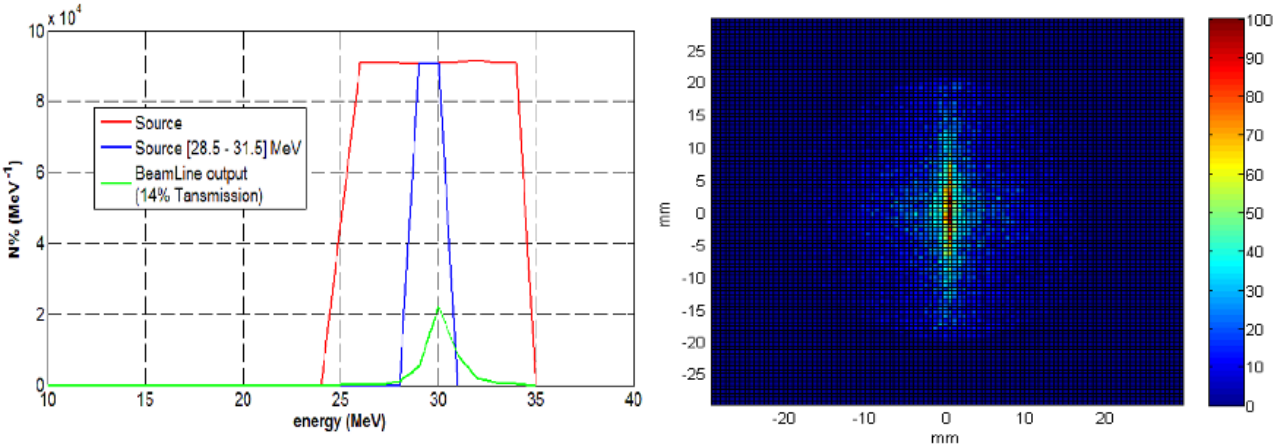

Figure 4.15*: Transmission efficiency along the beamline for 28,5-31,5 MeV protons with gaussian angular aperture (left side) and output beam profile (right side)*

5 Conceptual design of an high energy Thomson Parabola for ELIMAIA, first upgrade of the Energy Selection System

C. Verdone, from the movie “Un sacco bello”:
"Alfio che c'è? hai bisogno di qualcosa?
Allora risposi: Mamma non vedi che sto
parlando con me stesso?
Cioè, come vedete anche in questo racconto,
o paraBBola, a seconda di quella che la
vogliamo considerare, ci sono anche molti
elementi analoghe... analoghe..." .

5.1 Introduction

Thomson Parabola is an important tool for ion beam diagnostics, especially for in laser-target acceleration experiment, as it provide a complete set of information on a a wide-energy-spread and multi-species ion beam due to the combined deflection of (anti-)parallel magnetic and electric fields.

Most of Thomson Parabolas used in laser-target interaction experiments are compact devices with a permanent magnet dipole and electrostatic dipole in the deflection sector. It has been shown in [1] that the use of an electromagnet can significantly improve the device dynamic and, hence, resolution and upper energy limit. Moreover, magnetic field quality and long term controllability of electromagnets are much better than permanent magnet, which are important for precision in data processing and the possibility to have relatively big gap is important for the device compactness as the magnetic and electric field can be overlapped.

ELIMAIA beamline, as described in the previous chapters, is already equipped with a series of magnets in order to improve the laser-driven beam quality before its delivery to the irradiation point and also a set of diagnostics devices (mostly Time-Of-Flight and dosimetry detectors) for analysing the beam along its propagation axis. A Thomson Parabola, named TP@30° in the following, is already realized and it will be used for diagnostics at 30 degrees with respect to the main beam axis.

Sketch of ELIMAIA beamline is in Figure 5.1, Figure 5.2 provides a description of the TP.

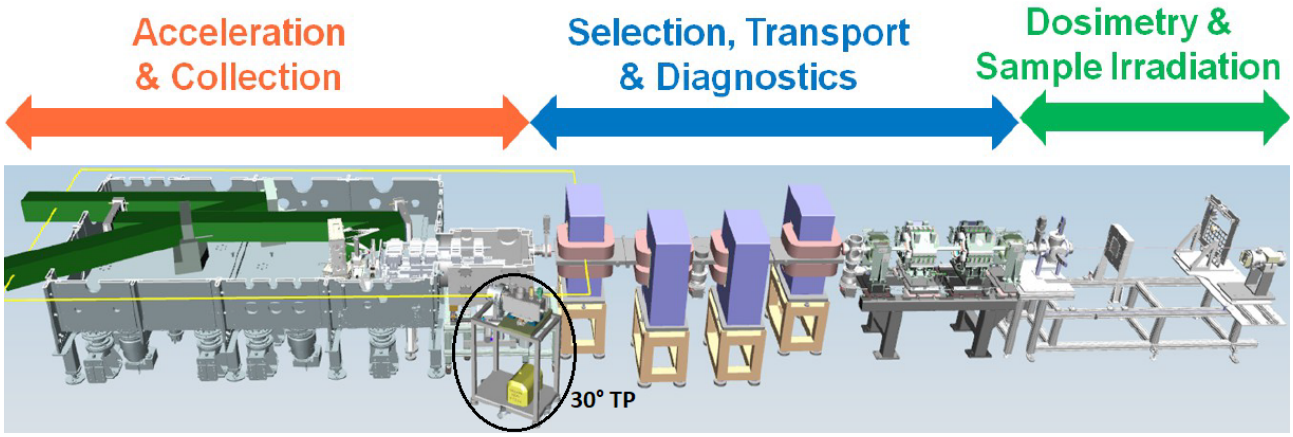

***Figure 5.1**: Scheme of ELIMAIA beamline, TP@30° is highlighted with a black circle*

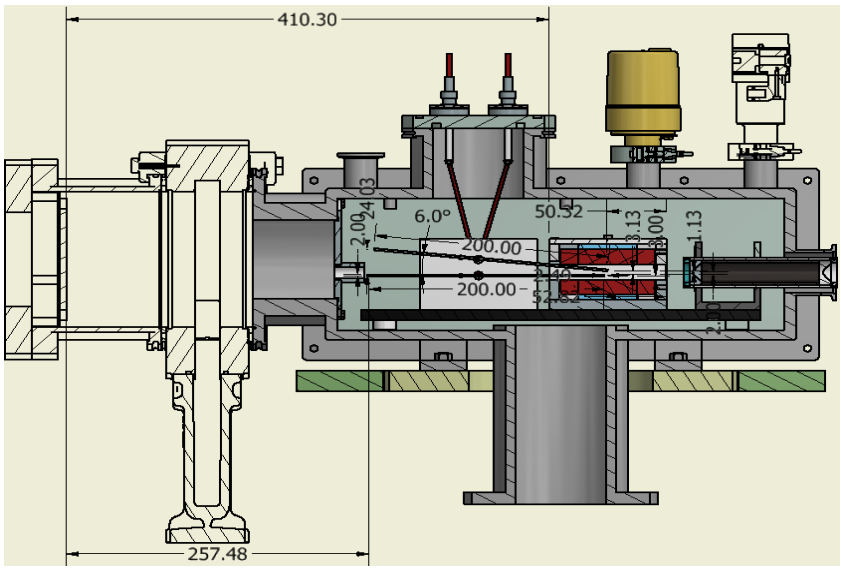

***Figure 5.2:** Scheme of the TP@30°, input flange is on the left side*

The TP@30° is a compact device already successfully used with low energy ion beams in several experimental campaign, it has a permanent magnet dipole and a set of tilted electrodes partially overlapping with the magnetic field. Analytic studies and particle tracking simulations (SIMION FEA) of the device show it is efficient up to 100 MeV protons, being its energy resolution below 10%. Also good charge separation is ensured for heavier ion up to 100 MeV (total energy) as shown in Figure 5.3.

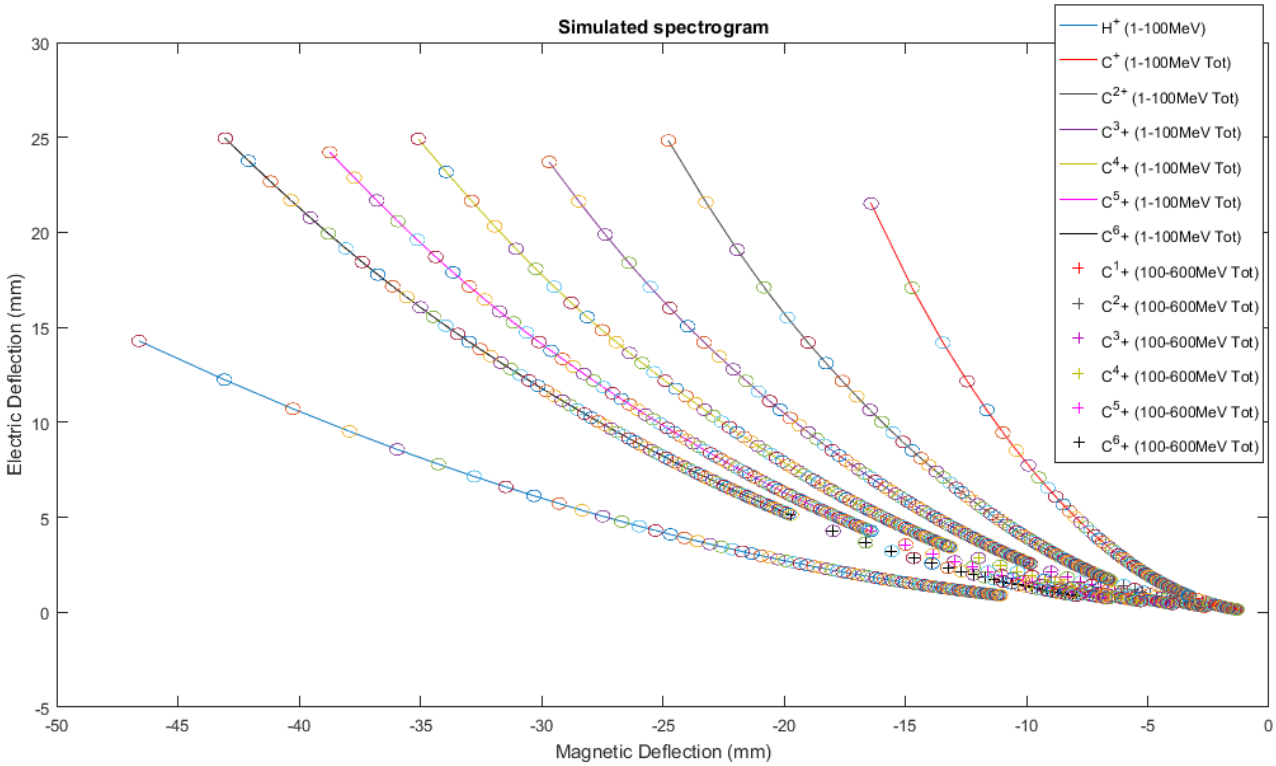

Figure 5.3: *Simulated spectrogram of TP@30°*

Circles drawn on the parabolic traces represent the beam spot-size at the detector plane (0.3 mm), which depends on the collimation system (1mm pinhole 100mm upstream a 0.2mm pinhole) and the path between collimator and detector. Figure shows that proton and carbon ions are well separated up to 100MeV, for higher energies the q/a resolution is pour. In any case the device is suitable to operate at 30° where expected maximum energy will be lower than the central part of the beam.

Even if the device is compact and shows nice performances, it cannot be placed on the beam main axis because of the other magnets along the beamline. Hence, at the moment ELIMAIA is not equipped with a Thomson parabola at 0°, which would be an important diagnostics. A possible solution is to use part of the already installed magnetic chicane for the magnetic deflector and using the large space in its vacuum chamber for placing the electrodes. This solution, from now on called on-axis TP, as shown in the following, offers the possibility to have, in the same device a Thomson Parabola with a low resolution but wide dynamic range and a TP with a reduced dynamic rage but an extremely high resolution.

The conceptual design is fully described and analysed in the following.

5.2 High energy Thomson Parabola @ ELIMAIA

The design of the electric deflection sector of the on-axis TP has been performed firstly with a simple analytic study based on the model proposed in [1], taking into account the geometric constraint of the existing ESS vacuum chamber. This process allow a fast setup of the electrodes with the aim of providing the best performances. Then, the analytic study is compared with simulations and, finally with experimental data of particle tracking in the the chicane performed during the calibration of the ESS at INFN-LNS with Tandem and Cyclotron beam.

5.2.1 Analytic setup of the electric deflection sector

The ESS is shown on the upper side of Figure 5.4, vacuum chamber technical drawing is on the

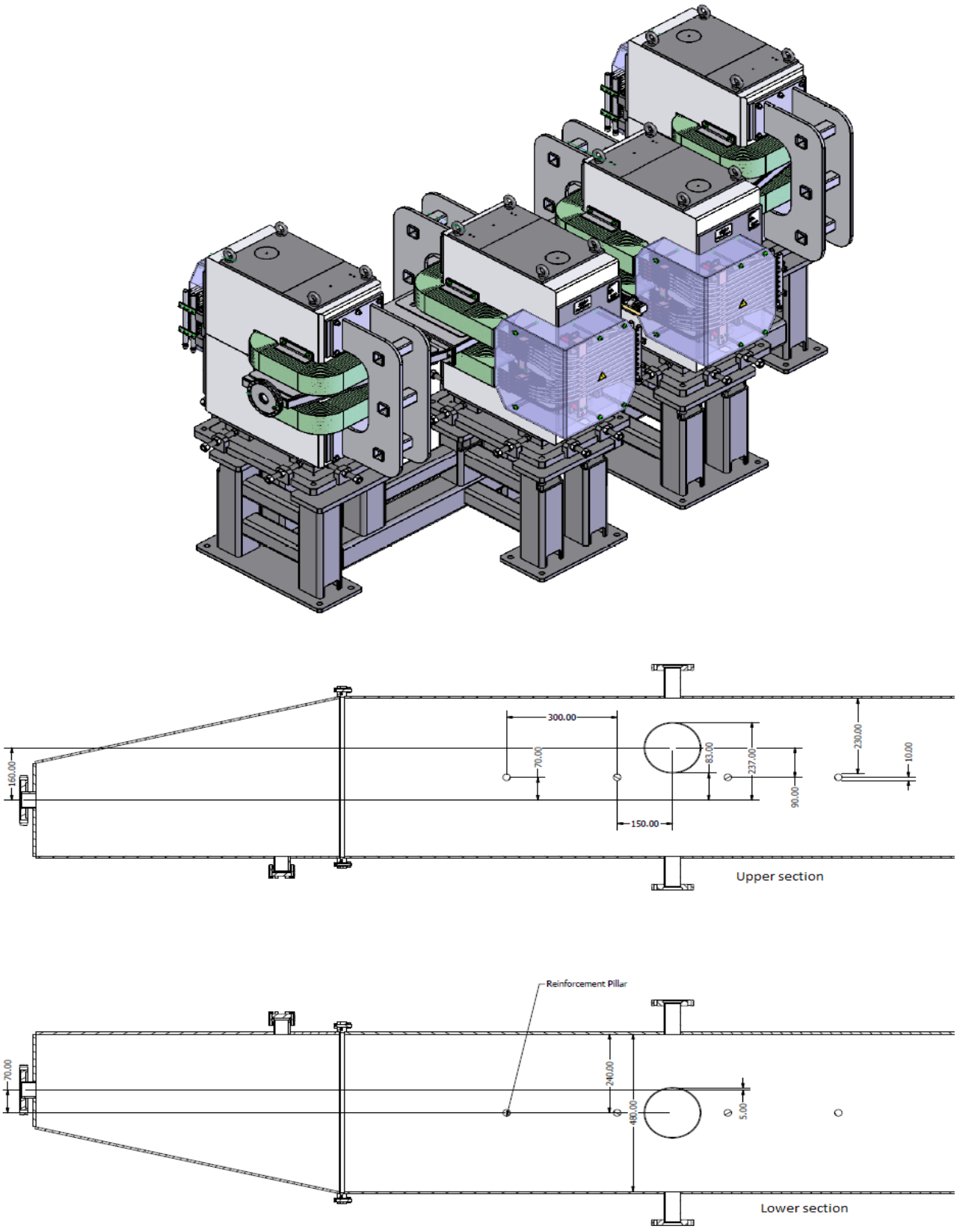

***Figure 5.4**: ESS design (upper side) and technical drawing of vacuum chamber (lower side)*

lower side. The vacuum chamber is divided in tree sections: the first and last section (not shown in the picture) have trapezoidal shape and are placed in the gap of dipole 1 and 4; the central section has a rectangular shape and is placed in the gap of dipole 2 and 3. In order to use the ESS as Thomson Parabola spectrometer just the first dipole will be used.

In the symmetry plane of the chicane there are two DN40 flanges on both side of the chamber for the selection slit. Lower and upper side of the chamber are equipped with DN160 flange; the one on the upper side is centred at the selection point (namely at 160mm with respect to the central axis) the one on the lower side is centred on the chamber main axis with its centre at 70mm from the input beam axis. Hence, the two flanges have a centre-to-centre distance of 90mm. These two flanges can be used to place the detectors for the on-axis TP (the most convenient option would be a scintillator with a 45° deg mirror and a CCD camera per flange).

As can be seen from the chamber technical drawing, the central section has four reinforcement pillars to increase chamber stability and guarantee 40mm inner clearance. The presence of these pillars and the position of the DN160 flanges are important to preliminary define the geometric detectable ranges, as marked in Figure 5.5. These ranges span from the input flange axis (namely 0 point position) to 85mm, if the beam is detected using the lower DN 160 flange, and from 85mm to 235mm, if the beam is detected using the upper DN 160 flange. These two ranges allow to use the spectrometer in two different modes.In fact, the first set of electrodes can be placed on the input beam axis side, namely at the right side with respect to the gray reinforcement pillar shown in Figure 5.5. This solution would allow to use the device in a low-resolution, wide-dynamic range configuration as lower magnetic fields values can be applied. In this case, assuming the magnet energized with the lowest nominal current of 15 Amp, i. e. B=0,063T, the detectable energy range is relatively wide: from 40 to 300 MeV protons with traces spanning over 85 mm on the horizontal plane and over 24 mm on the vertical plane, but the resolution would be low as it will be shown in the following.

Using higher magnetic field the high energy part of the spectrum can be deflected in the direction of the second set of electrodes increasing the energy resolution, but limiting the dynamics of the device. In fact if the magnets are energized with a current of 209Amp, i. e. B= 0,88T, the detectable energy range in this case will be between 220 and 300 MeV for protons. In this case the dynamics is limited but high energy resolution of few percent can be reached.

The description of the device is limited to two values of the magnetic field: 0,063T, which is the minimum field with good uniformity that can be used and 0,88T, which is not the maximum field that the magnet can reach but it is the highest value allowing to have still a reasonably good dynamic range.

Charge separation is guaranteed in both configurations as the maximum electric field (ΔV=300kV on the electrodes with a gap of 40mm) is applied on both sets of electrodes in the calculation reported in the following.

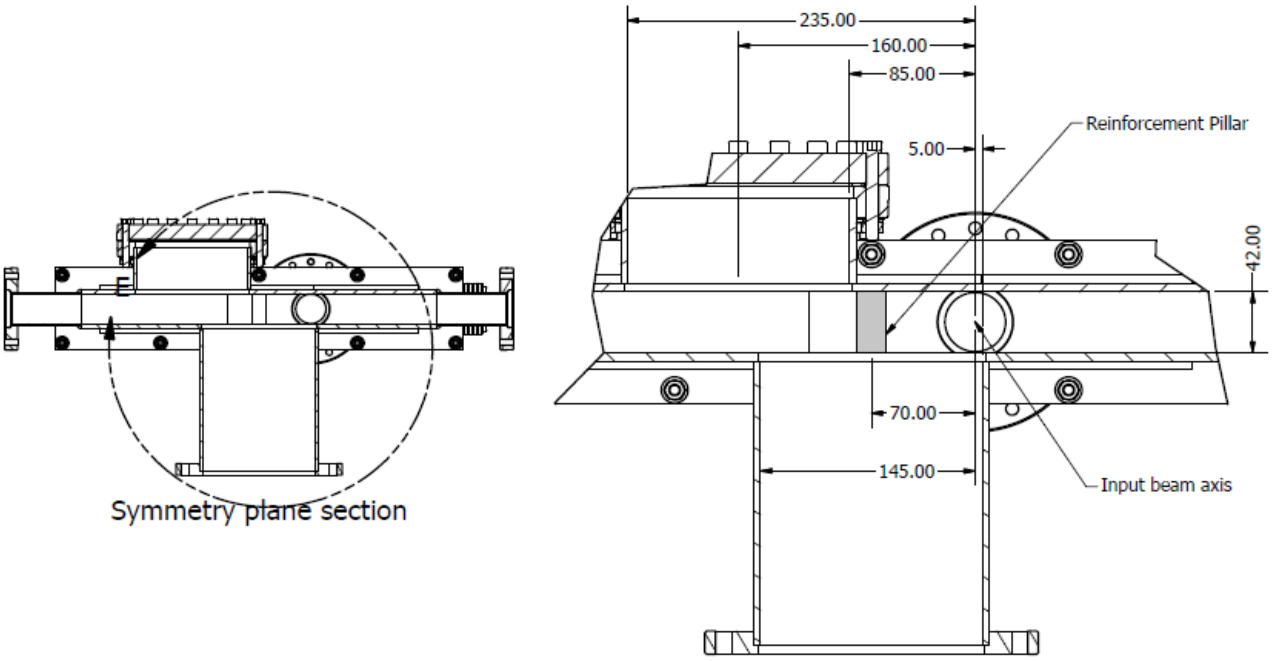

***Figure 5.5**: Cut section of the vacuum chamber on the symmetry plane. Chamber aperture is 42mm, but after manufacturing it is reduced to 40mm*

The above considerations, as stated at the beginning of this subsection, come from an analytic study which allows to set the geometric position of the electrodes inside the vacuum chamber in order to optimize the q/A resolution as the energy resolution depends on the magnetic field position which is fixed for this device as it is part of the already existing energy selector. The best option is shown in Figure 5.6, which is a compromise between applied voltage, electrodes connection with HV feed-through and charge separation.

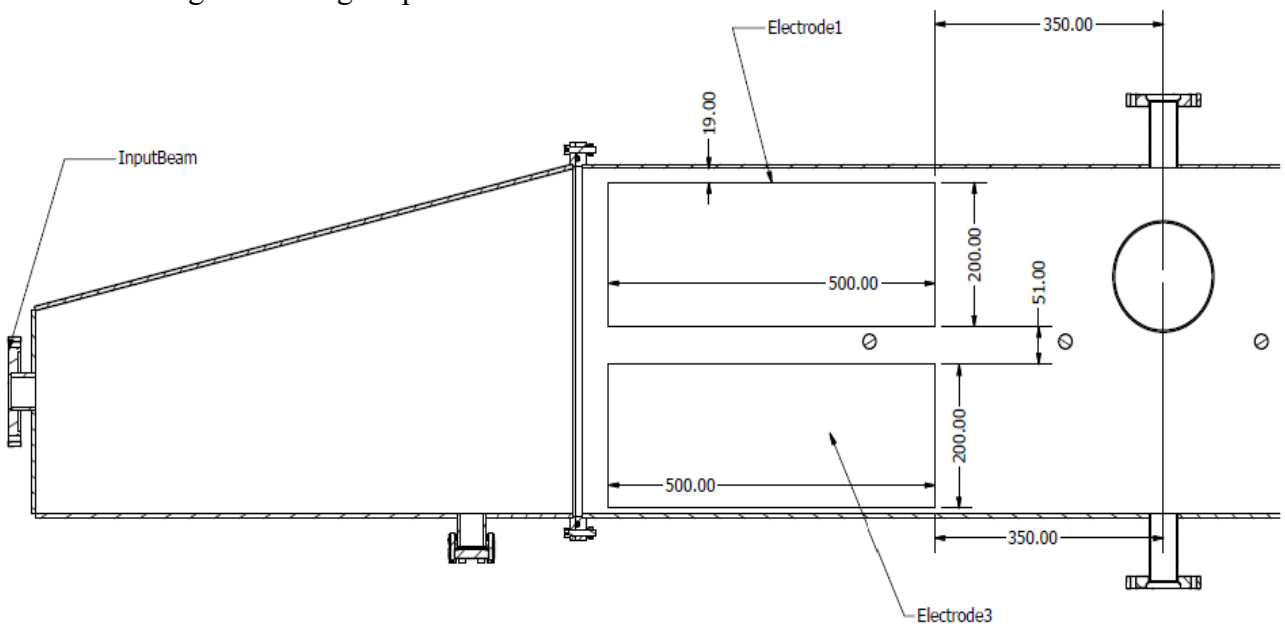

***Figure 5.6**: Scheme of the ESS vacuum chamber with electrodes position*

The main features, as defined with the analytic model, of the on-axis TP are reported in table 5.1. Data about magnetic dipole come from a previous studies [3, 4] and they are the actual geometry

and features of the chicane.

Magnetic dipole	
Mechanical Yoke length	400mm
Effective length (range)	450,23 - 448,34 mm
Magnetic field	0,063 – 1.226 T
Dipole Gap	60mm (55mm at pole radial shim)
Drift yoke-detection plane (mechanical)	1150 mm
Electrostatic dipole	
Mechanical Electrodes length	500 mm
Effective length (fixed)	537.19 mm
Applied Voltage (range)	0 kV – 100 kV
Electric Field	$< 2{,}94 \times 10^5$ – $6{,}25 \times 10^6$ V/m
Gap	32 mm
Drift electrodes-detection plane (mechanical)	350 mm

***Table 5.1**: On-axis TP main parameters*

The above features are sufficient to define electric and magnetic calibration of the on-axis TP, but energy and q/A resolution are strongly dependent on the beam spot-size at the detection plane. Hence, it is important to define which is the maximum size the beam can have in order to ensure good performances. Analytic parabolic traces for protons up to 300 MeV and for C+6 up to 900 MeV are shown in Figure 5.7.

The minimum distance between the two is 3 mm, which means that the beam spot-size at the detector plane should not be bigger than 2 mm in order to have fully resolved charge state. In any case, to resolve all the charge states of carbons a smaller beam spot size is required as the distance between, for example, C^{+5} and C^{+6} is of about one millimetre.

Considering the geometry of the whole beamline, the ideal position of the collimator would be in the small chamber where the collection system is placed. In this case the collimator would be set at about 2.08m far from the detection plane, see Figure 5.8. This means that the collimator size has to be extremely small. Moreover, the collimator has to be thick enough to stop high energy protons.

The best solution would be to realize a double-blade system with the first set of blades cutting the particles in the horizontal direction and the second set cutting in the vertical direction. Such double-blade system can be relatively long with not complication in its manufacturing. Simple geometric calculation and multiparticle tracing with beam optics code shown that two sets of blades, each of them with a length of 150 mm and 5 mm space between first and second set, closed in order to have a total aperture of 0,2mm would allow to have a beam spot size of 1mm in diameter (angular aperture of the collimated beam of about 0,17 mrad). Results of particle tracking

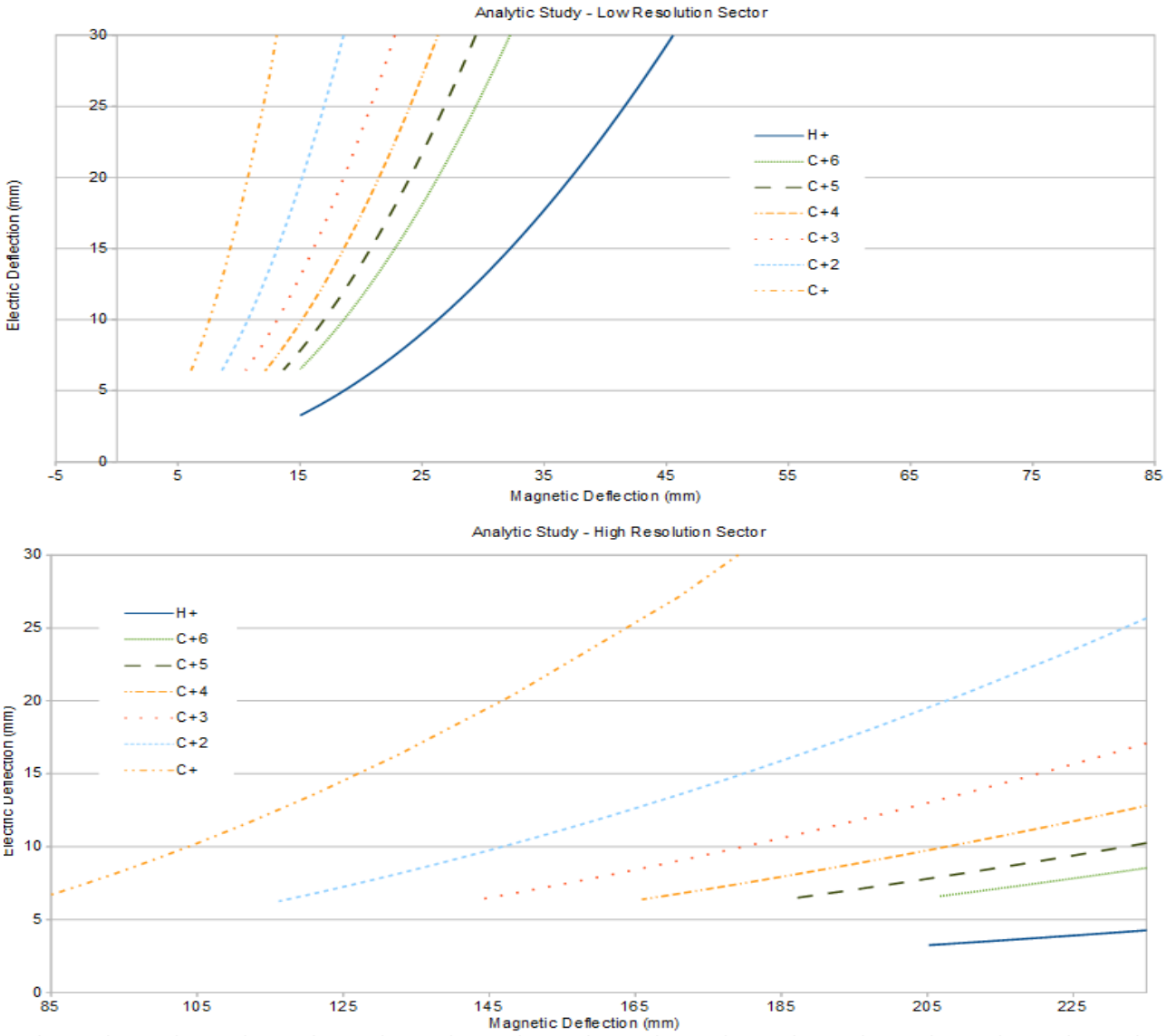

***Figure 5.7**: Analytic H^+ and C parabolas. Upper panel shows the low-resolution sector, the lower panel shows the high resolution sector.*

simulations are shown in Figure 5.8 and 5.9. Figure 5.10 shows the beam spot size at the detection plane if the double blade aperture is 0,1mm.

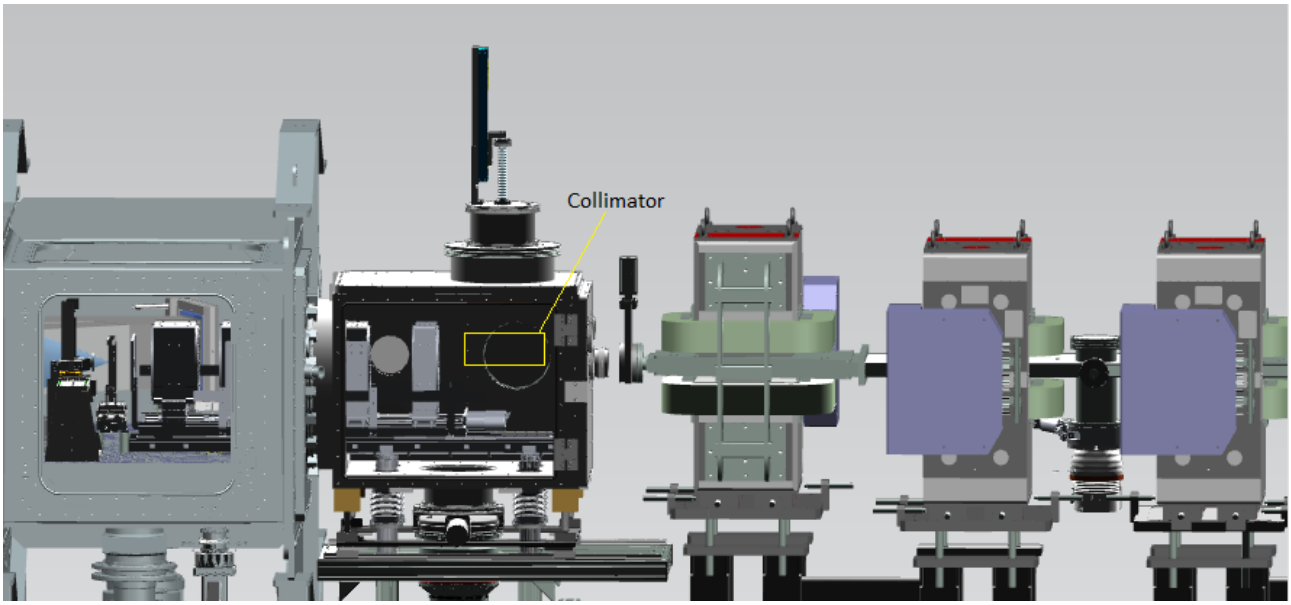

Figure 5.8: *On-axis TP collimator position*

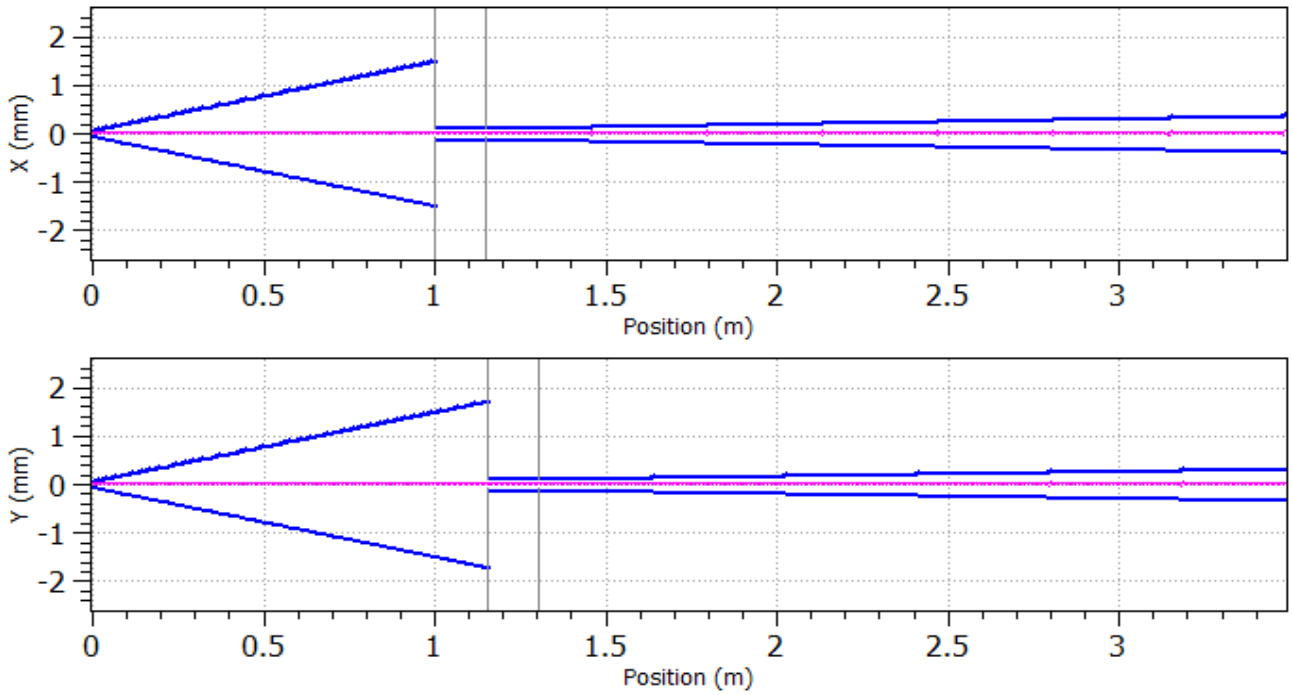

Figure 5.9: *Beam envelop through the double-blade collimator with correct distances*

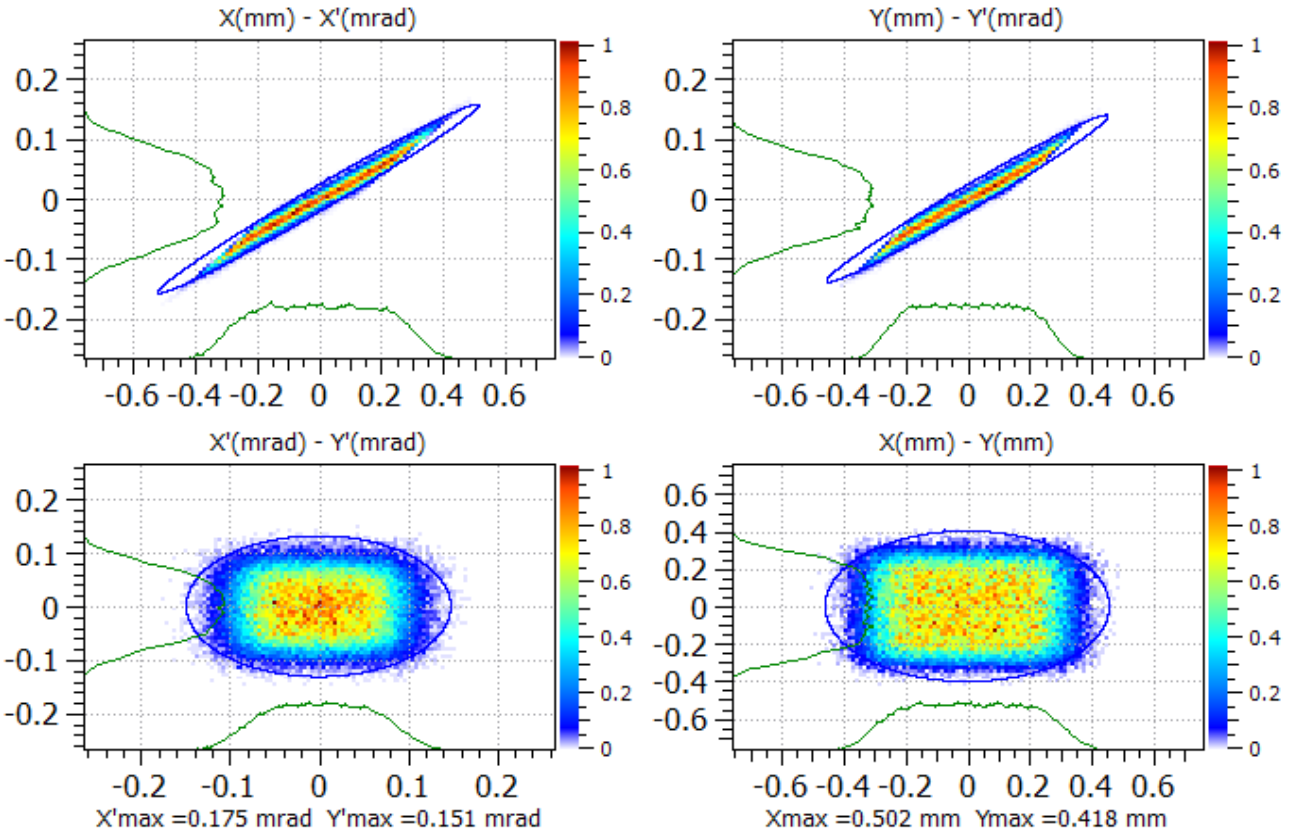

***Figure 5.10**: Beam phase space plot at the detection plan*

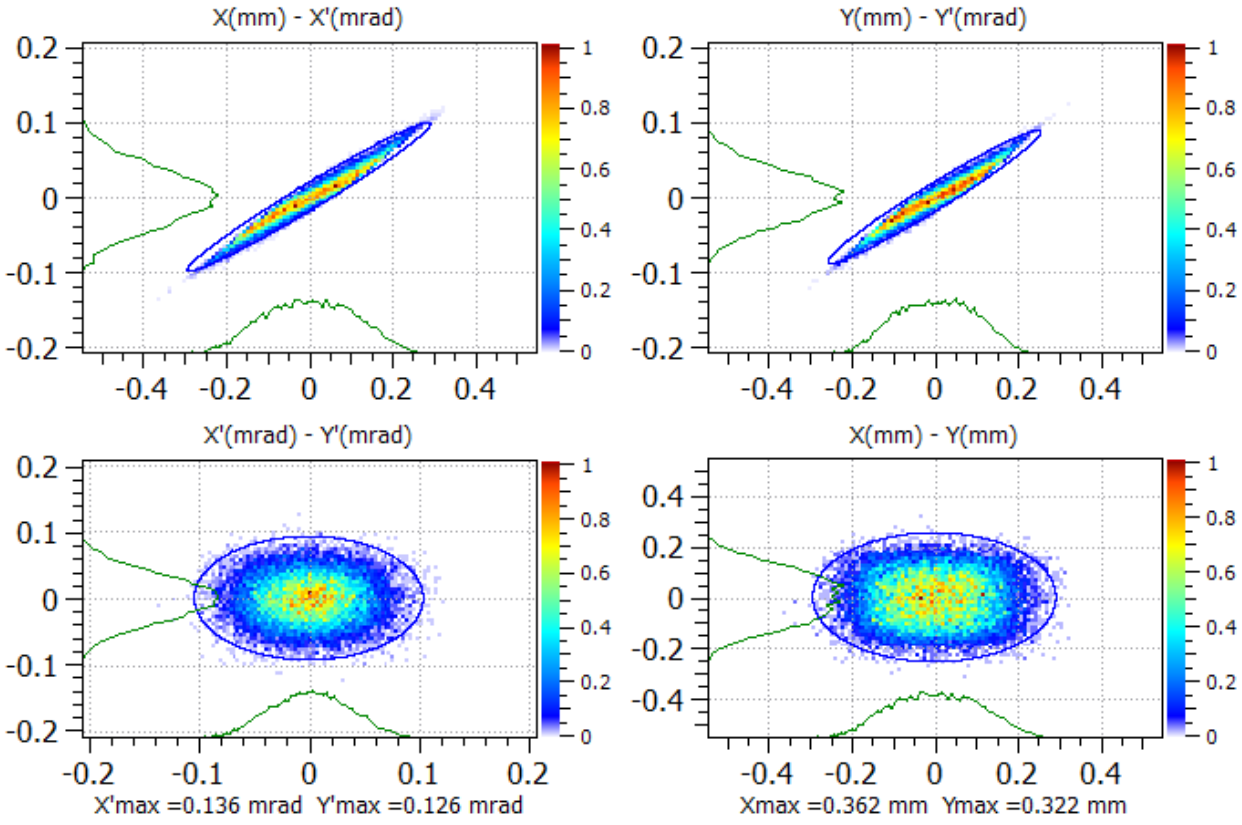

***Figure 5.11**: Beam phase space plot at the detection plan with a 0,1mm double-blade collimator*

Using the described collimation system, with a 0,1mm aperture size, the beam spot size is reduced to ~0,7 mm, which can improve the on-axis TP performances in terms of charge separation and energy resolution. To be more conservative the beam features at the collimator out will be slightly increased with respect to those reported in Figure 5.11; namely a 0,8mm beam spot size will be used to determine resolutions and 0,155mrad will be used as half angular aperture of the beam at the collimator output in the multiparticle simulations.

The on-axis TP has been analysed also using FEM codes Comsol (whose field maps are used for particle tracking simulations in SIMION) and OPERA 3D used also for particle tracking.

Results on the magnetic analysis are presented in [3], only the electric dipoles study is here briefly reported.

Figure 5.12 shows the geometry simulated in Comsol which includes the magnets, a simplified scheme of the vacuum chamber and the two electrostatic dipoles (in blue). Figure 5.13 shows the geometry in OPERA 3D which is limited to a more detailed scheme of the vacuum chamber (with pillars and flanges on the detection plane and the electrostatic dipoles. The magnet is simulated in a different model and result are imported in the electrostatic model for the particle tracking simulations. In all codes used z=0 is the position of the detection plane at the chamber centre.

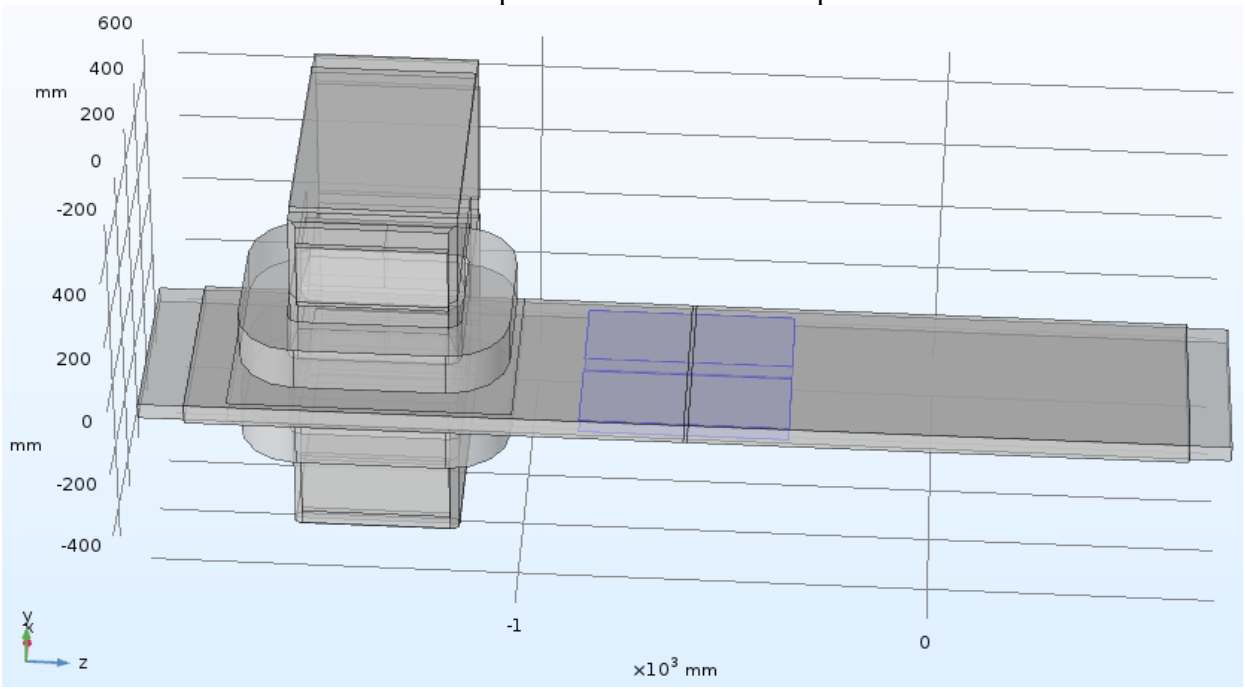

***Figure 5.12**: Geometry in Comsol, electrodes are in blue*

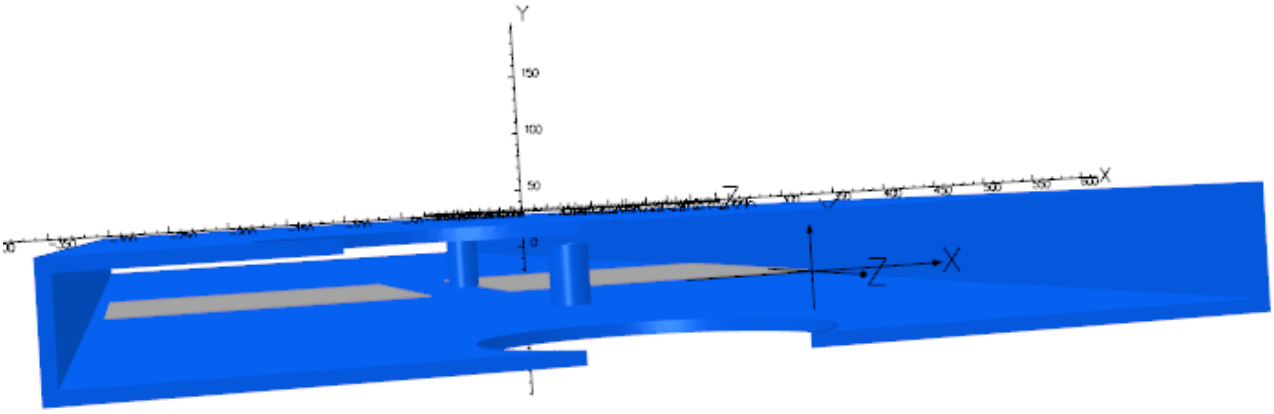

***Figure 5.13**: Geometry in OPERA 3, electrodes are in grey vacuum chamber in blue*

5.2.2 Electric field analysis

Results on the electric field analysis are exactly the same with both FEM codes and also for both set of electrodes. Main data are summarized in the next table 5.2.

	Emax (V/m)	Int(E) (V/m*mm)	Effective length (mm)
±100 kV	$5{,}88X10^{6}$	$3{,}16X10^{9}$	537,19
±50 kV	$2{,}94X10^{6}$	$1{,}58X10^{9}$	537,19
±25 kV	$1{,}47X10^{6}$	$7{,}90X10^{8}$	537,19
±10 kV	$5{,}8X10^{5}$	$3{,}16X10^{8}$	537,19
±5 kV	$2{,}94X10^{5}$	$1{,}58X10^{8}$	537,19

***Table 5.2**: Electrostatic dipoles analysis*

Figure 5.14 shows the electric field along the main axis for the voltages reported in table 5.2.

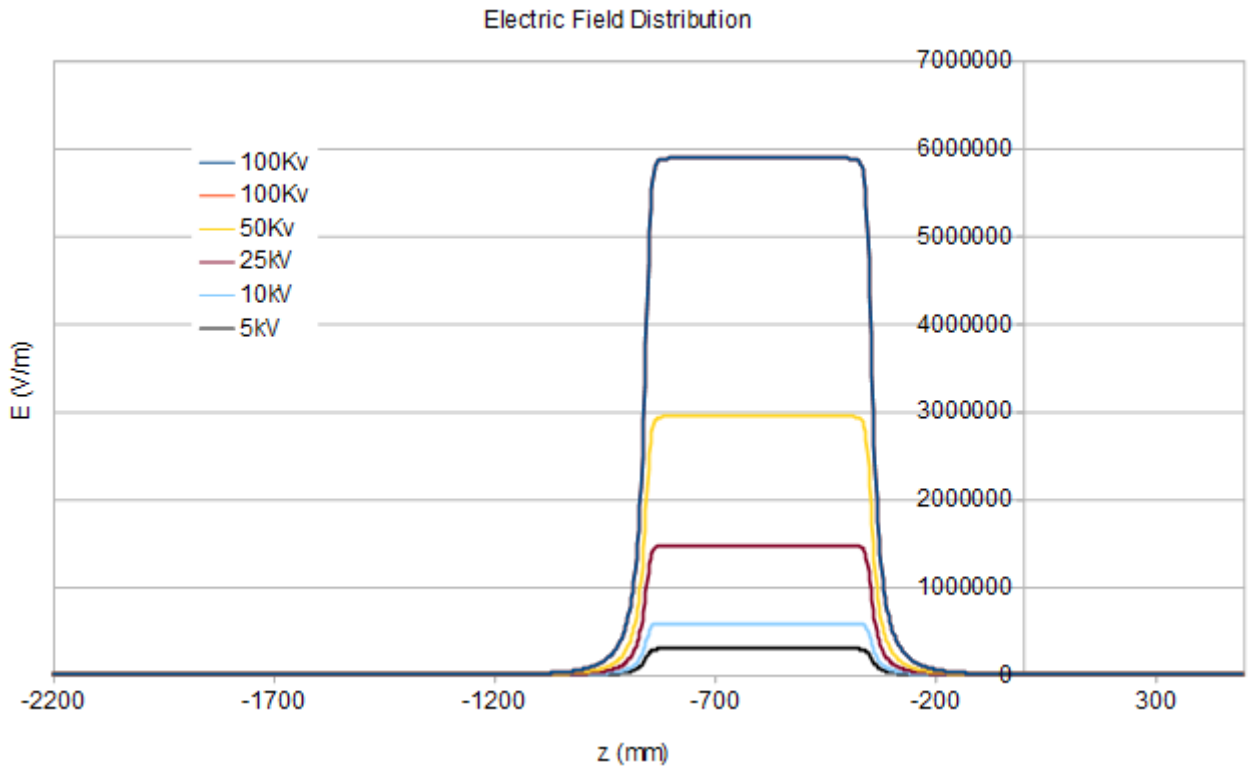

***Figure 5.14**: Electric field distribution along the central axis*

The setup, made by two sets of identical electrodes, may eventually suggest to use both set at the same time for increasing the dynamics of the on-axis Thomson Parabola. On the other hand, the two set are very close to each other and the idea to detect the beam using the DN160 flanges placed on the chamber symmetry plane (see Figure 5.5) implies that the electric field in the electrostatic dipoles must be in the opposite direction, hence, the cross talking between them must be taken into account.

Table 5.3 shows how the effective length of the electric field is considerably reduced when the maximum voltage is applied to one dipole and a lower voltage is applied to the other dipole.

	Emax (V/m)	**Int(E) (V/m*mm)**	**Effective length (mm)**
±100 kV (low resolution sector)	$5{,}88X10^{6}$	$3{,}16X10^{9}$	537,12
±25 kV (high resolution sector)	$1{,}47X10^{6}$	$7{,}90X10^{8}$	532,12
±5 kV (high resolution sector)	$2{,}94X10^{5}$	$1{,}56X10^{8}$	531,76

***Table 5.3**: Electrostatic field analysis in case of both dipoles are energized.*

As can be seen from results in Table 3, the simultaneous use of both electrostatic dipoles cannot guarantee the nominal resolution of the device due to the cross talking effect.

The electric field peak ($5{,}88x10^{3}$ V/mm) is well below the electrical breakdown limit in air for small gaps ($4{,}36x10^{4}$ V/mm), as predicted by Paschen's Law [5]. Considering that the vacuum chamber, without any heating system, can reach $1x10^{-7}$ mbar, discharges between the electrodes are not an issue. In any case the problem of discharges with vacuum chamber has to be faced selecting a proper insulator and the correct shape as interference with the chicane reference trajectory must be avoided.

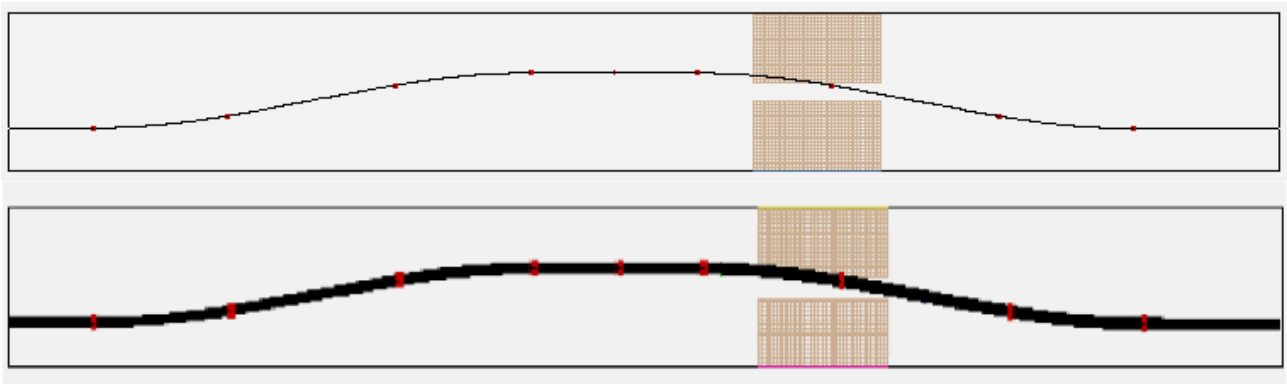

***Figure 5.15**: Reference orbit of the ESS and detail of the orbit in the electrodes position. In the free space between the two set of electrodes there are the reinforcement pillars*

From Figure 5.15, where the trajectory of a single particle (upper panel) and the trajectory of a 30mm radius beam (lower panel) are shown, it is evident that the electrodes should be fixed on the chamber roof and floor together with the insulator and no side structure can be used or it will clash with the chicane main reference trajectory.

A possible solution is shown in Figure 5.16, where the full ESS is shown. The vacuum feed-through are placed between the first and second dipole and connected to the electrodes. Figure 5.17 shows the detail of electrodes and insulator setup.

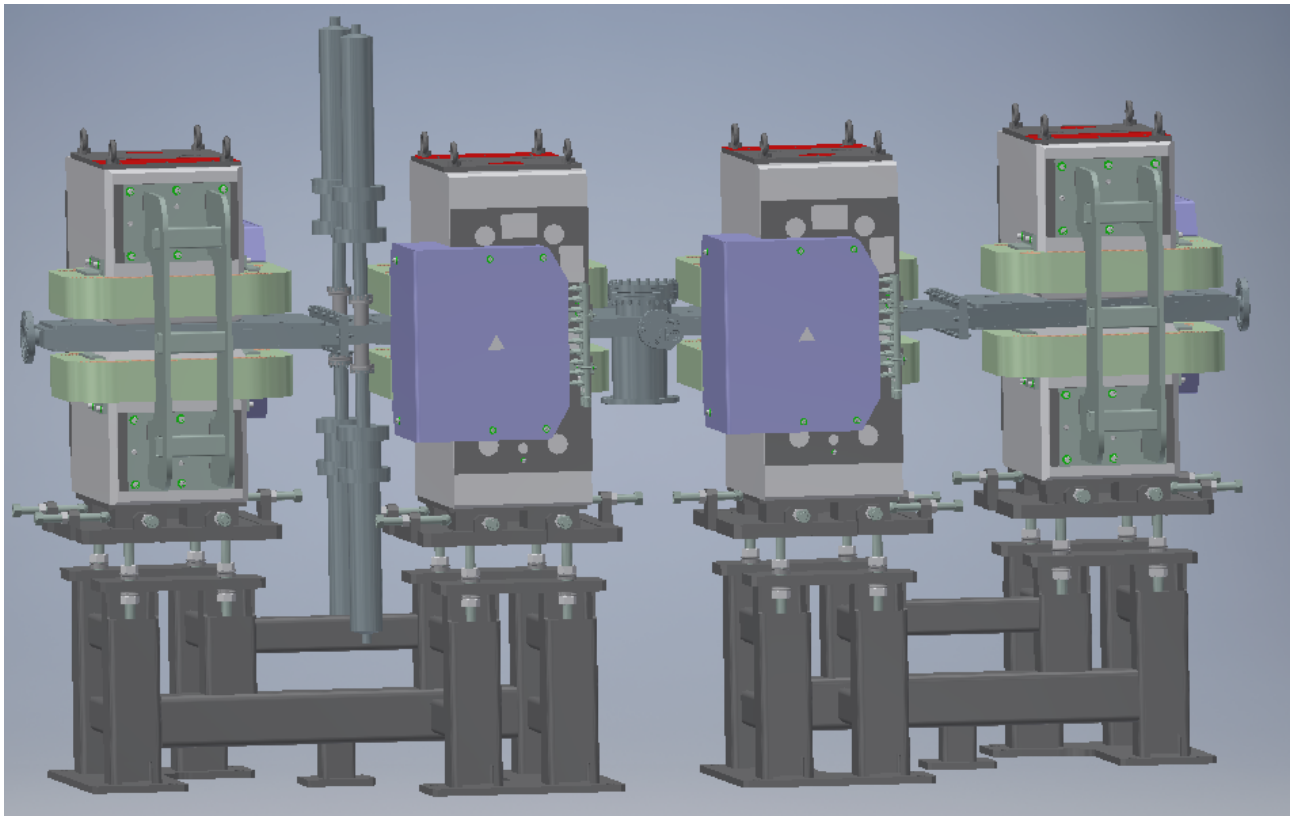

***Figure 5.16**: View of the chicane with high-voltage vacuum feed-through placed between the first and second dipole*

***Figure 5.17**: Details of the electrodes (dark gray) and insulator and insulator (light gray), in blue is shown a portion of the HV wire*

The insulator will consists in a double layer of high dielectric strength material (PBN, Pyrolytic Boron Nitride, with 230 kV/mm is the best choice [6]). Each layer will be 1mm thick, which is the standard thickness for PBN sheet, but the one directly in contact with the chamber wall will have a surface of 600x225mm and the one directly in contact with the electrodes will have a surface of

100x100mm. This solution would increase the robustness of the insulator as the possible path for a discharge will be considerably longer than what one we can have if the two layers would have the same dimensions as the electrodes.

As said above, the electrodes and the insulator must be glued together and to the chamber, hence it is important to calculate the electric force between them. The force can be calculated considering the maximum electric field and the area of the electrodes to obtain the charge as:

$$Q = E \cdot \epsilon_0 \cdot l \cdot d = 5.208 \cdot 10^{-6} C$$

being *l=500mm* and *d=200mm* the linear dimensions of the electrodes. The force depends on the charge and the electric field and it results to be:

$$F = \frac{Q \cdot E}{2} = 17.3\text{N}$$

From this result it is evident that the attraction force between the electrodes is not an issue as epoxy based vacuum glues have usually tensile shear higher that 1000psi which means that they can stand several kilo Newtons, considering the electrodes area. No force between electrodes and chamber is present as the chamber is grounded.

The above considerations shows that the electrodes assembly with the chamber should not be critical, but some more care on has to be used in order to reduce the probability of discharges. First of all the electrodes surface must have a limited roughness. 316L Stainless steel, which is the bests choice for this electrodes, can be polished to an average roughness (Ra) of few microns with standard treatment; electropolishing or other special treatment may produce better results with roughness below 1 micron. Obviously the electrodes will have no sharp edges, this means that a curvature radius on the electrodes cross section has to be defined in order to reduce the high voltage stress at the edge of the electrodes that could lead to sparks. A FEM analysis have been performed in order to study the field distribution between electrodes and chamber and how it changes for different gaps between electrodes and for different chamfering at the electrode edges. Figure 5.18, upper panel, shows the setup in the simulations, where vacuum chamber and electrodes are in gray and insulator layers are in blue. Figure 5.18, lower panel, shows the field distribution between electrodes and chamber walls in the case of a 30 mm gap between electrodes, i.e. 3mm of insulator layers and 2 mm thick electrodes for whose the chamfering has 1mm curvature radius. Calculation are done for different gaps (34, 32 and 30mm), hence for different insulator thicknesses and for different curvature radius (from 0,1 to 1 mm). Results are shown in Figure 5.19.

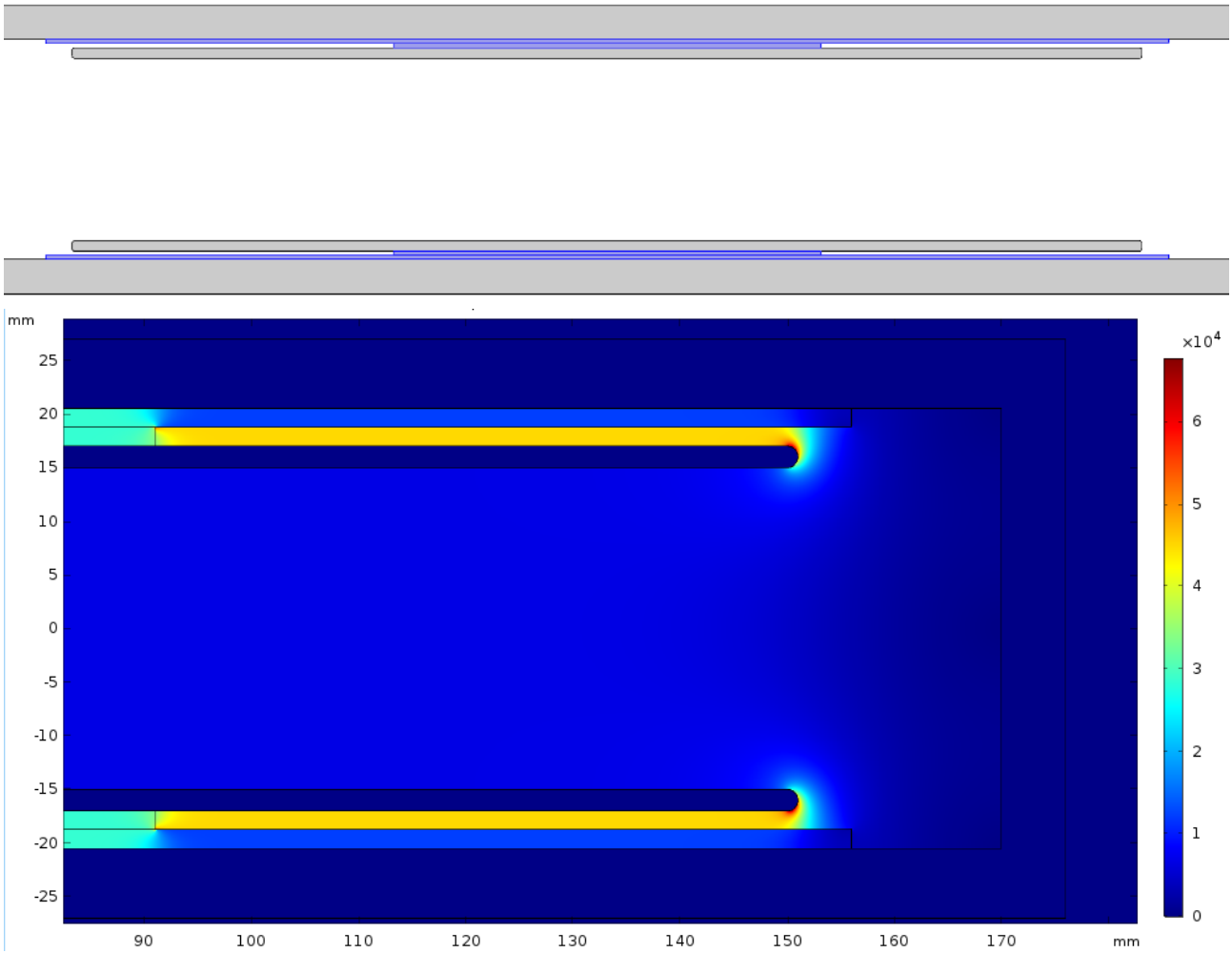

***Figure 5.18**: Setup of 2D FEM simulation for electric field distribution study (upper panel) and field distribution for a 1mm curvature radius chamber and 30mm gap between electrodes (lower panel)*

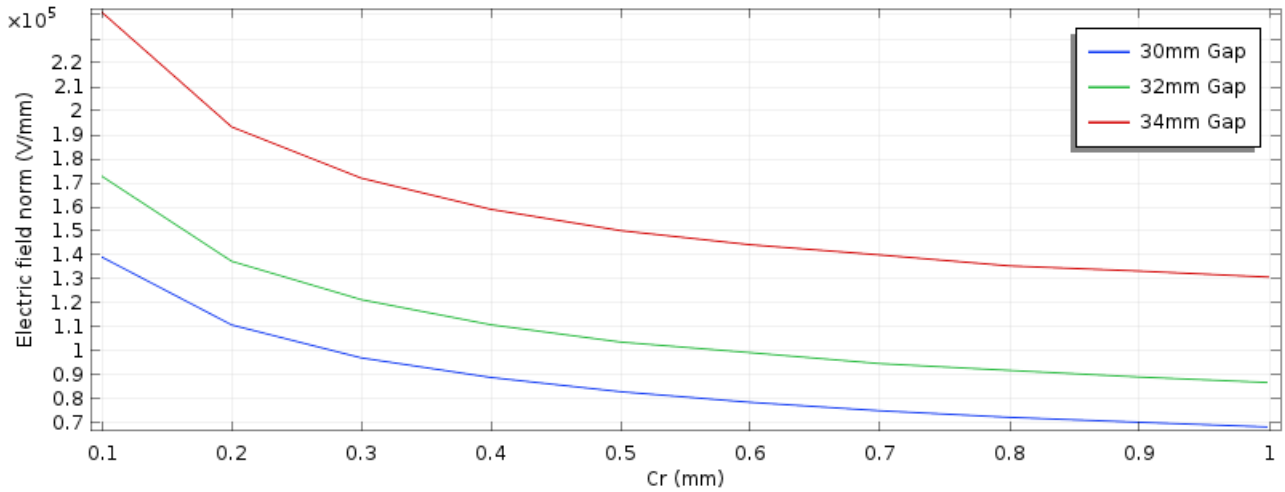

***Figure 5.19**: Electric field peak value as a function of the electrode edges chamfering curvature radius (Cr) and gap*

As can be seen the electric field peak value decreases with the electrode edges curvature radius and also with the gap. Best solution would be a 30mm gap with 1mm curvature radius for the chamfering, this would not affect the ESS performances as enough clearance for the beam in the

chicane is available. Anyway, some prototyping would be necessary, especially it is important to test the real properties of the PBN as a first stage and later would be important to test the electrode plus insulator assembly with connection to the HV feed-through before installation in the chamber. Another issue can be due to corona discharges that might be produced between electrodes and chamber. A solution could be a pulsed use of power supply, with a fast ramping up and down of the field. This might limit the corona discharges using the inertia of the media involved in the process. Prototyping will be also useful to define a proper conditioning cycle, which might be several hours for this setup.

In any case, in the following the electric field will be considered as produced applying 100kV to the electrodes with a 34mm gap in between. If the gap will be reduced the same voltage on the electrodes would produce a slightly higher field which will improve the charge separation.

5.3 Analysis of Thomson Parabola @ ELIMAIA performances

This section shows the performances of the proposed layout for the Thomson Parabola using single particle simulations, to define the nominal feature of the spectrometer. After multiparticle simulations results are analysed in order to take into account the physical dimensions of the beam. At the end calibration with standard accelerator of the first magnet is shown.

5.3.1 Electric and magnetic deflection sectors analysis

In this section is proposed a detailed analysis of the deflection sectors of the above described Thomson Parabola using single particle tracing in Simion and OPERA 3D. Results are compared with analytic calculations. The analysis is done considering protons with 300 MeV maximum energy and carbon ions from C^{+6} to C^{+1} whose maximum energy depends on the accelerating voltage of 150 MV, half of the voltage accelerating the protons [7]. Energy resolution and charge separation are here calculated assuming a beam spot size at the detector plane of 0,8mm, slightly bigger than what expected with a 0,1mm collimation, as shown in Figure 5.12. The analysis is firstly done for the low-resolution sector and after for the high-resolution sector. Only two values of the magnetic field are considered: 0,063 T for the low-resolution sector and 0,878 T for the other one. The electric field has always the maximum value, as the analysis is done to verify performances for the highest ion energies expected.

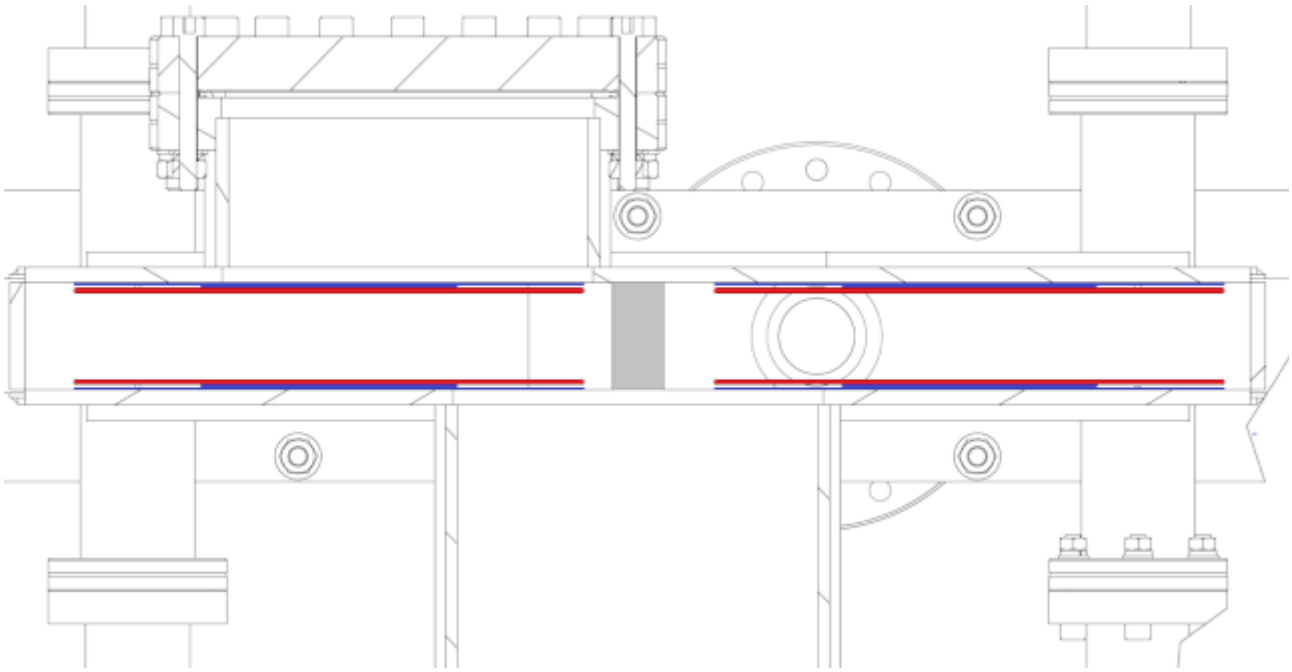

***Figure 5.20**: Chamber cross section at the detection plane. In blue is the PBN insulator layer, in red the electrodes and in grey the reinforcement pillar*

The choice of the magnetic field values depends on the setup and on some technical aspects. As can be seen from Figure 5.20 and from the detailed dimension in Figure 5.5, the low-resolution section has pretty large electrodes, but the use of positive magnetic field would allow to use only a small portion. On the other hand if the magnetic field is negative a wider region could be used but would make more complex the detection system which could be done, in a first step, using a scintillator with a 45° mirror behind it to send the produced light outside the two DN160 flanges. For this reason the magnetic field is, at the moment positive, which is also the polarity used for the first magnet in the chicane. In general revert polarity in a magnet, especially if its yoke is laminated, is straight forward. Moreover the magnetic field value used for the low-resolution sector is the minimum nominal magnetic field. Smaller field are off course possible for this Thomson Parabola setup, as the field quality is relatively important.

For the high-resolution sector the field value used in the following is the minimum field value which, according analytic calculations, allows to detect protons up to 300 MeV, smaller values would produce losses of the highest energy on the reinforcement pillar. Higher values, up to 1.2 T are possible, but the detectable proton spectrum will be progressively smaller till they will be completely lost. On the other hand, low-charged and/or heavier ions would be more accurately analysed. As it will be more clear in the following, the high-resolution sector might also be used to analyse specific ion with a certain charge over mass (q/A) ratio.

5.3.1.1 Low-resolution sector

Figure 5.21 shows the single particle tracking in the setup. Magnet is not visible as just the magnetic field is imported in the solved electrostatic model. Simulation shows traces of H^+ and carbon ions (form C^{+6} to C^{+1}). In this figure as well as in Figure 5.22 the colour of traces indicate difference in energy, it is not related to ion species.

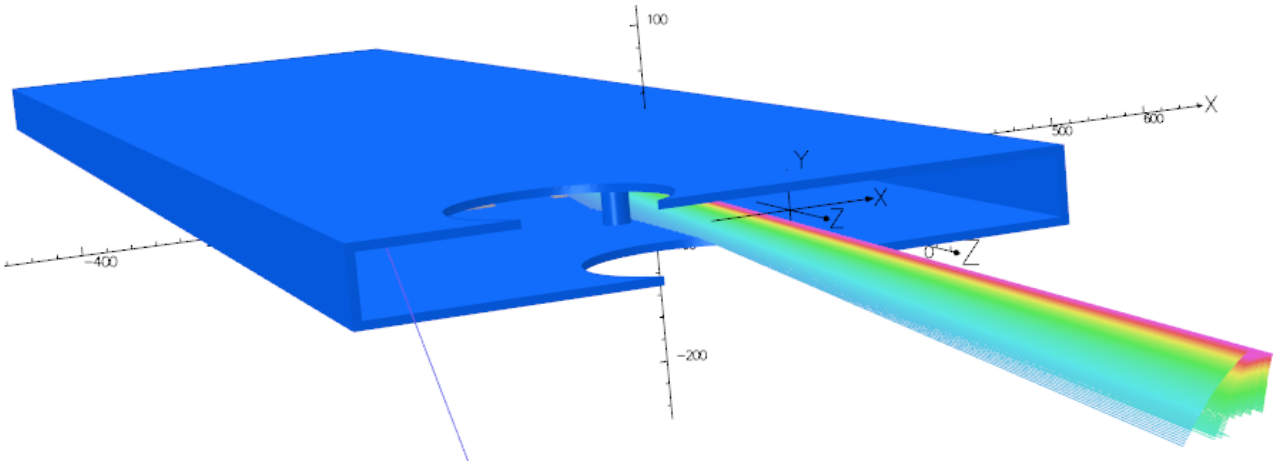

***Figure 5.21**: Single particle tracking in the ESS-TP*

Figure 5.22 gives a detailed view of the particle trajectories with respect to the electrodes position. It is evident that only a small portion of the electric field is used due to the magnetic deflection. If the magnetic field is reversed, a bigger portion of the electric field will be used and also the detectable energy range may be wider. This solution is not anyway investigated here.

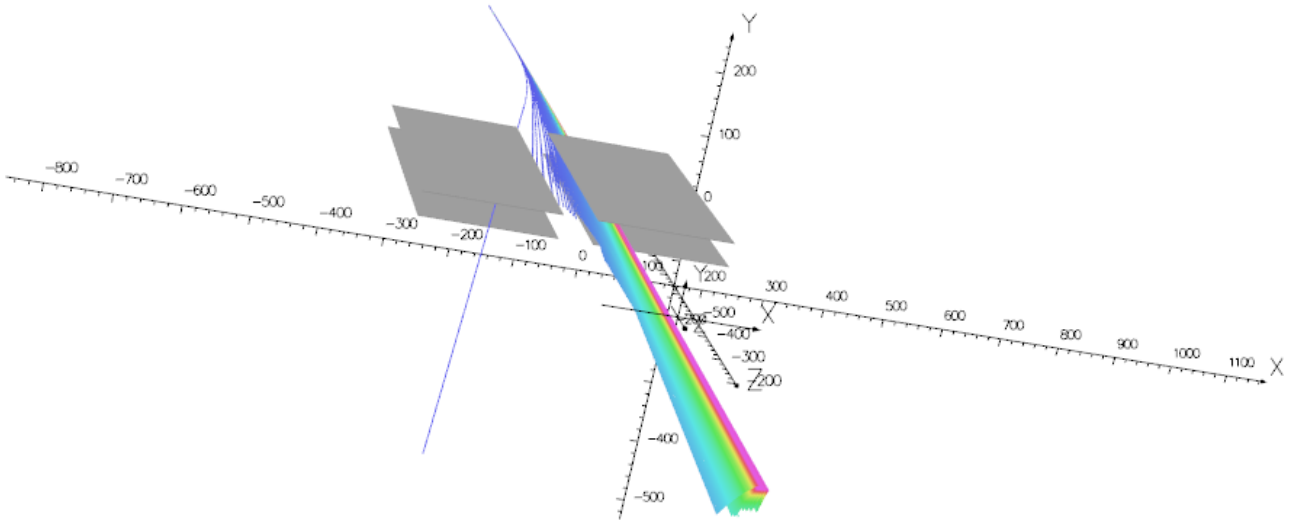

***Figure 5.22**: Details of particles trajectory in the low resolution electric deflection sector.*

In a Thomson Parabola magnetic and electric deflections are independent and are mainly responsible for energy and q/A resolutions. Hereafter, electric and magnetic deflections are analysed for protons up to 300 MeV and carbon ions with different charge states assuming they are accelerated by an electric potential of 150MV. Simulations have both fields during tracking. Analytic magnetic hyperbolas for protons and C^{+6} are shown in the following Figures 5.23 and Figure 5.24 together with simulated traces. Here simulated traces are reverted in sign, for both vertical and horizontal deflections, to match analytic results.

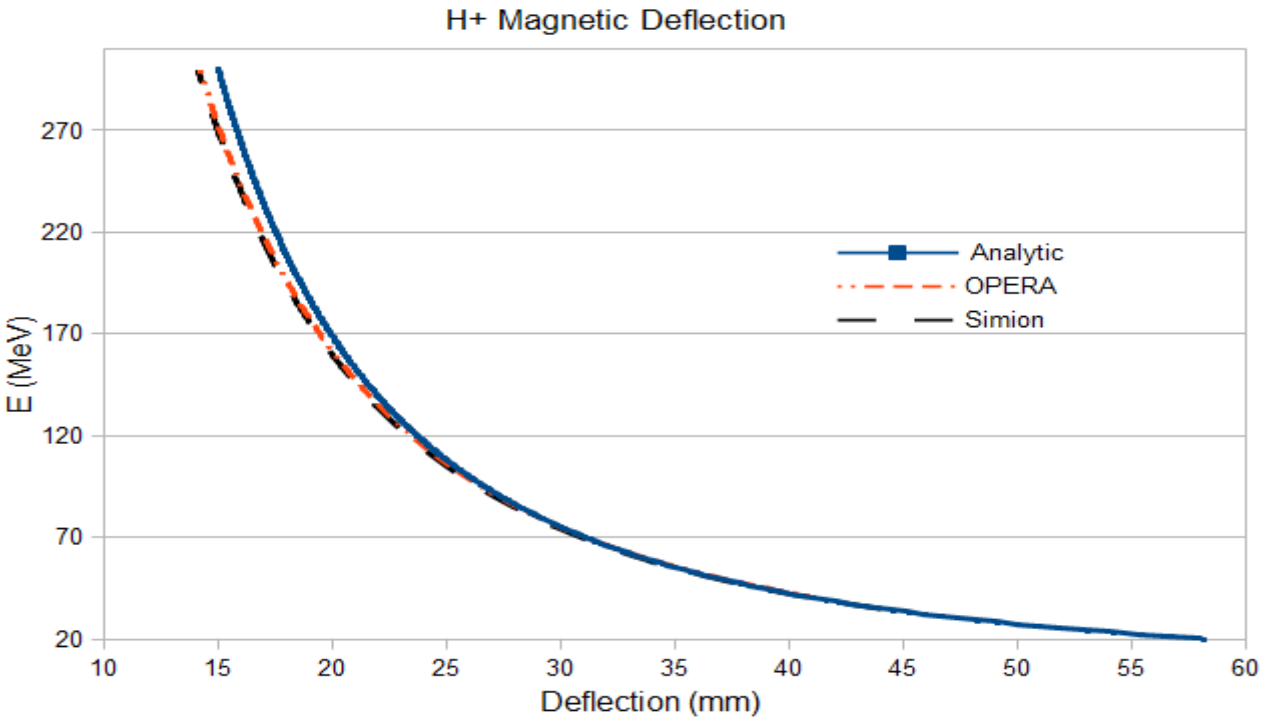

***Figure 5.23**: Magnetic deflection hyperbola for protons*

The plots show comparison between analytic calculations and simulations made with OPERA

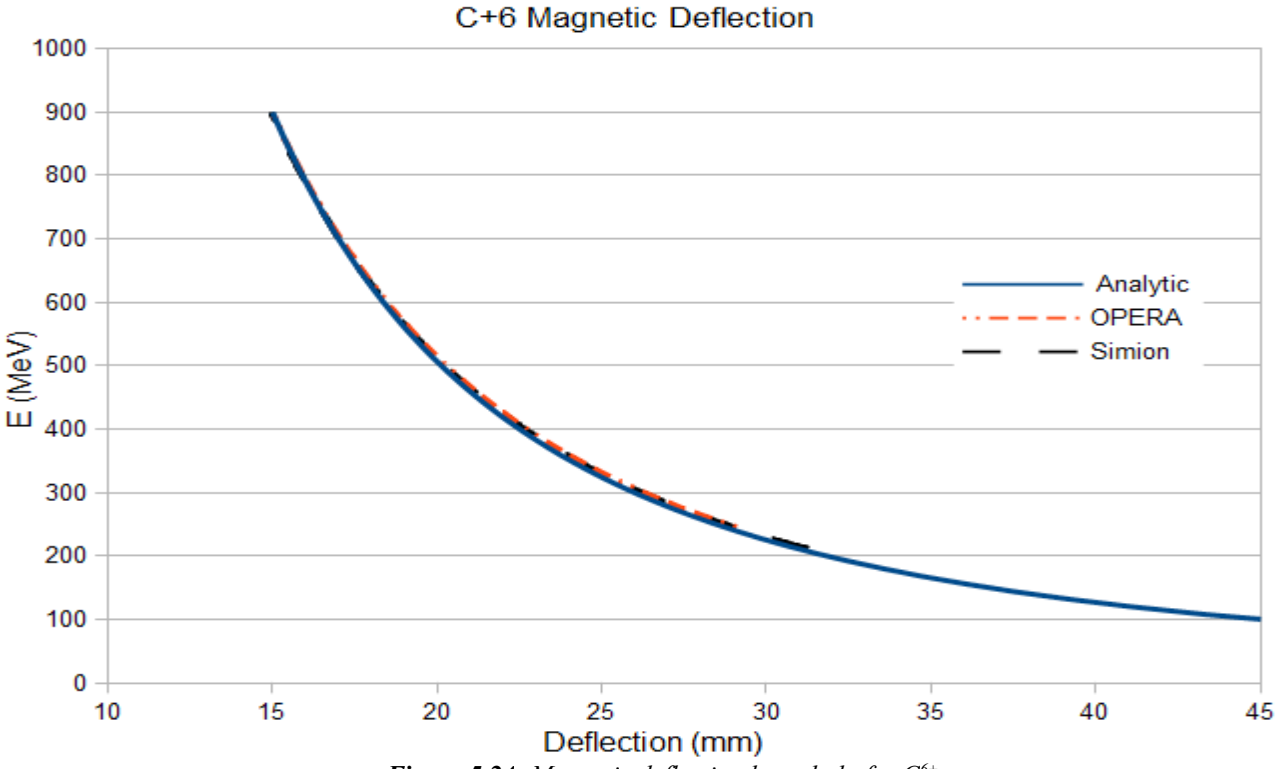

***Figure 5.24**: Magnetic deflection hyperbola for C^{6+}*

3D and Simion. OPERA 3D is used to calculate both electric and magnetic field, even if the magnetic field is imported in the the electrostatic simulation before performing the tracking. In Simion simulations the electric field is also calculated but the magnetic field is imported from COMSOL simulations. It is evident the good agreement between simulations and a small deviation in the analytic calculation mainly depending on the effective length of the magnet used.

The energy resolution is calculated as:

$$R = \frac{dE}{dx} \cdot s$$

where E and x are the particle energy and the deflection, and s is the beam spot size at the detector plane. Figure 5.25 and 5.26 show the energy resolution (in percentage) for H^+ and C^{6+}. As can be seen from the plots the maximum energy can be resolved with 10% of precision, which is already a good result. The resolution can be increased with the magnetic field, hence, this value is actually the lower resolution of the device.

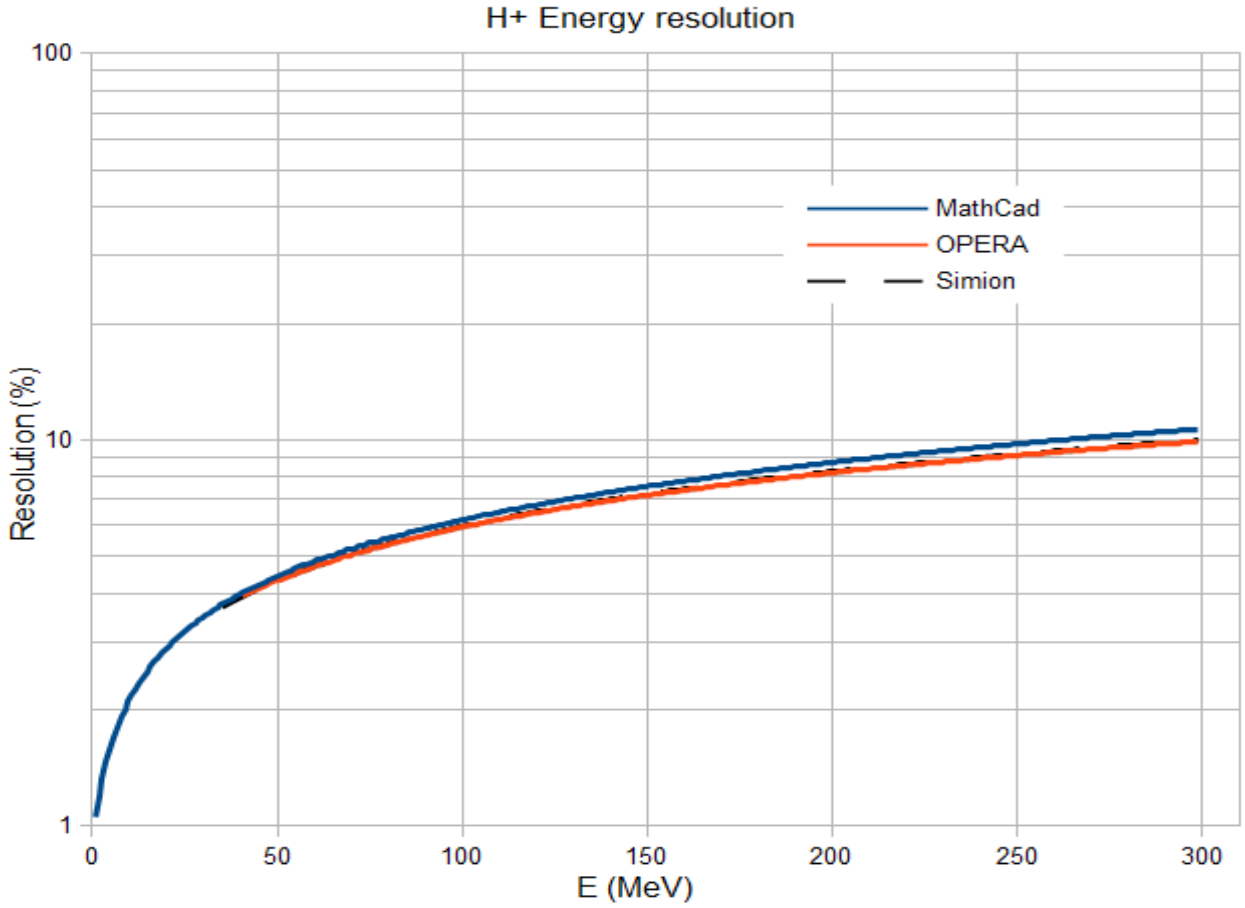

***Figure 5.25**: Energy resolution for protons*

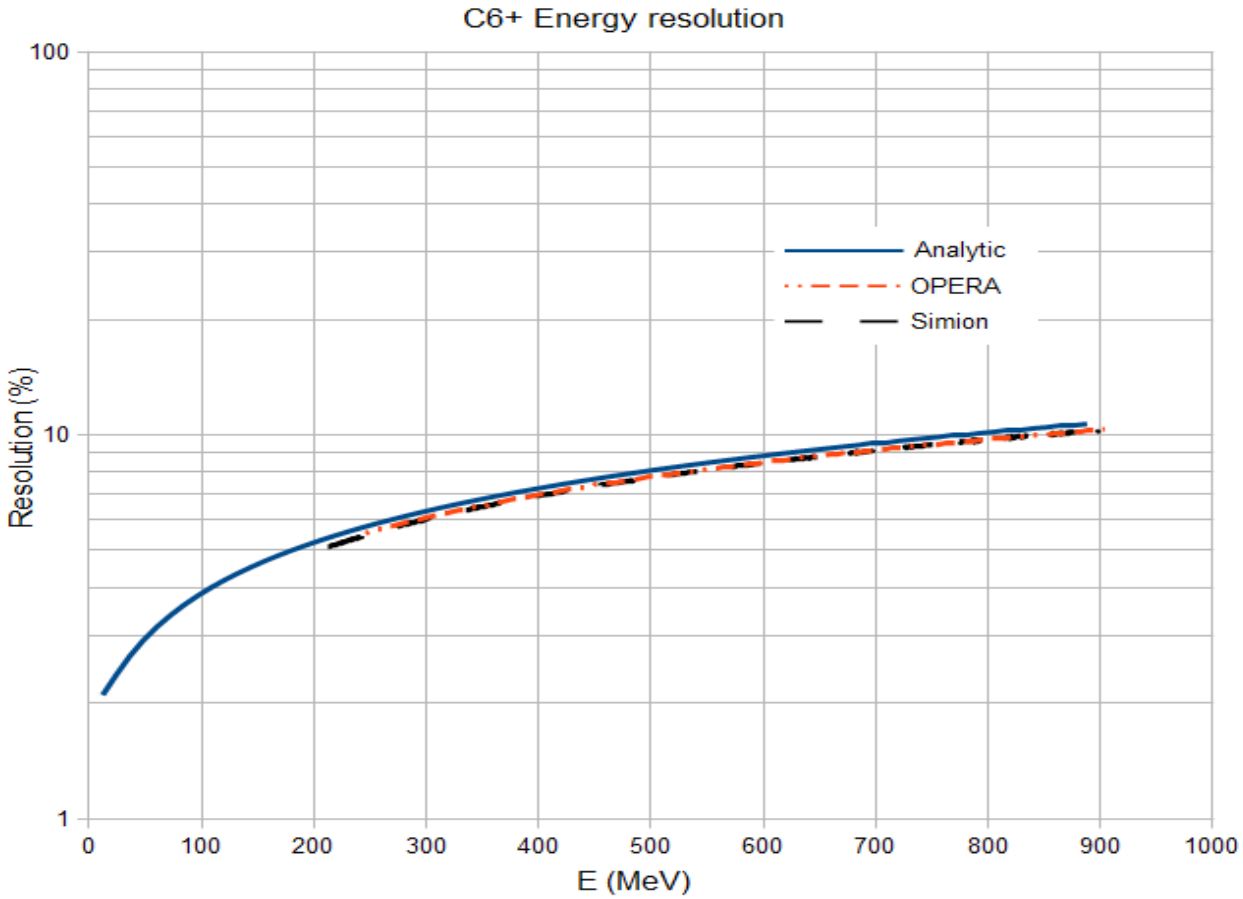

***Figure 5.26**: Energy resolution for C^{6+}*

Analytic electric hyperbolas for protons and C^{+6} are shown in the following Figures 5.27 and Figure 5.28 together with simulated traces.

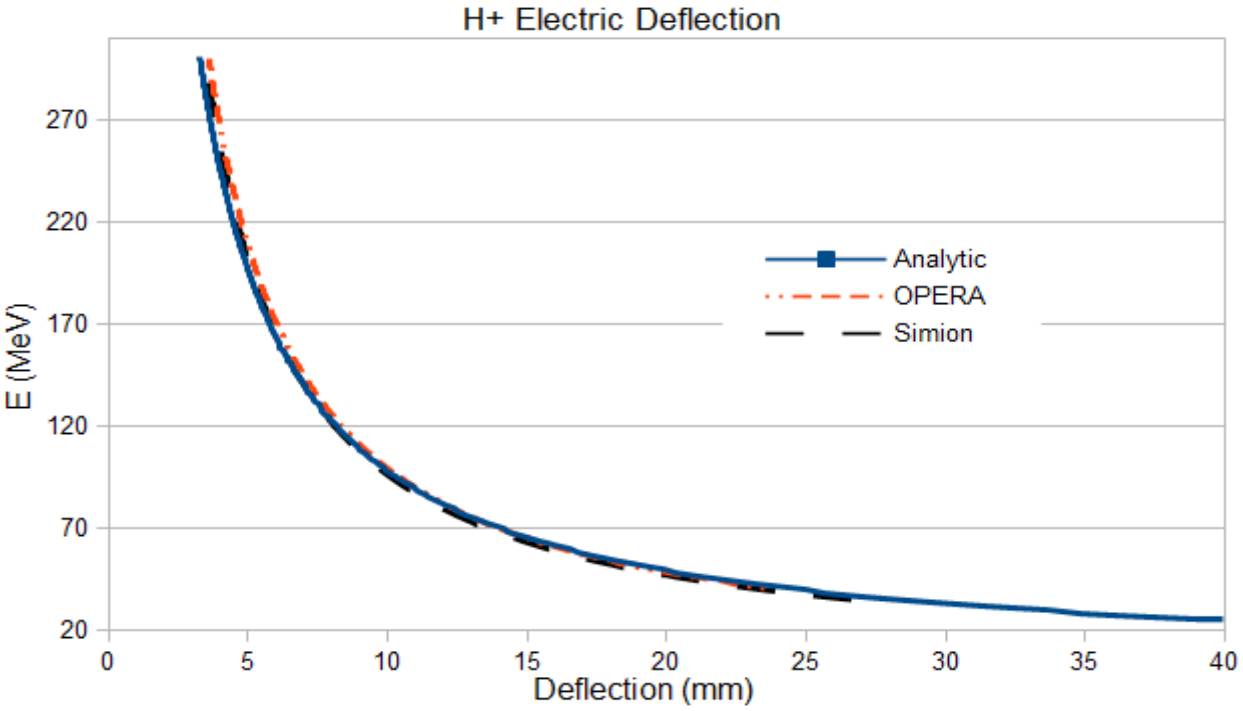

***Figure 5.27**: Electric deflection hyperbola for protons*

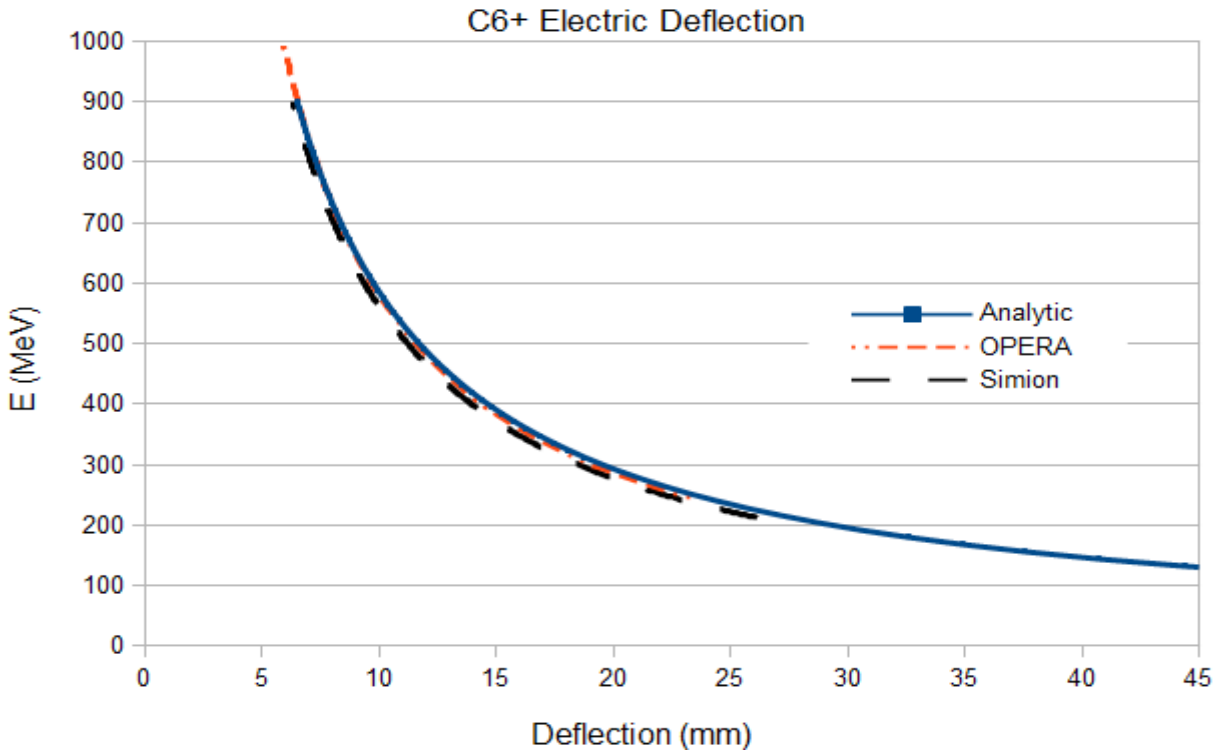

***Figure 5.28**: Electric deflection hyperbola for C6+*

Again there is an almost perfect agreement between simulations and in this case also the agreement with analytic calculation is better as effective length of the electrostatic dipoles is easier to calculate and does not depend on the field strength. Small deviations depends on small differences in the geometry. The electric field is used for charge separation and energy resolution is not relevant, anyway calculations shows it is below 20% for each ion species. Nominal charge separation, between contiguous ion species, is reported in table 5.4, which summarize the main results obtained and describing the nominal performances of the devices such as exact detectable energy range of the ions, maximum deflection in vertical and horizontal, due to the geometry, energy resolution and q/A separation for protons and all charge states of carbons.

	E_{min} (MeV)	E_{max} (MeV)	Geometric range (mm)	Resolution (%)	q/A separation (mm)
H^{+}	40	300	0 – 85 Horizontal 0 – 23 Vertical	10	H+/C6+:1,71
C^{6+}	230	900		10	C6+/C5+: 1,24
C^{5+}	200	750		12	C5+/C4+: 1,38
C^{4+}	150	600		15	C4+/C3+: 1,37
C^{3+}	120	450		15	C3+/C2+: 1,82
C^{2+}	80	300		20	C2+/C1+: 1,96
C^{1+}	40	150		30	

***Table 5.4**: Magnetic hyperbolas features*

OPERA and Simion simulations have a small difference in the lower energy limit. This limit

depends on the geometry as particles with lower energy are lost on the chamber walls mostly because of the vertical deflection due to the electric field. The difference in the lower energy limit depends on small difference in the geometry of the chambers used in the two different codes. In fact, for example, for protons the lower energy limit is 41 MeV in Opera and 36 MeV in Simion. The distance between these two energy is 2 mm in the magnetic deflection and 2,3mm in the electric deflection which depends on a smaller thickness in the chamber walls seen in Simion simulation, where the step file of the chamber is imported with a low resolution. In any case the lower energy limit is not crucial in this phase as we are anyway interested in the maximum energy. Moreover, the magnetic field is calibrated, as will be discussed in the following, which will make easier to verify the real limit after the device it set up.

Figure 5.29 shows a spectrogram as a result of single particle simulation.

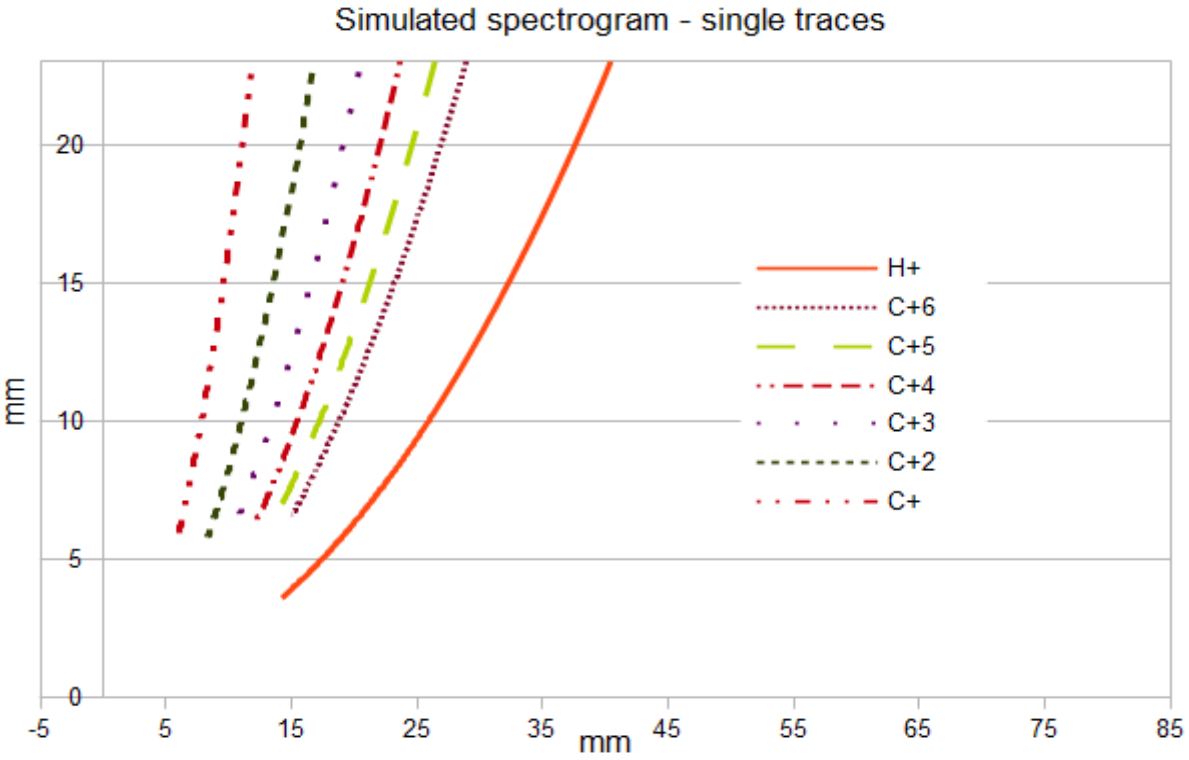

***Figure 5.29**: spectrogram from single particle simulation*

More interesting is the case of a spectrogram produced by realistic beam, taking into account the collimator effect, as shown in Figure 5.30. It should be noted that in this case the real deflection directions are reproduced.

As can be seen from Figure 5.30, protons are well separated but C^{6+} and C^{5+} are at the resolution limit of the device.

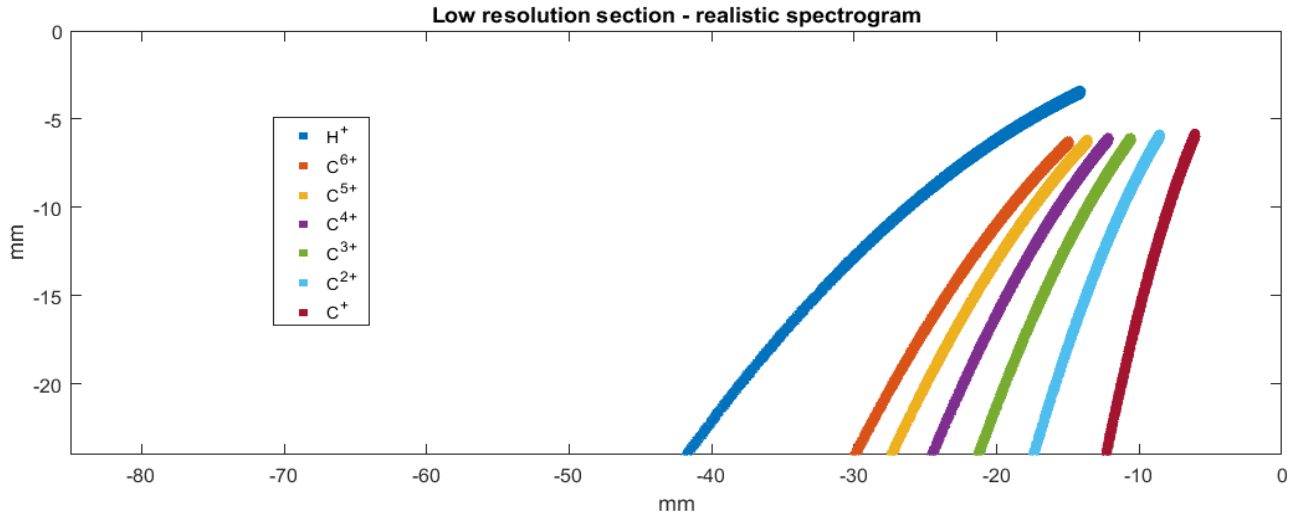

***Figure 5.30**: Spectrogram produced in simulation with a realistic beam*

5.3.1.2 High-resolution sector

Figure 5.31 shows the single particle tracking in the setup. Magnet is not visible as just the magnetic field is imported in the solved electrostatic model. Simulation shows traces of H^+ and carbon ions (form C^{+6} to C^{+1}). In this figure as well as in Figure 5.32 the colour of traces indicate difference in energy, it is not related to ion species.

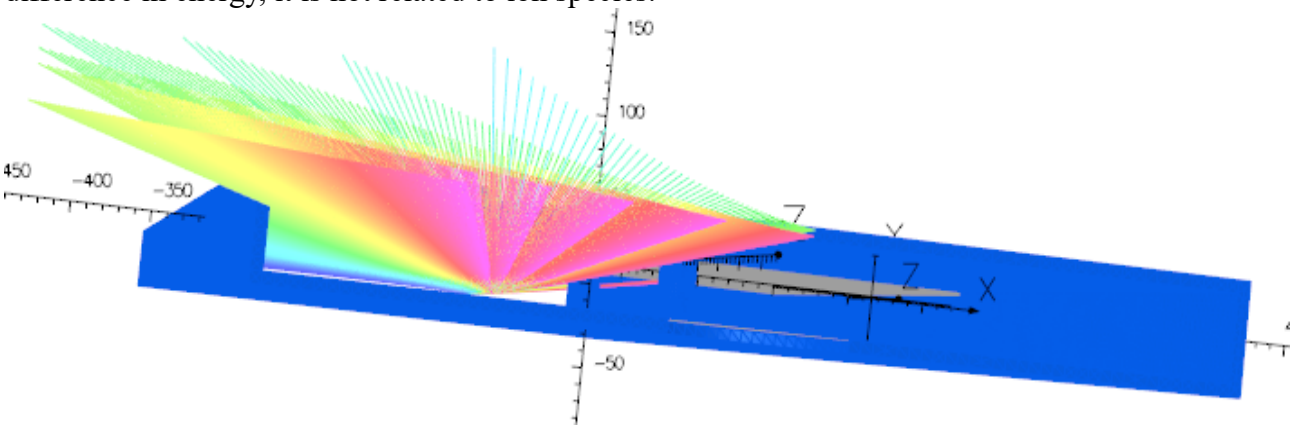

***Figure 5.31**: Single particle tracking in the ESS-TP*

Figure 5.32 gives a detailed view of the particle trajectories with respect to the electrodes position (grey plates). It is evident that the highest energies are travelling only in a small portion of the electric field (in the case of C^{1+} the highest energy component is not even entering the electric field). This is because a relatively small magnetic field is used as the goal is to analyse protons. If an higher magnetic field is used this is solved but the detectable dynamic range of proton will be reduced or protons may be completely lost. Hence this sector will allow to have an high energy resolution and also to selectively and precisely analyse different charge state of heavy ions, taking into account that other ion species can be deflected outside the detector.

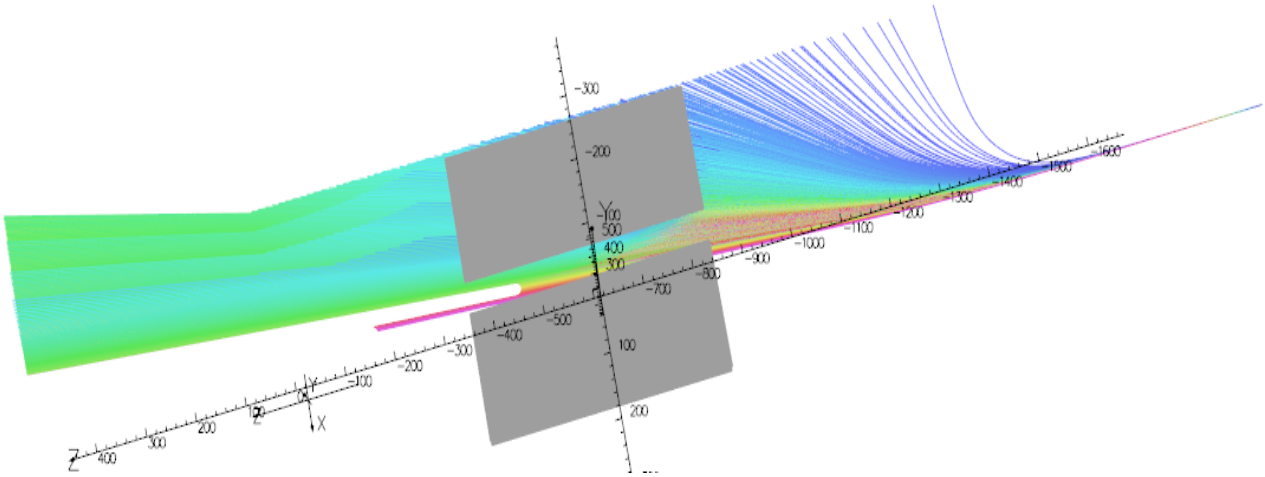

***Figure 5.32**: Details of particles trajectory in the high-energy resolution electric deflection sector.*

Hereafter, electric and magnetic deflections are analysed for protons up to 300 MeV and carbon ions with different charge states assuming the are accelerated by an electric potential of 150MV. Simulations have both fields during tracking. Analytic magnetic hyperbolas for protons and C^{+6} are shown in the following Figures 5.33 and Figure 5.34 together with simulated traces. Here simulated traces are reverted in sign, just for the horizontal deflections, to match analytic results.

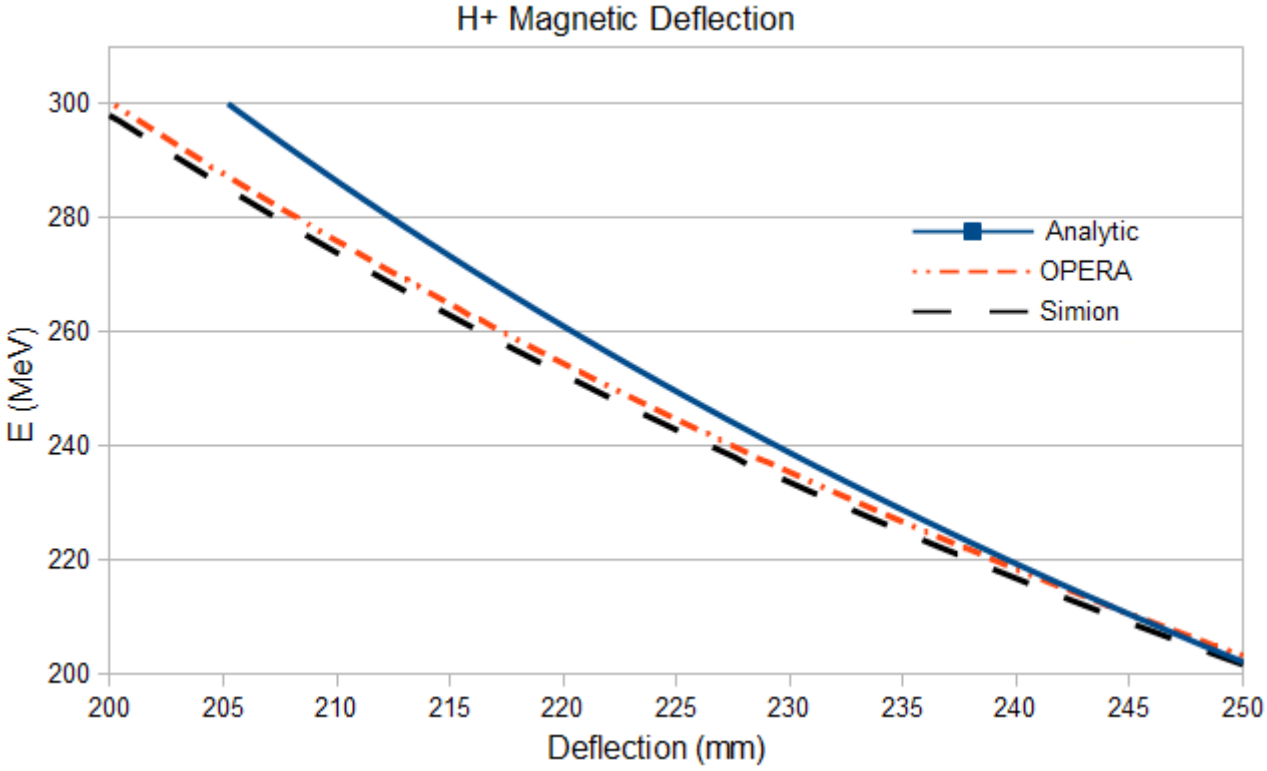

***Figure 5.33**: Magnetic deflection hyperbola for protons*

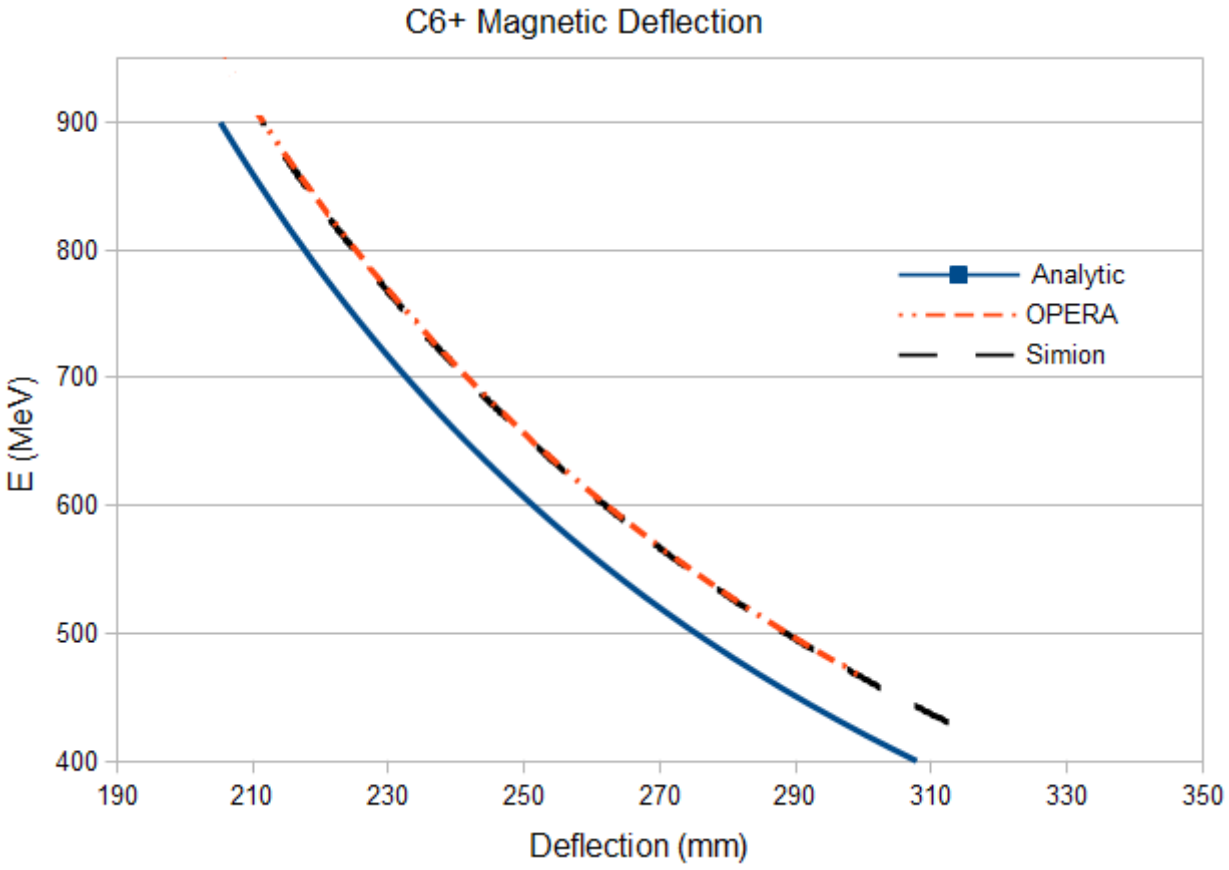

***Figure 5.34**: Magnetic deflection hyperbola for C^{6+}*

The plots in Figure 5.33 and 5.34 show comparison between analytic calculations and simulations made with OPERA 3D and Simion. OPERA 3D is used to calculate both electric and magnetic field, even if the magnetic field is imported in the the electrostatic simulation before performing the tracking. In Simion simulations the electric field is also calculated but the magnetic field is imported from COMSOL simulations. It is evident the shift between calculated and simulated trajectories due to the analytic approximation in the magnet effective length calculations which is more relevant in this case as the particles have a smaller curvature radius in the magnetic field and, hence, their path in the magnetic field is longer. In any case, as stated above, the magnet is already calibrated and this deviation can be easily adjusted.

Figure 5.35 and 5.36 show the energy resolution (in percentage) for H^+ and C^{6+}. As can be seen from the plots the maximum energy can be resolved with an error smaller than 1%. The resolution can be increased with the magnetic field, hence, this value is actually the lower resolution for this high resolution sector. On the other hand, increasing the resolution with the magnetic field will produce a reduction of the detectable range.

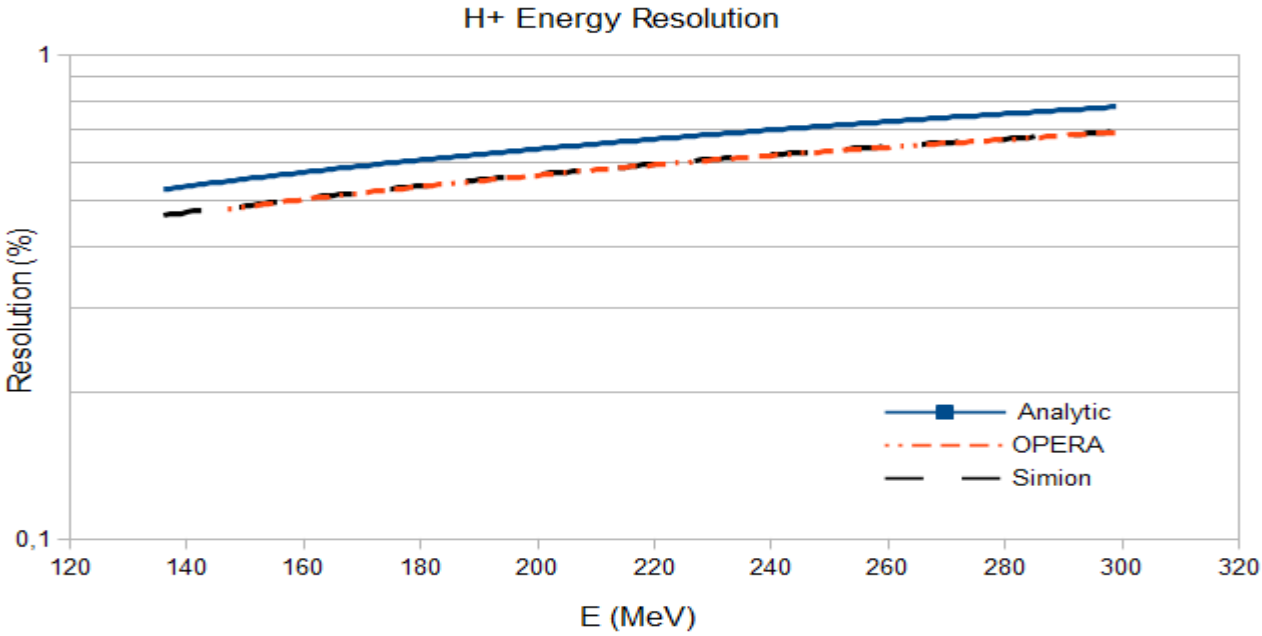

***Figure 5.35**: Energy resolution for protons*

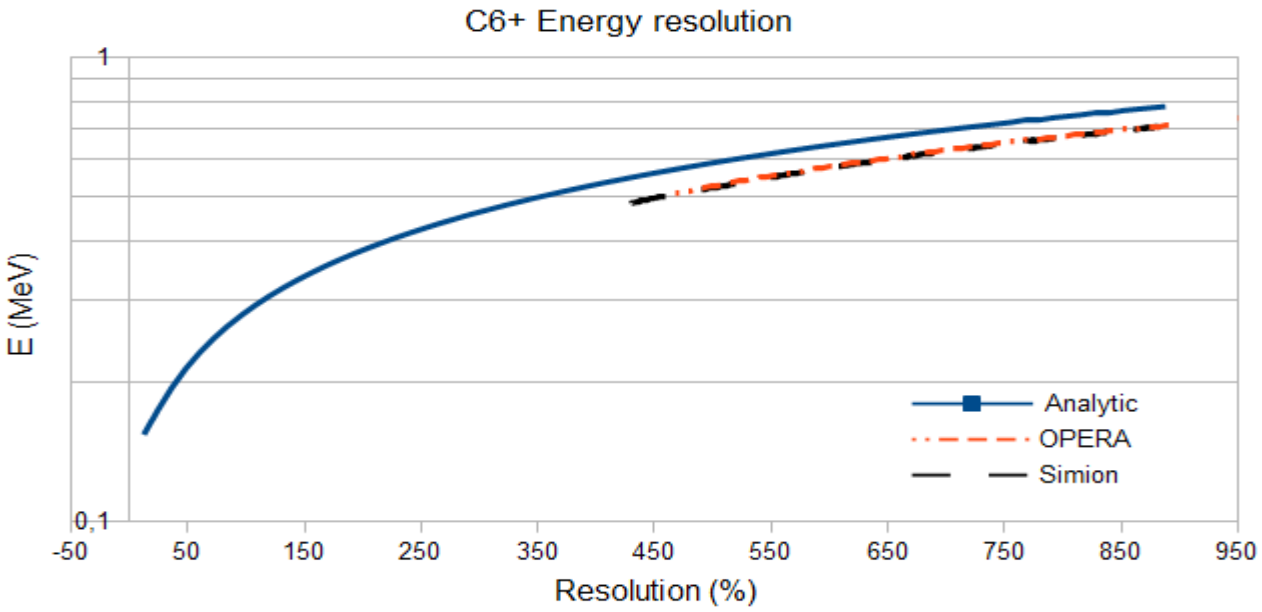

***Figure 5.36**: Energy resolution for C^{6+}*

Analytic electric hyperbolas for protons and C^{+6} are shown in the following Figure 5.37 and Figure 5.38 together with simulated traces.

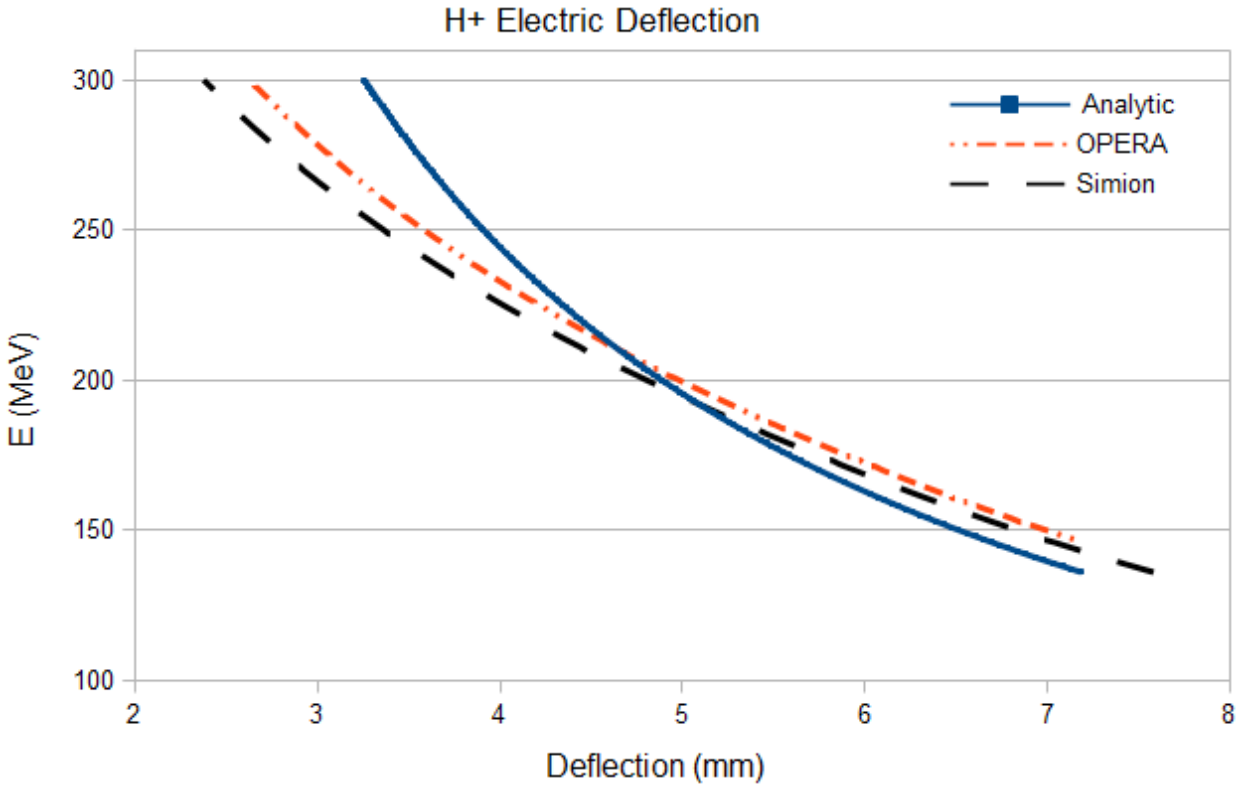

***Figure 5.37**: Electric deflection hyperbola for protons*

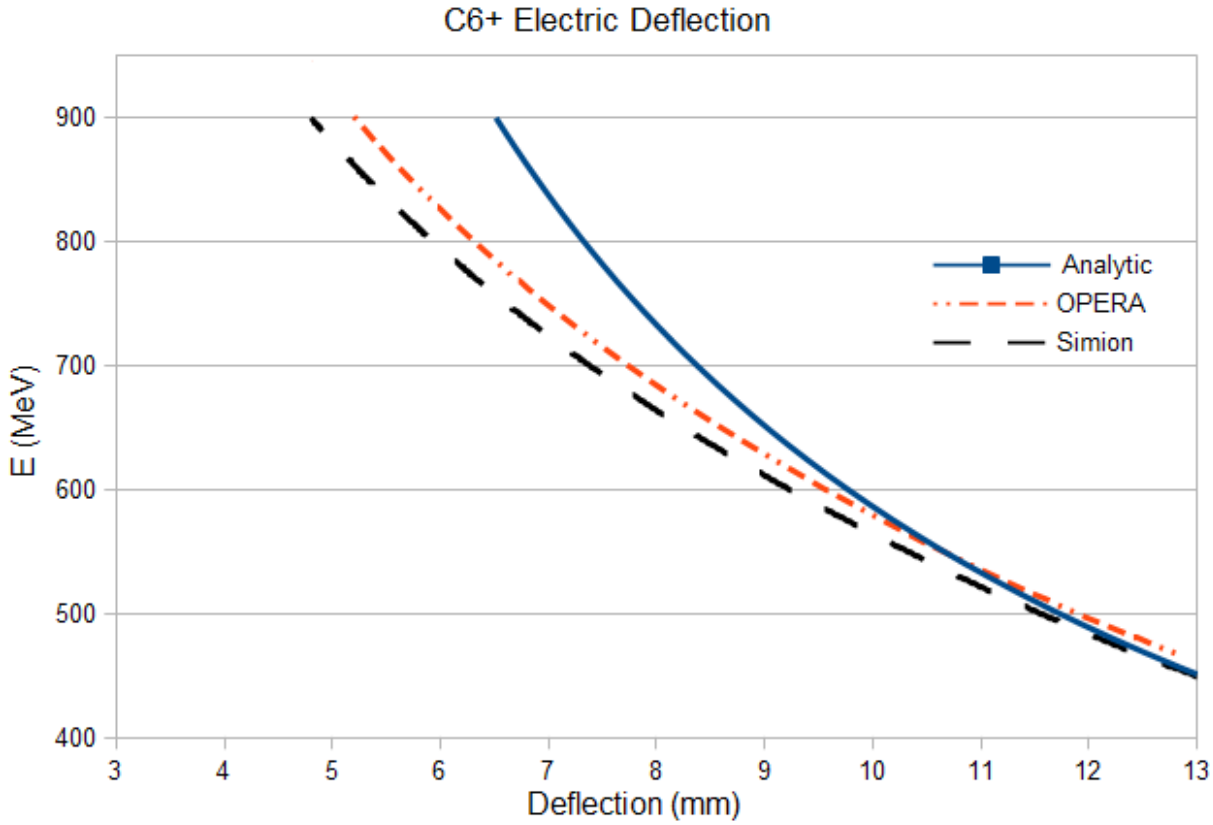

***Figure 5.38**: Electric deflection hyperbola for C6+*

As anticipated at the beginning of this section, particles with higher energy do not have their

path completely inside the electric field region. This is the reason of differences between analytic and simulated hyperbolas. Moreover, the two codes have some difference in the fringing field calculation and the tracking in it has some deviation, this is the reason of the difference between the two codes. The electric field is used for charge separation and energy resolution is not relevant, anyway, calculations show it is below 20% for protons and carbons between the charge states 6+ and 3+; C^{1+} and C^{2+} have higher error because of the above mentioned trajectory issue. Nominal charge separation, between contiguous ion species, is reported in table 5.5, which summarize the main results obtained and describing the nominal performances of the devices such as exact detectable energy range of the ions, maximum deflection in vertical and horizontal, due to the geometry, energy resolution and q/A separation for protons and all charge states of carbons.

	E_{min} (MeV)	E_{max} (MeV)	Geometric range (mm)	Resolution (%)	q/A separation (mm)
H^{+}	140	300	85 – 235 Horizontal 0 – 23 Vertical	< 1	H+/C6+:1,98
C^{6+}	450	900		< 1	C6+/C5+: 0,86
C^{5+}	330	750		< 1	C5+/C4+: 0,96
C^{4+}	250	600		< 1	C4+/C3+: 0,9
C^{3+}	170	450		<2	C3+/C2+: 0,86
C^{2+}	100	300		<2	C2+/C1+: 0,7
C^{1+}	30	110		2	

***Table 5.5**: Magnetic hyperbolas features*

As can be seen from the results in table 5.5 the detectable energy ranges in this sector are smaller than those reported in table 5.4, moreover, the highest energy components for C^{1+} are lost in the reinforcement pillar. Anyway, as said before, the magnetic field can be increased in order to properly analyse particle with the same q/A ratio and energy as C^{1+}.

Figure 5.39 shows a spectrogram as a result of single particle simulation.

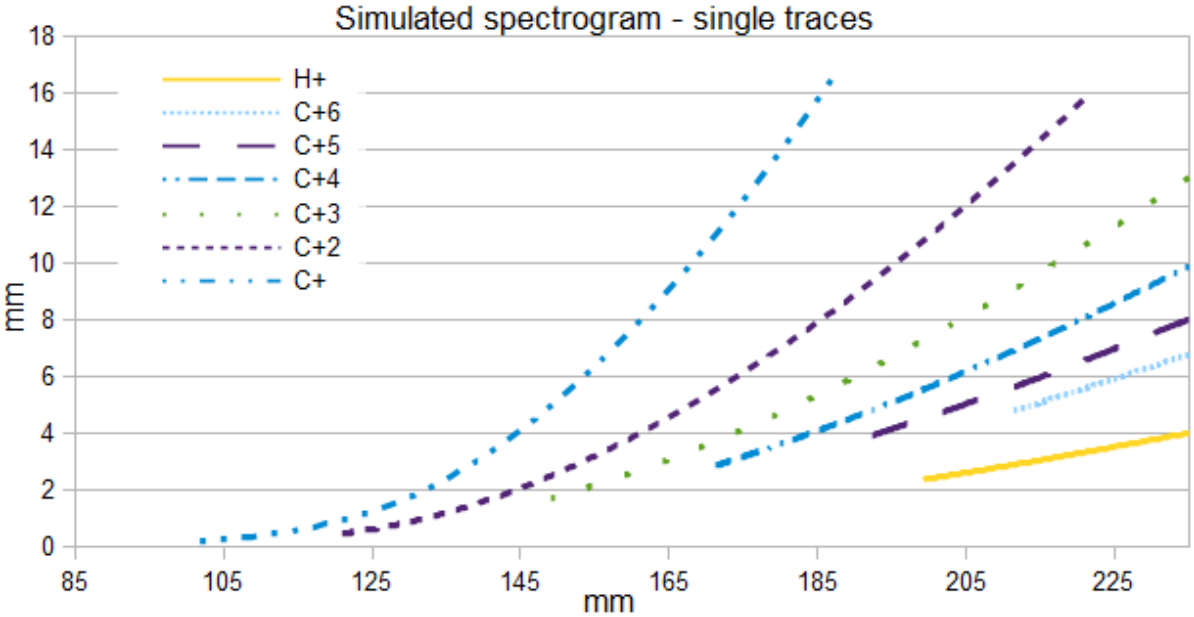

***Figure 5.39**: spectrogram from single particle simulation*

More interesting is the case of a spectrogram produced by realistic beam, taking into account the collimator effect, as shown in Figure 5.40. It should be noted that in this case the real deflection directions are reproduced.

As can be seen from Figure 5.40, traces of protons and C^{6+} to C^{3+} are well separated but C^{2+} and C^{1+} are overlapping.

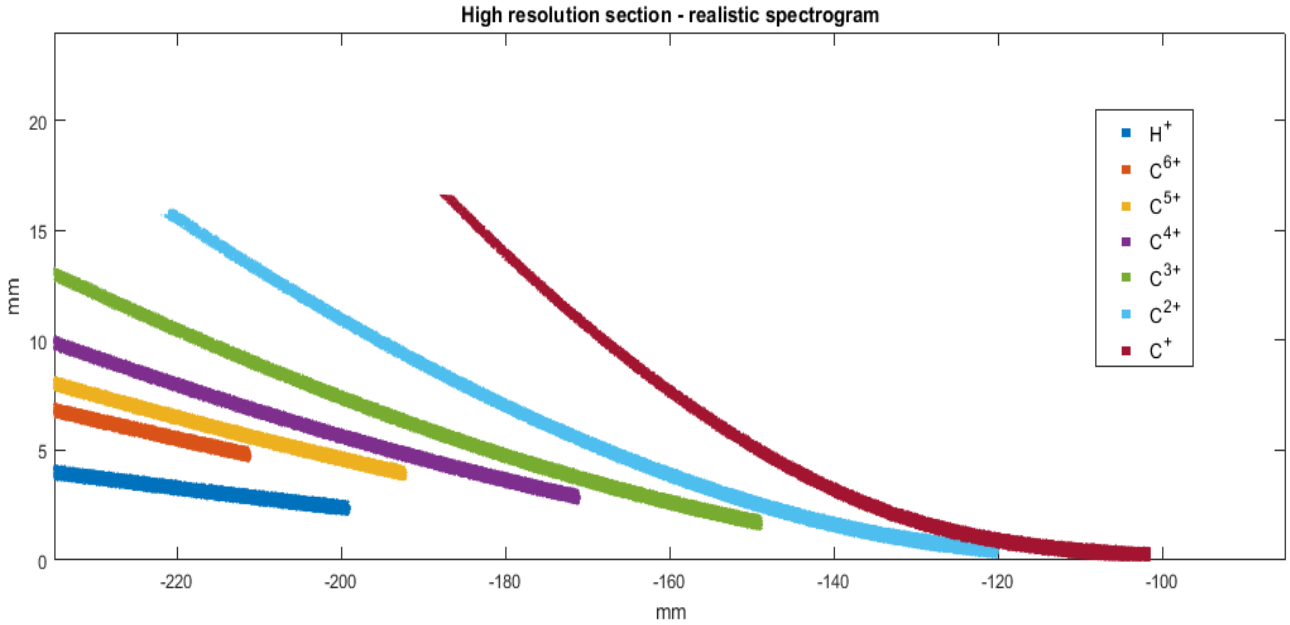

***Figure 5.40**: Spectrogram produced in simulation with a realistic beam*

5.3.2 Magnetic deflection sector calibration

The chicane has been calibrated at INFN-LNS in Catania using proton, carbon and helium beams produced by Tandem and Superconductive Cyclotron. In this occasion a small portion of the beamtime was used to calibrate the first dipole, in the view of using it as the magnetic deflection sector of a Thomson Parabola. Beam used for the calibration are: H^+ with 5, 10, 20, 24 and 62 MeV and He^{2+} C^{6+} with 62 MeV/u. The beam has been detected at the chicane symmetry plane (which is the position of the detector for its use as a Thomson Parabola) by means of radiochromic film. Two example of irradiated radiochromic films are shown in Figure 5.41.

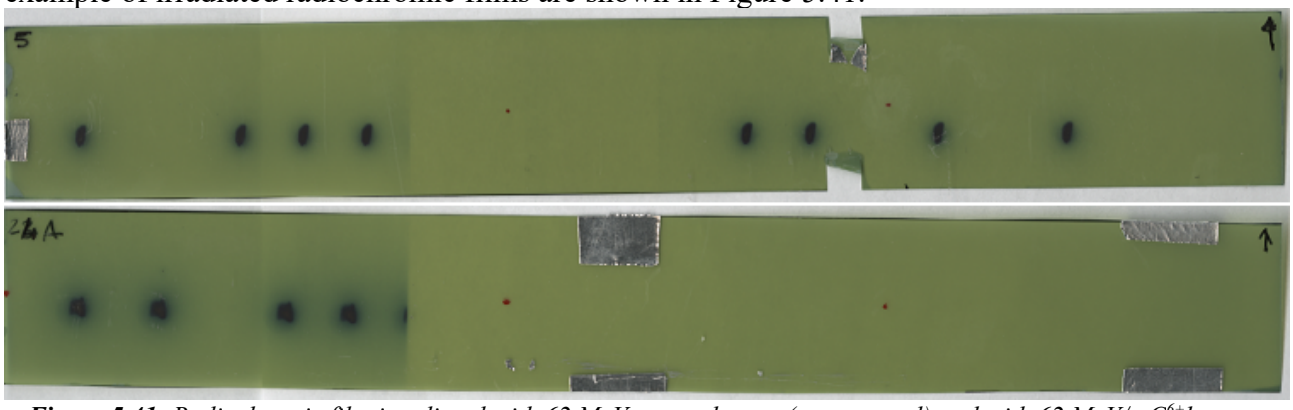

***Figure 5.41**: Radiochromic film irradiated with 62 MeV proton beams (upper panel) and with 62 MeV/u C^{6+} beam (lower panel) using different magnetic fields*

In both cases shown in Figure 5.41 the first spot from the left side is the zero point (i.e. the beam is not deflected as no magnetic field is applied). All the other points are obtained increasing the field. The radiochromic film showing C^{6+} ions has the last spot on the right side partially cut, this is due to the reinforcement pillar in the vacuum chamber. Images are processed in order to get coordinates of each point with respect to the zero point. For example, the plot in Figure 5.42 shows the position of each beam spot analysing the radiochromic film for 62 MeV protons.

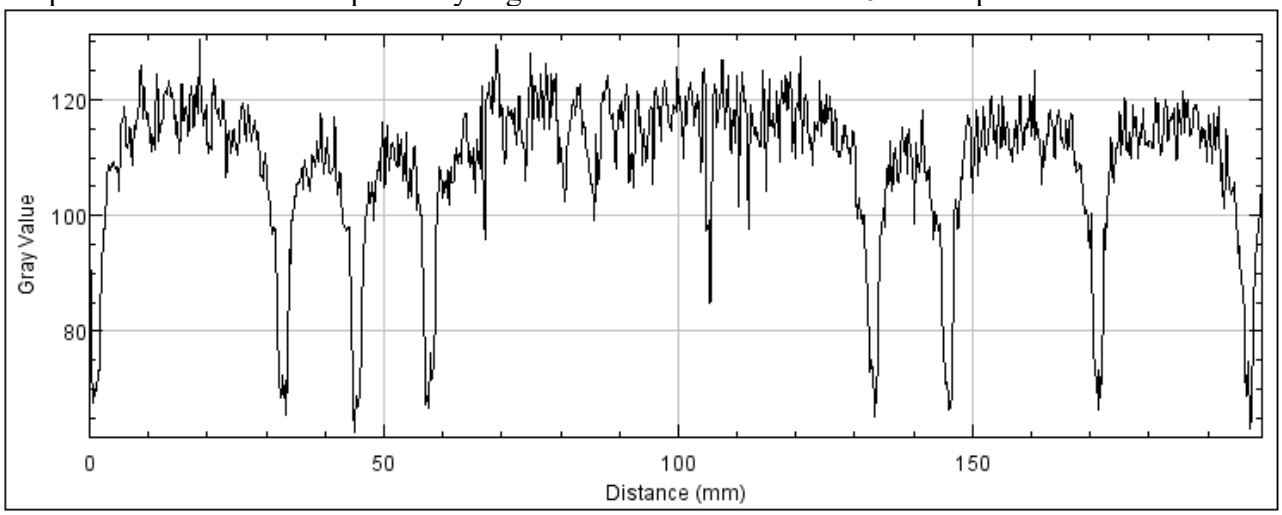

***Figure 5.42**: Position of 62 MeV protons spot on the radiochromic film after image processing*

H+	H+ 62MeV	B (T)	Exp. data	SIMION Deflection	SIMION Field	Analytic data	OPERA Deflection	OPERA Field
		0,37814	195,40	195,324000	0,375600	195,082000	200,250907	0,382790
		0,32965	169,66	171,345000	0,330100	170,092000	174,366846	0,334065
		0,28116	144,60	145,863000	0,281600	145,060000	148,376455	0,284837
		0,25692	132,07	133,171000	0,257320	132,594000	135,497559	0,260343
		0,11146	56,38	57,750700	0,111980	57,549000	58,660616	0,113151
		0,08722	44,02	45,256400	0,087820	45,035000	45,97	0,088713
		0,06297	32,51	32,428100	0,062512	32,519000	32,620311	0,062995
	H+ 24MeV	B (T)	Exp. data	SIMION	SIMION Field	Analytic data	OPERA Deflection	OPERA Field
		0,25692	216,40	217,675000	0,257320	213,157620	221,531687	0,260343
		0,23268	195,14	197,354000	0,233800	193,019991	200,264318	0,235846
		0,20843	174,66	176,465000	0,209400	172,921246	179,118113	0,211346
		0,18419	153,83	155,676000	0,185100	152,82	158,115875	0,186886
		0,15995	132,92	135,009000	0,160700	132,714833	137,196129	0,162406
		0,06297	51,72	52,659100	0,062512	52,266000	52,997329	0,062995
	H+ 20MeV	B (T)	Exp. data	SIMION	SIMION Field	Analytic data	OPERA Deflection	OPERA Field
		0,23268	216,90	216,821000	0,233800	211,442807	220,032773	0,235846
		0,20843	193,71	193,804000	0,209400	189,425734	196,724320	0,211346
		0,18419	171,02	170,914000	0,185100	167,41	173,598721	0,186886
		0,15995	146,46	148,181000	0,160700	145,381815	150,586179	0,162406
		0,06297	56,38	57,754000	0,062512	57,250000	58,124906	0,062995
	H+ 10MeV	B (T)	Exp. data	SIMION	SIMION Field	Analytic data	OPERA Deflection	OPERA Field
		0,15995	209,37	211,230000	0,160700	205,601000	214,694740	0,162406
		0,13570	176,77	178,672000	0,136400	174,450700	181,634348	0,137826
		0,11146	144,85	146,389000	0,111980	143,295000	148,722781	0,113151
	H+ 5MeV	B (T)	Exp. data	SIMION	SIMION Field	Analytic data	OPERA Deflection	OPERA Field
		0,13570	260,76	254,958000	0,136400	246,71	259,249126	0,137826
		0,11146	211,65	208,369000	0,111980	202,650000	211,724981	0,113151
		0,08722	164,07	162,693000	0,087820	158,583000	165,3	0,088713
		0,06297	117,17	116,248000	0,062512	114,510000	117,094002	0,062995

***Figure 5.43**: Summary of experimental data, simulated and analytical deflections for protons all positions are in mm*

Figure 5.43 and 5.44 resume all data for protons, C^{6+} and He^{2+}, they report the field used during the calibration, the measured deflection, data obtained with SIMION and OPERA simulations and in this case also the field is reported, as it can be slightly different from the applied one.

		B (T)	Exp. data	SIMION	SIMION Field	Analytic data	OPERA Deflection	OPERA Field
He (2+)	62 MeV/u 248MeV tot	0,25692	65,27	66,552200	0,257320	66,287000	67,526366	0,260343
		0,11146	28,36	28,394900	0,111980	28,769000	29,311906	0,113151
		0,06297	16,08	16,253700	0,062512	16,389000	16,314224	0,062995

		B (T)	Exp. data	SIMION	SIMION Field	Analytic data	OPERA Deflection	OPERA Field
C (6+)	62 MeV/u 744MeV tot	0,25692	65,36	66,591300	0,257320	66,287000	67,526366	0,260343
		0,20843	54,35	54,168900	0,209400	53,785000	54,793448	0,211346
		0,15995	41,31	41,558300	0,160700	41,279000	42,087680	0,162406
		0,06297	16,59	16,263200	0,062512	16,256000	16,314224	0,062995

***Figure 5.44**: Summary of experimental data, simulated and analytical deflections for C^{6+} and He^{2+}*

Next Figures from 5.45 to 5.50 show the plot of the deflections vs the magnetic field for the different beams used during the calibration.

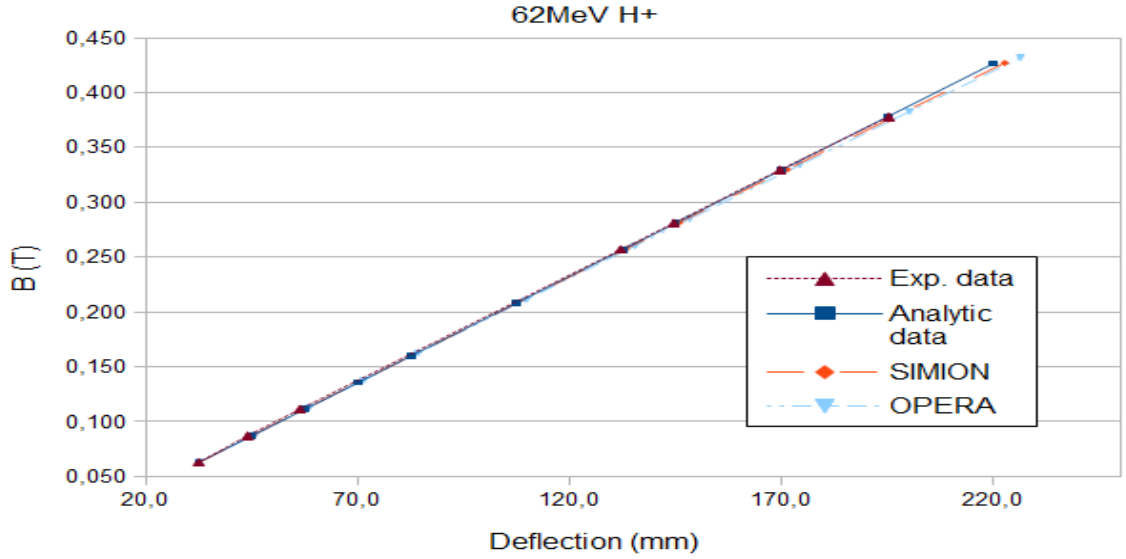

***Figure 5.45**: Plot of deflection as a function of the magnetic field for 62 MeV protons. Experimental data are here compared with analytic results and simulations*

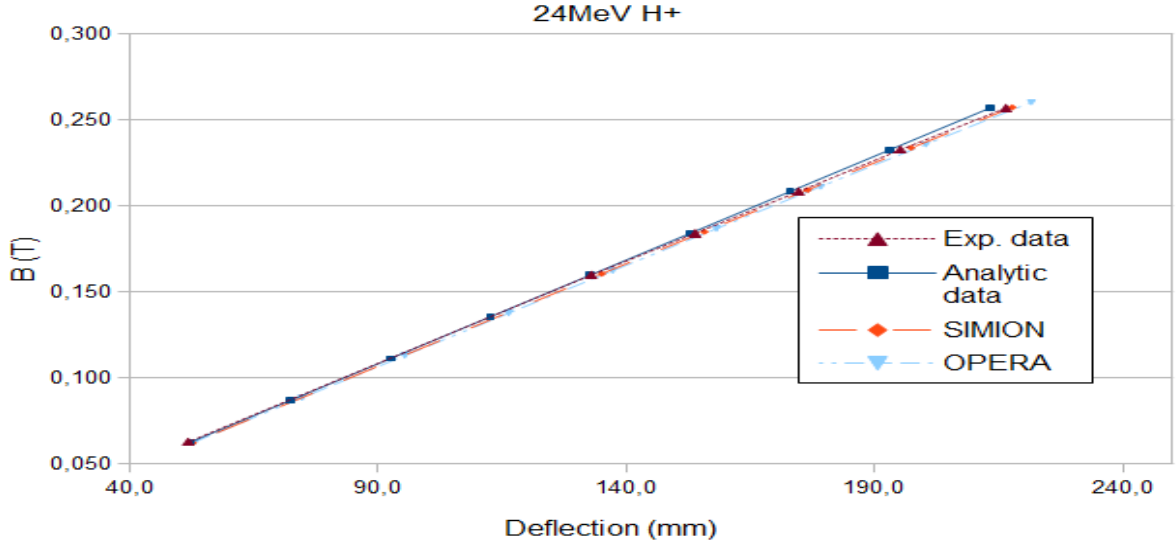

***Figure 5.46**: Plot of deflection as a function of the magnetic field for 24 MeV protons. Experimental data are here compared with analytic results and simulations*

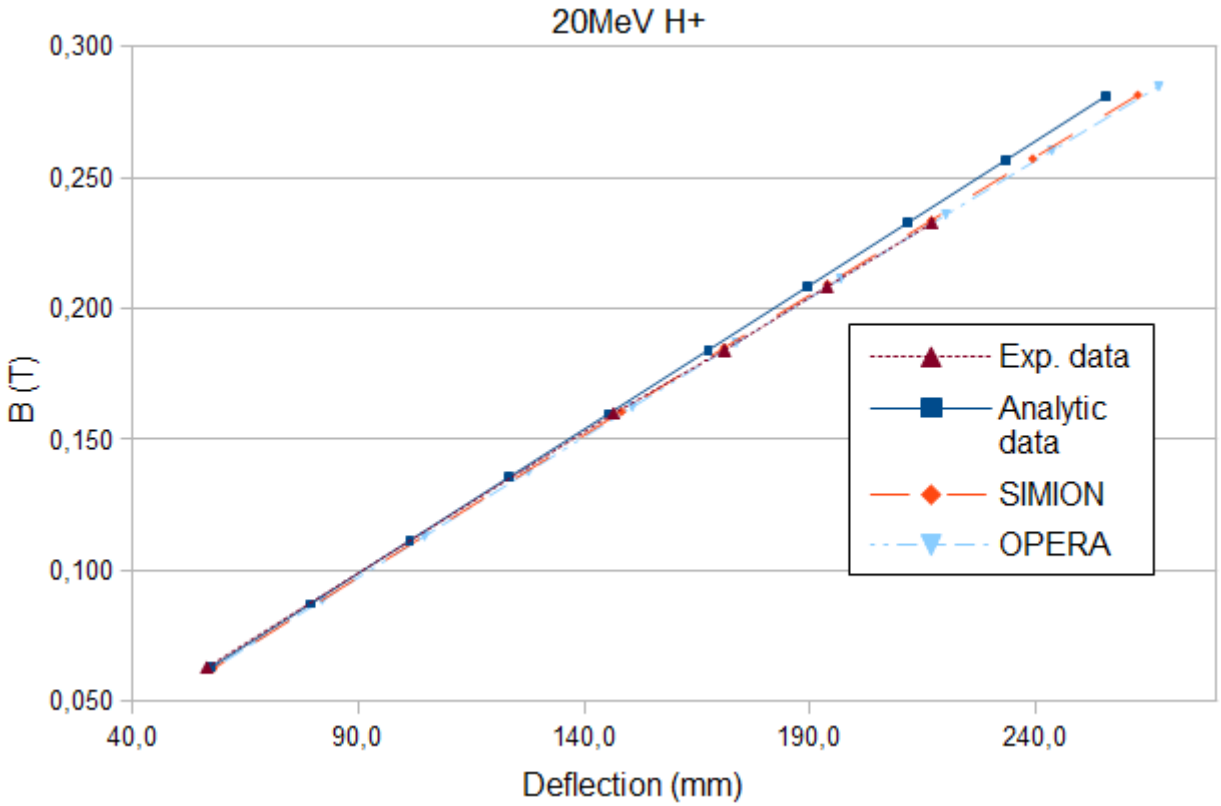

***Figure* 5.47:** *Plot of deflection as a function of the magnetic field for 20 MeV protons. Experimental data are here compared with analytic results and simulations*

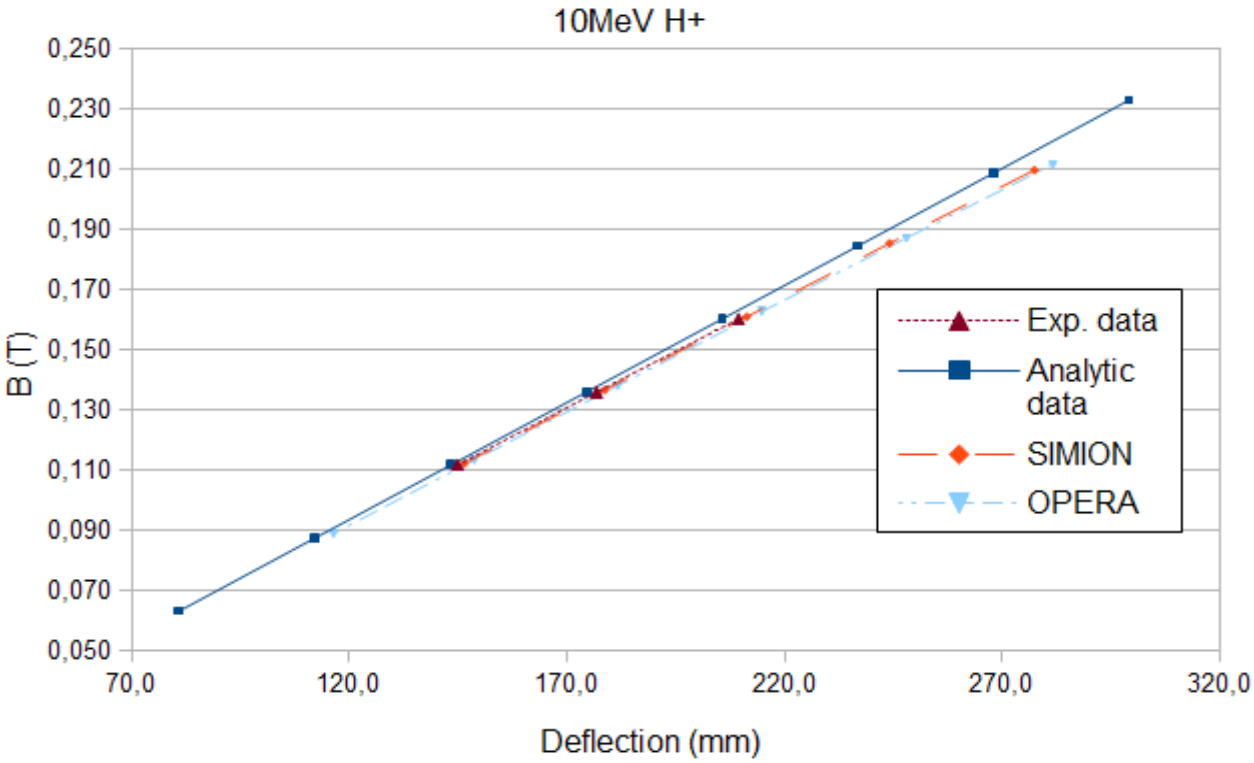

***Figure* 5.48**: *Plot of deflection as a function of the magnetic field for 10 MeV protons. Experimental data are here compared with analytic results and simulations*

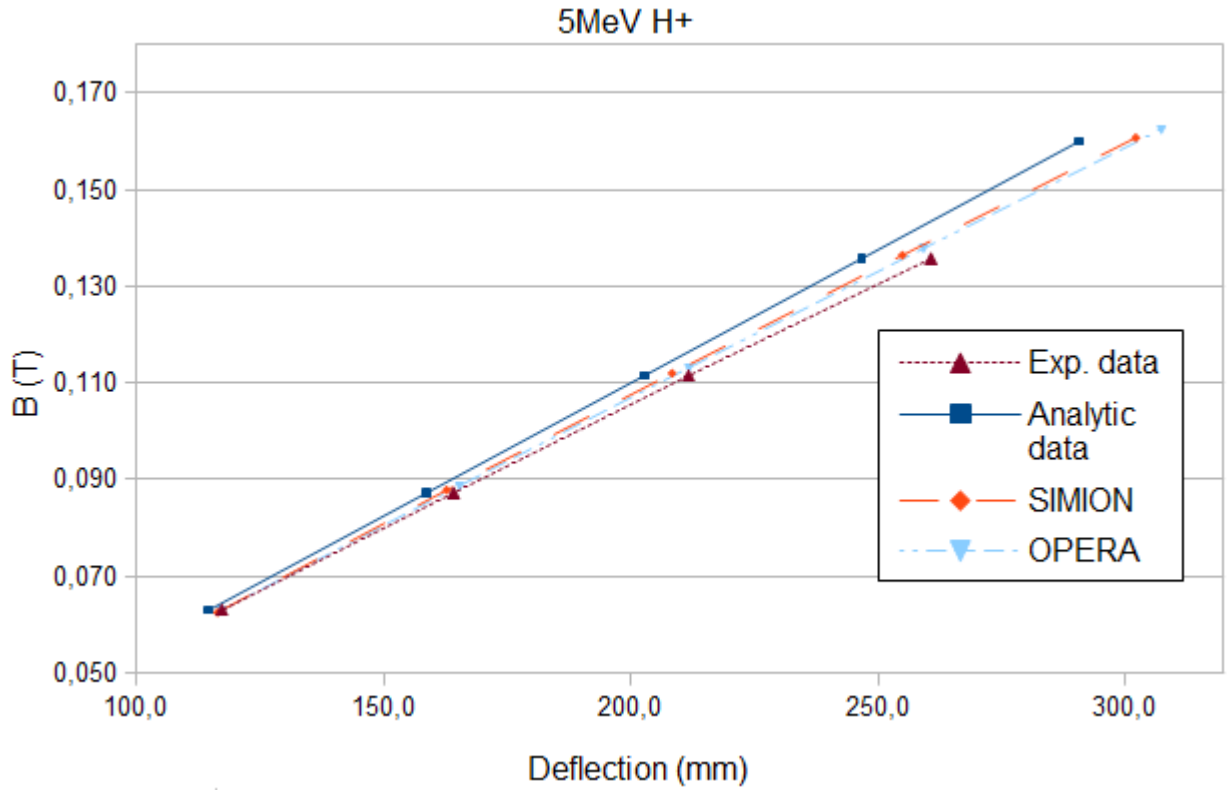

***Figure 5.49**: Plot of deflection as a function of the magnetic field for 5 MeV protons. Experimental data are here compared with analytic results and simulations*

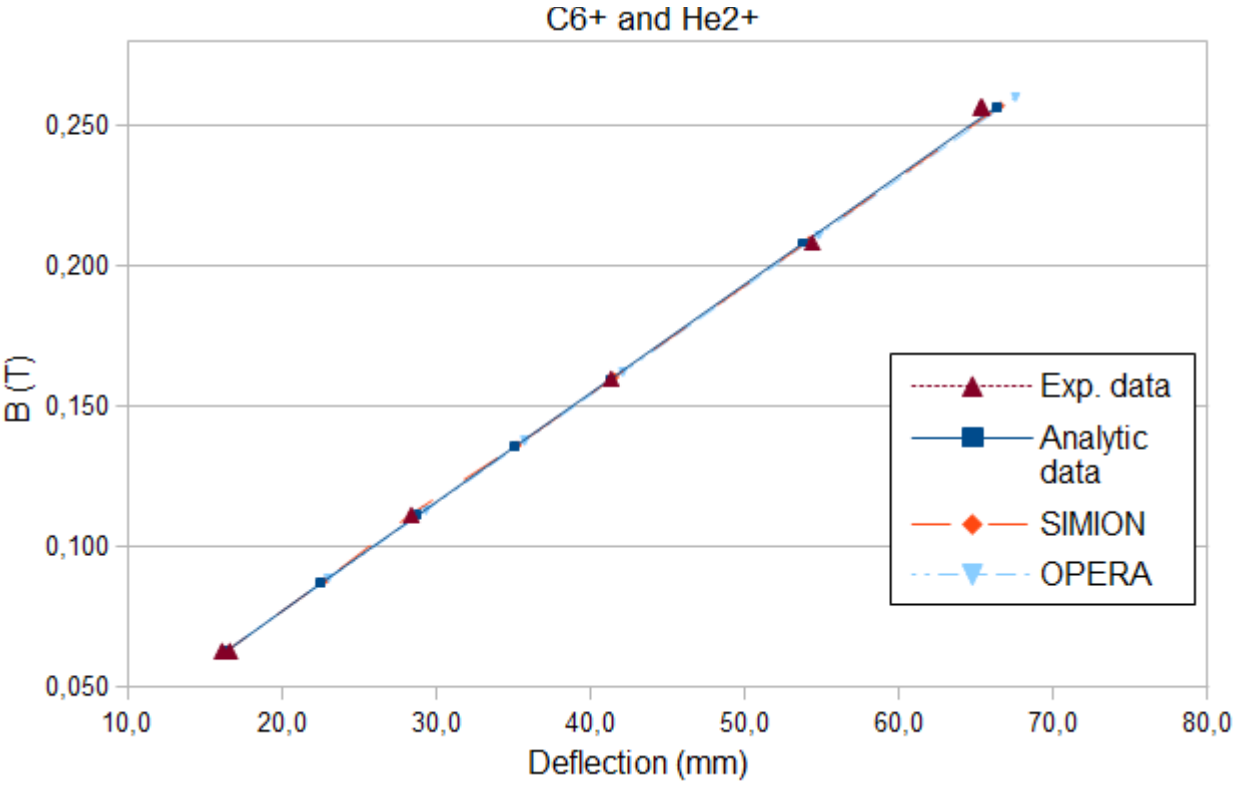

Figure 5.50: Plot of deflection as a function of the magnetic field for 62 MeV $C^{6}+$ and He^{2+}. Experimental data are here compared with analytic results and simulations

In general there is an almost perfect agreement between simulations and experimental data. Analytic results have some discordance due to a not perfect calculation of the effective length of the magnet, as already discussed. Situation is different for the 5 MeV protons, as they are more sensitive to the real field applied (real field uniformity, mostly) and, hence, also a small deviation between experimental data and simulation is present. In any case the calibration allows to rescale and fix errors in analytics and simulation results. Considering the alignment precision, discussed in chapter 3, the observed differences are not relevant. Moreover, the electric field could be cross-calibrated after the installation.

Figure 5.51 shows the magnetic deflection hyperbola for the lower magnetic field used during the calibration (which is also the lower field used in the previous discussed study). From the figure it is evident the good agreement between experimental data, simulations and analytical equation. This is the only case in which the hyperbolic equation can be determined using the experimental point, as, in general, 5 points are necessary to uniquely determine a hyperbola, and the equation, as reported in [1] is:

$$E_{kin} = \frac{Q^2 e^2 L_m^2 \left(D_m + \frac{L_m}{2} \right)^2}{2 m x^2}$$

where E_{kin} is the kinetic energy, Q is the charge state of the ion, e is the elementary charge, L_m and D_m are the magnet length (effective here) and drift between magnet and detection plane, m is the mass of the ion and x the deflection.

The point for protons at 228 MeV is taken from C^{6+}/He^{2+} results, considering that protons with this energy have tha same curvature radius (or magnetic rigidity) of 62 MeV C^{6+}/He^{2+}.

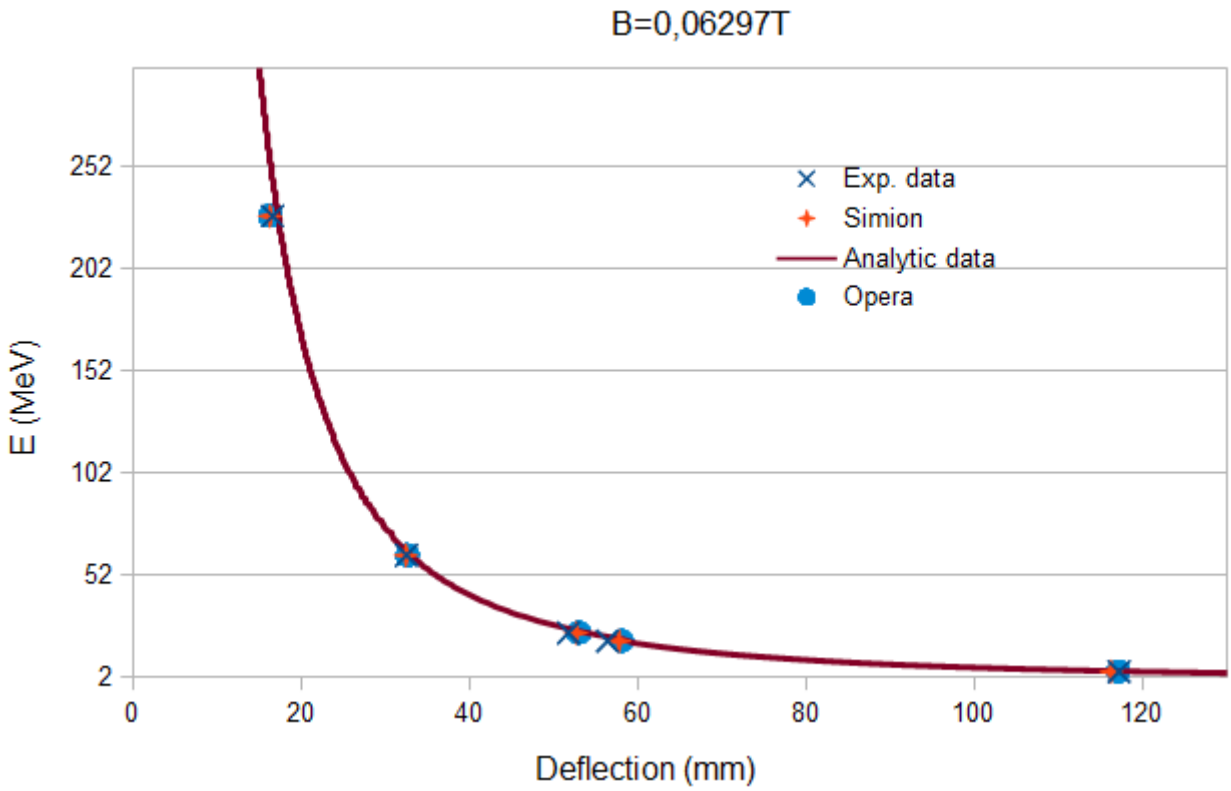

***Figure 5.51**: Magnetic deflection hyperbola for B = 0,06T*

For other field used are always available less than 5 points, so the equation should be calculated

using an additional condition, for example that the x-axis is an asymptote. In any case the previous equation is the general form of the magnetic deflection hyperbola and, for this reason, here we limit the comparison of this curve with the experimental points.

As an example, Figure 5.52 shows the magnetic deflection hyperbola for B = 0,11 T and comparison with experimental data and simulations.

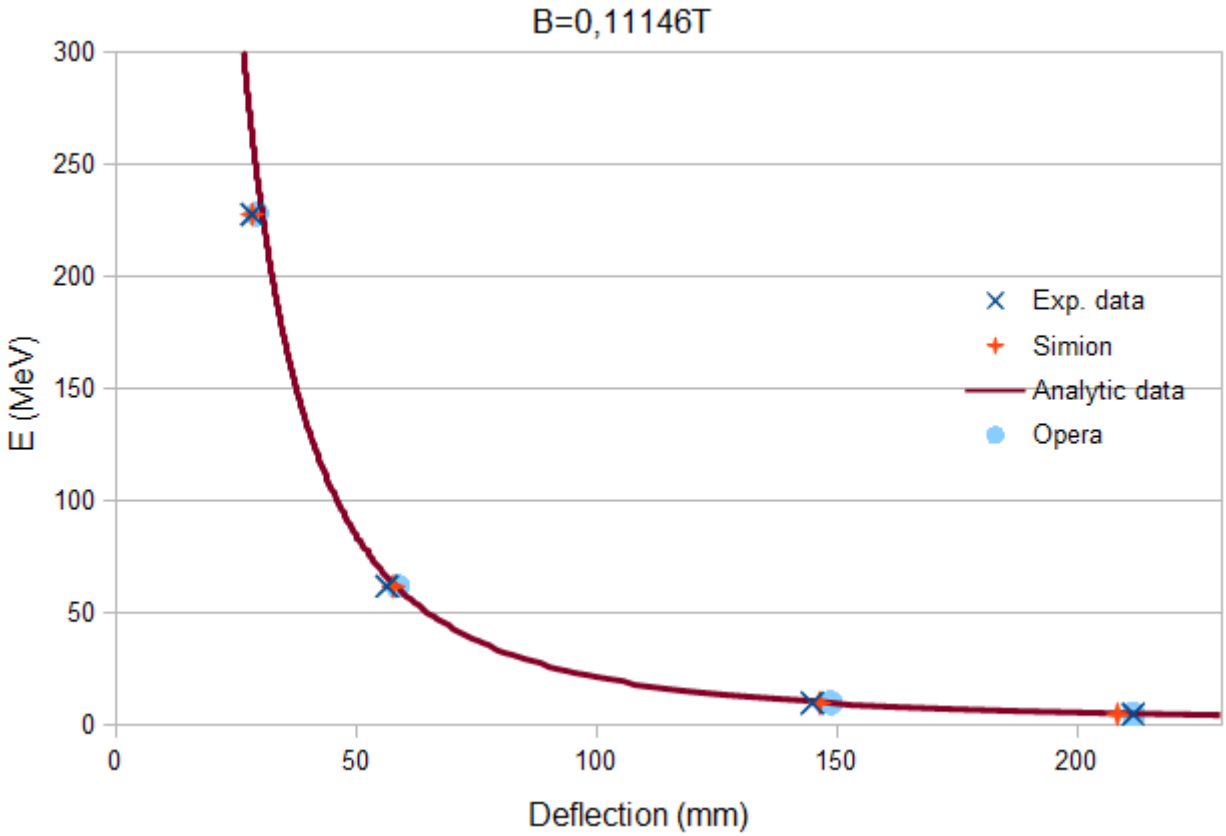

***Figure* 5.52**: *Magnetic deflection hyperbola for B = 0,11T*

5.4. PBN (Pyrolytic Boron Nitride) Test Report

A PBN sample, see Figure 5.53, has been tested in vacuum up to 45kV. The sample is a rounded plate with 40.64 mm diameter and 2.57 mm thickness. The test have been done in vacuum up to around 45 kV and then in oil up to 90kV. The reason of making the test with higher voltage in oil is that the available vacuum feedthrough can be used up top 40 kV.

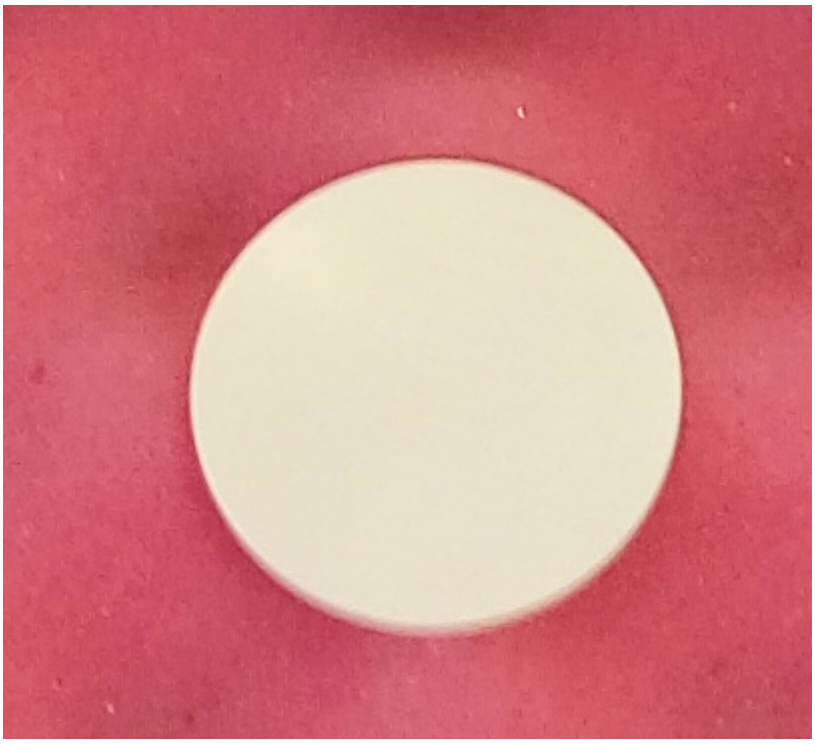

Figure* 5.53: PBN sample*

5.4.1 Test of PBN insulator in vacuum

The PBN was placed in a small vacuum chamber and the post used as electrode was fixed on it using non-vacuum compatible epoxy glue. The upper part of the electrode was connected to the power supply and the metal plate at the base of the chamber was grounded. Scheme is shown in Figure 5.54.

To protect the power supply (V), on the air side, two resistances (R1 and R2 – 39MΩ each) in series have been set up and a voltage monitor (VM) has been connected to the vacuum feed-through. A sketch of the circuit is in Figure 5.55, where the electrode + insulator are represented as a capacitor (C) connected to the same ground as the power supply. The voltmeter has 100 MΩ impedance while the resistances have 80 MΩ ± 10%.

The vacuum level in the vacuum chamber at the beginning of the test was $2x10^{-5}$ mbar, no conditioning on the insulator has been done.

In the first test, the power supply output was set at 65 kV and the rise time of the voltage was about 1-2 seconds and the voltmeter was measuring 40 kV applied. In this condition no spark was visible and the test was repeated for 3 times within about two minutes.

In the second test the voltage monitor was removed, in this condition the applied voltage is higher, but cannot be measured. The voltage was raised, again in 1-2 seconds, up to 45 kV and a small spark in the connection between the conductor and the insulator was visible. After visual inspection it is clear that the discharges occurred at the glue level, as can be seen in Figure 5.56. The insulator sample is not damaged, excluding the burn due to the spark.

***Figure 5.54**: PBN sampe placed in a small vacuum chamber, a standar post from ThorLab is used as electrode connected with the power supply*

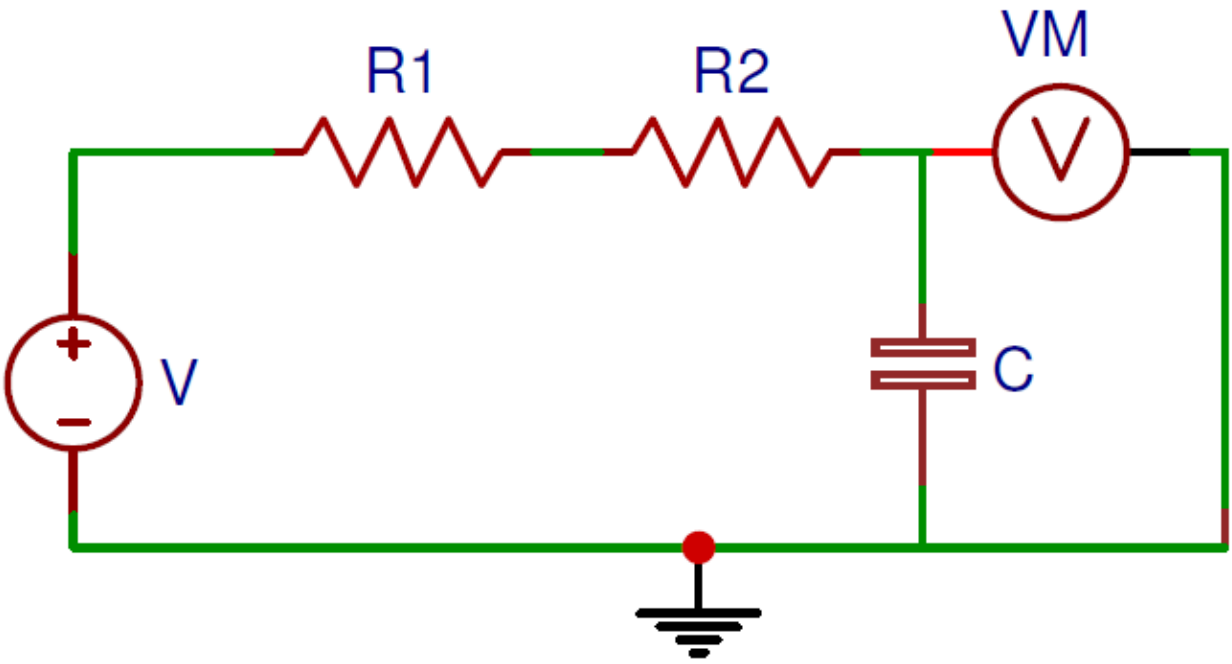

***Figure 5.55**: Electric scheme of the elements used for the test.*

***Figure* 5.56**: *PBN sample after test, the burn due to the discharge between the glue and the electrode circled in black*

This first test allows to conclude that, under vacuum, the PBN can hold at least 1.12 kV/mm along the surface and 17.51 kV/mm through is thickness. This last one result was expected, according the material specification (dielectric breakdown is 230kV/mm).

Moreover, the glue could be a critical point and the process must be done carefully. In the present case, a small layer of glue was not uniformly spread on the post surface, hence some air was probably trapped in this area. Finally a conditioning cycle could improve the situation.

It should be also noted that the electrode used has sharp edges and the electric field in this area exceeds 130kV/mm, as calculated with FEM simulations, see Figure 5.57.

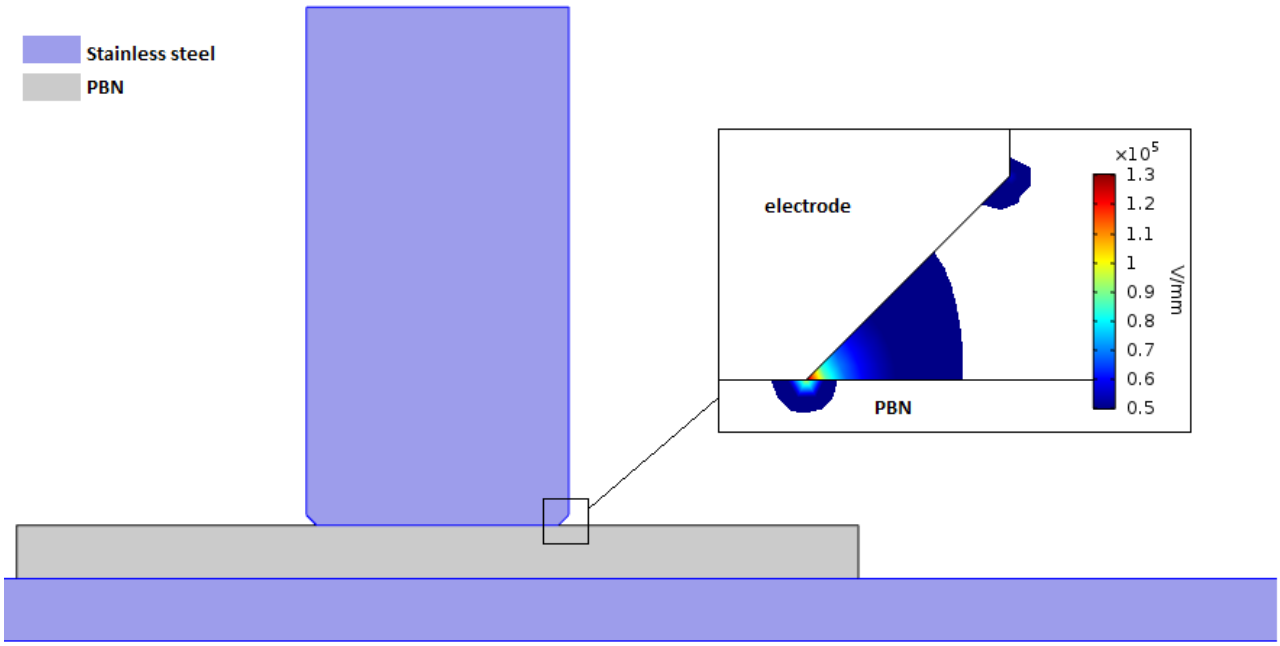

***Figure* 5.57**: *Simulated setup and electric field distribution at the interface between electrode and PBN*

5.4.2 Test of PBN insulator in oil

Higher voltage test was performed with the sample plunged into transformer insulating fluid MIDEL 7131. Nominal specification of MIDEL 7131 [8] relevant for the present case are the breakdown voltage > 75 kV/2,5 mm (IEC 60156) and the relative permittivity ε_o = 3,2. The fluid was already used in the past, hence, it is realistic that the above features might be different in the present case. Figure 5.58 shows the sample placed on a grounded black metal plate with the circuit used for the protection of the power supply protection (3 resistance) and an equivalent capacitor of (1.2 nF each, equivalent 300pF in total) to store the energy and see the discharge.

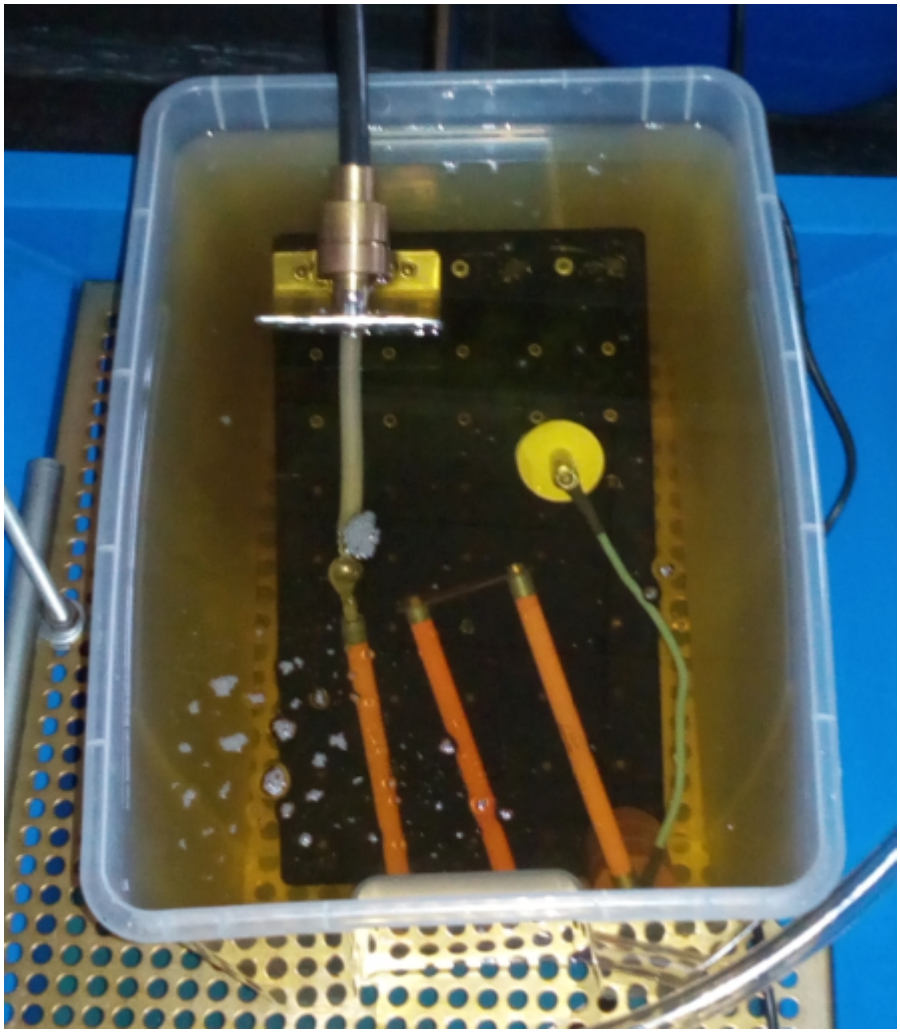

***Figure 5.58**: PBN sample placed in oil, a standard post from ThorLab is used as electrode connected with the power supply (black cable on the top) through a series of resistors and capacitors*

Again the voltage was raised in a couple of seconds up to 65kV. Some bubbles indicating a discharge near the HV cable where present. More oil was then added and the voltage was raised up to 85kV with no issue. In the voltage range between 87kV and 90kV there was a discharge between the electrode and the insulator which broke the glue. The grounded black metal plate was tilted inside the recipient used, so the conductor jumped and backward and it start discharging on the insulator. Contact between electrode and insulator in this case was, for few seconds, as sketched in Figure 5.59.

According simulations the electric field at the interface between electrode and insulator can reach 261kV/mm when the electrode is glued to the insulator sample, same setup as in Figure 5.57.

When it is tilted, like in Figure 5.59, the field is about 280kV. In this case the insulator shown a damaged surface and the break is through the thickness, as can be seen in Figure 5.60 in which the LHS shows the upper surface with some annotations, the the RHS shows the lower surface.

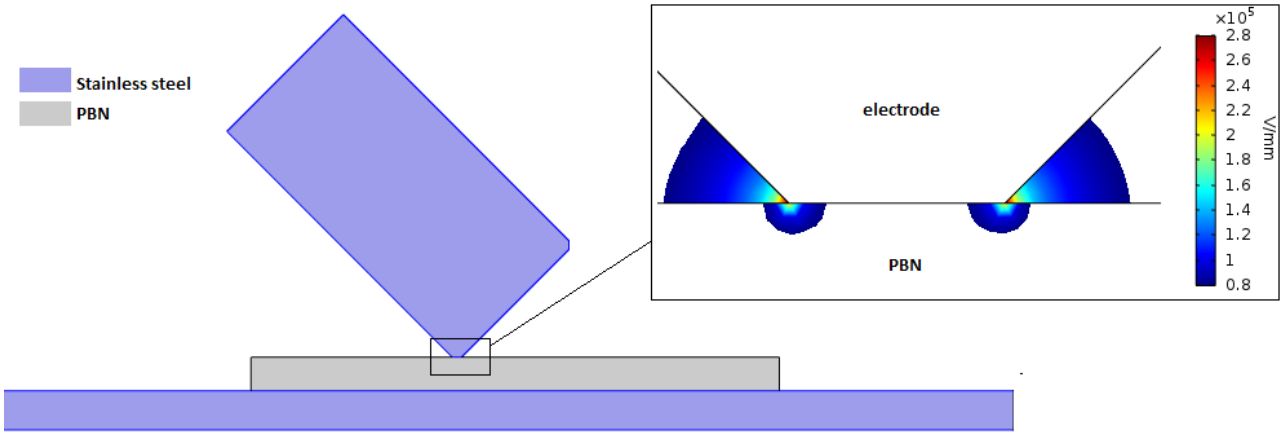

***Figure* 5.59**: *Simulated setup after the discharge and electric field distribution at the interface between electrode and PBN*

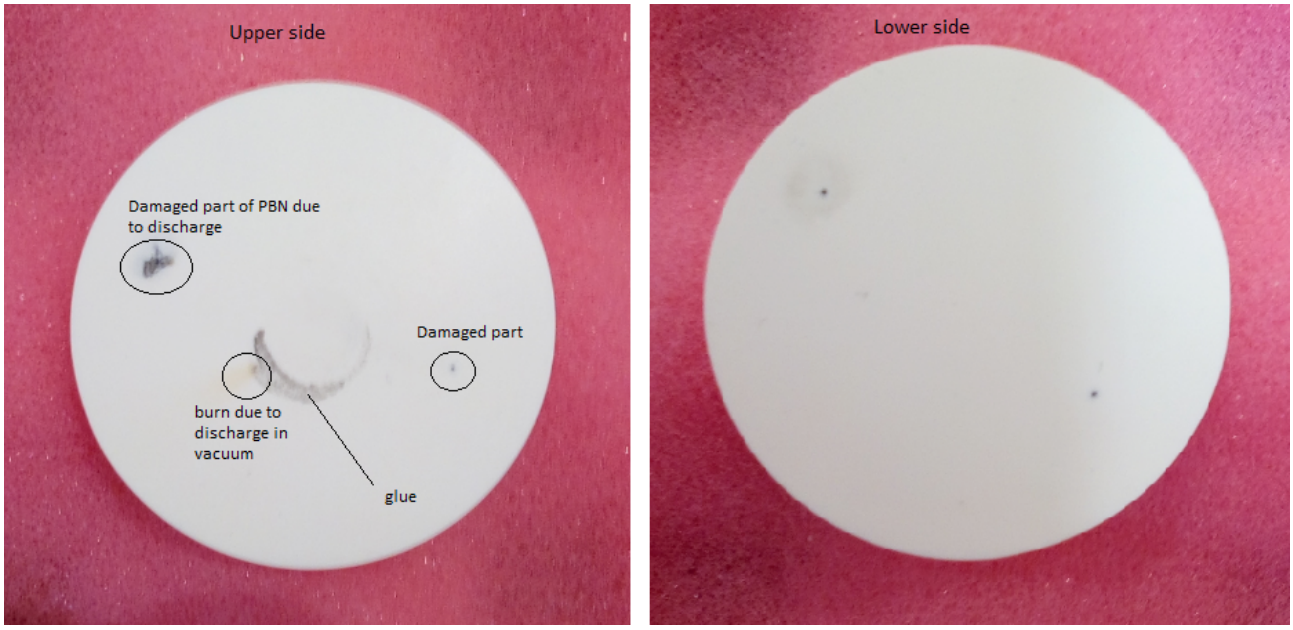

***Figure* 5.60**: *Upper surface of the insulator (LHS) and lower surface (RHS) after the test in oil.*

It is not clear the reason of the small damage on the opposite side with respect to the bigger one due to the discharge after break in the glue, maybe also the insulator fluid experienced a breakdown.

The configuration used during the test is not optimal, in fact the field enhancement at the interface between electrodes and insulator is relevant.

In any case, the peak field reached during this test is about four times higher than the field expected in the final setup (70kV/mm). Moreover the final configuration should reduce the field enhancement problem. Another important information is that the gluing must be done carefully as it represents a critical point. Also a conditioning cycle could help.

5.5 Bibliography

[1] F. Schillaci, M. Maggiore, A. Velyhan, G.A.P. Cirrone, G. Cuttone, D. Margarone, G. Parasiliti Palumbo, P. Pisciotta, D. Rifuggiato, F. Romano, G. Russo, V. Scuderi, C. Stancampiano, A. Tramontana, A. Amato, G.F. Caruso and S. Salamone*, Calibration and energy resolution study of a high dispersive power Thomson Parabola Spectrometer with monochromatic proton beam,* 2014 JINST 9 T10003 (2014)
[2] F. Schillaci et al., *Design of the ELIMAIA ion collection system*, 2015 *JINST **10** T12001*.
[3] F. Schillaci et al., *Design of a large acceptance, high efficiency energy selection system for the ELIMAIA beam-line*, 2016 *JINST **11** P08022.*
[4] F. Schillaci et al, *Status of the ELIMED Beamline at the ELIMAIA facility*, 2016 2016 JINST **11** C12052
[5] Friedrich Paschen (1889). "*Ueber die zum Funkenübergang in Luft, Wasserstoff und Kohlensäure bei verschiedenen Drucken erforderliche Potentialdifferenz* (On the potential difference required for spark initiation in air, hydrogen, and carbon dioxide at different pressures)". *Annalen der Physik*. **273** (5): 69–75. doi:10.1002/andp.18892730505
[6] PBN data-sheet from Morgan Advanced Materials (http://www.morgantechnicalceramics.com/media/2315/pbn-datasheet.pdf)
[7] M. Roth and M. Schollmeier, *Ion Acceleration – Target Normal Sheath Acceleration,* Proceedings of CAS-CERN Accelerator School: Plasma Wake Accelerator (2016)
[8] MIDEL 7131 datasheet (https://soltexinc.com/wp-content/uploads/2017/12/MIDEL_7131_.pdf)

6. Conclusions

This work focuses on the design of a compact ion transport beamline (ELIMED) for laser-driven ion beams realized and installed at ELI-Beamlines in the dedicate ion acceleration experimental hall (ELIMAIA). The ideas behind the technical solutions adopted for the realization of each magnetic element have been highlighted in the text. The main elements of the beamline, namely the collection system and the energy selector, have been also characterized with conventional ion beams at INFN-LNS showing promising results in terms of performances. Hereafter, the most important points of this work are summarized .

The PMQs system have been designed to have high field quality and all the possible issues related to the magnetic design have been investigated and solved (demagnetization analysis, thermal stability and the neutron flux study). The attraction/repulsion forces between quadrupoles are a crucial issue and they have been deeply investigated and used for the design of the displacement system which has been studied and realized to withstand these huge forces.

Laser-driven ion beams are typically characterized by an exponentially decreasing energy spectrum and a huge angular aperture which varies from few tens of degrees for the faster particles to an almost 2π for the slower ions. Moreover, the angular distribution cannot be easily modeled because it is investigated only from the theoretical point of view and, according simulations, it shows the presence of two peaks, both of them symmetric with respect to the main axis, similar to a sombrero hat. Saying that, the beam transport simulations results in the whole beamline have to be considered preliminary as the divergence of the beam is worst than those coming from the PIC (Particle In Cell) simulations output. In fact, each energy component has a uniform divergence between $\pm\theta$, being θ the maximum angle of Figure 2.17. More realistic simulations would have to use a gaussian angular distribution with a FWHM smaller than $\pm\theta$. Due to this approximations the transmission efficiency is below the 10% for the energy range to be selected and a more realistic case would provide better results.

The tolerance study has been performed considering the harmonic content of the PMQs. This is an important aspects not only from the magnetic point of view but also for the design of the mechanics associated with the system and its related precision and reproducibility. According to the results on this study performed in collaboration with SigmaPhi, manufacturer of the magnets and the mechanics, a precision of 2-3° on the single magnet magnetization direction and 2-3% on its remanence is needed, regarding the precision on the magnet positioning in the array could be around 0.2-0.1 mm. These tolerances have been easily achieved during the manufacturing process and should be enough to keep the field quality and to reduce the harmonic contribution coming from high order components, both normal and skew. Moreover, the tolerances on the magnet blocks positioning can be extended to the PMQs positioning and alignment as well.

The characterization performed with the standard ion beams at INFN-LNS shows that the PMQs optics can be controlled with acceptable accuracy, even if these magnets result to be sensitive to misalignment, as can be expected considering the tight tolerances.

The ESS system has been designed to be not just a chicane for selecting energies but to be used also as an active energy modulator able to deliver beamlets with different energy per each laser shot. This is an important aspects for radiobiological applications as the beam line could, in principle, delivery a spread-out Bragg peak within a certain number of consecutive shots. In this view, the interactions between dipoles have been carefully evaluated and eddy currents on the

vacuum chamber have been studied. Eddy currents could be an issue as they can produce an induced sextupole components which would have disruptive effects on the device performances. This effect results anyway negligible, according to both simulations performed in collaboration with the manufacturer Sigma Phi and magnetic measurements, and the system can operate with fields varying from 0,085 T up to 1,2 T with a frequency of 1 Hz. In this way protons from 3 MeV up to 250 MeV and carbon ions up to 60 MeV/u can be selected with a minimum energy resolution of 4%. Considering this feature, the ESS is an important device and the core of the ELIMAIA beamline in fact, it is already designed, realized and optimized to be used with the laser accelerated ions produced with the L3 Peta-watt laser but also with the L4 10 Peta-watt laser.
In any case, at the present state, the bottle-neck of the whole beamline is represented by the collection system that cannot be adjusted within one second. In fact, the PMQs do not allow to select a reasonable high amount of particle in different energy range without changing their position and the mechanics is robust but, obviously, extremely slow. Hence, to exploit the active modulator feature of the energy selector, it would be necessary to design a collection system based on electromagnets, most probably superconductive solenoids.

The error study on the beam line has been also performed, according to source centering and pointing errors foreseen at ELIMAIA. Results shows that, due to the large acceptance of the beam line, especially of the ESS, the output beam is not affected by random errors from the source, as long as the errors are in the range presented in Chapter 3.
The results coming from these preliminary simulations show that the beam line performances are strongly affected by the beam quality at the source. Hence, the next phase of the beam line optimization should be accomplished using more precise and updated data coming from PIC simulations and, which is extremely important, a precise experimental characterization of the beam source (in terms of energy spread, divergence and beam spot size) should be performed before the commissioning of the beam-line. In anycase, the installed devices have been calibrated with standard beams and, once the real laser-driven source term will be known the final commissioning should be straight forward.

The additional beam-transport elements have been defined from both the magnetic and geometric point of view. They result to be standard lenses and optimization of field has been left to manufacturer (SigmaPhi). This would allow to have a transport system based on the same technology and able to work at 1Hz repetition rate. Transport performances are satisfactory in terms of transmission in the last part of the beam-line. Optics can be easily adapted to different users request as this last part of the beamline results to be quite flexible.

Transmission efficiency in the last section (after the ESS) is of about 90% of the ESS output for each proton energy. This section has been designed using standard and simple electromagnetic quadrupoles with a big bore and a relatively high gradient in order to have margin for improving the beam quality before the irradiation point.

Moreover, some very preliminary calculations on the dose associated with the transported beam show encouraging results even if the beam uniformity has to be improved. This considerations are also supported by experimental results obtained with the prototype of the ELIMED beam line [1] used at a low power laser facility. During this campaign cell irradiation experiments have been performed showing comparable results with conventional accelerators in terms of dose and RBE è [2].

Finally, the preliminary conceptual design of a Thomson Parabola spectrometer has been finalized in order to provide a high quality analysis for the high energy ions expected at the

6. Conclusions

ELIMAIA beamline. The high voltage to be used presents some complication but a good insulator (PBN for example) could be enough to prevent discharges considering the simulated field distribution. In any case some prototyping would be necessary to test the assembling and fixing method in the ESS vacuum chamber, to check if some discharge can occur, and to define a proper conditioning cycle. The complete realization has still some points to be fixed. A proper tool for inserting and fixing the insulator and the electrodes onto the chamber roof and ceiling has to be designed and realized. The collimator, based on a double blade system, and the detector, based on a scintillator with a 45 mirror and camera, have to be designed and realized. The design of these devices will require some precision mechanics with actuators and remote control in order to have a reliable and user friendly device at the end of the realization.

The actual status of prototyping face started with support of an expert mechanical company a company specialized in electric field production in vacuum. Preliminary tests on a first mock-up of the chamber are expected to be completed by the end of 2019. These tests would fix the final insulator material, and the installation procedure of the electrodes in the chamber.

[1] F. Schillaci et al., *Characterization of the ELIMED Permanent Magnets Quadrupole system prototype with laser-driven proton beams*, 2016 JINST 11 T07005
[2] L. Pommarel et al., *Spectral and spatial shaping of a laser-produced ion beam for radiation-biology experiments,* Phy. Rev. AB 20, 032801 (2017)